# DESIGN AND OPTIMIZATION OF ULTRATHIN SILICON FIELD EFFECT TRANSISTOR'S FOR SENSITIVE, ELECTRONIC-BASED DETECTION OF BIOLOGICAL ANALYTES

BY

BRIAN DORVEL

DISSERTATION

Submitted in partial fulfillment of the requirements
for the degree of Doctor of Philosophy in Biophysics and Computational Biology
in the Graduate College of the
University of Illinois at Urbana-Champaign, 2013

Urbana, Illinois

Doctoral Committee:

Professor Gary Olsen, Chair
Professor Rashid Bashir, Director of Research
Professor Hyun Joon Kong
Assistant Professor Gang Logan Liu

# ABSTRACT

Noncommunicable diseases (NCD) are currently the leading cause of death worldwide. Over 57 million deaths occur globally each year, with close to 36 million of them attributed to NCD's, and 80% of those in low and middle income countries. Most of these were due to such chronic illnesses as cancer, cardiovascular disease, diabetes, and lung disease. Moreover, the prevalence of these diseases is rising fastest in low-income regions which have little resources to combat these large, yet avoidable costs. In particular, over 1.6 million cases of cancer are caused each year in the United States, with nearly 600,000 of these cases being fatal. Cancer is an uncontrolled growth and spread of abnormal cells in the body, and unfortunately, can exist in many different cell types. The complexity in the causes of cancer has made it tougher to diagnose since several factors may weight into its prevalence such as: genetic factors, lifestyle factors, certain types of infections, and different environmental exposures. As a result, the protocols for the most cost-effective intervention are available across four main approaches to cancer prevention and control: primary prevention, early detection, treatment, and palliative care. Early diagnosis based on awareness of early signs and symptoms and, if affordable, population-based screening improves survival, particularly for breast, cervical, colorectal, skin and oral cancers.

If primary prevention of cancer fails, secondary prevention (early detection) may be the difference between irreversible spread of a malignant cancer, and the patient's survival. Early detection commonly refers to the diagnosis of a disease before individuals show obvious signs or symptoms of illness. With cancer, RNA and protein biomarkers of

cells are currently assayed to determine their serums level and if they have deviated from the normal ranges. However, these assays commonly require large centralized lab facilities, frequent monitoring during treatment, and expensive equipment and/or supplies. This has led to point-of-care diagnostics becoming a $16 billion global market, aimed at miniaturizing technology and making it cost-effective for individual patient testing and treatment without the use of centralized lab facilities. A main point-of-care testing platform being pursued utilizes Complementary Metal Oxide Semiconductor (CMOS) technology. CMOS-based products can enable clinical tests to be conducted in a fast, simple, safe, and reliable manner, with improved sensitivities. Moreover, CMOS products offer portability and low power consumption, in large part due to the explosion in the semiconductor and communications markets.

Silicon nanowires are of great interest for point-of-care testing as they are a CMOS compatible structure, require the use of no labels, and are highly sensitive to the binding of molecules to their surfaces. This is due to the large surface area to volume ratio afforded to nanowires. Moreover, arrays of silicon nanowires have demonstrated multiplexed, label-free sensing of cancer markers from undiluted serum samples. However, the research going into CMOS for point-of-care is in its infancy compared to other optical (surface plasmon resonance, fluorescence) or electrochemical methods (glucose sensors), although the technology for CMOS has been around for decades. Thus, the protocols for optimization of the sensors and their bioconjugation have not matured to the point DNA microarrays and ELISA's have. The protocols for creation of a dependable silicon nanowire biosensor revolve around three main aspects: semiconductor processing, device functionalization, and choice of analytes.

In this dissertation, I discuss our efforts to create a stable, silicon nanowire based sensor using CMOS compatible techniques and optimization processes. Moreover, I talk about our efforts into creating a device functionalization protocol using monofunctional silanes which affords the best sensitivity and specify for an electronic based biosensor. Finally, I discuss our look towards the future in silicon nanowires by using high-k dielectrics in our fabrication process, as well as an alternative monolayer deposition method which utilizes sub-nanometer thickness poly-l-lysine monolayers, for sensing clinically relevant targets of microRNA.

Using a special type of silane, called a monofunctional silane, and a vapor based deposition method, we were able to achieve sub-nanometer levels functional monolayers on thermally oxidized silicon surfaces. We employed a variety of characterization techniques (XPS, AFM, ellipsometry) to determine the densities of the monolayer, uniformity, topography, and their point of saturation. Furthermore, we demonstrate this method's applicability to biosensors by using it to functionalize substrates for silicon nanowires, gold nanoparticles, and protein microarrays.

In tandem with this work, we constructed a "top down" silicon nanowire processing protocol which yielded nanowires capable of long-term, stable measurements in aqueous solutions. The combination of anneals, dry etching, and final wet etching gave mV standard deviations in device threshold characteristics. This protocol combined with the monolayer protocol above allowed an in-depth characterization of the pH sensitivity of bare devices, ones with silanes, and ones conjugated with proteins to be determined. Similarly, different oxide thicknesses and their effect on device sensitivity for proteins were also explored. Using a bunch of different linker chemistries and characterizing their

conjugation of antibodies through fluorescence and the device, allowed for a chemistry to be chosen which was used to sense mouse immunoglobulins in pg/mL levels with high specificity.

Finally, we take the fabrication of nanowires to the next level by using high-k dielectrics ($HfO_2$) as the gate insulator. We deposit $HfO_2$ through ALD (atomic layer deposition) and optimize the anneals to provide nanowires with ~200mV subthreshold slopes, sub-mV threshold deviations, and sub nanoampere gate leakages. All these characteristics exceed the processes for thermal oxide gated silicon nanowires, some by an order of magnitude. Since $HfO_2$ is a high-k material, reaction of silanes and its density were unknown, but high-k materials do form stable amide linkages. Thus, we optimized a wet deposition of small molecular weight poly-l-lysine to provide a sub-nm conjugation layer for proteins and nucleotides by using AFM, XPS, and ellipsometry to understand the process. Using these combined protocols, we were able to conjugate probe oligonucleotides to surfaces and detect target microRNA's down to 100fM concentrations, with a dynamic range over 4 orders of magnitude. With these ranges well within the clinical levels (1pM-100pM), we believe silicon nanowires have the capability to become a well-established point-of-care diagnostic platform.

# ACKNOWLEDGMENTS

I would have to say achieving my Ph.D has been one of the toughest experiences of my life. I thought I understood what persistence was before starting graduate school, but I was gravely mistaken. The pursuit of a PhD at University of Illinois allowed me to be amongst some of the brightest individuals of this age, and more importantly, learn from them. I mean, there are few places in the world where you can see people each day like the inventor of the LED (Nick Holonyak) walking back and forth from lab to lab, and be able to interact with them! Not only has Illinois gifted me with great knowledge and skillsets, but everlasting friendships as well. Achieving my PhD would not have been possible without the moral and mental support of friends and family. I would like to acknowledge these individuals who have helped me achieve this goal.

First and foremost, I would like to thank my advisor, Rashid Bashir, for allowing me the opportunity to work in his lab and for him taking me on as a PhD student. I had started two years earlier in a previous lab, and then applied to work with Professor Bashir when my former advisor and I did not agree on some things. Professor Bashir gladly took me in and put me on a project. Professor Bashir is probably one of the most caring individuals I have encountered at UIUC when it comes to educating his students and taking care of them. Moreover, his knowledge base and insight into where research is heading was invaluable to my success as a grad student. I thank him for all his years of motivation and support, making sure me and my colleagues could achieve our goals and prepare for a bright future. Although we had our differences, I do thank my previous advisor Greg Timp for his knowledge and insight into semiconductors. Coming from a

chemistry background, my experience with semiconductors was minimal, and without his classes and notes my PhD may not have been possible. I would have to say he is one of the brightest individuals I have met and his knowledge passed to me about MOSFET's was invaluable to my PhD, as a lot revolved on this. I would also like to thank the few collaborating professors which I have worked with in the past on these projects. Professor Ashraf Alam at Purdue gave me a prominent understanding into the theory of semiconductors and their modeling. The knowledge gained about the theory of MOSFET's complemented the experimental understanding to give me a full picture of creating a stable, working device. Sue Clare at IUPUI was quite possibly the best clinical contact I could work with, and her insight into biological mechanisms of cancer and its progression gave me the understanding of which types of targets to work with for my thesis.

I would also like to thank the funding agencies which gave me the opportunity to work extensively on these exciting projects. Namely the NIH, Intel Corp., TSMC, and the Midwest Cancer Nanotechnology Center (M-CNTC). These agencies provided me with fellowships so I could solely focus on research, and funding of partnerships which helped build better devices and clinical information towards creating a true point-of-care device.

Knowledge about designing experiments and the physics of devices is excellent, but another crucial part which was needed is understanding instruments and fabrication. The Materials Research Lab staff on campus gave me the knowledge and training necessary to understand the materials properties of my devices, and contributed a lion's share to my thesis. Thus, I would like to thank Rick Haasch (XPS), Scott Maclaren (AFM), Tim Spila (TOF-SIMS), and Jianguo Wen (TEM) for their thorough training on

the instruments in parenthesis, and passing their knowledge of how to extract the most data from each instrument. The cleanroom at MNTL was my second home for the duration of my PhD (close to 7 years). Unfortunately, it's a cleanroom so a bed isn't able to fit with shedding particles, or I'm sure several of my colleagues may have never left and just slept in there. It is open 24/7 and has close to 300 users, meaning lots of equipment which has to be maintained and be in top condition for the most stringent processing. Thus I would like to thank our gracious staff who so diligently maintain this space for us users dedicated to the bunny suit: John Hughes (associate director), Hal Romans (deposition), Mike Hansen (CVD and lithography), Yaguang Lian (reactive ion etching), and Edmond Chow (characterization and e-beam lithography). Finally, I would like to thank our staff who helped with all my purchases, as research can't continue without supplies. And I know I couldn't order it all myself, or I would get no research done. Thus I thank Tasha Chambers, Nandini Topudurti, Karen Driscoll, and Ashley Childress for their help, and making my life a little easier.

Finally, I would like to thank those which have been closest to me during this 7 year adventure, giving me the moral and mental support needed to make it to the finish line. I would like to thank my partner in crime, Bobby Reddy Jr., as he is probably one of the smartest people I have met, and without his scripting skills and computer science knowledge I would have been in a world of pain. Bobby and I have suffered through thick and thin for close to 5 years together creating silicon nanowires in the cleanroom for biosensing, and we both were able to resolve any differences we may have had and make it through. I would also like to thank Murali Venkatesan for the good times we had and support when things got tough. He was a good friend all around. Similarly, my friend

Valentin Dimitrov was invaluable in helping me achieve my PhD, as we would frequently encounter failed experiments and somehow be able to shrug them off and persist. I would also like to thank Vincent Chan, Piyush Bajaj, and Elise Corbin for insightful conversations, and occasional laughs to help alleviate those days of failed experiments. Also, I could not have made it through without my most loving, trusting girlfriend, Sherine George. She means the world to me and has always supported me through thick and thin. Most importantly, I would like to thank my family for all their support. When times got tough for me, either financially, emotionally, or mentally, they would always be there for me. My mother, Paula Dorvel, and my father, Phillip Dorvel, are the best parents a child could ask for. Their care and support really paved the way for me to become the individual I am today, and to give me the strength to achieve my PhD by thinking about the hardships they had to overcome in life to be successful. There is also my sister, Rose Dorvel, and brother, Ben Dorvel, which would also be good listeners when I would complain and moan. Although younger siblings, each one has valuable advice to offer in situations, as two opinions are better than one! Most importantly, they gave me other things to think about outside of science. Although science is a great part of my life, if it was my entire life I think I might go insane. Thus, it would always be great to listen about things happening in other parts of the country and how their days are going.

“I don't understand. Why the legend about the city of gold? Well, the Ugha word for 'gold' translates as 'treasure.' But their treasure wasn't gold, it was knowledge. Knowledge was their treasure.”

- Indiana Jones and the Kingdom of the Crystal Skull

# TABLE OF CONTENTS

# CHAPTER 1: INTRODUCTION

Currently, cancer is a leading cause of death worldwide with over 7.6 million deaths in 2008. This number is expected to rise to over 13 million by 2030. Furthermore, the medical expenditures in the United States due to cancer are expected to reach $158 billion- and increase of over 27% from 2010.[1] Cancer usually arises from one single cell. The transformation into tumor cell is a multistage process, typically a progression from a pre-cancerous lesion to malignant tumors. Unfortunately, classical testing methodologies such as ELISA (Enzyme Linked Immunosorbent Assay) for biomarkers often provide sensitivities in the ng/mL range, which are quite often at a late stage of the disease where metastasis has already occurred. These changes in biomarker levels are the result of a complex interaction between a person's genetic factors and physical, chemical, or biological carcinogens. Thus, knowledge about the causes of cancer, and interventions to prevent and manage the disease is imperative to achieving a high chance of cure. In order to reduce costs of treatment as well as increase the chance of survival, several routes are currently being taken:

- Early detection of cancer, commonly using more frequent screening and education of symptoms, has shown to be directly correlated to the survival of patients
- Trending patient care away from the hospital by removing the need for costly centralized lab facilities, which commonly utilize large support staffs and multi-million dollar pieces of equipment
- More frequent monitoring of disease treatment to prevent relapses and chemotoxicity due to treatment

Point-of care (POC), or lab on a chip, devices essentially bring the lab to the site of patient care. POC testing shows promise for revolutionizing the way diagnostic testing is performed, not only for cancer but for all chronic diseases. Several drivers are pushing the analytical applications of POC devices forward. The flexibility of the platform and the compact design allows for the technology to be rapidly adopted since production costs are less. And with the discovery of more molecular biomarkers for diagnostic testing, the multiplexing capability and automation of processes make POC devices particularly enticing. The portability of POC devices removes the need for transport of samples to centralized facilities, while providing faster medical decisions. Moreover, POC devices are being manufactured to be disposable and easy to use, yet be cost effective. An example integrated silicon biochip device for PCR (polymerase chain reaction) of target genes is shown in Figure 1.1.[2,3] This device is made by ST Microelectronics, which is one of the many players in the POC testing market. It consists of a sample loading area of 1-4 ports (i), which then leads through microfluidics to a PCR amplification area with heaters for thermal cycling (ii), then through microfluidics (iii) to an arrayed detection area for targets (can be 120-400 probes).

Even though the POC market has grown considerably in the last decade, there is still much opportunity to improve the technology. Some issues which continuously plague the industry are: fabrication and increasing miniaturization of the devices, increasing sensitivity to low serum level biomarkers, and competing with the already automated practices (such as optical microarrays). CMOS technology has the possibility to alleviate many of these issues, as transistors are now passing the 32nm node, due to the

aggressive scaling of Moore's Law. This makes multiplexing and automation for 1000's of biomarkers plausible. In this dissertation we shall discuss the currently available technologies for biosensors and POC devices, as well as our efforts into improving the technologies using a CMOS compatible platform.

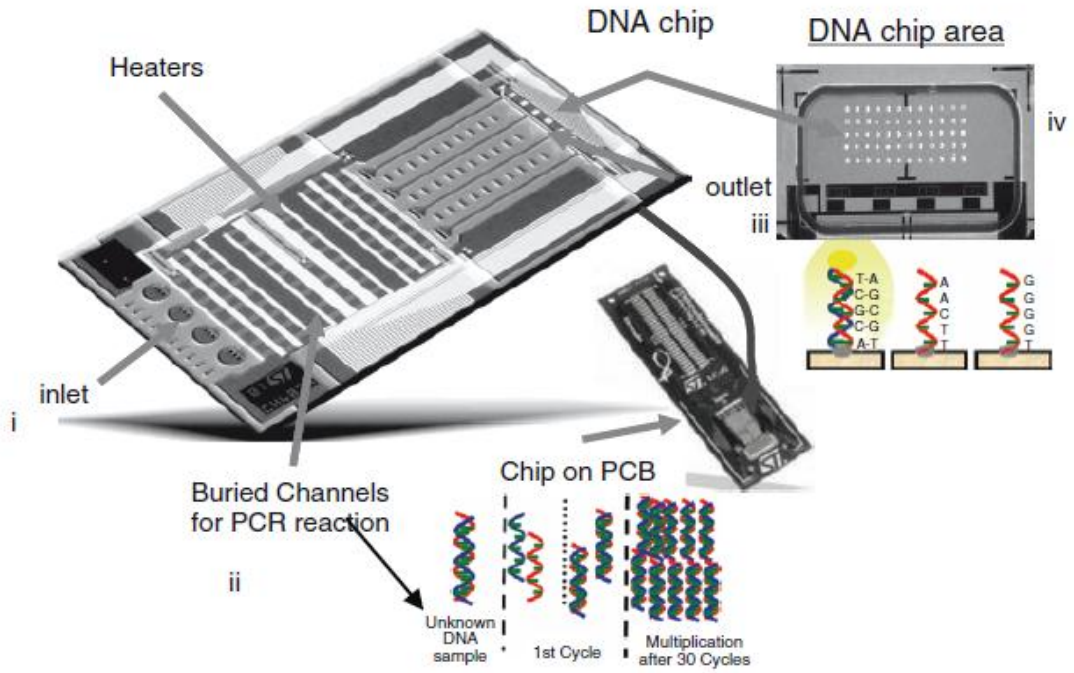


**Figure 1.1**. Architecture of the Lab-on-Chip: (i) Input microfluidics ports for sample loading, (ii) PCR DNA amplification region, (iii) microfluidics interconnection, (iv) DNA microarray region(ST Microelectronics), from [3].

In Chapter 2 a thorough review of the fundamentals of biosensors, the types of biosensor outputs, FET based sensors, the functionalization of these sensors, and the opportunities are covered. The beginning section discusses the main elements which make up biosensors and the types of output they provide, as well as the types of analytes they can process. We also go over the "classical" biosensing methods of DNA microarrays and ELISA as a beginning comparison. Furthermore, we discuss the two main types of sensor platforms in place at present: optical and non-optical detection.

Optical detection modalities such as surface plasmon resonance, waveguides, photonic crystals, and fluorescence will be the primary focus of this section. The current advantages, detection limits, and assaying principles will be covered. Similarly, the non-optical method of detection will be highlighted, focusing on electrochemical and impedance methods, quartz resonators, and micro-electromechanical devices. The advantages and variety of analytes detected will also be reviewed. The next section we go over the theory of field-effect transistor (FET) based sensors, a specific type of electrical sensor, and the types of analytes which have been sensed using classical FET's and silicon nanowires. Finally, we discuss the opportunities silicon nanowire CMOS technology holds for POC diagnostics.

Chapter 3 focuses on the interfacing of biological analytes to single molecule linking layers, commonly referred to as self-assembled monolayers, for high density linkage to silicon oxide surfaces, a common sensing interface for FET-based devices. Since the sensitivity of electrical and photonic based devices decays exponentially with the distance the antigen is to the surface, achieving uniform sub-nanometer layers for device functionalization is critical. In this chapter we discuss our characterization and use of monofunctional silanes to form high density, sub nanometer thick linking layers on $SiO_2$ surfaces. We determine a protocol using vapor based depositions for epoxy and amino functionalized silanes by characterizing the layers using x-ray photoelectron spectroscopy (XPS), atomic force microscopy (AFM), and ellipsometry. We finally demonstrate the use of these layers for conjugation to a wide variety of functional groups and to silicon nanowire FET devices using immunoglobulins for the antibody-antigen assay.

In chapter 4 we discuss the fabrication of $SiO_2$ based silicon nanowire devices and the design of protocols for their use as a protein biosensor. Protocols for functionalization of ELISA's, DNA microarrays, and other fluorescence assays have been well established, but are lacking when it comes to electronic based devices. In this chapter we use silicon nanowire devices, in conjunction with the vapor based deposition of silanes, to sense immunoglobulins at different concentrations and generate a dose response curve. We investigated different linking chemistries for antibodies to the amine modified surfaces through fluorescence and the nanowire devices, choosing a polyethylene glycol (PEG) based linker that gave the best signal-noise ratio. Since many FET based biosensors, such as enzyme FET's (EnFET's)[4] and the new DNA sequencing technologies[5], utilize pH as their readout sys We characterize the pH response of each of the layers as well, since many sensors rely on pH changes generated by enzymes for their response. Using this PEG based linker and vapor based aminosilane monolayer, we demonstrate this protocol to give negligible non-specific binding of similarly structured antigens. Moreover, we characterize the sensitivity of the devices based upon dielectric thickness, as thicker dielectrics are known to give poorer response.

In chapter 5 we discuss the next generation of CMOS compatible silicon nanowires which utilize high-k dielectrics to sense microRNA targets. The fabrication of the nanowire devices using hafnium oxide ($HfO_2$) is overviewed and the optimization of the gate dielectric. Capacitance-Voltage (CV) curves and wet etch tests were used to monitor the effect of anneals on the devices to passivate interface traps. This optimized process was able to give us ~200mV/decade subthreshold swings, which was %100 better than previous $SiO_2$ based processes. Since $HfO_2$ has different properties and binding of

normal silanes may be less than a $SiO_2$ layer, we use a monolayer of low molecular weight poly-l-lysine which can first be electrostatically adsorbed then crosslinked. We characterized and optimized this layer for binding of probe DNA to the poly-lysine surface. Using these devices and their corresponding functionalization, we were able to have a detection limit (3σ) of miRNA target (miR-10b) down to ~10fM, which is 3 times the standard deviation (3σ) generated from the non-specific target (miR-21).

In chapter 6 I briefly discuss the main conclusions of this dissertation and our future work. Currently, this work takes chapter 5 a step further, where we are now collaborating with semiconductor foundries for the fabrication of CMOS chips with extended metal gates for sensing. These chips contain various gate lengths and widths, as well as n-type and p-type devices. Furthermore, they are capped with $HfO_2$ sensing dielectrics on top of the gate for pH testing and device functionalization. We have optimized anneals on these devices to achieve excellent stability in fluid and are currently testing their sensing properties with RNA and proteins. By monitoring the device current vs. time in the most sensitive regime (subthreshold), we hope to achieve pg/mL limits of detection for both oligonucleotides and proteins. These detection limits are within range of most clinical cancer biomarkers, and would give credence to CMOS devices and silicon nanowires as a plausible molecular diagnostics platform.

# 1.1 REFERENCES

[1]. Yabroff, K. R.; Lund, J.; Kepka, D.; Mariotto, A., Economic Burden of Cancer in the United States: Estimates, Projections, and Future Research. *Cancer Epidemiology Biomarkers and Prevention* 2011, 20, 2006-2014.

[2]. Palmieri, M.; Alessi, E.; Conoci, S.; Marchi, M.; Panvini, G., Developments of the in-Check Platform for Diagnostic Applications. 2008, 688602-688602.

[3]. Vauchier, C.; Puget, P., Biochips. In *More Than Moore*, Zhang, G. Q.; Roosmalen, A., Eds. Springer US: 2009; pp 179-202.

[4]. Kharitonov, A. B.; Zayats, M.; Lichtenstein, A.; Katz, E.; Willner, I., Enzyme Monolayer-Functionalized Field-Effect Transistors for Biosensor Applications. *Sensors and Actuators, B: Chemical* 2000, 70, 222-231.

[5]. Rothberg, J. M.; Hinz, W.; Rearick, T. M.; Schultz, J.; Mileski, W.; Davey, M.; Leamon, J. H.; Johnson, K.; Milgrew, M. J.; Edwards, M., et al., An Integrated Semiconductor Device Enabling Non-Optical Genome Sequencing. *Nature* 2011, 475, 348-352.

# CHAPTER 2: BACKGROUND AND LITERATURE REVIEW

## 2.1 BIOSENSOR BASICS

The field of biosensor technology originally developed in the 1960's from electrochemical sensors to detect glucose[1] and urea[2]. These sensors immobilized enzymes (namely urease and glucose oxidase) onto an electrode and measured the concentration of the analyte by the current produced through enzymatic reaction. A biosensor is defined by The National Research Council (part of the U.S. National Academy of Sciences) as a detection device that incorporates a) a living organism or product derived from living systems (e.g., an enzyme or an antibody), b) a transducer to provide an indication, signal, or other form of recognition of the presence of a specific substance in the environment, and c) an output for statistical processing of the data generated. Ideally, biosensors must be designed to detect molecules of analytical significance, pathogens, and toxic compounds to provide rapid, accurate, and reliable information about the analyte of interrogation. A generalized schematic of a biosensor is in Figure 2.1, highlighting the flow of how a biosensor works.[3,4] Overall, there are several detection devices (recognition elements) which are utilized for analyte detection, and nearly as many transduction methods in practice to generate a measurable signal. A list of common recognition elements and transducers is highlighted in Figure 2.1, and will be reviewed below.

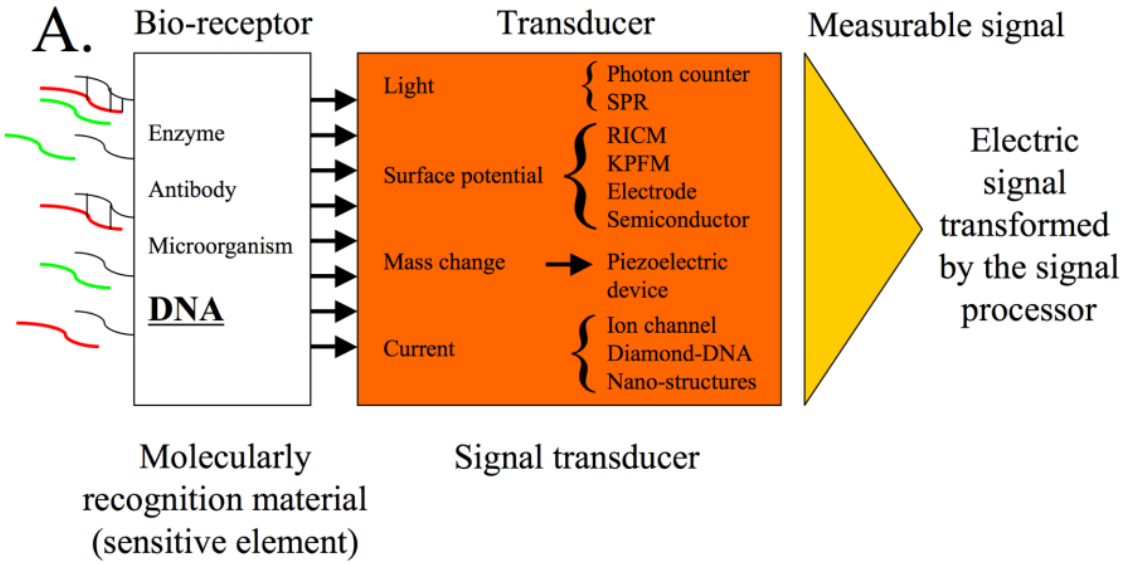


**Figure 2.1**. Generalized schematic of a biosensor setup, from [4].

## RECOGNITION ELEMENTS

Most biological processes implement the use of small molecules, proteins, and DNA/RNA in complex reactions so life can proliferate. Thus, the recognition elements for biosensors are geared towards sensing these biomolecules of interest. Since the beginning of the biosensor field in the 1960's, enzymes have been very popular, primarily due to the need for monitoring glucose in the blood, and the development of the glucose sensor. Enzymes are proteins which act as highly efficient catalysts, lowering the activation energy barrier for precursor molecules (substrates) to react and transform into products. Most reactions essential to life use enzymes so that they may occur at a reasonable rate. One particular type of biosensor, the enzyme electrode, is an electrochemical type of sensor which has a thin-film enzyme layer attached to it. The embedded enzymes produce a variety of products such as $H^+$, $O_2$, $CO_2$, $NH_4^+$, and $H_2O_2$, and these products can generate amperometric signals on conductive substrates through redox reactions (Figure 2.2) .[5] Some enzymes which have been used commonly to

generate output include oxidoreductases, glucose oxidase, horseradish peroxidase, and alkaline phosphatase. Several types of small molecules have been able to be detected utilizing enzyme catalysis in clinically relevant levels. Well studied molecules of interest have included glucose[6-11], bilirubin[12-14], lactose[15-17], urea[18-20], malate[21-24], NADH[25-29], acetycholine[30-32], and glutathione[33-35].

Other targets relevant to biologically processes typically include proteins and DNA/RNA. Changes in the expression levels of these analytes may signal onset of a variety of genetic or infectious diseases, as well as cancer. The detection of proteins relies around a class of biosensors known as immunosensors. Immunosensors are affinity ligand-based biosensor devices in which the immunochemical reaction is coupled to a transducer. Because of their high affinity and widespread availability, antibodies have become the prime choice for a recognition element in affinity biosensors.[36] Commonly, the antibodies or receptor proteins are immobilized on the sensor using covalent linking methods or physisorption, and have affinities to the antigen or ligand of interest. A certain type of antibody class, known as immunoglobulin G, are very similar in structure between variants, however, their affinities for antigens may vary widely. These differences in antigen specificity and binding affinity originate from the variations in amino acid sequence at the antigen binding site.[37] The antibody binding sites are located at the ends of two arms ($F_{ab}$ units) of this "Y-shaped protein." The base of the "Y" referred to as the Fc unit is less variant and contains species-specific structure, which is commonly used as an antigen for production of species-specific (anti-IgG) antibodies. The binding to this region is commonly employed in sandwich ELISA assays. The

differences in antibody–antigen binding characteristics influence the wide range of detection limits observed for antibody-based biosensors.

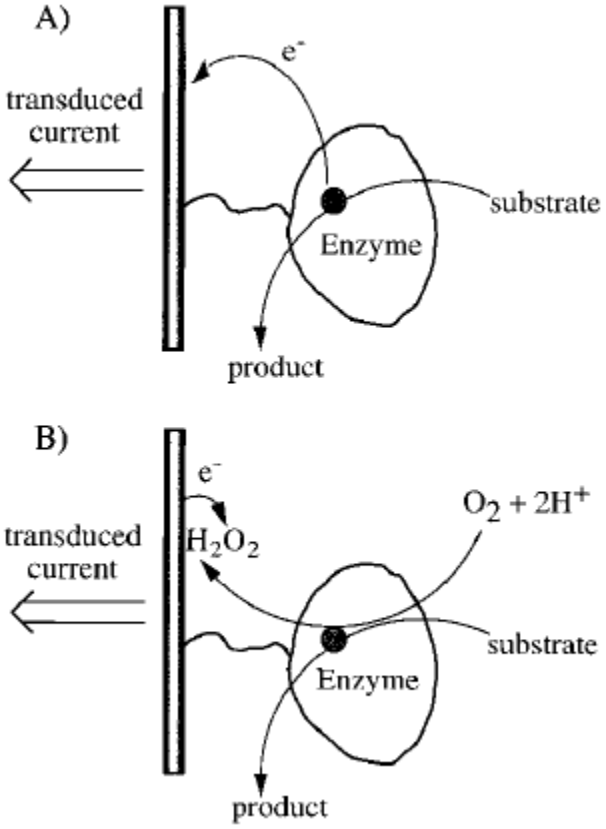


**Figure 2.2**. Integrated enzyme electrodes for bioelectronic applications: A) bioelectrocatalyzed oxidation of a substrate, B) electrochemical reduction of $H_2O_2$, which is formed upon the $O_2$-biocatalyzed oxidation of the substrate, from [5].

Another type of antigen for proteins in use, albeit more recently, is DNA and RNA aptamers. Aptamers are single stranded DNA or RNA analogues which can fold into unique tertiary structures in order to form high affinity and high specificity binding sites for ligands of interest.[38] One of the major fallbacks of antibodies is that an antigen has to be injected into a host animal, and this is not received well if the antigen is especially toxic. Aptamers, also known as “chemical antibodies”, sidestep this because of their artificial process of generation called Systematic Evolution of Ligands by

EXponential enrichment (SELEX), which is described in Figure 2.3.[39] Briefly, random oligo libraries are generated and flown with the target analyte, with the unbound molecules separated from bound molecules afterwards. The bound nucleic acids are eluted, amplified by PCR (polymerase chain reaction) and serve as an enriched library for the next cycle. For every target, 6–12 consecutive cycles are performed and the final enriched library is cloned and sequenced. The breadth of targets now able to be sensed by aptamers rivals antibodies in detecting proteins and peptides, whilst also demonstrating abilities to sense metal ions, small organics, and even whole cells.[40]

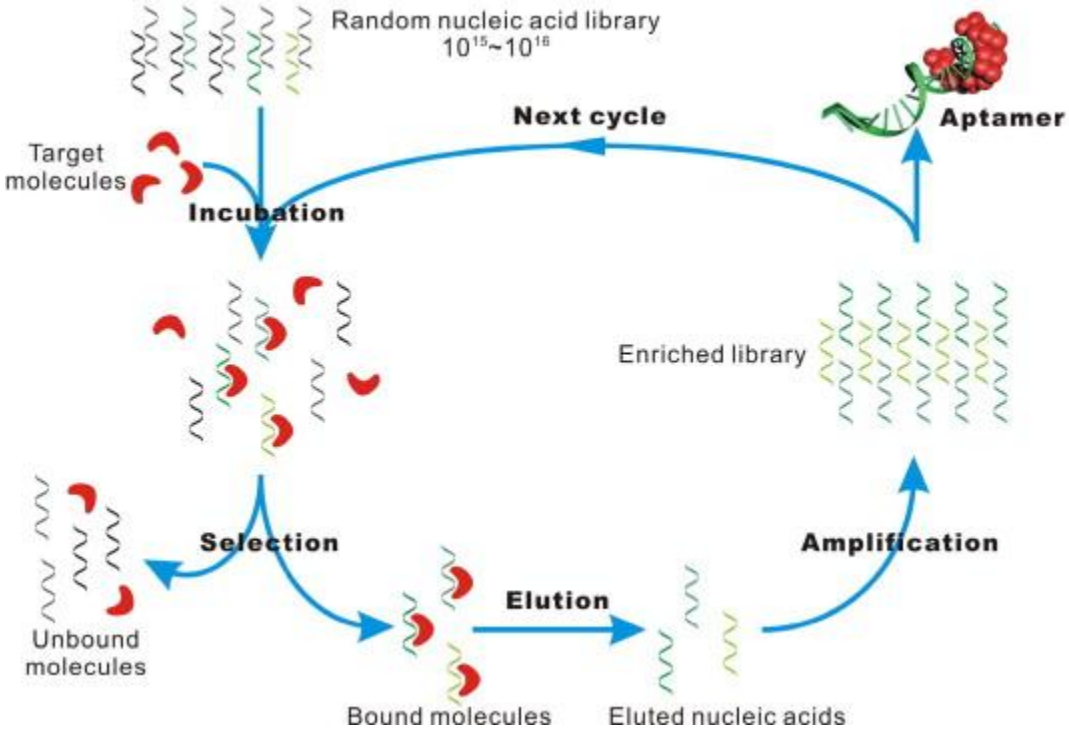


**Figure 2.3**. Scheme for the Systematic Evolution of Ligands by EXponential (SELEX) enrichment process for aptamer generation, from [39].

Nucleic acid sensing modalities have been around since the advent of DNA microarrays. Typically, oligonucleotides composing of RNA, DNA, or more recently, locked nucleic acids (LNA) [41] and peptide nucleic acid (PNA) [42], are covalently

bound to the sensor surface, and the target DNA or RNA is allowed to interact with these bound oligonucleotides. The oligo's are commonly referred to as probes. The hybridization of the complementary target to the oligo probe induces a response on the sensor either through optical or electrochemical means. In particular LNA's and PNA's have become popular since they create high stability duplexes through either, 1) a locked ribose ring, which stabilizes base stacking (LNA) or 2) a neutral backbone composed of peptide linkages, which removes electrostatic phosphate backbone repulsion (PNA). All of these recognition elements are currently utilized in biosensors today, with new recognition elements being conjured daily in the hopes of creating truly all-in-one immunoassays.

## TRANSDUCTION MECHANISMS

Biosensors can typically be grouped based upon their detection principle, or transduction method. The most common ones investigated are electrochemical, optical, and microgravimetric methods. A brief overview of the different types will be given in this section, followed by a more detailed review of optical and electrochemical technologies in subsequent sections. Typically with electrochemical methods, the reaction under investigation would generate a measurable current (amperometric), a measurable potential or charge accumulation (potentiometric), or measurably alter the conductive properties of a medium (conductometric) between electrodes.[43] Each of these methods has been thoroughly reviewed by several sources in excellent detail.[44-49]. Potentiometric sources measure the accumulation of surface charge, leading to a surface potential, on a working electrode vs. a reference electrode when zero to little current is allowed to flow between them. Thus, potentiometry essentially measures the

activity of the analyte or ion of interest. This potential is governed by the Nernst equation[50], which relates the concentration dependence of the measured potential to a standard reference potential (taken at a fixed analyte concentration). Amperometric devices constantly measure the current of an oxidation or reduction of an electroactive species at the surface of the electrode. Typically, the potential remains constant and the change in current is proportional to the concentration of the analyte. Capacitive or conductometric transducers measure the changes in electrical conductivity between two electrode nodes, typically caused by enzymatic reactions which remove or generate ions. However, this method has not achieved a large popularity due to the high salt concentrations in biological solutions, and the comparative minimal change in conductance by the enzymatic reactions.[51]

Optical methods of detection are still the most widely adopted biosensor transducer to this day. Currently the two most popular methods revolve around fluorescence based detection and label free detection, whereby a brief overview will be given below. In fluorescence based detection, a fluorescent tag is attached to either the target or the recognition molecule, and the intensity of the fluorescence emitted back to the detector is a measure of the concentration of the target analyte. Some major drawbacks, which have led to the development of label-free sensors, are the non-uniformity of the fluorophore labeling on molecules[52] and the degradation of target/analyte binding specificity due to the labels being in the binding site[53]. Fluorescence based methods have allowed the detection down to single molecules[53], but immunoassays rely upon statistics and ensemble measurements to make a diagnosis, and at this point in time measuring $10^9$ molecules individually, yet simultaneously has not

come to fruition. In label free based optical detection, the molecules are detected in their natural forms. Most commonly, the change in refractive index (RI) of the surface of the sensor is monitored, and will shift based on the concentration of target molecules in solution binding to the interface or changing the surface density. A few of the methods which will be discussed in detail are surface plasmon resonance, fiber optics, and photonic crystals. These methods claim a lion's share of the optical based, label-free market.

Microgravimetric sensors directly measure mass changes based upon the binding of target analytes to the sensor surface. The principle of operation is based on the propagation of acoustic shear waves in the substrate of the sensor. The velocity and phase of the propagating wave are influenced by the specific adsorption of target molecules onto the sensor surface. Piezoelectric materials, such as quartz ($SiO_2$), zinc oxide (ZnO) or others resonate mechanically at specific ultrasonic frequencies (in the order of tens of megahertz) when excited in an oscillating electrical field. The resonant frequency is determined by the distance between the electrodes on both sides of the quartz plate, which is equal to the thickness of the plate and the velocity of the acoustic wave within the quartz material.[54] Most microgravimetric sensors are based on quartz crystal microbalance (QCM), divided into thickness shear mode (TSM) and standing acoustic wave modes (SAW), each which will be discussed in subsequent sections. An excellent review of these sensors is given by Cavic [55] and by Janhshoff [56]. All these sensors are based upon the Sauerbrey equation, which states the change in mass is directly proportional to the change in frequency and the intrinsic properties of the crystal.[57]

## 2.2 CLASSICAL BIOASSAYS

### DNA MICROARRAYS

Ever since the 1990's, DNA microarrays (DNA chips) have been a major topic of research, becoming thoroughly developed and characterized. These type of devices have allowed for DNA and RNA hybridization to surfaces in miniaturized, highly parallel formats. As a result, they have been widely applied to genotyping expression and single nucleotide polymorphism (SNP) detection in target oligo strands. More recently, such microarray technologies have been branching away from typical genomics applications and towards pharmacogenetic research and cancer diagnostics. Since the platform uses substrates typically used in lab-on-a-chip devices, microarray diagnostics are being integrated with such platforms more and more frequently.

Typically these devices are fabricated on glass, plastic or silicon platforms. Moreover, they contain test sites which are 10-500um in size and are capable of having over $10^6$ binding sites/$cm^2$ of space. The principle of DNA microarray technology is based on the fact that complementary sequences of DNA can be used to hybridize to immobilized probe DNA molecules. This process involves three main steps[58]:

a. **Manufacturing of the microarrays**. There are currently two main approaches to microarrays being 1) pre-synthesized probe oligonucleotides or DNA are spotted onto the surface in nL/pL volumes using high density methods such as piezoelectric pin spotting or inkjet techniques[59] and 2) target oligo's are synthesized *in situ* on glass biochips using photolithographic techniques[60].

b. **Sample Preparation and hybridization**. The RNA or DNA targets must be specifically labeled or converted to a cDNA (complementary DNA) which is labeled, then hybridized to the surface.

c. **Data Analysis**. The microarray hybridization is scanned for the reporter or fluorescently labeled target and analyzed using highly-parallel software programs to interpret the data.

An example of both types of DNA microarray methods is shown in Figure 2.4. Although both types of manufacturing techniques have their advantages, the high density oligonucleotide arrays offered by Affymetrix, known as the GeneChip©, use this *in situ* technology of manufacturing and will be the main topic of discussion in the microarray field and its use in gene profiling as an example of how a microarray works. The Affymetrix GeneChip is currently the industry leader in microarray technology, with over 6.5 million features per array possible. The fabrication of an Affymetrix Genechip is shown in Figure 2.5.[61] Briefly, a silane layer containing hydroxyl groups is deposited on a quartz substrate, which a then reacted with linker groups that are photolabile. Using techniques from the semiconductor industry, photomasks are constructed which represent the sequence information and define the areas of the linker molecules which are to be deprotected by UV light. After deprotection, a phosphoroamidate nucleotide is reacted to that particular surface area and then oligonucleotide synthesis can continue through protection and deprotection to create ~25mer probe oligo strands directly on chip.

A typical sample preparation is shown in Figure 2.6. Most sample methods use *in vitro* transcription methods originally described by Eberwine.[62] In this method cDNA is generated from RNA using a T7 RNA polymerase primer composed of oligo dT's. the

synthesis of cDNA then starts adjacent to the polyA tail common to all messenger RNA (mRNA). After this, another transcription is carried out to generate a biotinylated RNA analogue. After overnight hybridization of these targets to the genechip, a fluorescent streptavidin is flown through the device to bind to the biotinylated targets on the chip, and can then be scanned using the appropriate photospectroscopic equipment.

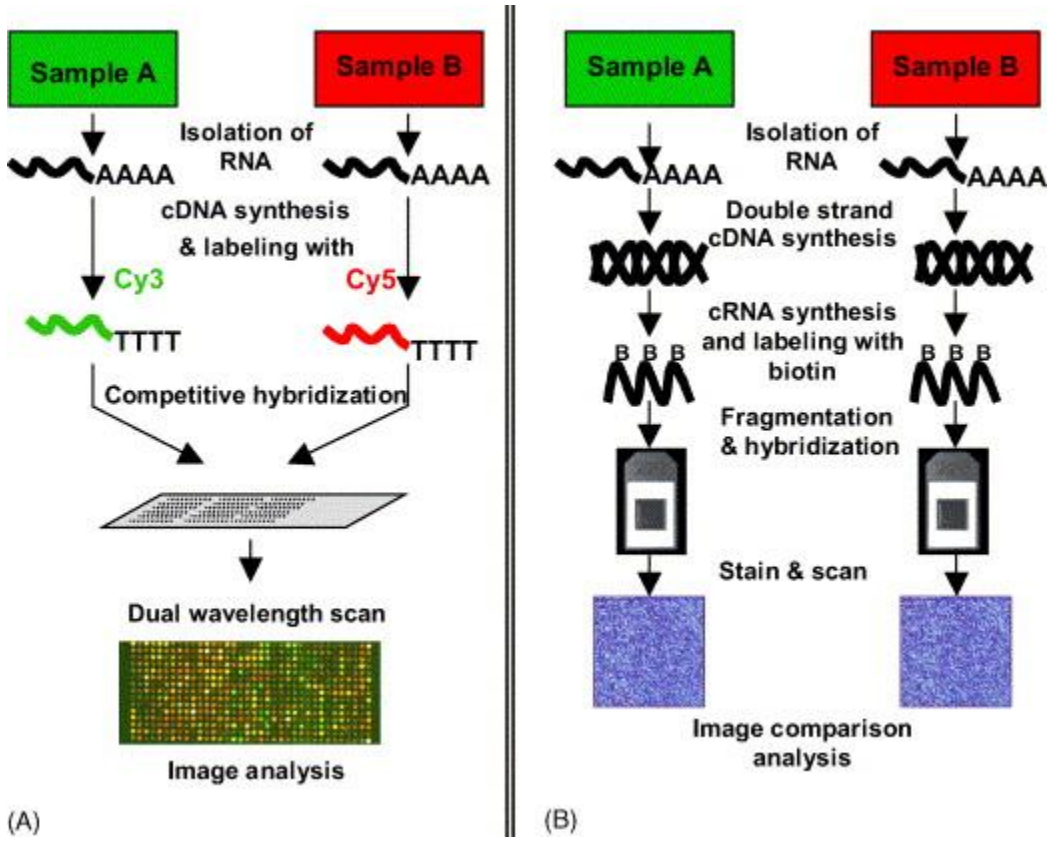


**Figure 2.4**. Outline of approach for spotted microarray (A) vs. high-density oligonucleotide microarray (B). Sample A: control; sample B: test. From [58]

The current technology is capable of scanning for over 100,000 single nucleotide polymorphisms on a single chip. Since the human genome on average contains over 3 million nucleotide differences from person to person, being able to measure over 100,000 SNP's has proven invaluable into mapping the human genome and discovering genes responsible for diseases. This technology has elucidated gene areas responsible for

predispositions to such diseases as lung cancer [63], ovarian cancer [64], and macular degeneration [65].

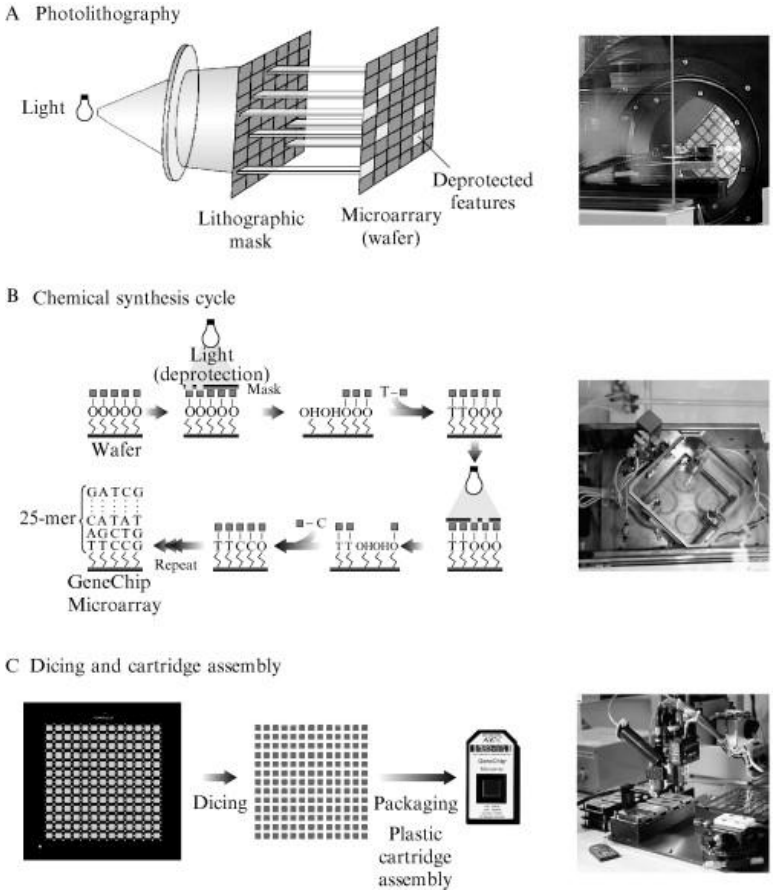


**Figure 2.5**. Manufacture of a GeneChip probe array. (A) Photolithography. (Left) Near-ultraviolet light is passed through a mask containing open windows. The size and the location of each open window delineate the surface on the quartz wafer that will be activated for chemical synthesis. The use of sequential masks in conjunction with the chemical synthesis creates a cycle that directs the precise sequence synthesis of oligonucleotides that compose the array. (Right) The photolithographic process. (B) (Left) Schematic representation of the nucleic acid synthesis cycle. Light removes protecting groups (squares) at defined areas on the array. A single nucleotide is washed over the array and couples to the deprotected areas. (Right) The chemical synthesis station, where nucleotide binding occurs. (C) (Left) Complete synthesis on the wafer results in many (49–400) identical high-density oligonucleotide microarrays in one wafer. Dicing of the wafer into individual microarrays occurs, and each microarray is inserted into a plastic cartridge. (Right) Machinery used to incorporate the diced microarray into the plastic cartridge. Taken from [61].

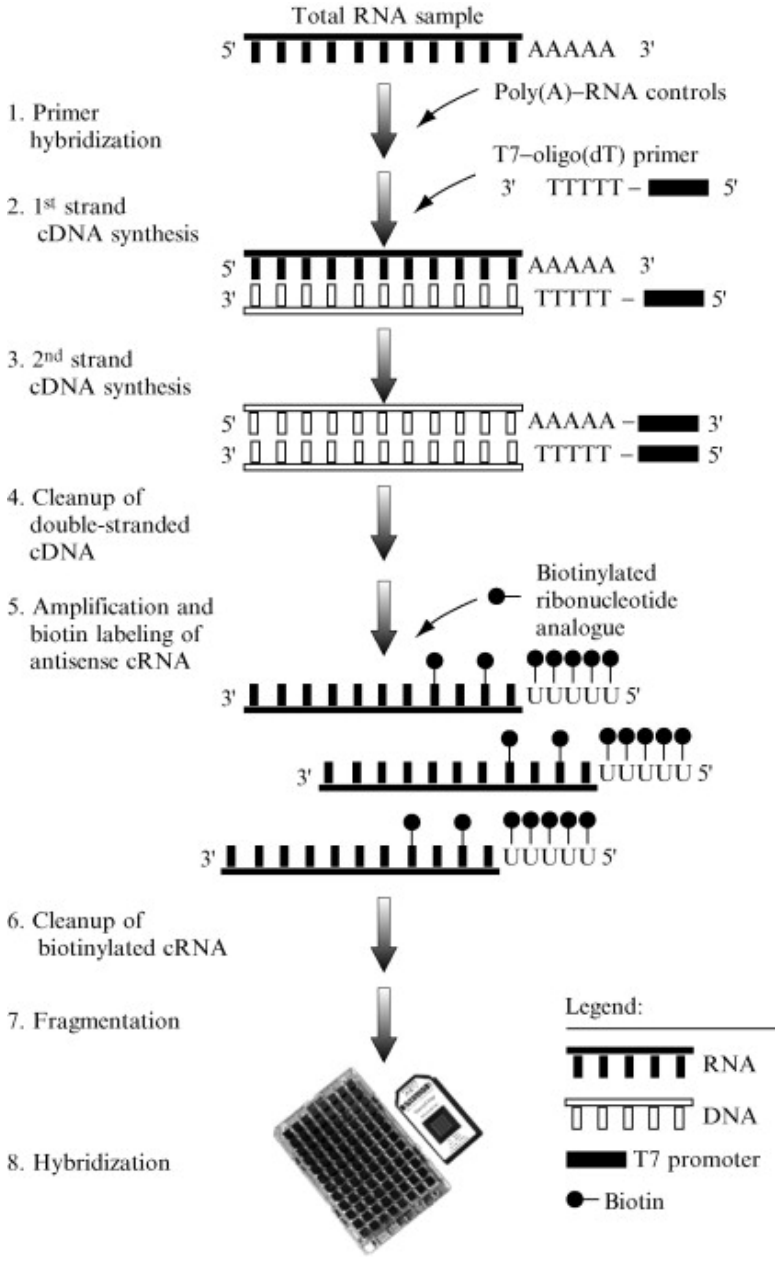


**Figure 2.6**. One-cycle sample preparation for gene expression profiling using RNA. Briefly, total RNA or poly(A)‑RNA is isolated. A primer that includes a poly(T) tail and a T7 polymerase-binding site [T7‑oligo(dT) primer] is used for reverse transcription, resulting in synthesis of cDNA. The second cDNA strand is completed, resulting in a double-stranded cDNA. In the one-cycle method, the double-stranded cDNA is used as a template with biotinylated ribonucleotides, resulting in a biotin-labeled RNA sample. After cRNA fragmentation, the sample is ready to be hybridized to the array, from [61].

# ENYZYME LINKED IMMUNSORBENT ASSAY (ELISA)

The ELISA is a classical bioassay method which detects specific antigen concentrations using antibodies and colorimetric or fluorescence changes. ELISA's are routinely used in scientific research, healthcare, and environmental applications. The fundamental principle of ELISA's is that the target analyte is recognized with high specificity by antibodies, which are proteins produced by the immune system of animals. The typical steps in an ELISA are shown in Figure 2.7. Briefly, the antigen is immobilized to the surface of polystyrene plate, then washed and blocked. A detection antibody is then added, which will bind to the antigen. A secondary antibody is then added, which recognizes the antibody-antigen complex, and it is labeled with a substrate modifying enzyme. The unbound antibody is then washed away and a substrate is added, which becomes chemiluminescent or fluorescent upon its catalysis by the enzyme.


**Figure 2.7**. Protocol for a direct ELISA. In 1) antigen is applied to the surface then blocked. The detection antibody is then added in 2) and washed away. The secondary antibody with the enzyme attached is added in 3) and the excess rinsed away. Finally, the substrate for the enzyme is added and the amount of antigen depends the magnitude of the signal from the enzyme-substrate reaction. Taken from [194]

One of the greatest advantages of ELISA tests is the ability to obtain quick and accurate results. All that is normally required is a blood sample, and no further post processing is necessary. Since ELISA's test for the presence of antibodies or antigens,

they have found large applicability towards HIV infection, as well as cardiac biomarkers and other infectious diseases like Dengue virus, malaria, and rotavirus. Moreover, the ELISA platform has been geared down toward the size of microarrays to form protein chips instead of DNA chips. [66,67] These protein microarrays can be spotted with up 30,000 spots per slide using the same robotic printing methods as DNA chips, and have wide applications[68] The microarrays are not just restricted to protein-protein interactions but can be used to analyze protein-lipid[69], protein-carbohydrate[70], and enzyme substrate interactions[71]. An example of the different types of assays is shown in Figure 2.8.[72]

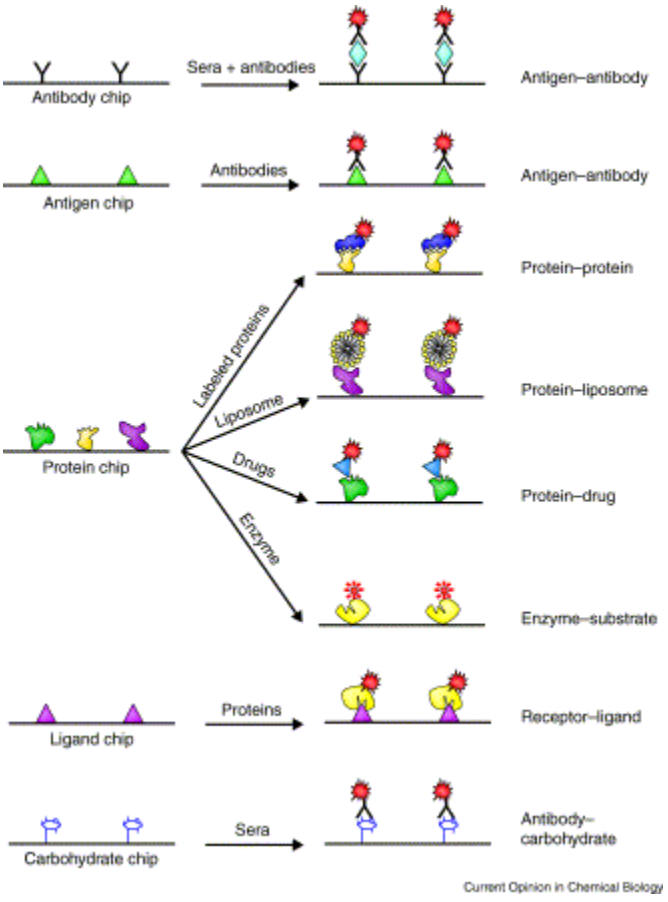


**Figure 2.8**. Different applications for protein chip and/or microarrays, from [72].

The ELISA protein chip is now becoming popular with modern lab-on-a chip devices and coupled into the latest diagnostic technology. Recently, Fan et. al. [73] demonstrated this protein chip technology integrated with microfluidics for sensing prostate specific antigen (PSA) along with 11 other cytokines at the same time. This technology coupled with a fluorescent readout was able to use single droplets of blood or serum to detect these biomarkers down to ~30pM in a time frame of only 10 minutes. Using protein microarray technology, Wu. Et. al.[74] came up with a fast, cheap, electrochemical immunoassay which could render a response within 5 mins. They spotted horseradish peroxidase antibodies coupled to gold nanoparticles onto an carbon electrode chip and embedded in a sol-gel matrix (Figure 2.9), where the HRP can generate an electrochemical response. By using electrophoresis of antigen to the antibodies, the assay incubation could be completed in under two minutes. The successfully used this technology to monitor carcinoembryonic antigens down to 30pg/mL, well within the clinical range.

## 2.3 LABEL-FREE OPTICAL TECHNOLOGIES

In this section I will highlight the latest technology in label-free optical biosensors. I will cover the most highly researched areas, mainly surface plasmon resonance, waveguides, and photonic crystals. Each of these techniques are based upon the binding of analytes creating a change in the refractive index of the surface, which will change either 1) the maximum angle of reflectance at a constant wavelength, or 2) the wavelength where the reflectance is maximum using a broadband source of excitation (white light). Each of these methods will be discussed below.

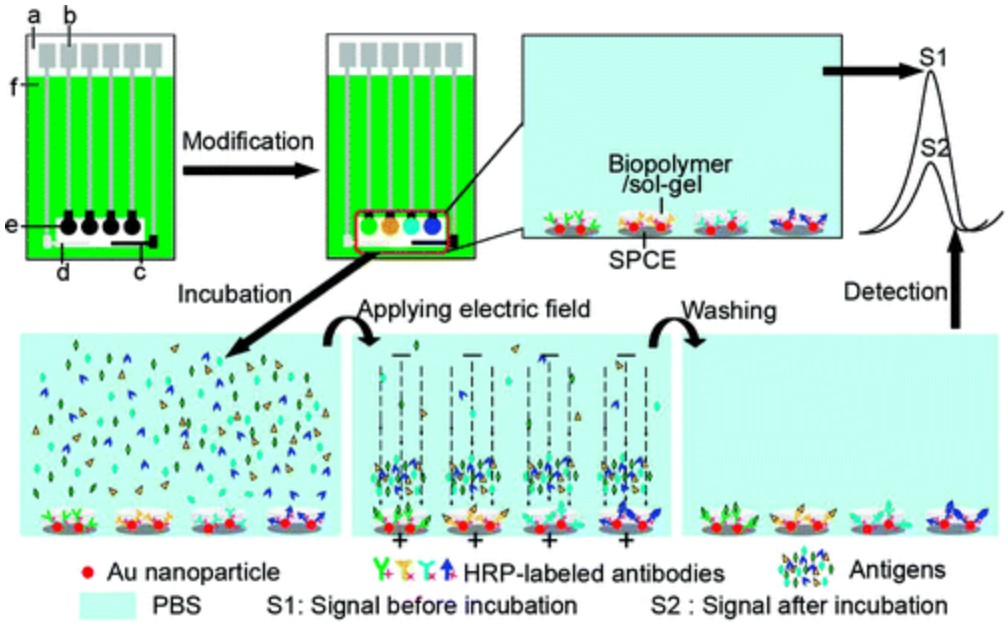


**Figure 2.9**. Schematic Representation of the Electrochemical Multiplexed Immunoassay with an Electric Field-Driven Incubation Process. (a) Nylon Sheet, (b) Silver Ink, (c) Graphite Auxiliary Electrode, (d) Ag/AgCl Reference Electrode, (e) Graphite Working Electrode, and (f) Insulating Dielectric.

## SURFACE PLASMON RESONANCE

Surface plasmon resonance as a technology for immunoassays has been thoroughly explored, and is currently commercialized by companies such as BiaCore International (GE Healthcare). A thorough review of SPR technology and its application has been done by Homola et. al. [75], and I refer the reader to this review if they wish for an in depth discussion of the topic. I will currently go over the basic theory of SPR, its latest configurations, and some of the most recent applications.

SPR is based on the concept of surface plasmons, which are electron oscillations that exist between materials of opposite refractive index, such as metals and a dielectric. When these surface plasmons couple with a photon, they form what are called surface

plasmon polaritons (SPP). These SPP's then may propagate in a parallel direction to the metal/dielectric interface until the energy is lost. In SPR, each metal has a particular photon energy which these surface plasmons may couple to, and may be referred to as a certain frequency or wavelength. Optical excitation of the surface plasmon can be achieved in the so-called Kretschmann configuration, where collimated light beam undergoes total internal reflection at a glass/thin-metal-film/dielectric interface. The angle at which the resonance occurs is extremely sensitive to any change in the refractive index (RI) of the medium adjacent to the metal surface, and such changes can be monitored by recording intensity of reflected light when the system goes out of resonance, or what the angle change of resonance is. Although the Kretschmann configuration, which commonly uses a prism, has the best limits of detection, it is quite bulky and tough to integrate. Thus, other methods outside of prism coupling [76] have surfaced, such as using waveguide coupling [77], fiber optic coupling[78], and grating coupling[79]. An outline of these types of configurations is shown in Figure 2.10. [80]

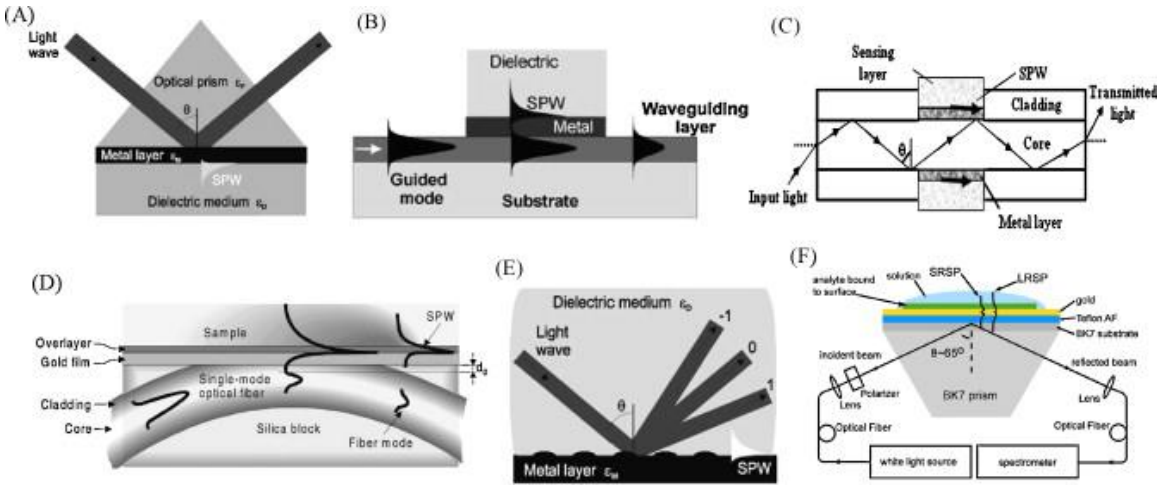


**Figure 2.10**. Various SPR sensor configurations. (A) Prism coupling, (B) waveguide coupling, (C) optical fiber coupling, (D) side-polished fiber coupling, (E) grating coupling and (F) long-range and short-range surface plasmon (LRSP and SRSP). From [80]

Commercialized systems from BiaCore typically yield sensitivities in the ng/mL for protein biomarkers, and can currently do about 100 protein evaluations/day. However, the systems are bulky and costly (~$500,000) and it is usually hard to detect proteins and carbohydrates <5000 MW. Despite these setbacks, it has still been successful in the healthcare field for cancer, neuroscience, and infectious disease research, with over 3000 publications attributed to it.[81] Currently SPR is being merged with microfluidics and fiber optics to create miniaturized sensors for multiplexed detection. A recent example comes from the work of Bhatia et. al.[82], where an SPR fiber optic based sensor demonstrated detection of urea, using the enzyme urease, coupled to a silicon/silver surface. They were able to demonstrate sensitivities from 1uM to >160mM which are all within the clinical levels found in the blood. Another example by Srivastava et. al. [83] monitors glucose levels in the blood, as an alternative to the electrochemical methods of detection using in industry today. The sensor is coated with glucose oxidase, and the catalysis of the glucose causes a change in the refractive index of the film. The dynamic range was well within the clinical range for glucose monitoring of diabetic patients.

## WAVEGUIDES

Optical wavelengths operate off the principle that light is reflected when traveling between materials of different refractive indices, with the refractive index of material A>B. At a certain angle the light is reflected with nearly zero loss, and this is known as total internal reflection (TIR). The principle of TIR is particularly important to fiber optic biosensors. Planar optical waveguides are usually comprised of a high refractive index guiding layer, and when the excitation light is coupled with this layer, TIR can occur over long distances. Although most of the light is confined within the guiding layer, there is an

small amount which penetrates into the medium (biological sample), known as the evanescent field. This evanescent field falls off exponentially as the distance from the waveguide surface increases, and is effectively zero at a distance less than one-half the wavelength of the coupled light. A schematic of this processed is in Figure 2.11.[84] Moreover, a thorough review of this technology was done by Mukundan et. al. [84]with reference to many clinical applications.

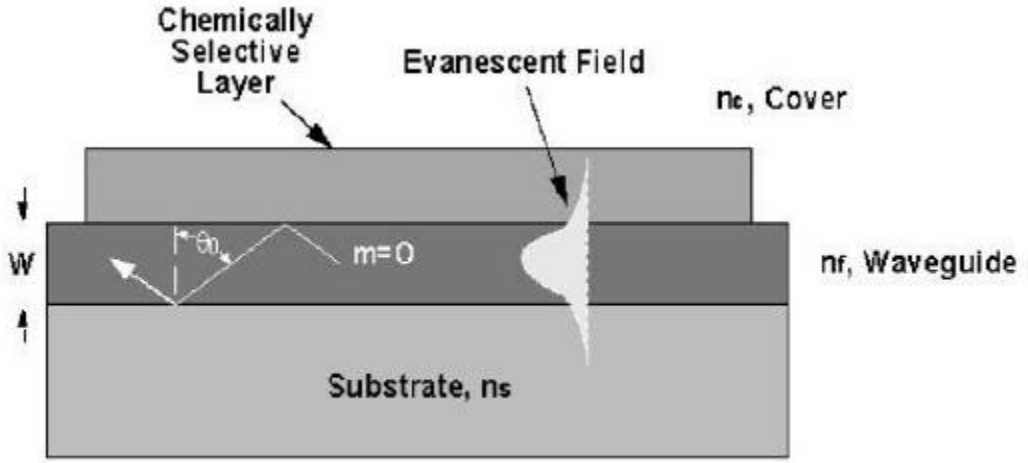


**Figure 2.11**. Waveguide cross-section schematic illustrating the zig-zag model of propagation, from [84].

A recent example towards immunosensing was performed by Im et. al. [85], using a metal clad waveguide sensor. Using nm scale thickness metal films, changes in refractive index were able to be measured down to $3x10^{-6}$ RIU. As a clinical example, human interleukin 5 was measured with limit of detections down to ~10ng/mL. Albeit the detection limit is much higher than SPR, coupling it with SPR may lead to even better limits of detection well within the clinical range.

# PHOTONIC CRYSTALS

Photonic crystal (PC) based biosensors are a novel type of label-free biosensor which has been presented in literature using multiple 1D and 2D configurations. [86-94] The underlying concept for all PC's is that each PC has a periodic dielectric structure on the order of a wavelength. This periodicity then forms a photonic bandgap (or disallowed wavelengths), whereby incident light within the bandgap cannot penetrate. Wavelengths that can penetrate are typically called modes, and the periodicity of the crystal, or cavity defect, must be on the order of half a wavelength to be maximally reflected. Some typical photonic crystal configurations are in Figure 2.12.[80]

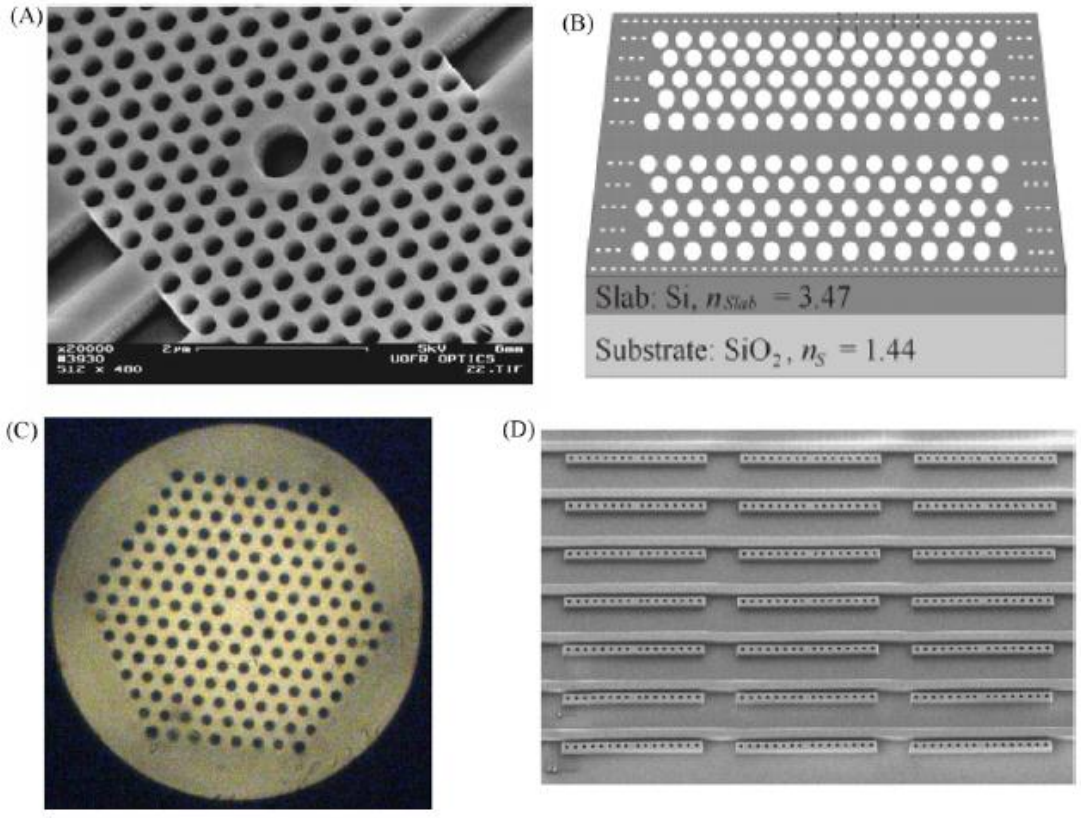


**Figure 2.12**. Photonic crystal biosensor configurations. (A) Photonic crystal microcavity based biosensor. (B) Photonic crystal waveguide based biosensor. (C) Photonic crystal fiber based biosensor. (D) 1D photonic crystal resonators array for parallel detection. From [80].

The microcavity configuration for an optical biosensor, shown in Figure 2.12A, has been used in a variety of clinical screening applications. It is formed by introducing a point defect into the periodic microstructure, either by increasing or decreasing the central hole. The presence of molecules inside the central hole and the first layer of surrounding holes will cause a local RI change, which can be monitored as the spectral shift of the resonant wavelength of the PC microcavity.[86] An example for protein detection was demonstrated by Lee and Fauchet [89] using a silicon based microcavity platform operating at a resonance wavelength of 1.58um. They demonstrate that the size of proteins changes the resonance of the hole, and detect BSA down to ~2.5fg inside the hole. Moreover, they verify his sensitivity experimentally and theoretically.

Another type of PC biosensor, which was developed by Cunningham et. al.[87], behaves as a narrowband reflectance filter, whereby nearly %100 of the incident at the resonant wavelength is reflected. This technology was then commercialized in the BIND scanner by SRU biosystems, with an excellent review of the capabilities by Cunningham et. al. in 2004 [95]. When molecules are attached to the surface, the reflected wavelength (color) is shifted due to the change of the optical path of light that is coupled into the grating. By linking receptor molecules to the grating surface, complementary binding molecules can be detected without the use of any kind of fluorescent probe or particle label. This detection principle allowed for monitoring of changes down to 0.1nm thickness of binding protein. Moreover, this technique can be applied wet or dry, and a schematic of the operating platform is shown in Figure 2.13. This method has been used in a label-free mode for screening of pharmaceutical targets on cell lines, by monitoring the attachment of cells to different antigens.[92]

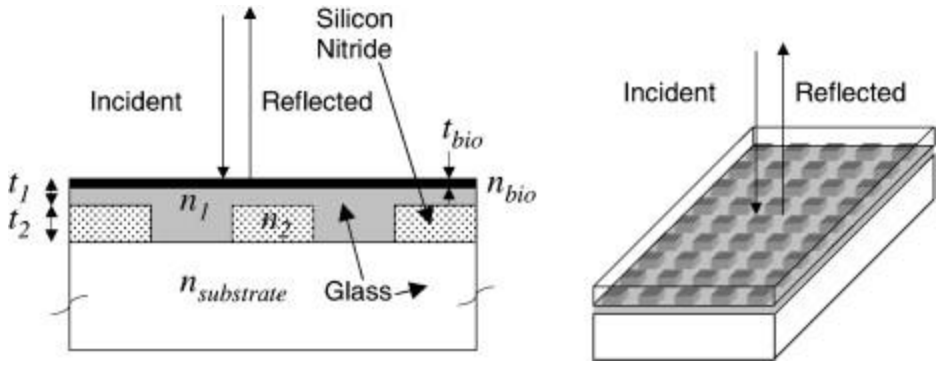


**Figure 2.13**. Schematic diagram of the optical grating structure used for the colorimetric resonant reflectance biosensor, from [87].

## 2.4 LABEL-FREE ELECTROCHEMICAL METHODS

In this section I will discuss the main types of electrochemical sensors, with emphasis on amperometric and potentiometric based sensors. In particular, I will discuss the operating principles of the amperometric sensor using the most widely accepted device (the glucose sensor), as an example. For potentiometric sensors, I will focus mainly on the ones based upon field-effect transistor (FET) technology, discussing ion selective field effect transistors (ISFET's) and the more recent nanoscale FET's. Furthermore, I will discuss their capabilities and potential applications to healthcare.

### THE GLUCOSE SENSOR: AN AMPEROMETRIC EXAMPLE

The glucose enzyme electrode is probably the most studied biosensor method to date, with its roots buried in the original patents by Clark and Lyons in 1962. Moreover, it is the ideal example for a point-of-care device already in high demand. An excellent review of the history of electrochemical glucose sensor was done by Joseph Wang in 2008 [96], and goes into depth about all the generations of glucose sensor up to the latest technologies. The basic mechanism of the glucose sensor uses the enzyme glucose

oxidase (GOx) and its reaction products to generate a measurable current. the immobilized GOx catalyzes the oxidation of β-D-glucose by molecular oxygen producing gluconic acid and hydrogen peroxide. In order to perform this, GOx need a redox catalyst –flavin adenine dinucleotide (FAD) to work as an electron acceptor, which then gets reduced to $FADH_2$ by the reaction below:

$$\mathrm{GOx(FAD)} + \mathrm{Glucose} \rightarrow \mathrm{Gluconlactone} + \mathrm{GOx(FADH_2)} \quad (1)$$

The $GOx(FADH_2)$ complex then reacts with oxygen, which regenerates the cofactor and produces hydrogen peroxide:

$$\mathrm{GOx(FADH_2)} + \mathrm{O_2} \rightarrow \mathrm{GOx(FAD)} + \mathrm{H_2O_2} \quad (2)$$

This hydrogen peroxide is then oxidized at a catalytic, Pt electrode (anode). The electrode recognizes the amount of electron transfers as a current, and this current is proportional to amount of glucose in the blood [6] with the reaction as follows:

$$\mathrm{H_2O_2} \rightarrow 2\mathrm{H^+} + \mathrm{O_2} + 2\mathrm{e^-} \quad (3)$$

The first generation of glucose sensors was built upon this principle, but later it was realized oxygen depletion was causing large drifts in the sensors responses which was hard to correct for and interference with competing oxidizers such as ascorbic acid [97] . The interference was in part due to the large anodic potentials (+0.6V vs. Ag/AgCl electrode) that had to be applied in order to oxidize the hydrogen peroxide. Thus, the second generation glucose sensors started using artificial electron carriers to substitute for oxygen in shuttling electron from the enzyme redox center to the electrode, as well as using the enzyme glucose dehydrogenase (GDH), which removes the need for oxygen in the reaction.[98] First, oxygen was replaced with an electron acceptor called a redox mediator. The mediator was reduced instead of oxygen being converted to hydrogen

peroxide, which then was reoxidized at the platinum electrode to regenerate the mediator. An example of this is in Figure 2.14B, whereby most glucose sensors operate on these principles today. Several types of redox mediators are in play, with most of them derivatives of ferrocene, ferricyanide, or quinines, with ferrocene derivatives being the most popular for current devices.[7] However, the Abbott Freestyle devices use an osmium based mediator, which has been the stable for all three generations of the technology.[99-101] GDH belongs to the class of quinoproteins, which use pyrroloquinoline quinone (PQQ) as cofactor to convert glucose to gluconolactone. GDH is also a dimeric enzyme composed of two identical protein monomers with each monomer binding a PQQ molecule and three calcium ions. These calcium ions activate the PQQ cofactor, and the reaction mechanism is similar to GOx with FAD, except PQQ is the cofactor and does not require oxygen in the reduction.

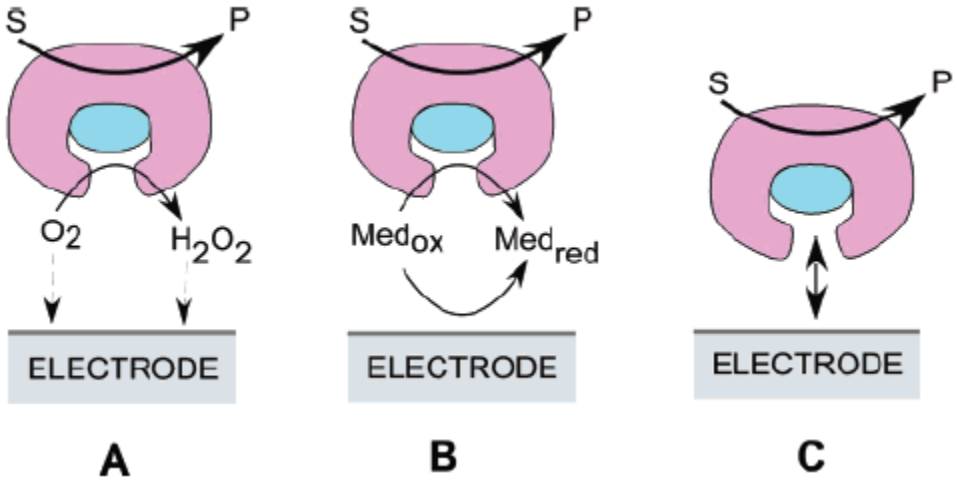


**Figure 2.14**. Three generations of amperometric enzyme electrodes for glucose based on the use of natural oxygen cofactor (A), artificial redox mediators (B), or direct electron transfer between GOx and the electrode (C), from [96].

An excellent review by Vashist et. al.[102] highlights the latest type of electrochemical glucose sensors in thorough detail. A table of the current technologies is shown in Table 2.1 below, along with the largest manufacturers of glucose point-of-care sensors. The main one which I will discuss as an example electrochemical platform is the Abbott Freestyle, which relies on an osmium redox mediator and GDH-PQQ enzyme complex.

| Features | Abbott FreeStyle® Lite | Bayer Contour™ USB | LifeScan OneTouch® Ultra® 2 | Roche Diagnostics Accu-Chek® Aviva |
|---|---|---|---|---|
| Sample volume (μL) | 0.3 | 0.6 | 1 | 0.6 |
| Test time (s) | 5 | 5 | 5 | 5 |
| Insufficient sample | Yes | Yes | May get ERROR 5 or an inaccurate result | Yes |
| 2nd sample application | Permits redosing within 60 s | – | Not allowed | Permits redosing within 5 s |
| Calibration | Plasma equivalent | Plasma equivalent | Plasma equivalent | Plasma equivalent |
| Precision (%) | CV ≤ 3 | CV ≤ 5.3 | CV ≤ 4.4 | CV ≤ 2 |
| Hematocrit (%) | 15–65 | 15–65 | 30–55 | 20–70 |
| Correlation efficient (γ) | 0.98 | 0.98 | 0.98 | – |
| Enzymes used | GDH | GDH | GOx | GDH |
| Mediators | Os complex | Ferricyanide | Ferricyanide | Ferricyanide |
| Enzyme loading | Screen-printing | Screen-printing | Screen-printing | Screen-printing |
| Strip need coding | No | No | Yes | Yes |
| CE/FDA approval | Yes | Yes | Yes | Yes |

**Table 2.1**. Comparison of recent commercially available glucose meters, from [102].

Each blood glucose meter (BGM) test strip has aimed to have high reproducibility, high accuracy, low-cost, rapid results, and low sample volume amounts. These values for the most widely used BGM's are in Table 2.1 as well. The three main components of the BGM strip are the working, counter, and reference electrodes. Additionally, fill electrodes are put on the device to make sure a proper amount of sample has filled the chamber. A small capillary chamber is located on the electrode substrate to work as reaction container and draw the blood into the device through capillary action. A mixture of enzymes, mediators and other chemical components is coated within the capillary chamber in dry form. This setup is discussed in Figure 2.15A, and is part of the Abbott Freestyle system. A working electrode, where the enzymes and mediators are dried, is typically composed of carbon ink or vapor deposited gold or palladium, and

auxiliary and reference electrode are usually combined and made of the same material. The auxiliary and reference electrode are usually composed of Ag/AgCl and are assembled facing the working electrode at a distance of 50 microns in modern devices. Previously, a large potential of 400-500mV must be applied to the working electrode vs. Ag/AgCl in coplanar electrode devices, but this would cause “redox shuttling” from the mediator back and forth, causing high background noise.

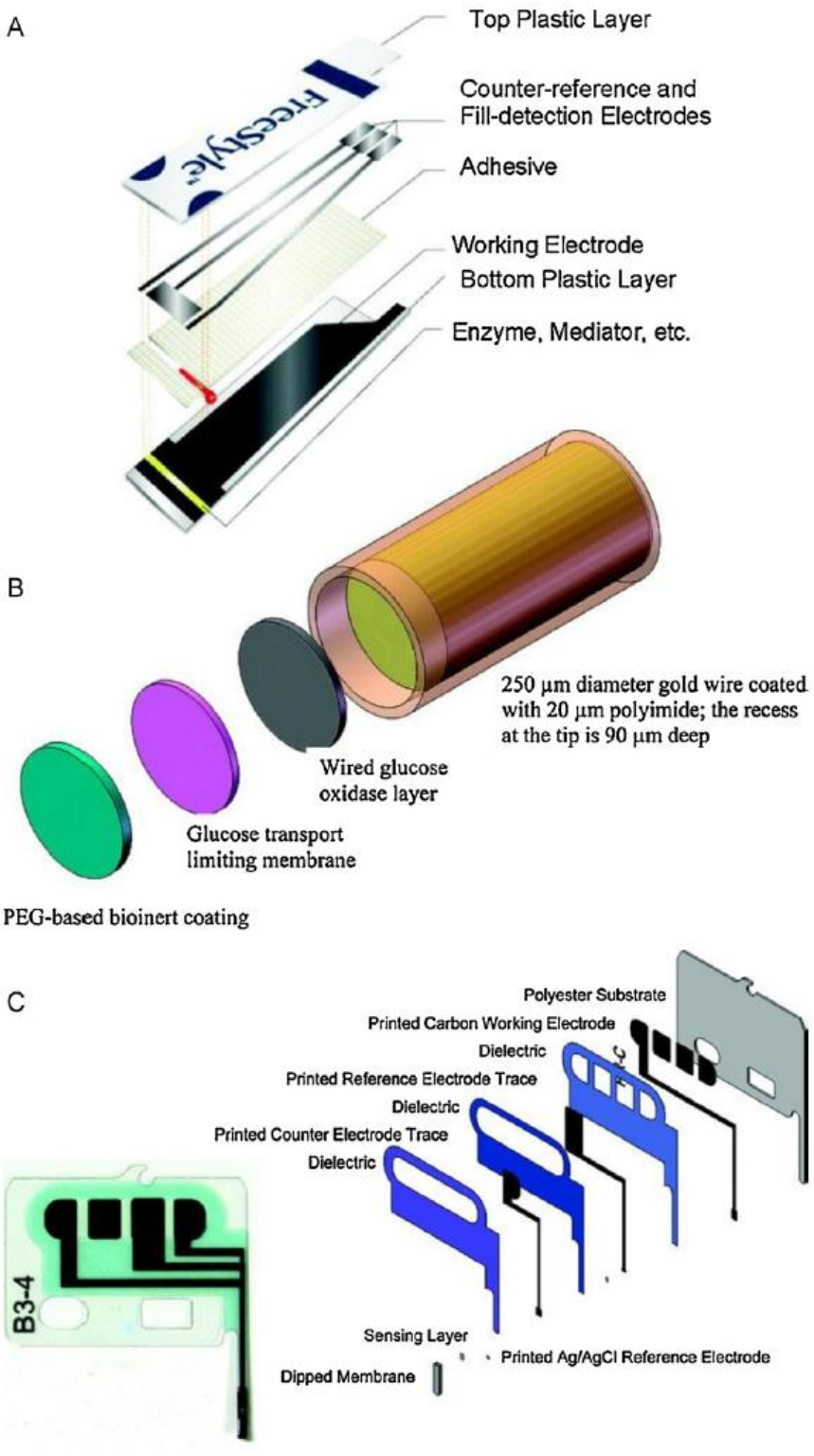


**Figure 2.15**. The expanded views of Abbott's (A) FreeStyle BGM test strip, (B) subcutaneous wired GOx electrode, and (C) FreeStyle Navigator sensor chip, from [102].

However, using osmium mediators, its oxidation potential is negative with respect to other interfering agents, making the other reactions impossible. Moreover, it decrease the diffusion time to the working electrode, and can give readouts within 5 seconds. Most electrochemical devices for various analytes work off the principles of the glucose sensor, but with different enzymes, electrodes, or redox mediators, to generate their signal.

## FIELD EFFECT TRANSISTOR BASED SENSORS

In this section I will discuss the most relevant literature and background into the operating theory of FET's and how they have been applied to biosensors. FET based devices operate on the principle that changes in the electric field across a dielectric (the gate) cause changes in the source-drain current of the underlying device. Since most biomolecules are charged, their binding to the gate causes a change in the electric field due to their charge density, making FET devices particularly enticing as a biosensor. A few of the benefits of using FET technology as a biosensor include:

- High sensitivity due to the current gains inherent in FET devices based on small surface potential changes
- Low cost due to the mass scaling and integration of FET devices in most electronics
- Label-free since it is able to use the intrinsic charge of a molecule as it detection principle

Each FET device is based upon a two-terminal device called a metal-oxide-semiconductor capacitor, or MOSCAP. This structure typically contains a top metal gate, an insulating oxide as the dielectric, and a p-type silicon body. A MOS structure, when a

bias is applied to the gate, can operate in three regimes, i) accumulation, ii) depletion, and iii) inversion. The three regimes are outline in Figure 2.16. When a negative bias is applied to the gate, holes (the majority carrier) from the p-type substrate collect at the silicon/oxide interface and the device is said to be in accumulation. Depletion starts to occur when positive voltages are applied to the gate and holes are repelled from the interface into the silicon, with the voltage between accumulation and depletion modes called the flatband voltage ($V_{FB}$). When negative charges (the minority) carrier start to collect at the interface the device is said to be at inversion, and the voltage where this occurs is called the threshold voltage. The equations which dictate the threshold voltage ($V_T$) are:

$$V_T = V_{FB} + 2\emptyset_f - \frac{Q_B}{C_{OX}} \tag{3}$$

Where $\phi_f$ is the Fermi level of the silicon, $C_{ox}$ the capacitance of the oxide, and $Q_B$ the effective total charge in silicon body. The flatband voltage ($V_{FB}$) can be further expressed as:

$$V_{FB} = \emptyset_{MS} - \frac{Q_F}{C_{OX}} - \frac{Q_{IT}}{C_{OX}} - \frac{Q_M}{C_{OX}} - \frac{Q_{OT}}{C_{OX}} \tag{4}$$

where:

- $\emptyset_{MS}$ represents the workfunction difference between the metal and the semiconductor
- $Q_F$ represents the fixed charge in the oxide, considered to all be at the semiconductor/oxide interface
- $Q_{IT}$ represents the interface oxide trapped charge, which is a function of the surface potential

- $Q_M$ is the mobile charge density, which is distributed throughout the oxide and change position due to applied biases over time
- $Q_{OT}$ is the oxide trapped charge, which is distributed throughout the oxide

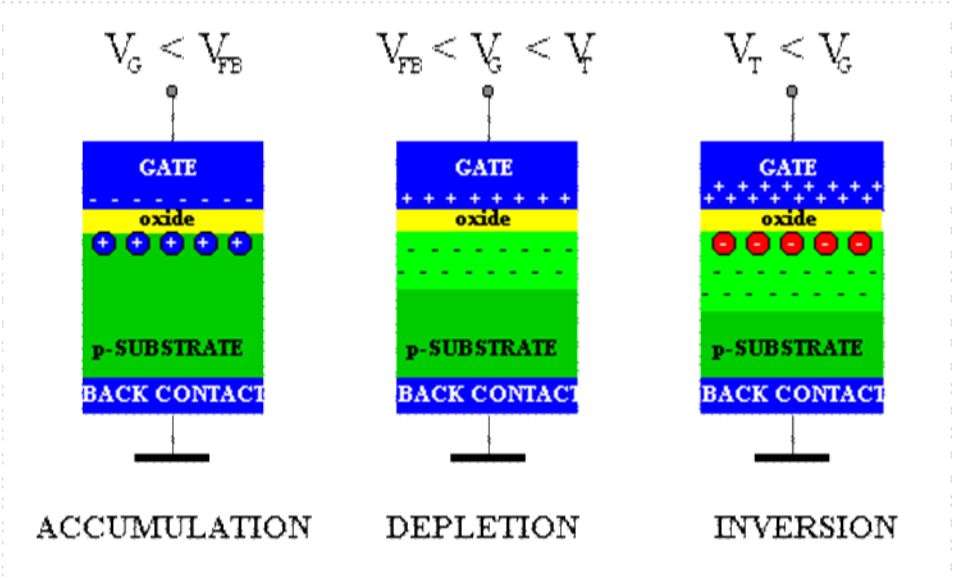


**Figure 2.16**. A MOS capacitor and schematic of its three different operation modes.

Ideally the flatband voltage should only rely on $\emptyset_{MS}$, but all devices contain some amount of the charge densities above. As will be discussed, it has been the goal to minimize these charges as much as possible in the CMOS industry, as they lead to non-ideal device characteristics and degradation of device integrity. Fixed charge is important because it can cause large shifts in threshold voltage, increasing the voltages needed to turn the device on. For transistors exposed to fluids, it is especially important to keep this as low as possible because applying higher voltages leads to higher possibilities of dielectric breakdown and gate leakage. Interface oxide trapped charge can lead to degradation of device turn-on, and mobile charge to device hysteresis when the voltage is swept.

Similarly, with fluid based devices these charges can lead to device drift and instability. The most efficient way to study the effect of these defects is using a MOSCAP and looking at the capacitance of the device vs. the gate voltage, most commonly referred to as C-V analysis. Using high frequency C-V's of a MOSCAP, the effect of these charges on the curve are overly apparent. Interface traps will draw the curve out, leading to poorer sensitivity to applied voltages, while fixed charges will shift the curve left or right from ideal, depending on the charge. A demonstration of how these charges affect C-V characteristics is in Figure 2.17.[103]

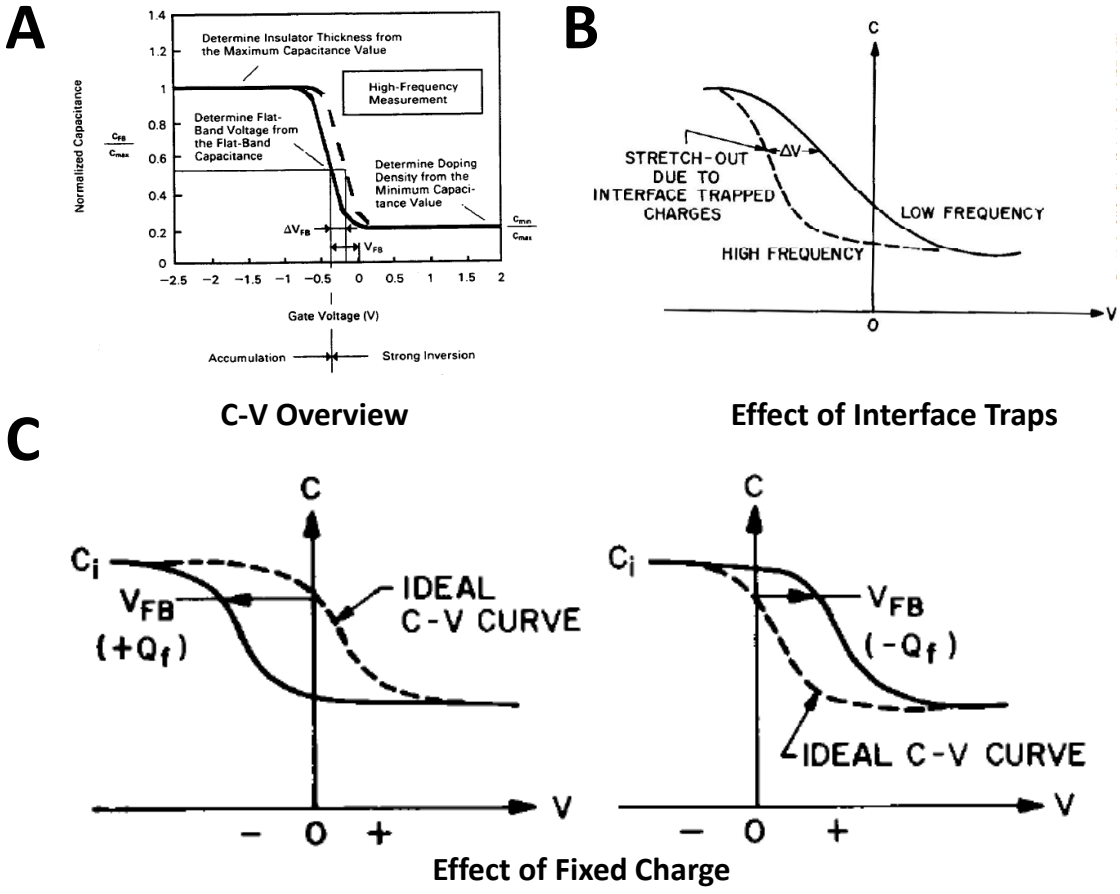


**Figure 2.17**. Capacitance-Voltage curve examples of a MOSCAP. The basic parameters that can be extracted are in **A** and how interface traps affect a curve are in **B**. The effect of fixed charge on a MOSCAP from the ideal are in **C**. From [103]

Several methods to remove these charges are currently in process. Removal of fixed charges revolves around very clean depositions of the gate oxide, commonly achieved by very clean high temperature furnaces or thin film dielectrics by atomic layer deposition. Similarly, interface traps have been passivated using several types of annealing conditions, which typically include oxygen and forming gas ($N_2$ /5% $H_2$).[104,105] The use and characterization of both of these methods into creating a more stable device are a core part of this dissertation, particularly for silicon nanowires. The characterization on ultrathin body MOSFET's[106,107], which are quite similar to our silicon nanowires, has been studied before. Yet, very little has been done in optimizing for nanowire with the newest high-k dielectrics, which is a main topic of discussion in Chapter 5.

A MOSFET is essentially a MOSCAP, but with a 3rd terminal added, known as the source and drain, which forms a conducting channel underneath the MOSCAP. When the surface potential of the oxide ($\phi_s$) reaches a critical value (threshold voltage), the underlying channel will conduct and this is dependent on the gate voltage. The equation for the drain current of a MOSFET is well known:

$$I_D = C_{OX}\mu\frac{W}{L}[(V_{GS} - V_T)V_D - \frac{1}{2}V_D^2] \quad (5)$$

for the triode region when $V_{DS} < V_{DS(sat)}$, where:

$$V_{DS(sat)} = V_{GS} - V_T \quad (6)$$

For the saturation region, when $V_{DS} > V_{DS(sat)}$, the drain current can be represented by:

$$I_D = C_{OX}\mu\frac{W}{L}(V_{GS} - V_T)^2 \quad (7)$$

where $C_{ox}$ is the insulator capacitance, μ is the mobility of the carriers, W is the width of the active area, L is the length of the device, $V_{GS}$ is the Gate voltage and Vt is the

threshold voltage, which was described in Equation 3. An important note here is that in the triode region, $I_D$ is proportional to $(V_{GS}-V_T)$, whereas in the saturation region, it is proportional to $(V_{GS}-V_T)^2$. Another case to address is when $V_{GS}$ is less than the threshold voltage. This is called the subthreshold region, and here the source -drain current is given by:

$$I_D = \frac{1}{S} e^{(V_{GS}-V_T)} \tag{8}$$

where S is the subthreshold slope, which has a physical limit of 60mV/decade. It is worthy to note that, as compared to the triode and saturation regions, this region is exponentially dependent on $V_{GS}$-$V_{T.}$ For any MOSFET or device which operates on a FET principle, these equations will hold. More importantly, they demonstrate the advantages each regime has to offer. The change in device current is most sensitive to voltage in the subthreshold regime, yet it is not linear and its dynamic range is greatly dependent on the subthreshold slope. The triode region the device current is linearly dependent on the gate voltage, and gives a larger dynamic range. These regimes have been used by FET based sensors for a wide range of biological analytes.

Ion Selective Field Effect Transistors, or ISFET's, are a particular type of FET where the top metal has been removed, and has been replaced by an electrolyte and an electrode, as shown in Figure 2.18. The ISFET was originally developed by Bergveld in 1970 [108], and since then over 600 papers have been published in regards to the ISFET. The main difference between the MOSFET and ISFET is the removal of the metal and replacing it with an electrolyte and an electrode. By doing this, we expose the gate insulator to the solution, and remove the workfunction of the metal, replacing it with a reference electrode potential. The new equation for the threshold voltage of an ISFET is:

$$V_T = E_{REF} + X^{SOL} - \varphi - \frac{Q}{C_{OX}} + 2\emptyset_f \quad (9)$$

where $E_{REF}$ is the reference electrode potential, and $X^{SOL}$ + Ψ is the interface potential. The Ψ is the surface potential at the electrolyte/oxide interface, and is a pH dependent parameter due to its charged groups. The $X^{SOL}$ is the surface dipole potential of the solvent and has a constant value. A schematic of these parameters is shown in Figure 2.19. The pH and ion selective nature of the dielectric layer allows for Ψ to change due to the interaction of the ions with the surface, this in turn changing the threshold voltage of the device and providing the devices sensing mechanism.

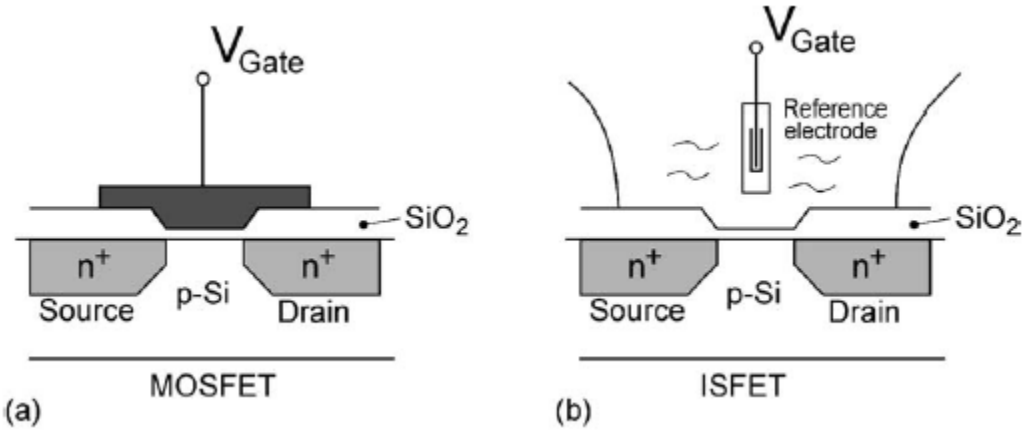


**Figure 2.18**. Schematic representation of MOSFET (a) and ISFET (b), from [195].

The pH and ion sensitivity of ISFET's can be described using a site-binding model specific to the electrolyte/insulator interface. An in-depth description for ISFET's using this model was done by Van Hal et. [109]. In this model, the oxide surface sites are said to be amphoteric, meaning the surface hydroxyl groups can be neutral, protonated, or deprotonated depending on the pH of the bulk solution. Moreover, Van Hal and Eijkel showed how the equation could be related to the equation for capacitors, Q=CV. Essentially, Q is the surface charge in the form of protonated ($OH_2^+$) or deprotonated ($O^-$)

OH groups of the oxide surface, C is the double-layer capacitance at the interface and V is the resulting surface potential, denoted as the familiar Ψ. The capacity for the surface to take up or release protons, in conjunction with the capacitance of the double layer, with a change in pH can be accounted for in a sensitivity factor ,α , and its influence on the surface potential is given by the following equation:

$$\Delta\Psi = -2.3\alpha \frac{RT}{F} \Delta pH_{Bulk} \tag{10}$$

with

$$\alpha = \frac{1}{(2.3kT/q^2)(C_S/B_S)+1} \tag{11}$$

where $B_S$ symbolizes the surface buffer capacity, or the ability of the oxide surface to deliver or take up protons, and $C_S$ is the differential double-layer capacitance, of which the value is mainly determined by the ion concentration and the Debye length due to that concentration. It can be seen that as α approaches 1, near Nernstian sensitivity of the device can be achieved.

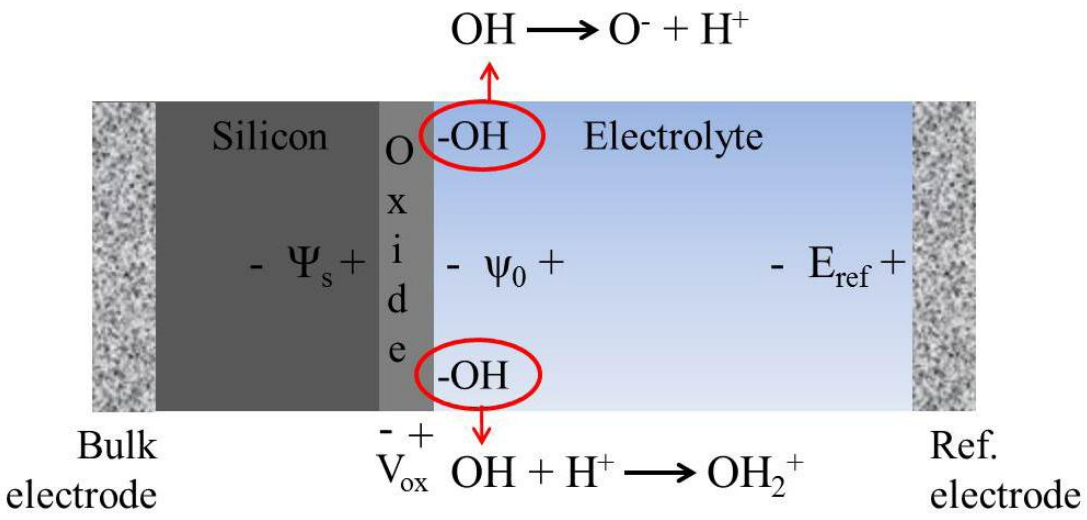


**Figure 2.19**. Schematic of the ISFET operating interface, as well as charged surface groups.

Different gate oxides contain different α values, and the effect of the dielectric properties on their sensitivities to pH and NaCl is shown in Figure 2.20. Since α is also dependent on the number of surface groups, according to the site binding model, the highest sensitivities should occur with the oxides with the highest surface group density. As we can see, $Al_2O_3$ and $Ta_2O_5$ contain the best pH sensitivity in Figure 2.20, and this is in part due to them having the highest density of OH groups for association and dissociation.

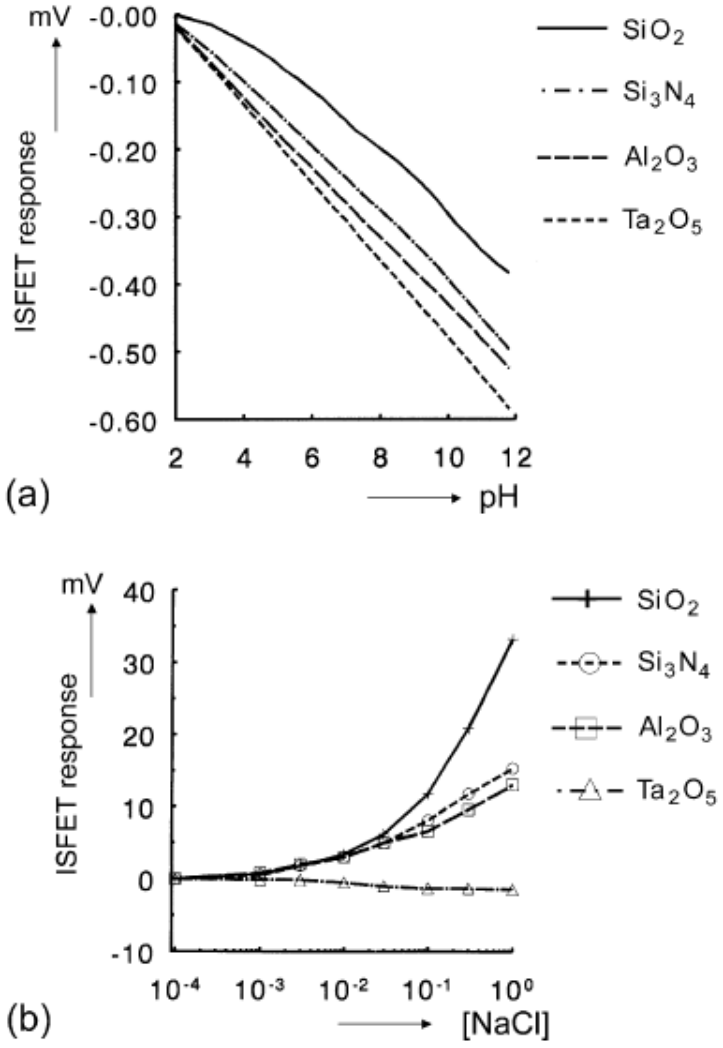


**Figure 2.20**. ISFET responses (a) to electrolyte pH and ISFET responses (b) to NaCl electrolyte, from [196].

The first use of ISFET's as a biosensor came with the use of enzymes and measuring their products, creating enzyme FETs (EnFET's). EnFET's contain immobilized enzymes which create products that can change the surface potential of the oxide insulator by interacting with OH groups. Thus, the basic equations governing the function of the ISFET still hold for EnFET biosensors. Enzyme FET's have been used to sense a variety of chemical analytes, most notably being penicillin [110-112], urea[19,113,114], creatinine [115,116], and organophosphates [117-120]. An excellent review of biological field effect devices was done by Schoning in 2006, highlighting the main types of FET based biosensors and the current challenges they face. [121] Briefly, ISFET's geared towards measuring biological reactions, or BioFET's, have utilized several types of signal generation such as:

- a pH or ion-concentration change due to an enzymatic reaction
- the adsorption of charged macromolecules (e.g., polyelectrolytes, proteins, DNA)
- the affinity binding of molecules (e.g., antigen-antibody affinity reaction, or DNA hybridization);
- potential changes that are coming from living biological systems as a result of complex processes, such as nerve action potentials or cell metabolism

The basic mechanism underlying biological FET's and their output response is shown in Figure 2.21. By using an ion selective or charge sensitive layer, which can be the native gate dielectric, polymer, or protein/DNA, this makes the device electrically sensitive to the changes induced by the type of mechanisms highlighted. Changes in the chemical

composition surrounding the charged layer will induce an electrical response by changing the surface potential of the device, and thus modulating the current of the channel underneath. A landmark report by Rothberg in 2011, introducing Ion Torrent's new semiconductor sequencing technology [122], uses a true CMOS process to fabricate ISFET's which are able sequence DNA instead of optical based methods. How this technology works using an ISFET platform will be highlighted below, and this has been one of the largest commercial successes to date of the ISFET sensor.

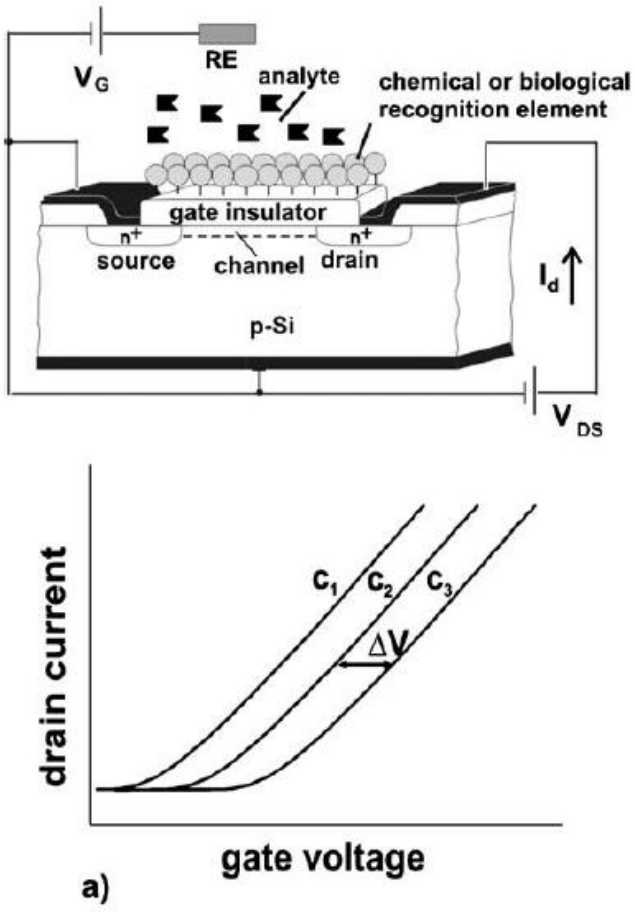


**Figure 2.21**. Structure and typical response of an ISFET (ion-sensitive field-effect transistor). A gate and bias voltage are applied via a reference electrode (e.g., Ag/AgCl liquid-junction electrode), to set the working point of the FED as well as to provide a stable potential in solution. Changes in the analyte concentration cause a change in the threshold voltage.

In this report they describe the fabrication of a 0.35um node CMOS based FET with an extended metal gate, which has a $Ta_2O_5$ ion sensitive layer. This type of ISFET is called and extended gate FET or EGFET. The metal layer is advantageous since it protects the main underlying dielectric from fluid, while still maintaining pH sensitivity by using a pH sensitive oxide deposited on top of the metal. Several papers explaining the use of EGFET's for sensing are available, and I refer the reader to them for a more extensive explanation.[123-128] When performing sequencing by synthesis, the whole process revolves around the addition of bases to a template strand by an enzyme known as DNA polymerase. Traditional sequencing technology has used optical detection of the fluorochromes released during the nucleotide incorporation process, but the Ion Torrent system rather uses the protons released from the addition of a nucleotide, sensing them with the EGFET.

The semiconductor sequencing chip made by Ion Torrent contains an integrated circuit of over 1.2 million sensors, and a schematic of the layout of an individual pixel is shown in Figure 2.22. How the device works will now be discussed. First, DNA is fragmented, ligated to adapters, and adaptor-ligated libraries are clonally amplified onto beads. These beads are then concentrated using magnetic enrichment, and polymerase attached template added. This is then pipetted onto the chip and spun on a centrifuge to allow the beads to settle into the opening wells, as shown in Figure 2.22. The remaining undeposited beads are flushed out and the sequencing can begin. Each base is flown in sequentially, and if a base is incorporated a pH shift of ~0.02 units will occur (two or more sequential bases will proportionally increase the signal 0.02 units/base) and be sensed on the underlying $Ta_2O_5$ layer as a shift in surface potential. The signal detection

on average takes 4s, allowing for enough time for data processing on all 1.5 million sensors before flowing in the next base. Using this methodology, the authors sequenced the genome of Gordon Moore, co-founder of Intel Corp. and author of "Moores Law".

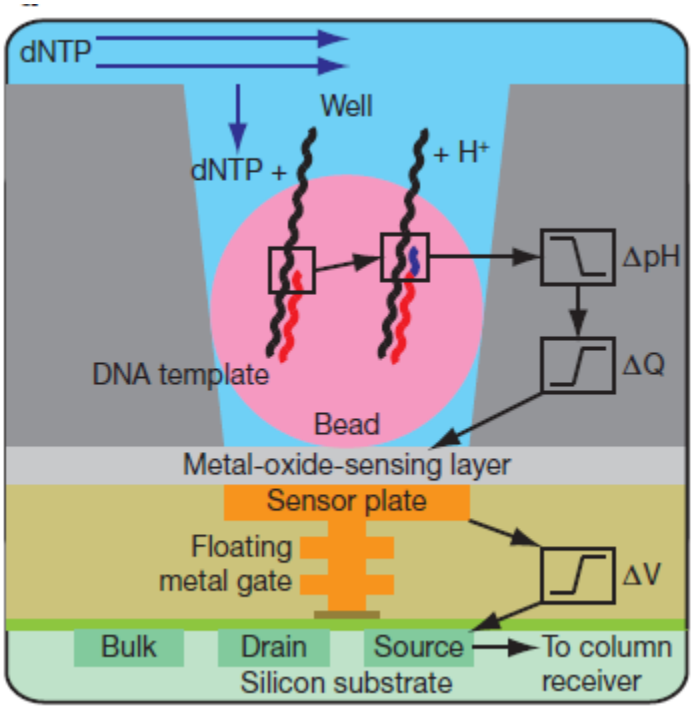


**Figure 2.22**. Simplified drawing of a single well in the Ion Torrent semiconductor chip containing the well, a bead with the template DNA, and the underlying electronic, from [122].

Although this technology has been applicable to DNA sequencing using pH changes, the surface charge densities of biomolecules (proteins, carbohydrates, DNA/RNA) are usually 10-100 times lower than that of oxide dielectrics. According to Fritz et. al in 2002 [129], a maximal change on the surface of a FET for DNA hybridization is 3mV, which would correspond to ~0.05 pH shift given the sensitivity of $Ta_2O_5$, which would be binding in near 1-10uM concentrations. This is essentially not

sensitive enough for sensing in clinically relevant levels, which are commonly in fM-pM ranges for targets like micro RNA.

Nanoscale FET's are a branch off of standard ISFET and FET based technology. Here the device dimensions are scaled down to the magnitude of the sizes of proteins and DNA (nanometers), and this has led to vastly improved sensitivities for biomolecule detection. The eventual goal of using nanoscaled FET's is to sense individual molecules by shrinking the dimensions down even further to this order. Currently two types of approaches have been demonstrated for fabricating nanoscale FET's : "bottom up" approaches and "top down" approaches. Bottom up approaches generally refer to devices which are grown by vapor liquid solid (VLS) methods using nanoclustered metals as the catalyst. The products are typically flow aligned onto a substrate and metal contacts defined on them afterwards, usually by e-beam lithography. A major group which has advanced this type of technology is Charles Lieber's group at Harvard. An example of the sensing capabilities of bottom up silicon nanowire with reference to their work will be discussed. Top down approaches usually start with a substrate, such as a silicon-on-insulator wafer (SOI), which can be lithographically defined and stepwise processed, dubbing the name "top down". There have been many advancements and progress in top-down fabrication processes and biosensing by multiple groups, however as an example of the latest work I shall use the results of the Reed group at Yale.

A landmark report by Cui et. al. in 2001 demonstrated the use of "bottom up" nanowires as a biosensor, which was published in Science.[130] Silicon nanowires of 20nm width were grown using a VLS method, and flow aligned a silicon oxide substrate, being contacted afterwards with Al/Au using e-beam lithography as a patterning agent.

By functionalizing the native oxide of the nanowires with aminopropyltriethoxysilane (APTES), they were able to demonstrate linear response to changes in pH over values from 2-9 by measuring the conductance of the device with an AC measurement technique and a lock-in amplifier. This conductance will change when a change in the surface charge occurs, whether from pH or binding of a biomolecule.

To demonstrate the preliminary biosensing ability of the devices, a model biotin-streptavidin detection scheme was employed, and shown in Figure 2.23. They show the detection of 25pM of streptavidin binding to the surface. What is important is that they perform several controls to make sure the binding is specific. They first monitor the device in pure buffer solution, then add 250nM streptavidin, which causes a large change in the conductance. To make sure the change was not due to the fluid, they performed a wash afterwards and showed it was a true binding event. Next, they showed the binding was specific to biotin by flowing streptavidin that had already been saturated with biotin. Introduction of the fluid yielded little change in the conductance of the device.

In 2004, Hahm demonstrated the ultrasensitive detection of DNA using these silicon nanowires. [131] The devices were functionalized with peptide nucleic acid (PNA) probes, which are electrically neutral. The DNA under question was a sequence in the cystic fibrosis transmembrane receptor gene, which had a wild type and mutant type. The PNA-DNA hybridization complexes were able to be detected down to 10fM levels with high levels of discrimination between the wild type and the mutant strand. Figure 2.24 shows the results of this experiment. Since then, silicon nanowires using bottom up methodologies have been able to sense whole viruses [132], enzymatic reactions [133], cancer markers [134], and action potentials from hearts [135].

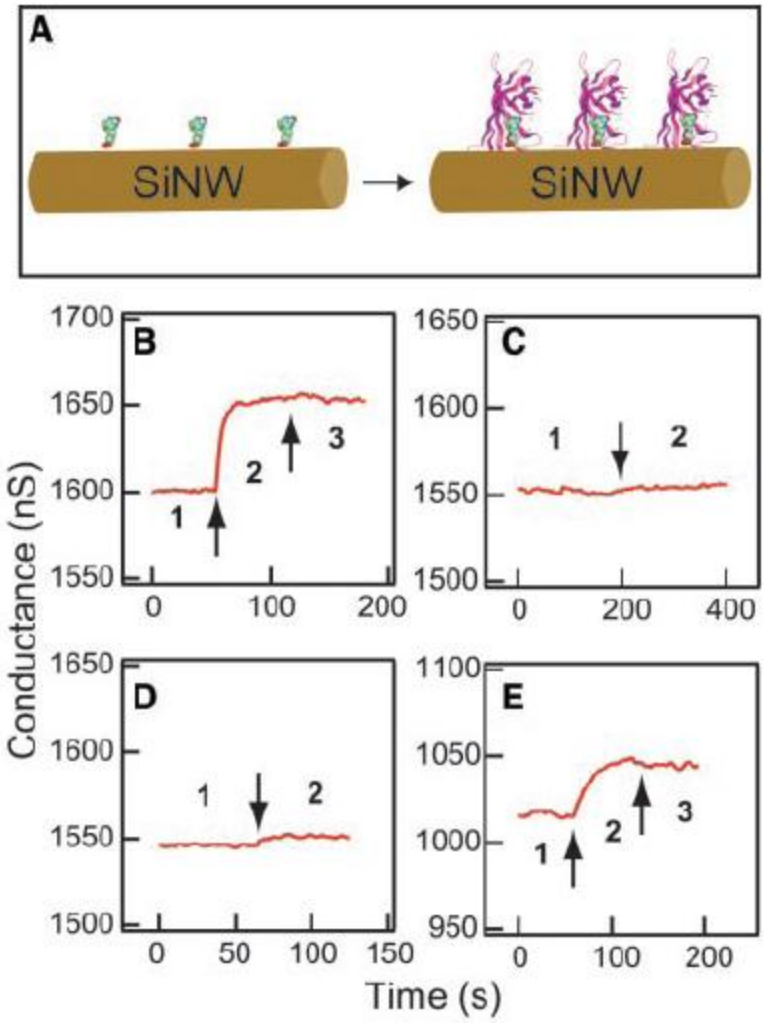


**Figure 2.23**. Schematic showing the real-time detection of protein-binding on a silicon nanowire. A general drawing of protein binding is shown in (A) Conductance versus time where region 1 is a buffer solution, region 2 shows the addition of 250 nM streptavidin, and region 3 is a buffer wash is in (B). Conductance versus time for an unmodified FET is in (C), showing no response to the streptavidin. Conductance versus time for a biotin-modified FET, but where the streptavidin has already been saturated with biotin is in (D). Conductance versus time for 25 pM streptavidin addition is in (E). From [130]

In 2007 the work of Stern et. al from Mark Reed's group published the first top down, CMOS-compatible nanowire process for the detection of proteins in Nature. [136] They used silicon-on-insulator (SOI) wafers and defined their nanowire sensors with e-beam lithography. They then etched the silicon patterns with an anisotropic wet etchant,

tetra-methyl-ammonium-hydroxide (TMAH). The gating oxide used was only the native oxide on top of the silicon. Although this method was the easiest to apply, the longevity of the devices in fluid suffered as a result. Nevertheless, they were able to demonstrate sensing of streptavidin down to 10fM and immunoglobulins to 100fM (Figure 2.25) as a proof of concept. Similar to the protocols by Lieber's group, several controls were implemented to make sure the sensing was real. The sensing experiments used 1nM concentrations to demonstrate the binding, based both on specificity and on charge. They demonstrate in a pH 7.4 solution that streptavidin yields a response, while the quenched streptavidin and PEG control do not. Moreover, they add avidin, which has a positive charge at pH 7.4 instead of negative (such as streptavidin), and this leads to an opposite response.

In 2010 they take this work even further by detecting biomarkers from whole blood using top down nanowires. In this approach they separate the microfluidic chip for protein isolation from the sensing platform. The microfluidic chip was functionalized with antibodies specific to the antigen of interest, and the blood was flown through the chip, binding the antigens. A wash was done to remove the excess blood and non-specific entities. Afterwards, a photolabile linker was cleaved by UV irradiation to release the proteins and these were flown over the device to be sensed. An example of this process is shown in Figure 2.26. They chose two proteins of interest for sensing, PSA (prostate specific antigen), and CA15.3 (carbohydrate antigen). Devices were functionalized with antibodies specific to these antigens, and detection limits of 2ng/mL for PSA and 15U/mL for CA15.3 were achieved, with minimal crosstalk between devices.

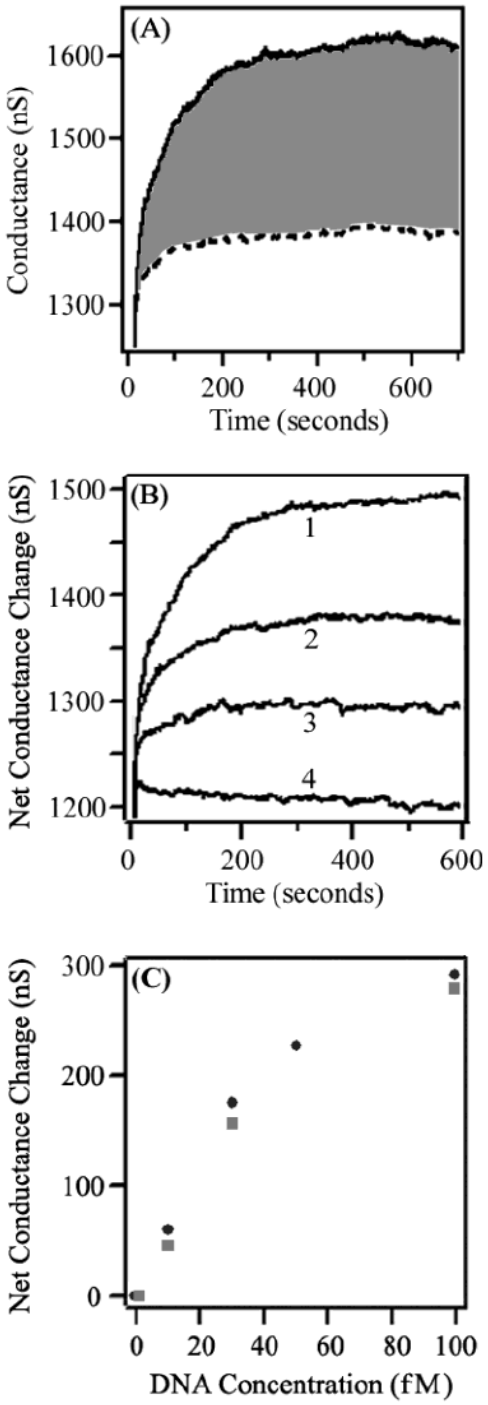


**Figure 2.24**. (A) Conductance graphs obtained from 100 fM of WT (solid line) and MU (dashed line) fragments on the same subject NW. (B) Net conductance changes vs time for 100 fM (1), 30 fM (2), 10 fM (3) and 1 fM (4) DNA samples. (C) Conductance vs DNA concentration where data points shown as squares and circles were obtained from two independent SiNW devices. From [131].

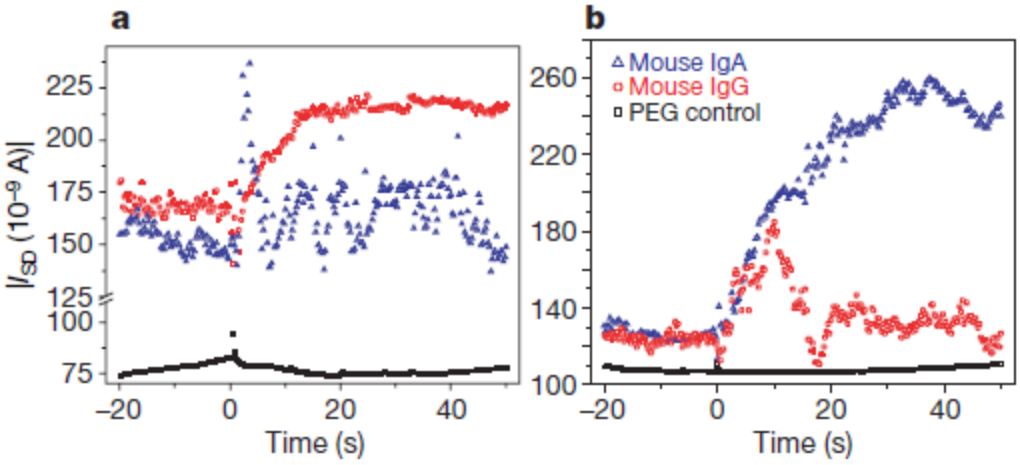


**Figure 2.25**. Demonstration of immunodetection using CMOS-compatible silicon nanowires. Devices were either functionalized with goat anti-mouse IgG (a) or goat anti-mouse IgA (b). The responses to 100 fM of Mouse IgG (red) and Mouse IgA (blue) are shown in each graph, with a PEG control. From [136]

Although I have specifically chosen these as example works, there are a plethora of results for both bottom up and top-down process nanowires for biosensing. In terms of biomolecules, sensing of DNA [137-142], RNA [143], cancer markers[144-148], and cellular processes [147,149-151] have been demonstrated. Extensive studies have also gone into different types of dielectrics, such as $Al_2O_3$ [152,153] and $HfO_2$ [154-159] for pH sensitive layers and gating dielectrics. Moreover, lots of work has gone into understanding the principles of how nanoscale FET's operate, such as what region gives the best sensitivity [160], the effect of device width [161], and the effect of the Debye screening length on the sensitivity [162,163].

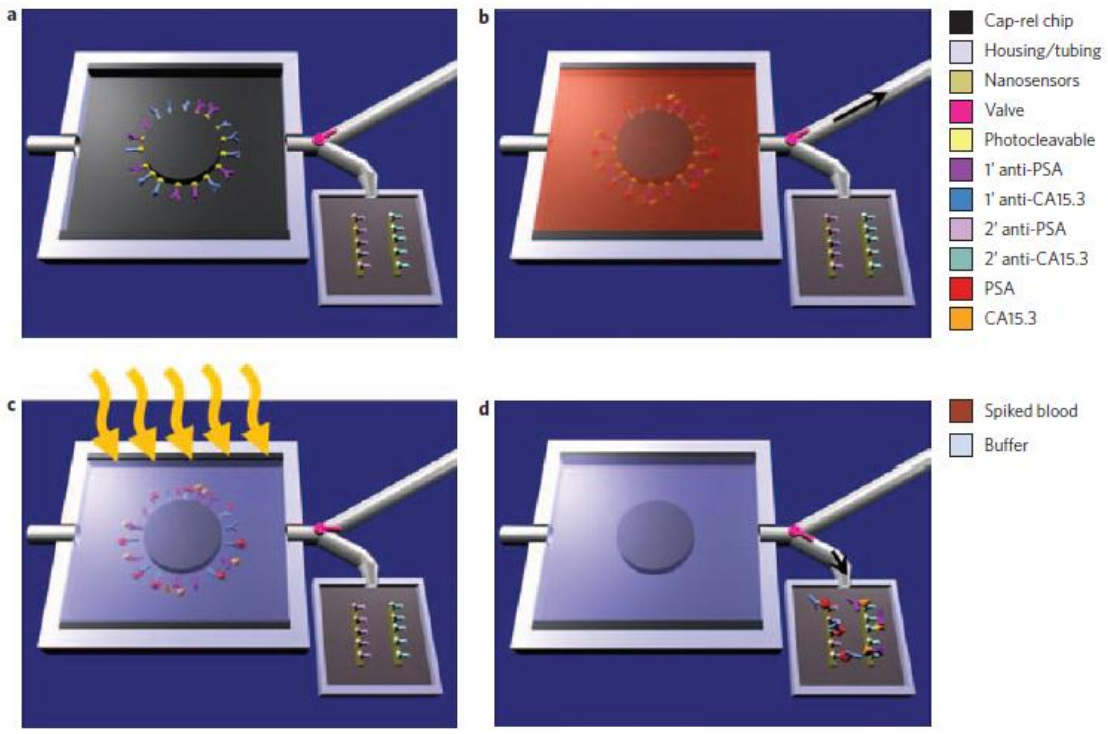


**Figure 2.26**. Schematic of the microfluidic purification of whole blood for sensing. Primary antibodies to multiple biomarkers are bound with a photocleavable crosslinker to the chip (a). The chip is placed in a plastic housing and a valve (pink) directs fluid flow exiting the chip to either a waste receptacle or the nanosensor chip (b). Whole blood is then injected into the chip and allowed to incubate. If the antigens are present in the sample they bind to the antibodies. Washing steps follow the blood incubation, and the chip volume (5 ml) is filled with sensing buffer before UV irradiation (orange arrows) (c). The photolabile crosslinker cleaves, releasing the antibody–antigen complexes into solution. The valve is set to the nanosensor reservoir (black arrow shows the direction of fluid flow) and the 5 ml volume is transferred for fluid flow over the sensor (d). From [197].

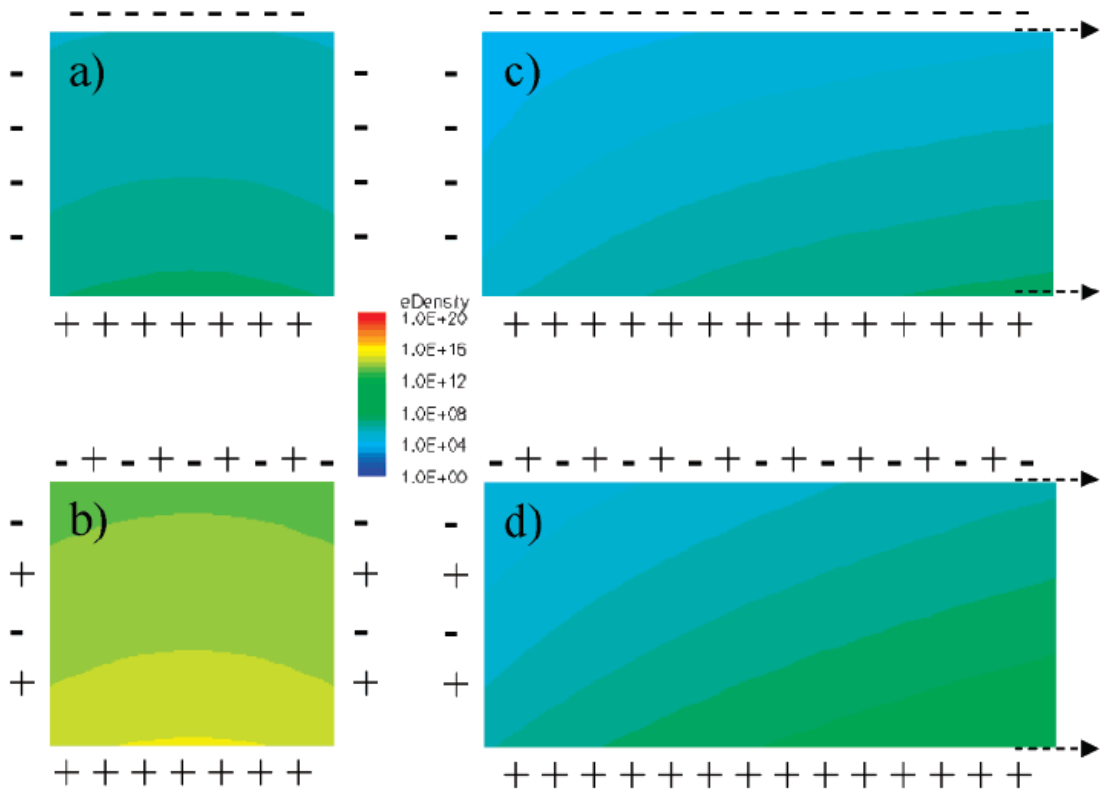


**Figure 2.27**. Simulated electron concentration profiles for a 100nm width wire (a-b) and a 1um width wire (c-d). The simulations in (a) and (c) use a constant charge density of -3.2 x $10^{10}$ /$cm^2$ and (b) and (d) use a charge density of -3.1x $10^{10}$/$cm^2$.

One of the main reasons into the pursuit of nanoscale FET's is the sensitivity achieved with such sensors. This is usually attributed to the improved electrostatics owing to the high surface area to volume ratio of the sensors. Also, such nanowire sensors have the potential to act as an electronic hose, in which depletion of only a segment of the wire will result in a dramatic decrease of total current through the wire. This was experimentally verified using pH by Elfstrom et. al. in 2007.[161] In this work they created top down nanowires of various widths using e-beam lithography, and measured their pH sensitivity and $I_d$-$V_g$ characteristics. They also performed simulations of carrier densities in the nanowires as a function of their width. Their simulation results

are discussed in Figure 2.27. The simulations demonstrate how the effect of applied charge density modulates the smaller width wire much more than the larger one. Moreover, they show that wires with widths <150nm show enhanced sensitivities to charge, and this is shown in Figure 2.28. An attempt to understand the scaling laws was investigated by Nair et. al. [164] and a set of design rules outlined for nanowire development. I refer the reader to this manuscript if they would like to peruse the theory of nanowire sensitivity further.

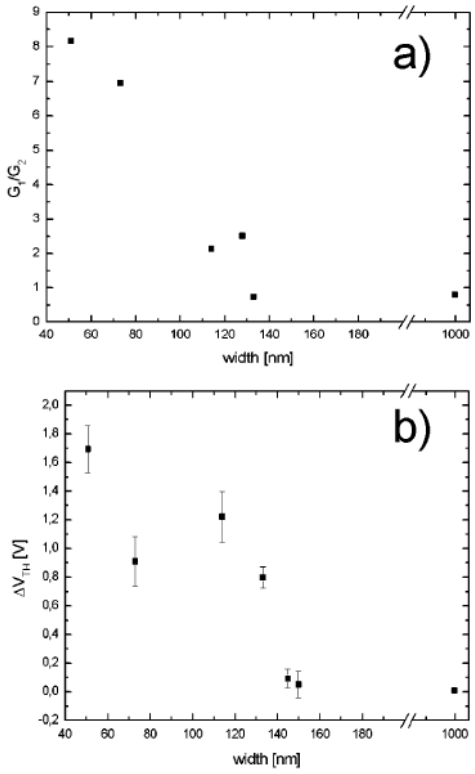


**Figure 2.28**. Conductance ratio vs width for nanowires in the range 50-100 nm and for a microwire (a). The conductance reference was a bare device, then a buffer solution of pH 3.0 was introduced. Threshold voltage shift vs. width for nanowires in the range 50-100 nm and for a microwire (b). The shift occurred when the pH value of the buffer solution added to the surface was changed from 3.0 to 7.4. From [161].

## 2.5 SURFACE FUNCTIONALIZATION OF ISFET'S

It is has been widely accepted that the interfacing of biological recognition elements to the surfaces of FET's or to any transducer is critical in achieving the highest sensitivities possible with the biosensor. In this section I will discuss the types of functionalization techniques which are utilized today on ISFET's for biomolecule immobilization. In general, a surface functionalization technique for any type of biosensor should adhere to a few guidelines which ensure optimized performance:

- A highly uniform surface coverage of the linking layer, as to maximize the biomolecule receptor density.
- A thermodynamically stable layer, which will help minimize dissociation and unintended removal of the layer.
- Proper orientation of the biological recognition element, as to maximize the efficiency of target binding.
- Minimal non-specific binding, meaning the surface can be blocked easily or inherently does not bind non-specific analytes appreciably.

In terms of surface functionalization, FET based devices with and without metal gates have tried to follow these guidelines by using a variety of different chemistries. The main two immobilization techniques have been assembled polymer layers and self-assembled monolayers (SAM's), which will both be addressed briefly in this section as they are thoroughly covered in the remaining chapters. An excellent review of both these types of technologies is available by Senarate et. al. [165] and their use in biosensors to date. A figure displaying some of the common surface chemistries used for sensor layers is shown in Figure 2.29.

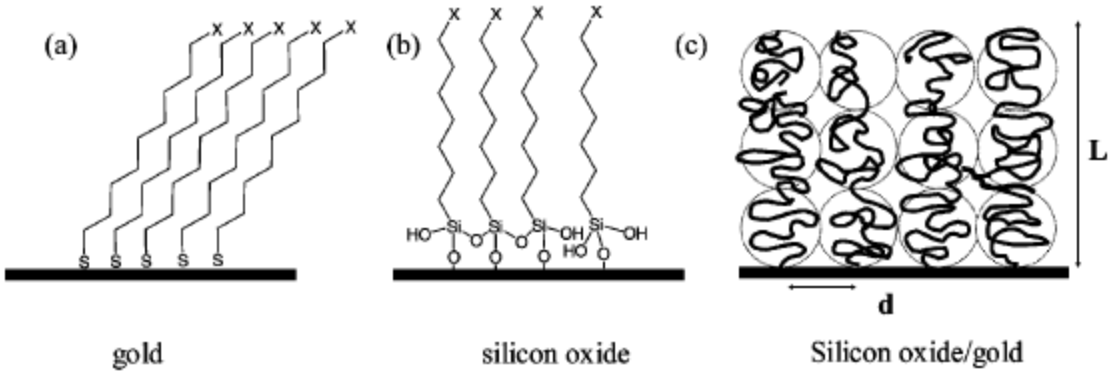


**Figure 2.29**. Schematic depicting SAMS (a) alkanethiols on gold, (b) alkylsilanes on silicon oxide (X terminal functional group) and (c) high-density grafted polymer brushes where d is the average distance between the tethering points and L is the thickness of the brush. From [165].

Polymer layers, sometime called polymer brushes, are typically formed from block copolymers or end grafted polymers, where the functional surface is exposed at the head.[166] They are typically deposited using physisorption to the surface, or by surface initiated polymerization (SIP). The SIP method has attracted much interested since it can be directly started from a monolayer or an electrode. This has made it attractive for FET with metal gates, since it can be directly deposited by applying a voltage. However, several other methods of polymerization have been used, such as free radical [167] and "living" polymerizations [168-170] for surface functionalization as well. For biosensors, electroactive polymerization of films have been the most popular of this field, and commonly use monomer agents such as anilines, thiophenes, and pyrroles. [171] The monomers align to the metal substrate, and when a voltage is applied, they will polymerize, and the amount of polymerization can be controlled by the voltage applied (typically using cyclic voltammetry). The immobilization of proteins or DNA to these layers used to be by chemical grafting of a linking group [172,173], but more recently

polymerizations already including these groups have surfaced [174,175]. They have had tremendous use in amperometric electrode based enzyme sensors[176-183] However, it is notoriously difficult to control the roughness and exact binding geometry of these films, which is why they have been less popular for direct interface based sensors

Self-assembled monolayers have received wide attention as a biointerfacing mechanisms due to their ability to form single molecular layers on substrates and have high versatility, easy deposition processes, and overly simple compared to polymerized films. Many systems undergo self-assembly, including long-chain carboxylic acids on metal oxides, organosilane species on hydroxylated glass, silicon oxides (Si$O_x$) and aluminum oxides (Al$_x$O$_y$), and organosulfur-based species on noble metal surfaces. A more detailed description can be found in an excellent review by Ulman [184] highlighting the intrinsic binding mechanisms. Organosulfur compounds, such as disulfides and thiols, are well known to coordinate to noble metals quite strongly, the most notable metal being gold. Moreover, the alkanethiol-gold linkage is probably the most studied monolayer of all time, and its binding structure detailed in several articles. [185,186]. It is no surprise then that thiol based monolayers have found their way into being regularly utilized on extended gate field effect transistors. Extended gate FET's with thiol based monolayers have been used to detect protein complexes [187] and DNA [188].

Alkoxysilanes have typically been utilized to functionalize oxide surfaces such as silicon oxide, aluminum oxide, and hafnium oxide. The reactive silane groups first undergo a fast hydrolysis to form silanols, followed by slow condensation to oligomers, which then hydrogen bond to the surface hydroxyl groups and lead to the formation of

covalent siloxane bonds. Moreover, the secondary functional groups can be tailored post-deposition or attached pre-deposition for the functionalization of surface that can react with a variety of functional groups. Tailoring the surface of the alkoxysilane monolayer with groups such as n-hydroxysuccinimide (NHS), cyano, azide, bromide, epoxides, and amines is thoroughly reviewed by Haensch et. al..[189] They provide and excellent in-depth discussion of how to modify these surfaces accordingly.

Moreover, these silanes can be mono-functional, bi-functional, or trifunctional for reacting with surfaces, and there tribological properties have been studied over two decades.[190-193] This means that one, two, or three groups are available for anchoring to the surface. Additionally, they can have different chain lengths, which have also been studied thoroughly. However, one thing which has not been thoroughly studied is how these types of monolayers interface with oxide covered FET devices and how to functionalize them for biosensing. This is a core part of this thesis and our advances into uncovering how these mechanisms work is presented in the coming chapters of this thesis.

## 2.6 WHAT'S NEEDED

In order for FET based sensors, in particular silicon nanowires, to become a reliable point-of-care device, several issues must be addressed:

- Increasing the lifetime of the electronic based sensors in fluids. This is imperative if the device it to be integrated into a sensing platform.
- Produce repeatable and accurate results. This is often glossed over in literature as it tough to obtain device with similar characteristics to compare.

- Contain protocols which provide repeatable, reproducible results. A thorough understanding of how to functionalize and fabricate sensors for multiplexing is currently lacking.
- Reduction of non-specific binding and false positives, which is particularly important when samples containing a multitude of analytes (serum, whole blood, genomic DNA) are to be analyzed. This will allow for efficient multiplexing.
- Demonstration of analyte sensing over a dynamic range which encompasses the clinical relevant levels of targets.

The rest of this thesis discusses our efforts to address each one of these issues in order to create a true point-of-care device based on top down silicon nanowires.

## 2.7 REFERENCES


[1]. Updike, S. J.; Hicks, G. P., The Enzyme Electrode. *Nature* 1967, 214, 986-988.

[2]. Guilbault, G. G.; Montalvo Jr, J. G., A Urea-Specific Enzyme Electrode [43]. *Journal of the American Chemical Society* 1969, 91, 2164-2165.

[3]. Martins, T. D.; Ribeiro, A. C. C.; Camargo, H. S. d.; Filho, P. A. d. C.; Cavalcante, H. P. M.; Dias, D. L., *New Insights on Optical Biosensors: Techniques, Construction and Application*. 2013.

[4]. Cagnin, S.; Caraballo, M.; Guiducci, C.; Martini, P.; Ross, M.; SantaAna, M.; Danley, D.; West, T.; Lanfranchi, G., Overview of Electrochemical DNA Biosensors: New Approaches to Detect the Expression of Life. *Sensors* 2009, 9, 3122-3148.

[5]. Willner, I.; Katz, E.; Willner, B., *Biosensors and Their Applications* 2000, 47-98.

[6]. Guilbault, G. G.; Lubrano, G. J., An Enzyme Electrode for the Amperometric Determination of Glucose. *Analytica Chimica Acta* 1973, 64, 439-455.

[7]. Cass, A. E. G.; Davis, G.; Francis, G. D.; Allen O Hill, H.; Aston, W. J.; John Higgins, I.; Plotkin, E. V.; Scott, L. D. L.; Turner, A. P. F., Ferrocene-Mediated Enzyme Electrode for Amperometric Determination of Glucose. *Analytical Chemistry*® 1984, 56, 667-671.

[8]. Koopal, C. G. J.; De Ruiter, B.; Nolte, R. J. M., Amperometric Biosensor Based on Direct Communication between Glucose Oxidase and a Conducting Polymer inside the Pores of a Filtration Membrane. *J. Chem. Soc., Chem. Commun.* 1991, 1691-1692.

[9]. Palmisano, F.; Centonze, D.; Guerrieri, A.; Zambonin, P. G., An Interference-Free Biosensor Based on Glucose Oxidase Electrochemically Immobilized in a Non-Conducting Poly(Pyrrole) Film for Continuous Subcutaneous Monitoring of Glucose through Microdialysis Sampling. *Biosensors and Bioelectronics* 1993, 8, 393-399.

[10]. Csöregi, E.; Schmidtke, D. W.; Heller, A., Design and Optimization of a Selective Subcutaneously Implantable Glucose Electrode Based on "Wired" Glucose Oxidase. *Analytical Chemistry* 1995, 67, 1240-1244.

[11]. Wang, J.; Wu, H., Highly Selective Biosensing of Glucose Utilizing a Glucose Oxidase + Rhodium + Nafion® Biocatalytic-Electrocatalytic-Permselective Surface Microstructure. *Journal of Electroanalytical Chemistry* 1995, 395, 287-291.

[12]. Shoham, B.; Migron, Y.; Riklin, A.; Willner, I.; Tartakovsky, B., A Bilirubin Biosensor Based on a Multilayer Network Enzyme Electrode. *Biosensors and Bioelectronics* 1995, 10, 341-352.

[13]. Tsujimura, S.; Kano, K.; Ikeda, T., Bilirubin Oxidase in Multiple Layers Catalyzes Four-Electron Reduction of Dioxygen to Water without Redox Mediators. *Journal of Electroanalytical Chemistry* 2005, 576, 113-120.

[14]. Otsuka, K.; Sugihara, T.; Tsujino, Y.; Osakai, T.; Tamiya, E., Electrochemical Consideration on the Optimum Ph of Bilirubin Oxidase. *Analytical Biochemistry* 2007, 370, 98-106.

[15]. Liu, H.; Li, H.; Ying, T.; Sun, K.; Qin, Y.; Qi, D., Amperometric Biosensor Sensitive to Glucose and Lactose Based on Co-Immobilization of Ferrocene, Glucose Oxidase, B-Galactosidase and Mutarotase in B-Cyclodextrin Polymer. *Analytica Chimica Acta* 1998, 358, 137-144.

[16]. Sirkar, K.; Revzin, A.; Pishko, M. V., Glucose and Lactate Biosensors Based on Redox Polymer/Oxidoreductase Nanocomposite Thin Films. *Analytical Chemistry* 2000, 72, 2930-2936.

[17]. Stoica, L.; Ludwig, R.; Haltrich, D.; Gorton, L., Third-Generation Biosensor for Lactose Based on Newly Discovered Cellobiose Dehydrogenase. *Analytical Chemistry* 2006, 78, 393-398.

[18]. Zhylyak, G. A.; Dzyadevich, S. V.; Korpan, Y. I.; Soldatkin, A. P.; El'skaya, A. V., Application of Urease Conductometric Biosensor for Heavy-Metal Ion Determination. *Sensors and Actuators: B. Chemical* 1995, 24, 145-148.

[19]. Magalhães, J. M. C. S.; Machado, A. A. S. C., Urea Potentiometric Biosensor Based on Urease Immobilized on Chitosan Membranes. *Talanta* 1998, 47, 183-191.

[20]. Rodriguez, B. B.; Bolbot, J. A.; Tothill, I. E., Development of Urease and Glutamic Dehydrogenase Amperometric Assay for Heavy Metals Screening in Polluted Samples. *Biosensors and Bioelectronics* 2004, 19, 1157-1167.

[21]. Mizutani, F.; Yabuki, S.; Asai, M., L-Malate-Sensing Electrode Based on Malate Dehydrogenase and Nadh Oxidase. *Analytica Chimica Acta* 1991, 245, 145-150.

[22]. Messia, M. C.; Compagnone, D.; Esti, M.; Palleschi, G., A Bienzyme Electrode Probe for Malate. *Analytical Chemistry* 1996, 68, 360-365.

[23]. Arvinte, A.; Rotariu, L.; Bala, C., Amperometric Low-Potential Detection of Malic Acid Using Single-Wall Carbon Nanotubes Based Electrodes. *Sensors* 2008, 8, 1497-1507.

[24]. Ruhal, A.; Rana, J. S.; Kumar, S.; Kumar, A., Immobilization of Malate Dehydrogenase on Carbon Nanotubes for Development of Malate Biosensor. *Cellular and Molecular Biology* 2012, 58, 15-20.

[25]. Kuhr, W. G.; Barrett, V. L.; Gagnon, M. R.; Hopper, P.; Pantano, P., Dehydrogenase-Modified Carbon-Fiber Microelectrodes for the Measurement of Neurotransmitter Dynamics. 1. Nadh Voltammetry. *Analytical Chemistry* 1993, 65, 617-622.

[26]. Bardea, A.; Katz, E.; Bückmann, A. F.; Willner, I., Nad+-Dependent Enzyme Electrodes: Electrical Contact of Cofactor-Dependent Enzymes and Electrodes. *Journal of the American Chemical Society* 1997, 119, 9114-9119.

[27]. Katakis, I.; Domínguez, E., Catalytic Electrooxidation of Nadh for Dehydrogenase Amperometric Biosensors. *Mikrochimica Acta* 1997, 126, 11-32.

[28]. Mano, N.; Kuhn, A., Immobilized Nitro-Fluorenone Derivatives as Electrocatalysts for Nadh Oxidation. *Journal of Electroanalytical Chemistry* 1999, 477, 79-88.

[29]. Isabel Álvarez-González, M.; Saidman, S. B.; Jesús Lobo-Castañón, M.; Miranda-Ordieres, A. J.; Tuñón-Blanco, P., Electrocatalytic Detection of Nadh and Glycerol by Nad+-Modified Carbon Electrodes. *Analytical Chemistry* 2000, 72, 520-527.

[30]. Tran-Minh, C.; Pandey, P. C.; Kumaran, S., Studies on Acetylcholine Sensor and Its Analytical Application Based on the Inhibition of Cholinesterase. *Biosensors and Bioelectronics* 1990, 5, 461-471.

[31]. Garguilo, M. G.; Huynh, N.; Proctor, A.; Michael, A. C., Amperometric Sensors for Peroxide, Choline, and Acetylcholine Based on Electron Transfer between Horseradish Peroxidase and a Redox Polymer. *Analytical Chemistry* 1993, 65, 523-528.

[32]. Riklin, A.; Willner, I., Glucose and Acetylcholine Sensing Multilayer Enzyme Electrodes of Controlled Enzyme Layer Thickness. *Analytical Chemistry* 1995, 67, 4118-4126.

[33]. Compagnone, D.; Federici, G.; Scarciglia, L.; Palleschi, G., Amperometric Glutathione Electrodes. *Biosensors and Bioelectronics* 1993, 8, 257-263.

[34]. Willner, I.; Lapidot, N.; Riklin, A.; Kasher, R.; Zahavy, E.; Katz, E., Electron-Transfer Communication in Glutathione Reductase Assemblies: Electrocatalytic, Photocatalytic, and Catalytic Systems for the Reduction of Oxidized Glutathione. *Journal of the American Chemical Society* 1994, 116, 1428-1441.

[35]. Ruiz-Díaz, J. J. J.; Torriero, A. A. J.; Salinas, E.; Marchevsky, E. J.; Sanz, M. I.; Raba, J., Enzymatic Rotating Biosensor for Cysteine and Glutathione Determination in a Fia System. *Talanta* 2006, 68, 1343-1352.

[36]. Luppa, P. B.; Sokoll, L. J.; Chan, D. W., Immunosensors - Principles and Applications to Clinical Chemistry. *Clinica Chimica Acta* 2001, 314, 1-26.

[37]. Rogers, K. R., Principles of Affinity-Based Biosensors. *Applied Biochemistry and Biotechnology - Part B Molecular Biotechnology* 2000, 14, 109-129.

[38]. Jayasena, S. D., Aptamers: An Emerging Class of Molecules That Rival Antibodies in Diagnostics. *Clinical Chemistry* 1999, 45, 1628-1650.

[39]. Song, S.; Wang, L.; Li, J.; Fan, C.; Zhao, J., Aptamer-Based Biosensors. *TrAC Trends in Analytical Chemistry* 2008, 27, 108-117.

[40]. Tombelli, S.; Minunni, M.; Mascini, M., Analytical Applications of Aptamers. *Biosensors and Bioelectronics* 2005, 20, 2424-2434.

[41]. Hunt, E. A.; Goulding, A. M.; Deo, S. K., Direct Detection and Quantification of Micrornas. *Analytical Biochemistry* 2009, 387, 1-12.

[42]. Wang, J.; Palecek, E.; Nielsen, P. E.; Rivas, G.; Cai, X.; Shiraishi, H.; Dontha, N.; Luo, D.; Farias, P. A. M., Peptide Nucleic Acid Probes for Sequence-Specific DNA Biosensors. *Journal of the American Chemical Society* 1996, 118, 7667-7670.

[43]. Grieshaber, D.; MacKenzie, R.; Vörös, J.; Reimhult, E., Electrochemical Biosensors - Sensor Principles and Architectures. *Sensors* 2008, 8, 1400-1458.

[44]. Janata, J., Electrochemical Sensors and Their Impedances: A Tutorial. *Critical Reviews in Analytical Chemistry* 2002, 32, 109-120.

[45]. Gooding, J. J., Electrochemical DNA Hybridization Biosensors. *Electroanalysis* 2002, 14, 1149-1156.

[46]. Fojta, M., Electrochemical Sensors for DNA Interactions and Damage. *Electroanalysis* 2002, 14, 1449-1463.

[47]. Lillie, G.; Payne, P.; Vadgama, P., Electrochemical Impedance Spectroscopy as a Platform for Reagentless Bioaffinity Sensing. *Sensors and Actuators, B: Chemical* 2001, 78, 249-256.

[48]. Ghindilis, A. L.; Atanasov, P.; Wilkins, M.; Wilkins, E., Immunosensors: Electrochemical Sensing and Other Engineering Approaches. *Biosensors and Bioelectronics* 1998, 13, 113-131.

[49]. Vadgama, P.; Desai, M.; Crump, P., Electrochemical Transducers for in Vivo Monitoring. *Electroanalysis* 1991, 3.

[50]. Buerk, D. G., *Biosensors: Theory and Applications* 1993.

[51]. Berney, H. C.; Alderman, J.; Lane, W. A.; Collins, J. K., Development of a Capacitive Immunosensor: A Comparison of Monoclonal and Polyclonal Capture Antibodies as the Primary Layer. *Journal of Molecular Recognition* 1998, 11, 175-177.

[52]. Cox, W. G.; Singer, V. L., Fluorescent DNA Hybridization Probe Preparation Using Amine Modification and Reactive Dye Coupling. *BioTechniques* 2004, 36, 114-122.

[53]. Moerner, W. E., New Directions in Single-Molecule Imaging and Analysis. *Proceedings of the National Academy of Sciences of the United States of America* 2007, 104, 12596-12602.

[54]. Aberl, F.; Kösslinger, C.; Wolf, H., Molecular Diagnostics of Infectious Diseases. *Methods in molecular medicine* 1997, 13, 519-527.

[55]. Čavić, B. A.; Hayward, G. L.; Thompson, M., Acoustic Waves and the Study of Biochemical Macromolecules and Cells at the Sensor-Liquid Interface. *Analyst* 1999, 124, 1405-1420.

[56]. Janshoff, A.; Galla, H. J.; Steinem, C., Piezoelectric Mass-Sensing Devices as Biosensors - an Alternative to Optical Biosensors? *Angewandte Chemie - International Edition* 2000, 39, 4004-4032.

[57]. Sauerbrey, G., Verwendung Von Schwingquarzen Zur Wägung Dünner Schichten Und Zur Mikrowägung. *Z. Phys.* 1959, 155, 206-222.

[58]. Liu-Stratton, Y.; Roy, S.; Sen, C. K., DNA Microarray Technology in Nutraceutical and Food Safety. *Toxicology Letters* 2004, 150, 29-42.

[59]. Schena, M.; Shalon, D.; Davis, R. W.; Brown, P. O., Quantitative Monitoring of Gene Expression Patterns with a Complementary DNA Microarray. *Science* 1995, 270, 467-470.

[60]. Lockhart, D. J.; Dong, H.; Byrne, M. C.; Follettie, M. T.; Gallo, M. V.; Chee, M. S.; Mittmann, M.; Wang, C.; Kobayashi, M.; Horton, H., et al., Expression Monitoring by Hybridization to High-Density Oligonucleotide Arrays. *Nature Biotechnology* 1996, 14, 1675-1680.

[61]. Dalma-Weiszhausz, D. D.; Warrington, J.; Tanimoto, E. Y.; Miyada, C. G., [1] the Affymetrix Genechip® Platform: An Overview. Kimel, A.; Oliver, B., Eds. 2006; Vol. 410, pp 3-28.

[62]. Van Gelder, R. N.; Von Zastrow, M. E.; Yool, A.; Dement, W. C.; Barchas, J. D.; Eberwine, J. H., Amplified Rna Synthesized from Limited Quantities of Heterogeneous Cdna. *Proceedings of the National Academy of Sciences of the United States of America* 1990, 87, 1663-1667.

[63]. Jemal, A.; Murray, T.; Samuels, A.; Ghafoor, A.; Ward, E.; Thun, M. J., Cancer Statistics, 2003. *Ca-A Cancer Journal for Clinicians* 2003, 53, 5-26.

[64]. Presneau, N.; Dewar, K.; Forgetta, V.; Provencher, D.; Mes-Masson, A. M.; Tonin, P. N., Loss of Heterozygosity and Transcriptome Analyses of a 1.2 Mb Candidate Ovarian Cancer Tumor Suppressor Locus Region at 17q25.1-Q25.2. *Molecular Carcinogenesis* 2005, 43, 141-154.

[65]. Klein, R. J.; Zeiss, C.; Chew, E. Y.; Tsai, J. Y.; Sackler, R. S.; Haynes, C.; Henning, A. K.; SanGiovanni, J. P.; Mane, S. M.; Mayne, S. T., et al., Complement Factor H Polymorphism in Age-Related Macular Degeneration. *Science* 2005, 308, 385-389.

[66]. Borrebaeck, C. A. K.; Ekström, S.; Malmborg Hager, A. C.; Nilsson, J.; Laurell, T.; Marko-Varga, G., Protein Chips Based on Recombinant Antibody Fragments: A Highly Sensitive Approach as Detected by Mass Spectrometry. *BioTechniques* 2001, 30, 1126-1132.

[67]. Borrebaeck, C. A. K., Antibodies in Diagnostics - from Immunoassays to Protein Chips. *Immunology Today* 2000, 21, 379-382.

[68]. MacBeath, G.; Schreiber, S. L., Printing Proteins as Microarrays for High-Throughput Function Determination. *Science* 2000, 289, 1760-1763.

[69]. Yang, T.; Jung, S. Y.; Mao, H.; Cremer, P. S., Fabrication of Phospholipid Bilayer-Coated Microchannels for on-Chip Immunoassays. *Analytical Chemistry* 2001, 73, 165-169.

[70]. Wang, D.; Liu, S.; Trummer, B. J.; Deng, C.; Wang, A., Carbohydrate Microarrays for the Recognition of Cross-Reactive Molecular Markers of Microbes and Host Cells. *Nature Biotechnology* 2002, 20, 275-281.

[71]. Jain, K. K., Applications of Aplichip™ Cyp450. *Molecular Diagnosis* 2005, 9, 119-127.

[72]. Zhu, H.; Snyder, M., Protein Chip Technology. *Current Opinion in Chemical Biology* 2003, 7, 55-63.

[73]. Fan, R.; Vermesh, O.; Srivastava, A.; Yen, B. K. H.; Qin, L.; Ahmad, H.; Kwong, G. A.; Liu, C. C.; Gould, J.; Hood, L., et al., Integrated Barcode Chips for Rapid, Multiplexed Analysis of Proteins in Microliter Quantities of Blood. *Nature Biotechnology* 2008, 26, 1373-1378.

[74]. Wu, J.; Yan, Y.; Yan, F.; Ju, H., Electric Field-Driven Strategy for Multiplexed Detection of Protein Biomarkers Using a Disposable Reagentless Electrochemical Immunosensor Array. *Analytical Chemistry* 2008, 80, 6072-6077.

[75]. Homola, J., Surface Plasmon Resonance Sensors for Detection of Chemical and Biological Species. *Chemical Reviews* 2008, 108, 462-493.

[76]. Matsubara, K.; Kawata, S.; Minami, S., Optical Chemical Sensor Based on Surface Plasmon Measurement. *Appl. Opt.* 1988, 27, 1160-1163.

[77]. Liedberg, B.; Lundström, I.; Stenberg, E., Principles of Biosensing with an Extended Coupling Matrix and Surface Plasmon Resonance. *Sensors and Actuators: B. Chemical* 1993, 11, 63-72.

[78]. Sharma, A. K.; Jha, R.; Gupta, B. D., Fiber-Optic Sensors Based on Surface Plasmon Resonance: A Comprehensive Review. *IEEE Sensors Journal* 2007, 7, 1118-1129.

[79]. Alleyne, C. J.; Kirk, A. G.; McPhedran, R. C.; Nicorovici, N. A. P.; Maystre, D., Enhanced Spr Sensitivity Using Periodic Metallic Structures. *Optics Express* 2007, 15, 8163-8169.

[80]. Fan, X.; White, I. M.; Shopova, S. I.; Zhu, H.; Suter, J. D.; Sun, Y., Sensitive Optical Biosensors for Unlabeled Targets: A Review. *Analytica Chimica Acta* 2008, 620, 8-26.

[81]. Luong, J. H. T.; Male, K. B.; Glennon, J. D., Biosensor Technology: Technology Push Versus Market Pull. *Biotechnology Advances* 2008, 26, 492-500.

[82]. Bhatia, P.; Gupta, B. D., Fabrication and Characterization of a Surface Plasmon Resonance Based Fiber Optic Urea Sensor for Biomedical Applications. *Sensors and Actuators, B: Chemical* 2012, 161, 434-438.

[83]. Srivastava, S. K.; Verma, R.; Gupta, B. D. In *Surface Plasmon Resonance Based Fiber Optic Glucose Biosensor*, Sydney, NSW, Sydney, NSW, 2012.

[84]. Mukundan, H.; Anderson, A. S.; Grace, W. K.; Grace, K. M.; Hartman, N.; Martinez, J. S.; Swanson, B. I., Waveguide-Based Biosensors for Pathogen Detection. *Sensors* 2009, 9, 5783-5809.

[85]. Im, W. J.; Kim, B. B.; Byun, J. Y.; Kim, H. M.; Kim, M. G.; Shin, Y. B., Immunosensing Using a Metal Clad Leaky Waveguide Biosensor for Clinical Diagnosis. *Sensors and Actuators, B: Chemical* 2012, 173, 288-294.

[86]. Chow, E.; Grot, A.; Mirkarimi, L. W.; Sigalas, M.; Girolami, G., Ultracompact Biochemical Sensor Built with Two-Dimensional Photonic Crystal Microcavity. *Optics Letters* 2004, 29, 1093-1095.

[87]. Cunningham, B.; Li, P.; Lin, B.; Pepper, J., Colorimetric Resonant Reflection as a Direct Biochemical Assay Technique. *Sensors and Actuators, B: Chemical* 2002, 81, 316-328.

[88]. Ganesh, N.; Block, I. D.; Cunningham, B. T., Near Ultraviolet-Wavelength Photonic-Crystal Biosensor with Enhanced Surface-to-Bulk Sensitivity Ratio. *Applied Physics Letters* 2006, 89.

[89]. Lee, M.; Fauchet, P. M., Two-Dimensional Silicon Photonic Crystal Based Biosensing Platform for Protein Detection. *Optics Express* 2007, 15, 4530-4535.

[90]. Lee, M. R.; Fauchet, P. M., Nanoscale Microcavity Sensor for Single Particle Detection. *Optics Letters* 2007, 32, 3284-3286.

[91]. Li, P. Y.; Lin, B.; Gerstenmaier, J.; Cunningham, B. T., A New Method for Label-Free Imaging of Biomolecular Interactions. *Sensors and Actuators, B: Chemical* 2004, 99, 6-13.

[92]. Lin, B.; Li, P.; Cunningham, B. T., A Label-Free Biosensor-Based Cell Attachment Assay for Characterization of Cell Surface Molecules. *Sensors and Actuators, B: Chemical* 2006, 114, 559-564.

[93]. Lin, B.; Qiu, J.; Gerstenmeier, J.; Li, P.; Pien, H.; Pepper, J.; Cunningham, B., A Label-Free Optical Technique for Detecting Small Molecule Interactions. *Biosensors and Bioelectronics* 2002, 17, 827-834.

[94]. Skivesen, N.; Têtu, A.; Kristensen, M.; Kjems, J.; Frandsen, L. H.; Borel, P. I., Photonic-Crystal Waveguide Biosensor. *Optics Express* 2007, 15, 3169-3176.

[95]. Cunningham, B. T.; Li, P.; Schulz, S.; Lin, B.; Baird, C.; Gerstenmaier, J.; Genick, C.; Wang, F.; Fine, E.; Laing, L., Label-Free Assays on the Bind System. *Journal of Biomolecular Screening* 2004, 9, 481-490.

[96]. Wang, J., Electrochemical Glucose Biosensors. *Chemical Reviews* 2008, 108, 814-825.

[97]. Wang, J.; Liu, J.; Chen, L.; Lu, F., Highly Selective Membrane-Free, Mediator-Free Glucose Biosensor. *Analytical Chemistry* 1994, 66, 3600-3603.

[98]. D'Costa, E. J.; Higgins, I. J.; Turner, A. P. F., Quinoprotein Glucose Dehydrogenase and Its Application in an Amperometric Glucose Sensor. *Biosensors* 1986, 2, 71-87.

[99]. Pravda, M.; Jungar, C. M.; Iwuoha, E. I.; Smyth, M. R.; Vytras, K.; Ivaska, A., Evaluation of Amperometric Glucose Biosensors Based on Co-Immobilisation of Glucose Oxidase with an Osmium Redox Polymer in Electrochemically Generated Polyphenol Films. *Analytica Chimica Acta* 1995, 304, 127-138.

[100]. Reiter, S.; Habermüller, K.; Schuhmann, W., A Reagentless Glucose Biosensor Based on Glucose Oxidase Entrapped into Osmium-Complex Modified Polypyrrole Films. *Sensors and Actuators, B: Chemical* 2001, 79, 150-156.

[101]. Laurinavicius, V.; Razumiene, J.; Ramanavicius, A.; Ryabov, A. D., Wiring of Pqq-Dehydrogenases. *Biosensors and Bioelectronics* 2004, 20, 1217-1222.

[102]. Vashist, S. K.; Zheng, D.; Al-Rubeaan, K.; Luong, J. H. T.; Sheu, F.-S., Technology Behind Commercial Devices for Blood Glucose Monitoring in Diabetes Management: A Review. *Analytica Chimica Acta* 2011, 703, 124-136.

[103]. Sze, S. M., *Physics of Semiconductor Devices*. John Wiley and Sons: 2007; Vol. 1.

[104]. Faynot, O.; Cristoloveanu, S.; Auberton-Herve, A. J.; Raynaud, C., Performance and Potential of Ultrathin Accumulation-Mode Simox Mosfet's. *IEEE Transactions on Electron Devices* 1995, 42, 713-719.

[105]. Wong, H.; Zhan, N.; Ng, K. L.; Poon, M. C.; Kok, C. W., Interface and Oxide Traps in High-Kappa Hafnium Oxide Films. *Thin Solid Films* 2004, 462-63, 96-100.

[106]. Colinge, J. P.; Flandre, D.; Van De Wiele, F., Subthreshold Slope of Long-Channel, Accumulation-Mode P-Channel Soi Mosfets. *Solid-State Electronics* 1994, 37, 289-294.

[107]. Zhang, Z.; Li, Z.; Tan, K.; Zhang, J.; Li, K. In *Subthreshold Performance of Double-Gate Accumulation-Mode P-Channel Soi Mosfet*, Guilin, Guilin, 2007.

[108]. Bergveld, P., Development of an Ion-Sensitive Solid-State Device for Neurophysiological Measurements. *Ieee Transactions on Biomedical Engineering* 1970, 17, 70-71.

[109]. Van Hal, R. E. G.; Eijkel, J. C. T.; Bergveld, P., A General Model to Describe the Electrostatic Potential at Electrolyte Oxide Interfaces. *Advances in Colloid and Interface Science* 1996, 69, 31-62.

[110]. Poghossian, A.; Yoshinobu, T.; Simonis, A.; Ecken, H.; Lüth, H.; Schöning, M. J., Penicillin Detection by Means of Field-Effect Based Sensors: Enfet, Capacitive Eis Sensor or Laps? *Sensors and Actuators, B: Chemical* 2001, 78, 237-242.

[111]. Poghossian, A.; Thust, M.; Schroth, P.; Steffen, A.; Lüth, H.; Schöning, M. J., Penicillin Detection by Means of Silicon-Based Field-Effect Structures. *Sensors and Materials* 2001, 13, 207-223.

[112]. Poghossian, A.; Schöning, M. J.; Schroth, P.; Simonis, A.; Lüth, H., An Isfet-Based Penicillin Sensor with High Sensitivity, Low Detection Limit and Long Lifetime. *Sensors and Actuators, B: Chemical* 2001, 76, 519-526.

[113]. Lakard, B.; Herlem, G.; Lakard, S.; Antoniou, A.; Fahys, B., Urea Potentiometric Biosensor Based on Modified Electrodes with Urease Immobilized on Polyethylenimine Films. *Biosensors and Bioelectronics* 2004, 19, 1641-1647.

[114]. Aouni, F.; Mlika, R.; Martelet, C.; Ben Ouada, H.; Jaffrezic-Renault, N.; Soldatkin, A. P., Modelling of the Potentiometric Response of Enfets Based on Enzymatic Multilayer Membranes. *Electroanalysis* 2004, 16, 1907-1911.

[115]. Sant, W.; Pourciel-Gouzy, M. L.; Launay, J.; Do Conto, T.; Colin, R.; Martinez, A.; Temple-Boyer, P., Development of a Creatinine-Sensitive Sensor for Medical Analysis. *Sensors and Actuators, B: Chemical* 2004, 103, 260-264.

[116]. Ho, W. O.; Krause, S.; McNell, C. J.; Pritchard, J. A.; Armstrong, R. D.; Athey, D.; Rawson, K., Electrochemical Sensor for Measurement of Urea and Creatinine in Serum Based on Ac Impedance Measurement of Enzyme-Catalyzed Polymer Transformation. *Analytical Chemistry* 1999, 71, 1940-1946.

[117]. Simonian, A. L.; Flounders, A. W.; Wild, J. R., Fet-Based Biosensors for the Direct Detection of Organophosphate Neurotoxins. *Electroanalysis* 2004, 16, 1896-1906.

[118]. Simonian, A. L.; Grimsley, J. K.; Flounders, A. W.; Schoeniger, J. S.; Cheng, T. C.; DeFrank, J. J.; Wild, J. R., Enzyme-Based Biosensor for the Direct Detection of Fluorine-Containing Organophosphates. *Analytica Chimica Acta* 2001, 442, 15-23.

[119]. Singh, A. K.; Flounders, A. W.; Volponi, J. V.; Ashley, C. S.; Wally, K.; Schoeniger, J. S., Development of Sensors for Direct Detection of Organophosphates. Part I: Immobilization, Characterization and Stabilization of Acetylcholinesterase and Organophosphate Hydrolase on Silica Supports. *Biosensors and Bioelectronics* 1999, 14, 703-713.

[120]. Flounders, A. W.; Singh, A. K.; Volponi, J. V.; Carichner, S. C.; Wally, K.; Simonian, A. S.; Wild, J. R.; Schoeniger, J. S., Development of Sensors for Direct Detection of Organophosphates. Part Ii: Sol-Gel Modified Field Effect Transistor with Immobilized Organophosphate Hydrolase. *Biosensors and Bioelectronics* 1999, 14, 715-722.

[121]. Schöning, M. J.; Poghossian, A., Bio Feds (Field-Effect Devices): State-of-the-Art and New Directions. *Electroanalysis* 2006, 18, 1893-1900.

[122]. Rothberg, J. M.; Hinz, W.; Rearick, T. M.; Schultz, J.; Mileski, W.; Davey, M.; Leamon, J. H.; Johnson, K.; Milgrew, M. J.; Edwards, M., et al., An Integrated Semiconductor Device Enabling Non-Optical Genome Sequencing. *Nature* 2011, 475, 348-352.

[123]. Goda, T.; Miyahara, Y., Label-Free and Reagent-Less Protein Biosensing Using Aptamer-Modified Extended-Gate Field-Effect Transistors. *Biosensors and Bioelectronics* 2013, 45, 89-94.

[124]. Chiang, J. L.; Kuo, C. Y. In *Study on the Characterizations and Applications of the Ph-Sensor with Gzo/Glass Extended-Gate Fet*, 2013; pp 498-501.

[125]. Chen, C. P.; Ganguly, A.; Lu, C. Y.; Chen, T. Y.; Kuo, C. C.; Chen, R. S.; Tu, W. H.; Fischer, W. B.; Chen, K. H.; Chen, L. C., Ultrasensitive in Situ Label-Free DNA Detection Using a Gan Nanowire-Based Extended-Gate Field-Effect-Transistor Sensor. *Analytical Chemistry* 2011, 83, 1938-1943.

[126]. Bian, C.; Tong, J.; Sun, J.; Zhang, H.; Xue, Q.; Xia, S., A Field Effect Transistor (Fet)-Based Immunosensor for Detection of Hba1c and Hb. *Biomedical Microdevices* 2011, 13, 345-352.

[127]. Hsieh, C. H.; Huang, I. Y.; Wu, C. Y. In *A Low-Hysteresis and High-Sensitivity Extended Gate Fet-Based Chloride Ion-Selective Sensor*, 2010; pp 358-361.

[128]. Cao, Z.; Xiao, Z. L.; Dai, Y. L.; Kamahori, M.; Shimoda, M., Electrical Characteristics of Extended Gate Fet Sensing Chip Constructed for Detection of DNA. 2010; Vol. 97-101, pp 4189-4192.

[129]. Fritz, J.; Cooper, E. B.; Gaudet, S.; Sorger, P. K.; Manalis, S. R., Electronic Detection of DNA by Its Intrinsic Molecular Charge. *Proceedings of the National Academy of Sciences of the United States of America* 2002, 99, 14142-14146.

[130]. Cui, Y.; Wei, Q. Q.; Park, H. K.; Lieber, C. M., Nanowire Nanosensors for Highly Sensitive and Selective Detection of Biological and Chemical Species. *Science* 2001, 293, 1289-1292.

[131]. Hahm, J.; Lieber, C. M., Direct Ultrasensitive Electrical Detection of DNA and DNA Sequence Variations Using Nanowire Nanosensors. *Nano Letters* 2004, 4, 51-54.

[132]. Patolsky, F.; Zheng, G. F.; Hayden, O.; Lakadamyali, M.; Zhuang, X. W.; Lieber, C. M., Electrical Detection of Single Viruses. *Proceedings of the National Academy of Sciences of the United States of America* 2004, 101, 14017-14022.

[133]. Wang, W. U.; Chen, C.; Lin, K. H.; Fang, Y.; Lieber, C. M., Label-Free Detection of Small-Molecule-Protein Interactions by Using Nanowire Nanosensors. *Proceedings of the National Academy of Sciences of the United States of America* 2005, 102, 3208-3212.

[134]. Zheng, G. F.; Patolsky, F.; Cui, Y.; Wang, W. U.; Lieber, C. M., Multiplexed Electrical Detection of Cancer Markers with Nanowire Sensor Arrays. *Nature Biotechnology* 2005, 23, 1294-1301.

[135]. Timko, B. P.; Cohen-Karni, T.; Yu, G. H.; Qing, Q.; Tian, B. Z.; Lieber, C. M., Electrical Recording from Hearts with Flexible Nanowire Device Arrays. *Nano Letters* 2009, 9, 914-918.

[136]. Stern, E.; Klemic, J. F.; Routenberg, D. A.; Wyrembak, P. N.; Turner-Evans, D. B.; Hamilton, A. D.; LaVan, D. A.; Fahmy, T. M.; Reed, M. A., Label-Free Immunodetection with Cmos-Compatible Semiconducting Nanowires. *Nature* 2007, 445, 519-522.

[137]. Li, Z.; Chen, Y.; Li, X.; Kamins, T. I.; Nauka, K.; Williams, R. S., Sequence-Specific Label-Free DNA Sensors Based on Silicon Nanowires. *Nano Letters* 2004, 4, 245-247.

[138]. Bunimovich, Y. L.; Shin, Y. S.; Yeo, W. S.; Amori, M.; Kwong, G.; Heath, J. R., Quantitative Real-Time Measurements of DNA Hybridization with Alkylated Nonoxidized Silicon Nanowires in Electrolyte Solution. *Journal of the American Chemical Society* 2006, 128, 16323-16331.

[139]. Gao, Z.; Agarwal, A.; Trigg, A. D.; Singh, N.; Fang, C.; Tung, C. H.; Fan, Y.; Buddharaju, K. D.; Kong, J., Silicon Nanowire Arrays for Label-Free Detection of DNA. *Analytical Chemistry* 2007, 79, 3291-3297.

[140]. McAlpine, M. C.; Ahmad, H.; Wang, D.; Heath, J. R., Highly Ordered Nanowire Arrays on Plastic Substrates for Ultrasensitive Flexible Chemical Sensors. *Nature Materials* 2007, 6, 379-384.

[141]. Zhang, G. J.; Chua, J. H.; Chee, R. E.; Agarwal, A.; Wong, S. M.; Buddharaju, K. D.; Balasubramanian, N., Highly Sensitive Measurements of Pna-DNA Hybridization Using Oxide-Etched Silicon Nanowire Biosensors. *Biosensors and Bioelectronics* 2008, 23, 1701-1707.

[142]. Zhang, G. J.; Zhang, G.; Chua, J. H.; Chee, R. E.; Wong, E. H.; Agarwal, A.; Buddharaju, K. D.; Singh, N.; Gao, Z.; Balasubramanian, N., DNA Sensing by Silicon Nanowire: Charge Layer Distance Dependence. *Nano Letters* 2008, 8, 1066-1070.

[143]. Zhang, G. J.; Chua, J. H.; Chee, R. E.; Agarwal, A.; Wong, S. M., Label-Free Direct Detection of Mirnas with Silicon Nanowire Biosensors. *Biosensors & Bioelectronics* 2009, 24, 2504-2508.

[144]. Fang, Z.; Kelley, S. O., Direct Electrocatalytic Mrna Detection Using Pna-Nanowire Sensors. *Anal. Chem.* 2009, 81, 612-617.

[145]. Zhang, G. J.; Chua, J. H.; Chee, R. E.; Agarwal, A.; Wong, S. M., Label-Free Direct Detection of Mirnas with Silicon Nanowire Biosensors. *Biosensors Bioelectron.* 2009, 24, 2504-2508.

[146]. Chen, Y.; Wang, X.; Hong, M. K.; Rosenberg, C. L.; Reinhard, B. M.; Erramilli, S.; Mohanty, P., Nanoelectronic Detection of Breast Cancer Biomarker. *Appl. Phys. Lett.* 2010, 97.

[147]. Chen, K. I.; Li, B. R.; Chen, Y. T., Silicon Nanowire Field-Effect Transistor-Based Biosensors for Biomedical Diagnosis and Cellular Recording Investigation. *Nano Today* 2011, 6, 131-154.

[148]. Penner, R. M., Chemical Sensing with Nanowires. 2012; Vol. 5, pp 461-485.

[149]. Qing, Q.; Pal, S. K.; Tian, B. Z.; Duan, X. J.; Timko, B. P.; Cohen-Karni, T.; Murthy, V. N.; Lieber, C. M., Nanowire Transistor Arrays for Mapping Neural Circuits in Acute Brain Slices. *Proceedings of the National Academy of Sciences of the United States of America* 2010, 107, 1882-1887.

[150]. Toumazou, C.; Georgiou, P., Piet Bergveld - 40 Years of Isfet Technology: From Neuronal Sensing to DNA Sequencing. *Electron. Lett* 2011, 47, S7-S12.

[151]. Schaffhauser, D. F.; Patti, M.; Goda, T.; Miyahara, Y.; Forster, I. C.; Dittrich, P. S., An Integrated Field-Effect Microdevice for Monitoring Membrane Transport in Xenopus Laevis Oocytes Via Lateral Proton Diffusion. *PLoS ONE* 2012, 7.

[152]. Chen, S. Y.; Bomer, J. G.; Carlen, E. T.; van den Berg, A., Al(2)O(3)/Silicon Nanoisfet with near Ideal Nernstian Response. *Nano Letters* 2011, 11, 2334-2341.

[153]. Reddy Jr, B.; Dorvel, B. R.; Go, J.; Nair, P. R.; Elibol, O. H.; Credo, G. M.; Daniels, J. S.; Chow, E. K. C.; Su, X.; Varma, M., et al., High-K Dielectric Al2o3 Nanowire and Nanoplate Field Effect Sensors for Improved Ph Sensing. *Biomedical Microdevices* 2011, 13, 335-344.

[154]. Wong, H.; Iwai, H., On the Scaling Issues and High-Kappa Replacement of Ultrathin Gate Dielectrics for Nanoscale Mos Transistors. *Microelectronic Engineering* 2006, 83, 1867-1904.

[155]. Chen, Y. W.; Liu, M. Z.; Kaneko, T.; McIntyre, P. C., Atomic Layer Deposited Hafnium Oxide Gate Dielectrics for Charge-Based Biosensors. *Electrochemical and Solid State Letters* 2010, 13, G29-G32.

[156]. Hsu, P. Y.; Wu, C. Y.; Cheng, H. C.; Wu, Y. L.; Chang, W. T.; Shen, Y. L.; Chang, C. M.; Wang, C. C.; Lin, J. J. In *Comparison of Multiple-Polysilicon-Nanowire Ph-Sensors Coated with Different Ald-Deposited High-K Dielectric Materials*, Tianjin, Tianjin, 2011.

[157]. Jang, H. J.; Cho, W. J., High Performance Silicon-on-Insulator Based Ion-Sensitive Field-Effect Transistor Using High-K Stacked Oxide Sensing Membrane. *Applied Physics Letters* 2011, 99.

[158]. Lin, Y. T.; Yu, Y. H.; Chen, Y.; Zhang, G. J.; Zhu, S. Y.; Yang, C. M.; Lu, K. Y.; Lai, C. S., Vertical Silicon Nanowires with Atomic Layer Deposition with Hfo 2 Membrane for Ph Sensing Application. *Journal of Mechanics in Medicine and Biology* 2011, 11, 959-966.

[159]. Oh, J. Y.; Jang, H. J.; Cho, W. J.; Islam, M. S., Highly Sensitive Electrolyte-Insulator-Semiconductor Ph Sensors Enabled by Silicon Nanowires with Al 2o 3/Sio 2 Sensing Membrane. *Sensors and Actuators, B: Chemical* 2012, 171-172, 238-243.

[160]. Gao, X. P. A.; Zheng, G. F.; Lieber, C. M., Subthreshold Regime Has the Optimal Sensitivity for Nanowire Fet Biosensors. *Nano Letters* 2010, 10, 547-552.

[161]. Elfstrom, N.; Juhasz, R.; Sychugov, I.; Engfeldt, T.; Karlstrom, A. E.; Linnros, J., Surface Charge Sensitivity of Silicon Nanowires: Size Dependence. *Nano Letters* 2007, 7, 2608-2612.

[162]. Stern, E.; Wagner, R.; Sigworth, F. J.; Breaker, R.; Fahmy, T. M.; Reed, M. A., Importance of the Debye Screening Length on Nanowire Field Effect Transistor Sensors. *Nano Letters* 2007, 7, 3405-3409.

[163]. Lee, J.; Shin, M.; Ahn, C. G.; Ah, C. S.; Park, C. W.; Sung, G. Y., Effects of Ph and Ion Concentration in a Phosphate Buffer Solution on the Sensitivity of Silicon Nanowire Biofets. *Journal of the Korean Physical Society* 2009, 55, 1621-1625.

[164]. Nair, P. R.; Alam, M. A., Design Considerations of Silicon Nanowire Biosensors. *Ieee Transactions on Electron Devices* 2007, 54, 3400-3408.

[165]. Senaratne, W.; Andruzzi, L.; Ober, C. K., Self-Assembled Monolayers and Polymer Brushes in Biotechnology: Current Applications and Future Perspectives. *Biomacromolecules* 2005, 6, 2427-2448.

[166]. De Gennes, P. G., Conformations of Polymers Attached to an Interface. *Macromolecules* 1980, 13, 1069-1075.

[167]. Prucker, O.; Rühe, J., Synthesis of Poly(Styrene) Monolayers Attached to High Surface Area Silica Gels through Self-Assembled Monolayers of Azo Initiators. *Macromolecules* 1998, 31, 592-601.

[168]. Husseman, M.; Malmström, E. E.; McNamara, M.; Mate, M.; Mecerreyes, D.; Benoit, D. G.; Hedrick, J. L.; Mansky, P.; Huang, E.; Russell, T. P., et al., Controlled Synthesis of Polymer Brushes by "Living" Free Radical Polymerization Techniques. *Macromolecules* 1999, 32, 1424-1431.

[169]. De Boer, B.; Simon, H. K.; Werts, M. P. L.; Van Der Vegte, E. W.; Hadziioannou, G., `Living' Free Radical Photopolymerization Initiated from Surface-Grafted Iniferter Monolayers. *Macromolecules* 2000, 33, 349-356.

[170]. Hodges, J. C.; Harikrishnan, L. S.; Ault-Justus, S., Preparation of Designer Resins Via Living Free Radical Polymerization of Functional Monomers on Solid Support. *Journal of Combinatorial Chemistry* 2000, 2, 80-88.

[171]. Cosnier, S., Biosensors Based on Immobilization of Biomolecules by Electrogenerated Polymer Films. *Applied Biochemistry and Biotechnology - Part A Enzyme Engineering and Biotechnology* 2000, 89, 127-138.

[172]. Yang, S. T.; Witkowski, A.; Hutchins, R. S.; Scott, D. L.; Bachas, L. G., Biotin-Modified Surfaces by Electrochemical Polymerization of Biotinyl-Tyramide. *Electroanalysis* 1998, 10, 58-60.

[173]. Deshpande, M. V.; Hall, E. A. H., An Electrochemically Grown Polymer as an Immobilisation Matrix for Whole Cells: Application in an Amperometric Dopamine Sensor. *Biosensors and Bioelectronics* 1990, 5, 431-448.

[174]. Uchiyama, S.; Hasebe, Y.; Tanaka, M., L-Ascorbate Sensor with Polypyrrole-Coated Carbon Felt Membrane Electropolymerized in a Cucumber Juice Solution. *Electroanalysis* 1997, 9, 176-178.

[175]. Cosnier, S.; Innocent, C., A New Strategy for the Construction of a Tyrosinase-Based Amperometric Phenol and O-Diphenol Sensor. *Bioelectrochemistry and Bioenergetics* 1993, 31, 147-160.

[176]. Wang, W.; Wang, F.; Yao, Y.; Hu, S.; Shiu, K. K., Amperometric Bienzyme Glucose Biosensor Based on Carbon Nanotube Modified Electrode with Electropolymerized Poly(Toluidine Blue O) Film. *Electrochimica Acta* 2010, 55, 7055-7060.

[177]. Reisberg, S.; Acevedo, D. F.; Korovitch, A.; Piro, B.; Noel, V.; Buchet, I.; Tran, L. D.; Barbero, C. A.; Pham, M. C., Design of a New Electrogenerated Polyquinone Film Substituted with Glutathione. Towards Direct Electrochemical Biosensors. *Talanta* 2010, 80, 1318-1325.

[178]. Piro, B.; Zhang, Q. D.; Reisberg, S.; Noel, V.; Dang, L. A.; Duc, H. T.; Pham, M. C., Direct and Rapid Electrochemical Immunosensing System Based on a Conducting Polymer. *Talanta* 2010, 82, 608-612.

[179]. Noh, H. B.; Kumar, P.; Biswas, T. K.; Kim, D. S.; Shim, Y. B., Improved Performance of an Amperometric Biosensor with Polydiaminonaphthalene on Electrochemically Deposited Au Nanoparticles. *Electroanalysis* 2010, 22, 632-638.

[180]. Hafaid, I.; Chebil, S.; Korri-Youssoufi, H.; Bessueille, F.; Errachid, A.; Sassi, Z.; Ali, Z.; Abdelghani, A.; Jaffrezic-Renault, N., Effect of Electrical Conditions on an

Impedimetric Immunosensor Based on a Modified Conducting Polypyrrole. *Sensors and Actuators, B: Chemical* 2010, 144, 323-331.

[181]. Baur, J.; Holzinger, M.; Gondran, C.; Cosnier, S., Immobilization of Biotinylated Biomolecules onto Electropolymerized Poly(Pyrrole-Nitrilotriacetic Acid)-Cu2+ Film. *Electrochemistry Communications* 2010, 12, 1287-1290.

[182]. Wang, Z.; Liu, S.; Wu, P.; Cai, C., Detection of Glucose Based on Direct Electron Transfer Reaction of Glucose Oxidase Immobilized on Highly Ordered Polyaniline Nanotubes. *Analytical Chemistry* 2009, 81, 1638-1645.

[183]. Kazimierska, E.; Muchindu, M.; Morrin, A.; Iwuoha, E.; Smyth, M. R.; Killard, A. J., The Fabrication of Structurally Multiordered Polyaniline Films and Their Application in Electrochemical Sensing and Biosensing. *Electroanalysis* 2009, 21, 595-603.

[184]. Ulman, A., Formation and Structure of Self-Assembled Monolayers. *Chemical Reviews* 1996, 96, 1533-1554.

[185]. DiMilla, P. A.; Folkers, J. P.; Biebuyck, H. A.; Härter, R.; López, G. P.; Whitesides, G. M., Wetting and Protein Adsorption of Self-Assmebled Monolayers of Alkanethiolates Supported on Transparent Films of Gold. *Journal of the American Chemical Society* 1994, 116, 2225-2226.

[186]. Bain, C. D.; Whitesides, G. M., Formation of Monolayers by the Coadsorption of Thiols on Gold: Variation in the Length of the Alkyl Chain. *Journal of the American Chemical Society* 1989, 111, 7164-7175.

[187]. Kim, D. S.; Park, J. E.; Shin, J. K.; Kim, P. K.; Lim, G.; Shoji, S., An Extended Gate Fet-Based Biosensor Integrated with a Si Microfluidic Channel for Detection of Protein Complexes. *Sensors and Actuators, B: Chemical* 2006, 117, 488-494.

[188]. Cao, Z.; Xiao, Z. L.; Zhang, L.; Luo, D. M.; Kamahori, M.; Shimoda, M., Molecule Counting with Alkanethiol and DNA Immobilized on Gold Microplates for Extended Gate Fet. *Materials Science and Engineering C* 2013, 33, 1481-1490.

[189]. Haensch, C.; Hoeppener, S.; Schubert, U. S., Chemical Modification of Self-Assembled Silane Based Monolayers by Surface Reactions. *Chemical Society Reviews* 2010, 39, 2323-2334.

[190]. Booth, B. D.; Vilt, S. G.; Lewis, J. B.; Rivera, J. L.; Buehler, E. A.; McCabe, C.; Jennings, G. K., Tribological Durability of Silane Monolayers on Silicon. *Langmuir* 2011, 27, 5909-5917.

[191]. Brandow, S. L.; Chen, M. S.; Dulcey, C. S.; Dressick, W. J., Formation of Aromatic Siloxane Self-Assembled Monolayers. *Langmuir* 2008, 24, 3888-3896.

[192]. Takahara, A.; Kojio, K.; Kajiyama, T., Effect of Aggregation State on Nanotribological Behaviors of Organosilane Monolayers. *Ultramicroscopy* 2002, 91, 203-213.

[193]. Fadeev, A. Y.; McCarthy, T. J., Self-Assembly Is Not the Only Reaction Possible between Alkyltrichlorosilanes and Surfaces: Monomolecular and Oligomeric Covalently Attached Layers of Dichloro- and Trichloroalkylsilanes on Silicon. *Langmuir* 2000, 16, 7268-7274.

[194]. Biotech, G. Direct Elisa Protocol. http://www.genwaybio.com/technologies/direct-elisa.

[195]. Bergveld, P., Thirty Years of Isfetology - What Happened in the Past 30 Years and What May Happen in the Next 30 Years. *Sensors and Actuators B-Chemical* 2003, 88, 1-20.

[196]. Bergveld, P., Thirty Years of Isfetology: What Happened in the Past 30 Years and What May Happen in the Next 30 Years. *Sensors and Actuators, B: Chemical* 2003, 88, 1-20.

[197]. Stern, E.; Vacic, A.; Rajan, N. K.; Criscione, J. M.; Park, J.; Ilic, B. R.; Mooney, D. J.; Reed, M. A.; Fahmy, T. M., Label-Free Biomarker Detection from Whole Blood. *Nature Nanotechnology* 2010, 5, 138-142.

# CHAPTER 3: VAPOR PHASE DEPOSITION OF MONOFUNCTIONAL ALKOXYSILANES FOR SUB-NANOMETER LEVEL BIOINTERFACING ON SILICON OXIDE SURFACES

## 3.1 ABSTRACT

Improving the performance and lowering the analyte detection limits of optical and electronic biosensors is essential for advancing wide ranging applications in diagnostics and drug discovery. Most sensing methods require direct linkage of a recognition element and a sensor, which is commonly accomplished through an organic monolayer interface. Alkoxyorganosilanes are typically used to prepare sensor surfaces on dielectric oxides. However, many silanes lead to roughened or thick interfaces that degrade device sensitivity. We have found that controlled vapor phase deposition of monoalkoxysilanes leads to monolayers resistant to elevated temperatures and extreme pH conditions. The formation of high density, subnanometer monolayers is demonstrated by ellipsometry, XPS, and AFM. We demonstrate the uniform attachment of these monofunctional silanes to such biosensing platforms as microarrays, field effect devices, and the formation of SERS substrates. The advantages of using this silane deposition protocol for the above technologies are also discussed.

## 3.2 INTRODUCTION

A typical biosensor contains three components; a receptor element, which recognizes or captures the biological or chemical analyte; the transducer, which converts the stimulus to an output signal; and an output system, which translates the output signal to an interpretable format. In the construction of biosensors, a variety of chemistries have been used to link receptor elements to surfaces, however this step remains a limiting factor in device sensitivity, reliability and reproducibility.[1,2]The output signal relies on transduction by optical[3-7], electrochemical[8-10], piezoelectric techniques[11], or other methods, and hence sensitivity increases with proximity of the analyte to the surface. Consequently the linkage distance from the surface to the receptor elements must be reduced in order to maximize the contributions to the signal from the bound analyte. Self-assembled monolayers (SAMs) are commonly employed for interfacing biological receptors to a transducer. Many optical and electrochemical methods contain oxides as part of the transducer, which are effective substrates for conjugation of alkoxy- and halo-substituted organosilanes. The mechanism of their reaction with oxide surfaces has been well studied[12], and their aqueous and thermal stabilities have been established[1,2,13,14].

Self assembled monolayers are commonly deposited through either liquid or vapor based methods. There has been some success in the formation of trialkoxysilane monolayers in solution phase[15] and by using dip pen lithography[16,17], but there exists much room for improvement. There is a need to make the deposition processes simpler and more reliable, to reduce the generation of contaminated effluents and polymerized products, and to lower the production costs.[18] Processes which utilize

vapor phase deposition can eliminate some of the problems that are seen in liquid-based deposition and also make themselves amenable to be used in batch and microelectronics-compatible processes.[19,20] In these vapor-phase processes, the precursor chemistry is easily controlled and efficient mass transport ensures coating of high-aspect-ratio structures (such as those found in MEMS devices). Moreover, it has been shown that the performance of SAM coatings that are grown in vapor phase is comparable or superior to SAMs that are grown in liquid phase [21], and the vapor phase methods can be applied at the wafer scale level [22]. Indeed, vapor phase deposition of trialkoxysilane SAM's with a variety of terminal functional groups has been achieved on oxide surfaces previously.[23-28] However, these trifunctional silanes are also known to polymerize in either aqueous or vapor phase deposition methods over a wide range of temperatures and environmental conditions.[29-33] Consequently, high quality monolayer formation may require very stringent and specialized processing conditions, making them more challenging to integrate with VLSI or wafer scale microelectronics devices and processes.

Organosilanes with trifunctional reactive groups, such as octadecyltrichlorosilane and aminopropyltriethoxysilane, have been frequently conjugated to devices by vapor and liquid methods[34-37] , with the latter silane of particular importance because the amino group allows simple conjugation to reactive functional groups, including active esters, aldehydes and ketones and isocyanates.[38] However, the possible difficulties with trialkoxysilanes mentioned earlier may compromise device performance by having nonuniformities on the active areas of the sensor or by increasing the length of the interfacial region . Monofunctional silanes possess the ability to alleviate these issues since only one functional group is available to react with the surface and since these films

have been shown to successfully be deposited on oxide surfaces[39,40] Other added advantages include a higher vapor pressure than equivalent trifunctional silanes and the fact that these monofunctional silanes do not displace amine catalysts unless covalent linkage occurs. These advantages allow for extended high temperature deposition and curing times, variables known to influence the quality and robustness of the films, as well as facilitate vapor phase deposition which is the preferred passivation method in the semiconductor industry. However, to-date only limited characterization has been performed on monofunctional silanes and little is known about their performance in solution and applicability to biosensing platforms.

In the present study, we evaluate vapor phase deposition of two monoethoxysilanes, one amino-terminated and another glycidoxy-terminated, and demonstrate their applicability to biosensor fabrication. The kinetics of monolayer formation was measured with ellipsometry and found to follow a diffusion-limited Langmuir model. X-Ray photoelectron spectroscopy (XPS) confirmed the elemental compositions of completed monolayers. Atomic Force Microscopy (AFM) images of the complete monolayers contain roughness values close to that of silicon, and the topography indicated high density coverage. A critical issue surrounding these monolayers is their aqueous stability under stressed conditions, particularly at elevated temperatures, and extreme pH values. To assess the stability, the aminoalkyl-derived surface was first allowed to react with an amine-reactive fluorophore. The fluorescent intensities were then compared for monolayers subjected to temperatures of 25 ˚C and 60 ˚C, and aqueous solution pH values ranging from 1 to 13 for time periods up to 6 hours.

No measureable changes in fluorescence intensity and fluorescence uniformity were observed.

Subsequently, we applied this deposition method to optical and electrochemical biosensing platforms, including microarrays, field-effect devices, and SERS-active substrates. We show the high deposition uniformity and decreased background noise when applied to microarrays. We also demonstrate that the conjugation technique can be applied to field effect devices for possible applications in potentiometric sensing. Finally, we demonstrate high coverage densities of Au nanoparticles for the formation of surface enhanced raman spectroscopy (SERS) active substrates for Raman detection capabilities. Overall, the ease of this functionalization method and its high stability show promise for increasing the performance and longevity of biosensors. As a result, this silanization can be widely applied across many biosensing platforms.

## 3.3 EXPERIMENTAL

### MATERIALS

3-Aminopropyldimethylethoxysilane (APDMS) and 3-glycidoxypropyldimethylethoxysilane (GPDMS) were purchased from Gelest, Inc. and used without further purification. Triethylamine, toluene, and methanol were obtained from Sigma and dried with 3A molecular sieves. The fluorescent dyes 7-amino-4-methylcoumarin, rhodamine B isothiocyanate, and 4-carboxyfluorescein NHS-ester were purchased from Sigma-Aldrich and used without further purification. Phosphate buffered saline (PBS), pH 7.4 was purchased from Gibco and degassed at 30 Torr in a dessicator for 10 minutes prior to use. All glassware prior to use was soaked in a NaOH:EtOH base bath for at least one hour and rinsed in DI water. The glassware was then dried at 150°C

in a convection oven. Four inch Si(100) wafers from SiliconQuest Intl. were diced into 4x7 mm chips for AFM, XPS, and ellipsometry experiments. A 4-inch Si(100) wafer was thermally oxidized at 1050°C for 24 hours to an $SiO_2$ thickness of ~1μm, which was confirmed by ellipsometry, and then diced into 4x7 mm chips for fluorescence stability measurements. Low autofluorescence Nexterion B microscope slides purchased from Schott were used for deposition uniformity experiments. Streptavidin-Cyanine-5 (SA-Cy5) for microarray spotting was purchased from Invitrogen. Silicon field effect devices were fabricated in our lab using SOI wafers and a VLSI compatible process.[63,64] Colloidal Au nanoparticles (Au-NP's) of 5 nm mean diameter were purchased from Sigma and used as received.

## SILANE DEPOSITION

Before silane depositions, each substrate was degreased in acetone and methanol, then immersed in $H_2SO_4$:$H_2O_2$ (7:3) for 30 minutes. The substrates were then rinsed in DI water, dried under a stream of $N_2$, and then subjected to a 300W $O_2$ plasma at a pressure of 500 mTorr for 10 minutes. The deposition of silanes on 4x7 mm chips was performed in 20$cm^3$ glass vials at a temperature of 100 °C and at a pressure of 30 Torr. Silanes were mixed with TEA to a 1% v/v solution, kept at 100 °C and 30 Torr, and transferred into the vials by a glass syringe using an 18 gauge stainless steel hypodermic needle through a viton septum. The reactions were quenched by purging the vials with $N_2$ at least 3 times. Chips were removed from the vials and then sonicated in vials containing toluene and methanol for 2 minutes each, respectively. The chips were then dried under a stream of $N_2$ for 5 minutes and stored in a vacuum desiccator until use.

Microscope slides and 6” Si wafers were prepared in a 0.75 $ft^3$ vacuum oven equipped with an $N_2$ and a vacuum port, preheated to 100 $^oC$. The slides were mounted horizontally in a glass rack which contained a rectangular bottom well for the silane solution. A volume of 1 mL silane solution was deposited in the bottom well and the rack was evacuated to a pressure of 30 Torr. The slides were subjected to the silane vapor for 12 hours. After 12 hours, the reaction was quenched by 3 purges with $N_2$ and then vacuum. The slides were then removed from the glass rack and sonicated in baths of toluene and methanol for 2 minutes, respectively. The slides were then rinsed with deionized water and dried under a stream of $N_2$ for 5 minutes.

The 6” Si wafers were silanized using the same vacuum oven setup and same conditions , except the $N_2$ inlet port was modified with a t-junction for carrying the silane vapor from outside the oven. The silane was put in a fused silica vial with a vacuum port to a total volume of 1 mL, connected to the t-junction via polytetrafluoroethylene (PTFE) tubing, and heated on a hot plate. A copper heating tape was put around the PTFE tubing to ensure isothermal conditions for the vapor leading into the chamber. The vacuum oven, PTFE tubing and the silane were both preheated to 100 °C, and the 6” wafer inserted into the vacuum oven. The oven was purged with $N_2$ and then vacuumed out 3 times. The t-junction was then opened to allow the silane to flow into the vacuum oven for 12 hours. After the deposition, the t-valve was closed to the silane and $N_2$ was cycled in to quench the reaction 3 times. The wafer was then removed from the oven and sonicated in toluene and methanol for 2 minutes each.The wafers were then carefully dried with a stream of $N_2$ to avoid spotting.

# SILANE CHARACTERIZATION

The ellipsometry measurements were taken on a Rudolph FE-III ellipsometer at an angle of 70 degrees and a wavelength of 6328 Å. The refractive indices utilized were 1.46 for the native oxide and 1.43 for the silanes. The chips were measured before and after silanization at 5 different spots. The native oxides for each dye ranged from 10-14 Å in thickness as determined by ellipsometry and X-ray Photoelectron Spectroscopy (XPS). Contact angle measurements were taken on a KSV CAM200 system in static mode using the sessile drop technique. A 10 uL drop of ultrapure water (18.2 MΩ-cm) was allowed to stabilize for 10 minutes before the measurement was taken. Error for each measurement is approximately ± 0.5 degrees. TOF-SIMS  XPS analysis was done on a KRATOS AXIS ULTRA at a take-off angle of 90 degrees. Monochromatic $Al_{k\alpha}$ X-Rays were used as the source. The control sample was carefully cleaned to remove carbonaceous material according to Seah et. al.[67] Silanized samples were subjected to a similar treatment, but without the use of $O_2$/plasma to keep the monolayer intact. Survey spectra were taken at a pass energy of 120 eV and high-resolution spectra at a pass energy of 40 eV. Each dye was mounted using a conductive copper tape and the C1s, N1s, and Si2p spectra recorded at a dwell time of 200 ms and 10 passes. All spectra were processed using CASA XPS software. The spectra were fitted with a modified Gaussian-Lorenztian algorithm using a Shirley background.

Atomic Force Microscopy (AFM) images were taken on an Asylum Research MPF-3D AFM with a silicon tip at 300 kHz in AC Mode. The amplitude and phase images were both recorded and image sizes ranged from 1x1 $um^2$ to 5x5 $um^2$. Microarray spotting was done using a non-contact piezoelectric spotter (Perkin Elmer Piezoarray)

with a pattern containing 350 pL spots of 10 pg/mL SA-Cy5 in phosphate buffered saline (PBS) at pH 7.4 with 0.05% trehalose to prevent spot drying. This SA-Cy5 concentration and volume equates to 70 attomol/spot. The spots were incubated at 4°C for 12 h, rinsed in 0.1% Tween in PBS for 5 min with agitation, then briefly with $dH_20$. The spots were imaged with a fluorescence laser scanner (Tecan LS Reloaded) at a gain of 190 and a 10□m pixel size. Processing of the collected images was done using ArrayPro software to calculate trimmed-mean (10%) intensities of a 14 pixel diameter region inside each spot. Background intensities were calculated as a trimmed-mean (10%) of the local corners around each spot. Images of silicon field effect devices were taken on a Nikon TE20 fluorescent microscope with a Pixera 16 bit CCD camera. The integration time for each fluorescent image was 5 seconds.

## 3.4 RESULTS

Since monofunctional silane reaction kinetics has seldom been studied[39], we deposited silanes for various time intervals in the vapor phase using the procedure described in the experimental section and then removed any physisorbed material by sonication. This allows for a more accurate determination of the extent of silane reaction as compared to real time measurements such as quartz crystal microbalance (QCM) or surface plasmon resonance (SPR), since fluidic rinses or gaseous purges may not desorb excess reagents leading to an overestimation of silane attachment.[41] The ellipsometric thickness of the silane layer versus the deposition time is displayed for 3-aminopropyldimethylethoxysilane (APDMS) and (3-glycidoxy)propyldimethylethoxysilane (GPDMS) in Figure 3.1. Assuming that the film is uniform, the adsorbed mass can be correlated to the thickness if the molar refractivity and

refractive index of the film are known.[42] The molar refractivity (A) of molecular species may be calculated by summation of the individual atomic bond refractivities which comprise the molecule. The molar refractivities for APDMS (A=35.4) and GPDMS (A=49.1) were calculated using the individual bond refractivites by Vogel[43], and the adsorbed mass was calculated for each point. The right axis in Figure 3.1 shows the theoretical adsorbed mass for each silane. For both silanes, the thickness results indicate the deposition follows Langmuir kinetics. The first hour is dominated by rapid and as the adsorption sites become occupied, the deposition slows and finally saturates between 6-12 hours. Using trifunctional silanes with epoxy and amino functionalities, we performed the same deposition procedures, which readily gave multi-layers with thicknesses in agreement with recent literature values (Figure 3.2).[30] Contact angle measurements were also taken at the same deposition times (Figure 3.3), and the values saturate at 49.5 and 58.0 degrees for APDMS and GPDMS, respectively.

Although the early stages of monolayer adsorption are known to be described well by Langmuir kinetics[44,45], extended depositions have been known to follow second-order or diffusion-limited forms of the Langmuir model with several growth process regimes[46]. In order to gain insight into the deposition mechanism, the data was fit using three Langmuir models: a first order process, a second-order process, and a diffusion limited process. By analyzing the residuals of the fit, the kinetics appear to follow a diffusion limited process which is described well by Rahn & Hallock.[47]

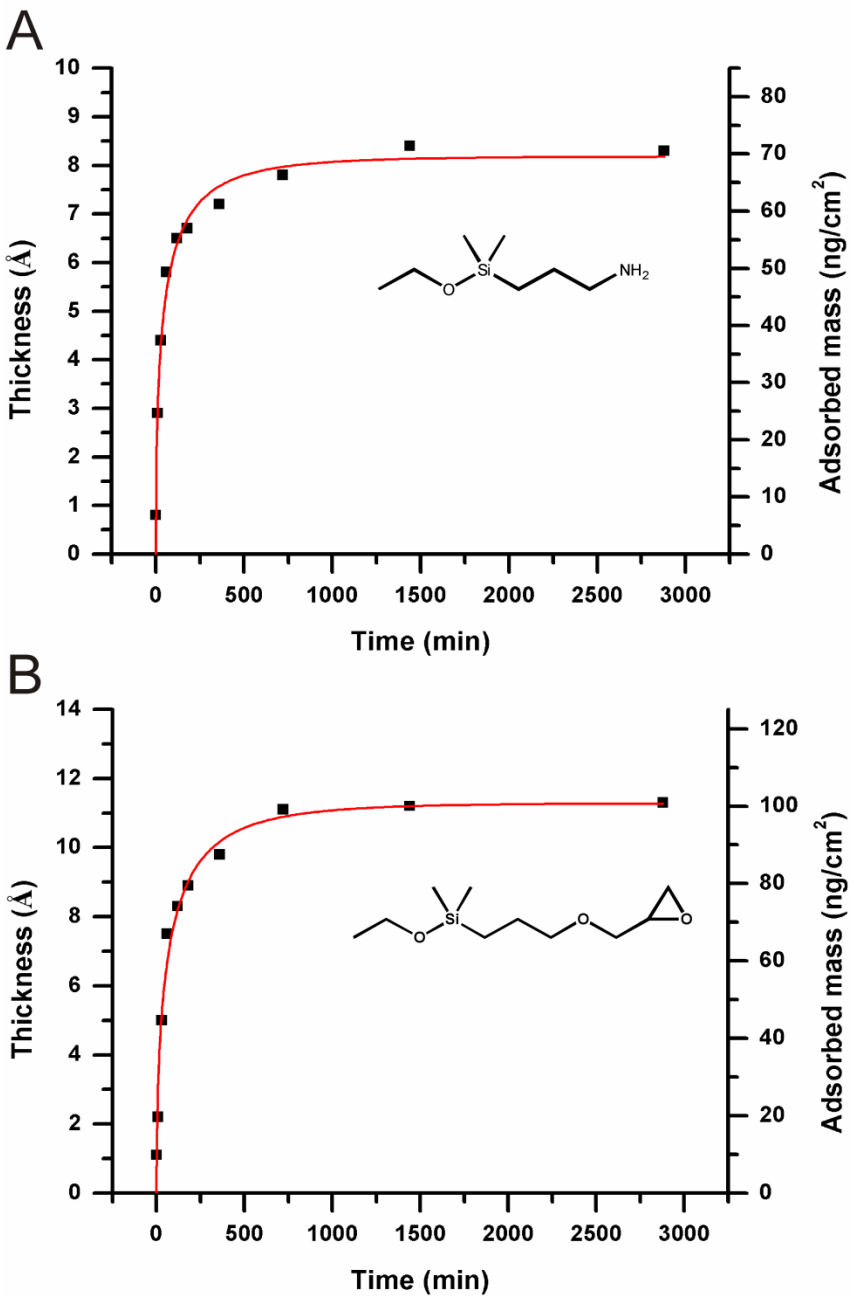


**Figure 3.1**. The thickness of APDMS (**A**) and GPDMS (**B**) versus deposition time as measured by ellipsometry. The points are fit to a diffusion limited Langmuir equation (red line) for each molecule.

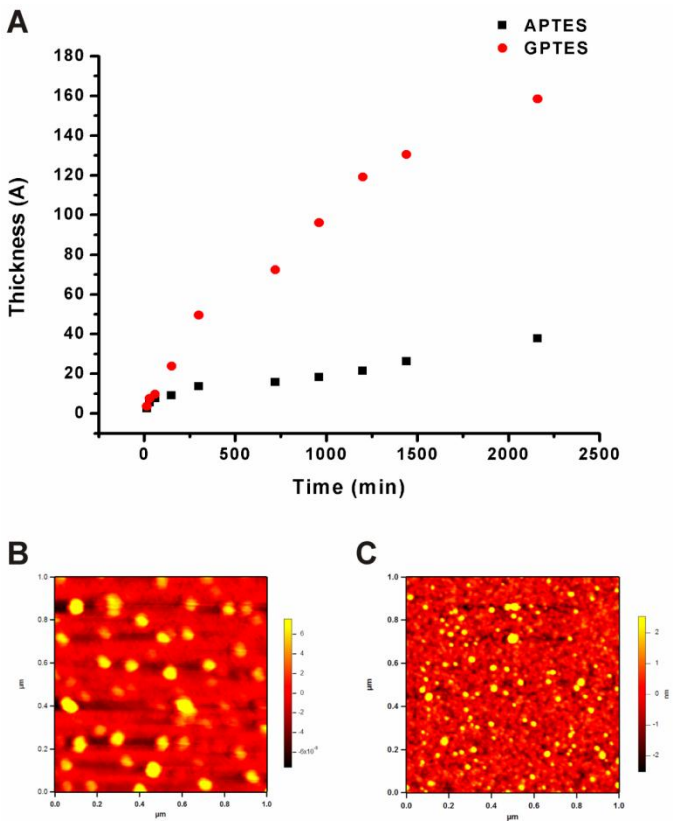


**Figure 3.2**. The trifunctional silanes APTES and GPTES were deposited using the same protocol as the monofunctional analogues and monitored versus time using ellipsometry (**A**). Multiple layers are formed as time progresses. AFM images of the APTES deposition (**B**) and the GPTES deposition (**C**) after a 12 hour time period. The average heights correlate well with ellipsometry.

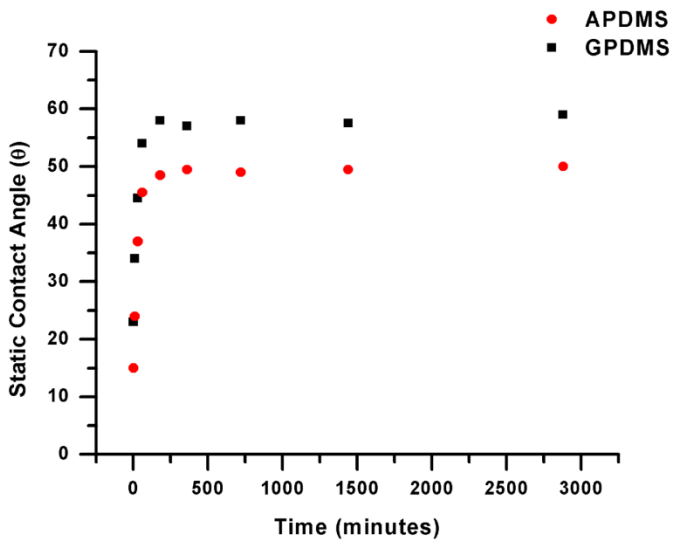


**Figure 3.3**. Static contact angle measurements taken for APDMS and GPDMS versus deposition time. A 10 uL drop of ultrapure water was allowed to stabilize on the substrate for 10 minutes before measuring.

Using this model, the maximum thickness and diffusion limited rate constant ($k_{1D}$) were calculated and are displayed in Table 3.1 for the aminosilane and epoxysilane. A purely diffusion limited process should be described by equation 1:

$$\Gamma(t) \approx \Gamma_f \left( 1 - \exp^{\left( -\frac{t}{\tau_D} \right)^{1/2}} \right) \qquad (1)$$

where $\tau_D$ is the diffusion limited time constant and $\Gamma_f$ is the final thickness. To evaluate the validity of the model, the power exponent of ½ in the equation was turned into a stretched exponential creating the exponent variable α. By allowing α to be a parameter in the fit, the optimal values of α were determined for APDMS and GPDMS. The values are displayed in Table 3.1, and both are close to ½ indicating a true diffusion limited process for the vapor deposition. The theoretical adsorbed masses saturate at 101.6

ng/cm$^2$ and 69.8 ng/cm$^2$ for the GPDMS and the APDMS, respectively. Taking the molecular weights of the compounds, this corresponds to 5.8 molecules/nm$^2$ for the epoxysilane and 6.1 molecules/nm$^2$ for the aminosilane. The high densities described for both silanes are not unreasonable, given the density of silanols achievable on crystalline silicon surfaces.[48,49] By cleaning the substrates properly and depositing the silanes at 100˚C, we are able to inhibit dehydroxylation at the surface, and maximize surface silanol density.

The vapor deposition of these silanes in vacuum and at temperature above their boiling points allow for simultaneous deposition and curing, with curing known to play an important role in stabilizing the attachment of the silane to the surface.[1,50] The ellipsometry results indicate saturated values for both monolayers by 12 hours deposition time. To confirm the compositions of the monolayers and correlate the ellipsometry thicknesses, XPS was taken for each silane after 12 hours deposition time.

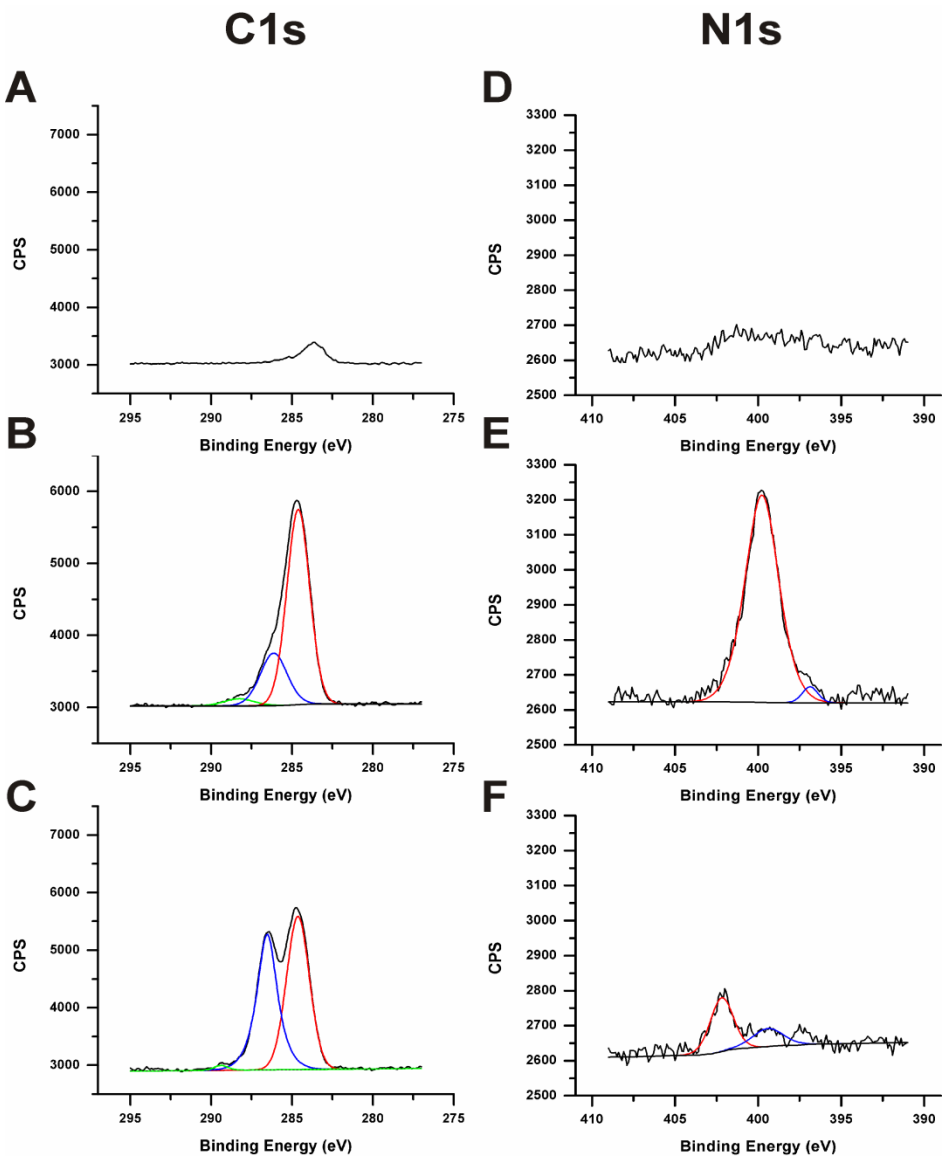


**Figure 3.4**. XPS high resolution spectra of C1s (**A-C**) and N1s (**D-F**) peaks after 12 hours deposition time. A blank substrate (**A, D**) shows little carbon or nitrogen contamination. The APDMS spectra for C1s (**B**) are curve fitted to show the peak assignments C-C (red), C-N (blue), and C=N (green) regions. The APDMS N1s spectra (**E**) show the peak assignments $NH_2$ (red) and silicon bound nitrogen (blue). The GPDMS spectra for C1s (**C**) shows the peak assignments C-C (red), C-O (blue), and C=O (green), while the N1s spectra (**F**) shows traces of adsorbed nitrogen gas (red) and protonated nitrogen (blue).

Figure 3.4 shows the C1s and N1s high resolution spectra for a native oxide control, APDMS, and GPDMS, respectively. Within each spectrum, the curves were

fitted to extract the localized bonding of each carbon or nitrogen atom. The native oxide shows very little carbon or nitrogen contamination, confirming that the signal results from the C1s and N1s of the attached silanes. The C1s spectra for each of the silanes contain binding energies for aliphatic (284.5-285.5 eV), slightly polar (286-287 eV), and highly polar (288-290 eV) carbons. The N1s spectra are split into $NH_2$ (399 eV) and $NH_3^+$ (401 eV) domains, which suggests that the amino groups of APDMS exist in both neutral and protonated form under the conditions of XPS analysis.

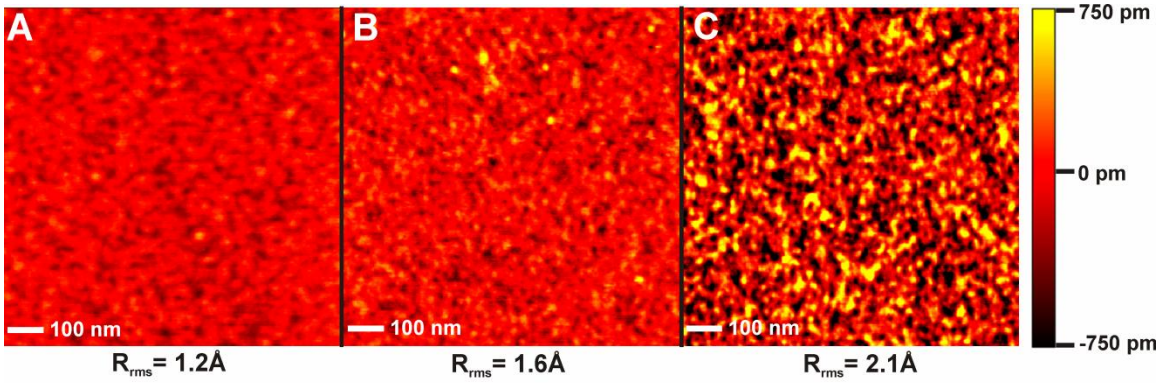


**Figure 3.5**. AFM Tapping Mode images of a native oxide substrate (**A**), an APDMS coated substrate after 12 hours deposition (**B**), and a GPDMS coated substrate after 12 hours deposition (**C**). The scale bar for all images is located on the right. The root mean square roughness ($R_{RMS}$) values for the substrates are displayed below each image.

The ratios of each of the elements and the ratios of the carbon types are displayed in Table 3.1. The C1s:N1s ratio provides information about the elemental composition of the silanes. For APDMS, the ratio is close to the stoichiometric value of 5:1, while GPDMS, which does not contain nitrogen, has a very high C1s:N1s ratio. Similarly, the ratio of aliphatic carbons ($C_a$) to slightly polar carbons ($C_p$) can give us insight into the chemical composition of the sample. Slightly polar carbons may be regarded as O-C-O, C-O, or C-N bonded, while aliphatic carbons are assigned as C-C or C-H bonded. The $C_a$:$C_p$ for GPDMS and APDMS are very close to the stoichiometric values of 1:1 and 4:1,

respectively. Most importantly, if the silane layer was damaged or oxidized during the long deposition time, the highly polar C1s peaks, indicating C=O or C=N, would be quite large. There is no evidence of this in the C1s spectra of either silane, indicating intact functional groups after the 12 hour deposition/curing period.

| | Ellipsometric Thickness (Å) | XPS Thickness (Å) | $k1_D$ ($min^{-1/2}$) | α | $\frac{C1s}{N1s}$ | $\frac{C-C}{C-O/C-N}$ | $R_{RMS}$ (Å) | Contact Angle (θ) |
|---|---|---|---|---|---|---|---|---|
| **APDMS** | **8.2 ± 0.4** | **8.6 ± 0.8** | **0.15** | **0.52** | **5.08** | **4.11** | **1.6** | **49.5** |
| **GPDMS** | **11.1± 0.5** | **11.7 ± 1.1** | **0.11** | **0.48** | **192.12** | **1.12** | **2.1** | **58.0** |

**Table 3.1**. Table of values for a 12 hour deposition period of APDMS and GPDMS. The various parameters gathered from ellipsometry, XPS, AFM, and contact angle are tabulated above.

The N1s spectrum for APDMS shows greater than 97% $NH_2$ terminations. This is an important result, since it indicates that the silanes on the surface are covalently attached instead of absorbed in the inverted state. In an inverted state, the silane would form an $NH_3^+Si\text{-}O^-$ ion pair, which commonly occurs in trifunctional silanes such as APTES.[51,52] Moreover, the data also indicates that triethylamine is not absorbed on the surface, which would block binding sites. The N1s spectra of GPDMS show peaks close to the noise of the control spectrum, as would be expected. The thickness (t) of the monolayers was calculated by equation 2 from the intensity of the Si2p electrons from the substrates (I) and the attenuation length of a hydrocarbon monolayer (λ):

$$t = -\lambda \sin\theta \ln\left(\frac{I}{I_o}\right) \qquad (2)$$

where, $I_o$ is the Si2p electron intensity from a blank sample and sinθ reflects the take-off angle, which is 90°, making sinθ equal to 1. The attenuation length for the electrons in the hydrocarbon layer is dependent upon the kinetic energy of the electron being ejected,

which for an Si2p electron is 1388 eV. The attenuation length as a function of kinetic energy λ(KE) was estimated for a hydrocarbon layer based upon the equation by Laibinis et. al[53], i.e. $\lambda(KE) = 9 + 0.022KE$. Using this equation, the attenuation length was estimated at 39.5 Å for the monolayer. The thicknesses were then calculated using equation 2, and are displayed in Table 3.1. For both silanes, the XPS appears to overestimate, but within error, the thickness of the silanes, in comparison to ellipsometry. However, both techniques complement each other and support the formation of a true, high density monolayer.

The morphologies of the formed monolayers were visualized using AFM in tapping mode after 12 hours deposition. The results of the AFM are displayed in Figure 3.5 for the control oxide, APDMS, and GPDMS, respectively. The morphologies look quite similar to the control image, lacking island domains which would be indicative of incomplete monolayers or solution phase depositions. Below each image is the RMS roughness ($R_{rms}$) for that image, and the values may also be found in Table 3.1. The control oxide contains an $R_{rms}$ of 1.2 Å, which is well known to be the case for native oxides on silicon, while APDMS and GPDMS contain $R_{rms}$ values of 1.6 Å and 2.1 Å, respectively. The fact the $R_{rms}$ values are so close to the control and less than the heights of the molecules affirm the formation of homogeneous layers. Although the GPDMS $R_{rms}$ is larger than APDMS, this is to be expected since the overall length of the molecule is longer and has a greater tendency to aggregate. AFM images were also taken for the same deposition times for their trifunctional analogues, showing large multilayer domains and $R_{rms}$ values larger than the lengths of the molecules (Figure 3.2).

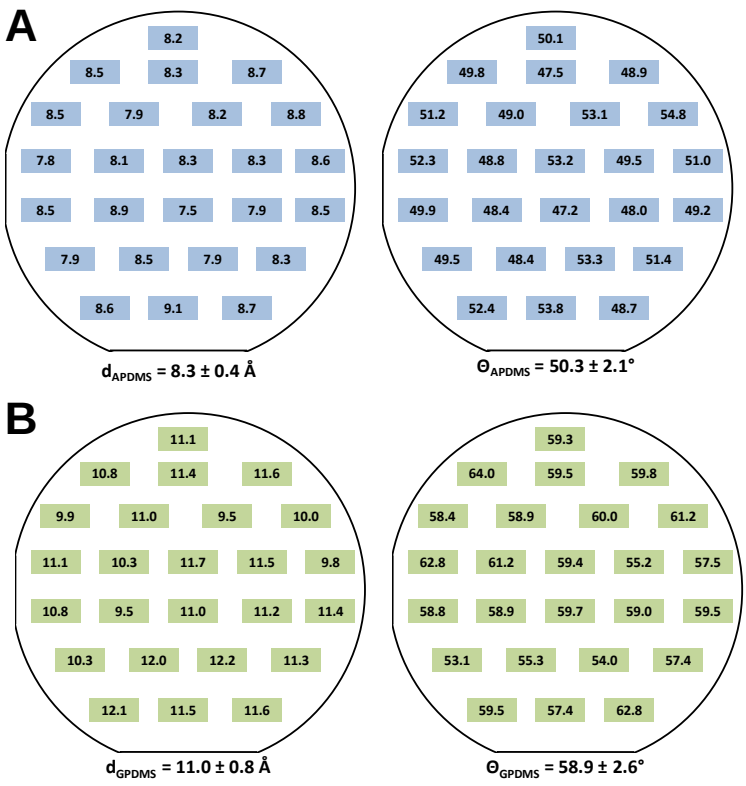


**Figure 3.6**. The ellipsometric thickness (**d**) and contact angle (**θ**) for APDMS (**A**) and GPDMS (**B**) were mapped on 2 different 6" Si wafers which were silanized for 12 hours. The wafers were measured at 25 different points for both thickness and contact angle and are displayed above. The mean value and standard deviation is below each wafer map in the figure.

To demonstrate applicability of this vapor based method to the semiconductor industry, both APDMS and GPDMS were deposited on 6" Si wafers with <100> silicon orientation . The deposition time for each silane was also 12 hours and took place in a 0.75 $ft^3$ vacuum oven with 1mL of silane for each deposition. The ellipsometric thickness and static contact angle was taken over 25 spots on each wafer, and the wafer maps for APDMS and GPDMS can be found in Figure 3.6. The values indicate a thickness of 8.3 ± 0.4 Å and a contact angle of 50.3 ± 2.1° for APDMS, while GPDMS had a thickness of 11.0 ± 0.8 Å and a contact angle of 58.9 ± 2.6°. These values over entire 6" Si wafers

match, within the standard deviation, the values determined with 4x7mm test chips. Moreover, the standard deviations are less than 10% the mean value, indicating highly uniform depositions over large areas are achievable using this process.To gain insight into the resistance of the monolayers to hydrolysis, APDMS was subjected to various conditions over a period of 6 hours, and then allowed to react with a ROX-NHS ester. The fluorescence was then measured and is displayed over a period of 6 hours in Figure 3.7. Figure 3.7A shows the fluorescent intensity after incubation in 0.1M HCl and 0.1M NaOH.. There is little decrease in fluorescent intensity over 6 hours for both solutions, and is within the error of each measurement. A similar experiment was performed but with the silanes incubated in PBS, pH 7.4 at 60°C and 90°C and is shown in Figure 3.7B. Again, the fluorescent intensity decay is within the errors of the measurement for both solutions. Overall, Figure 3.7 demonstrates the resistance of the monolayers to harsher conditions than one would encounter in the ambient. This behavior of monofunctional silanes has been observed before, and is believed to be due to increased reactivity with surface hydroxyl groups.[54]

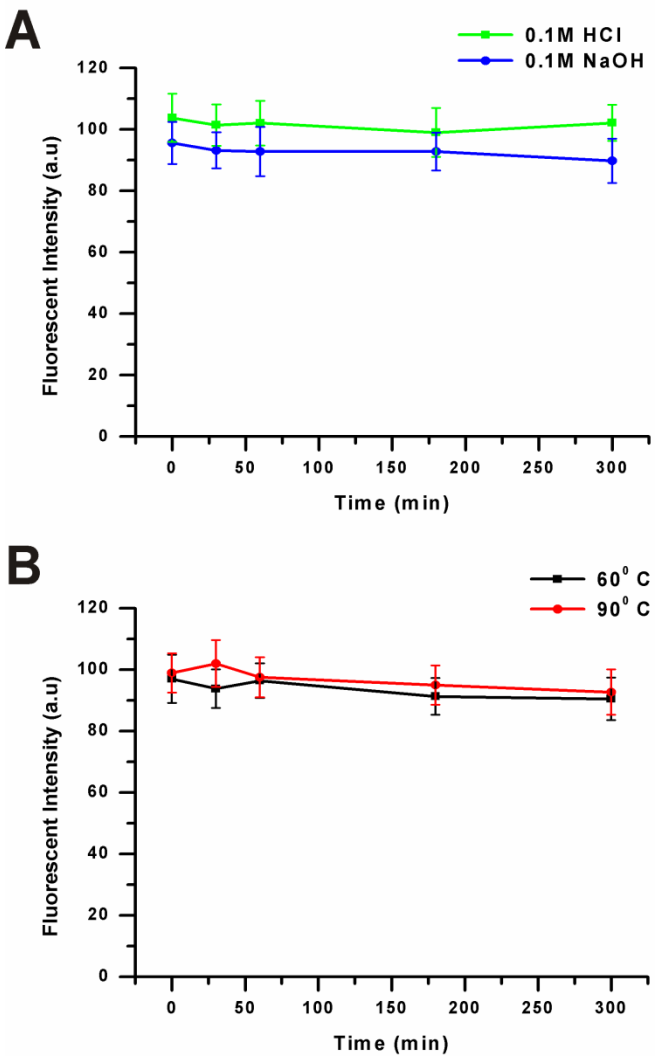


**Figure 3.7**. Substrates coated with APDMS over a 12 hour deposition period were subjected to 0.1M HCl and 0.1M NaOH (**A**) for up to 6 hours, allowed to react with rhodamine NCS for 1 hour, and then the fluorescent intensity measured. Similarly, substrates were immersed in PBS, pH 7.4 buffer at 60 ˚C and 90 ˚C (**B**) for up to 6 hours, allowed to react with rhodamine NCS for 1 hour, and then the fluorescent intensity measured. The integration time for each measurement was 5 seconds.

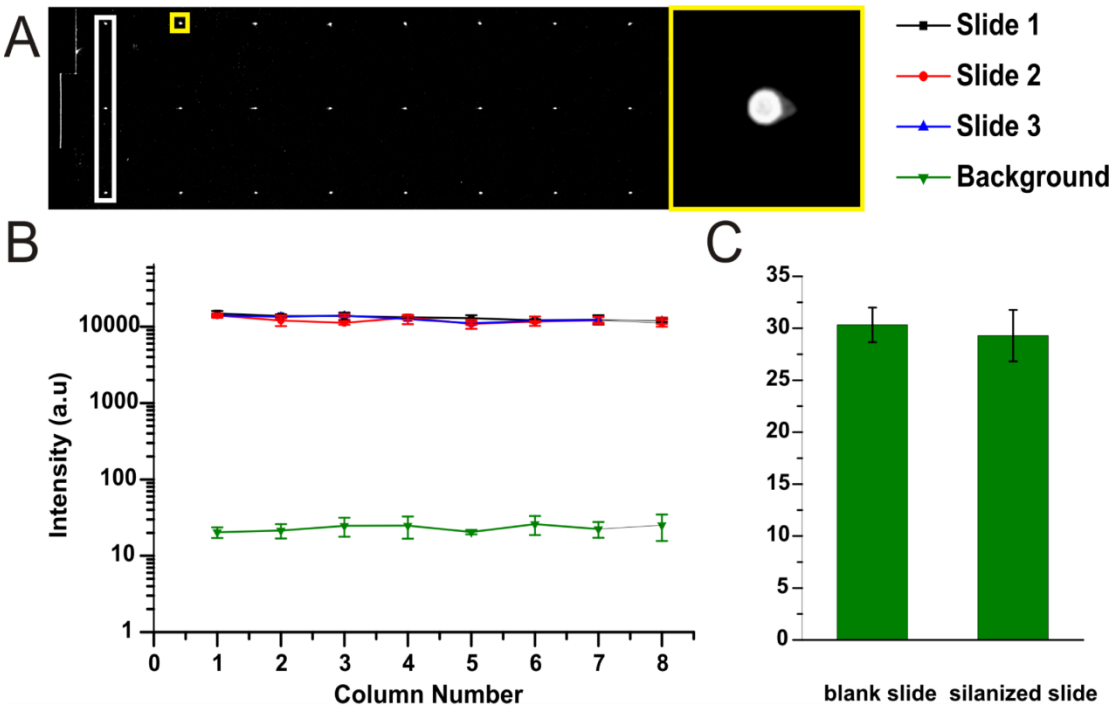


**Figure 3.8**. Low-autofluorescence microscope slides were coated with GPDMS over a 12 hour period and then spotted with Streptavidin-Cy5 in a volume of 350 pL. A representative slide spotted in a 3x8 array is shown in **A** showing a single column (white rectangle) and a magnified image of an individual spot (yellow square). The fluorescence intensity of each column and its surrounding background are shown for 3 slides in **B**. The intensity is plotted on a logarithmic scale. The background of a bare slide versus a GPDMS slide is shown in **C**, indicating no difference in background within experimental error.

Next, the monolayers were applied to biosensing devices to demonstrate their versatility and application. Figure 3.8A shows a GPDMS coated microscope slide spotted with streptavidin-Cy5 (SA-Cy5) in a 3x8 array format. The columns are boxed in white, with a zoomed-in area of an individual spot in yellow. Each pixel of the scan was 10 µm square. Three slides were spotted in the same manner and scanned to obtain the fluorescence intensity of the spots and the background. Figure 3.8B shows the intensity of the background and of the SA-Cy5 spots for each slide versus the column number. The

intensity distribution of fluorescence and uniformity of background noise from the columns across all three slides is very uniform. The background noise of a silane-derivatized slide and an underivatized slide were also measured, and are displayed in Figure 3.8C. The silane adds no background fluorescence, within error, to the measurement. Given the high gain of the photomultiplier tube at which these measurements were taken, it is likely that background noise due to substrate autofluorescence and the detection electronics will dominate over background contributions from the silane layer for any fluorescence assay. The low autofluorescence of these layers is an important advantage in ultimately maximizing the signal-to-noise ratio of fluorescence assays performed using this chemistry, and apparently leads to better background intensity than other slide formats[55]. The coefficient of variation across the slides is 8%, which includes effects from the variability of the spotting procedure as well as the surface chemistry.

The application of ion selective field effect transistors (ISFET's) and silicon nanowires to biosensing has become pronounced in recent years.[56-58] Silicon oxide is the most common dielectric due to its ease of growth and integration.However, silicon oxide performance is known to degrade extensively over time, due to factors such as dissolution and ion diffusion.[59-62] Organic monolayers have proven to provide resistance to this phenomena[38], but the effect of polymerization degrades the device sensitivity by adding to the dielectric thickness and trapping charges within the polymerized matrix. Moreover, functional group density may be affected due to groups being buried in the matrix. These variables may affect the ability of the silane chemistry to conjugate recognition agents, such as primary antibodies or DNA, close enough to the

surface to regulate the devices surface potential. Here, we demonstrate the applicability and versatility of monoalkoxysilylation chemistry to biosensors. We have constructed silicon field effect devices based upon silicon-on-insulator ( SOI) technology in our lab[63,64] with 30 nm silicon thickness, 2 μm device width, and 20 μm device length. A bright field top-view micrograph of a device is displayed in Figure 3.9 (top left). We allowed the devices to react with the monofunctional silylating reagents according to the aforementioned protocol, and then with fluorophores of varying functionalities, including an amine, an NHS ester, and an isothiocyanate. Each device was then fluorescently imaged for 5 seconds (Figure 3.9). The presence of the fluorophores is demonstrated by the uniformly strongly intensity across the device. Since device response can depend on the distribution of recognition molecules on the surface[65], this is an important step to optimizing silicon nanowire sensitivity and repeatability.

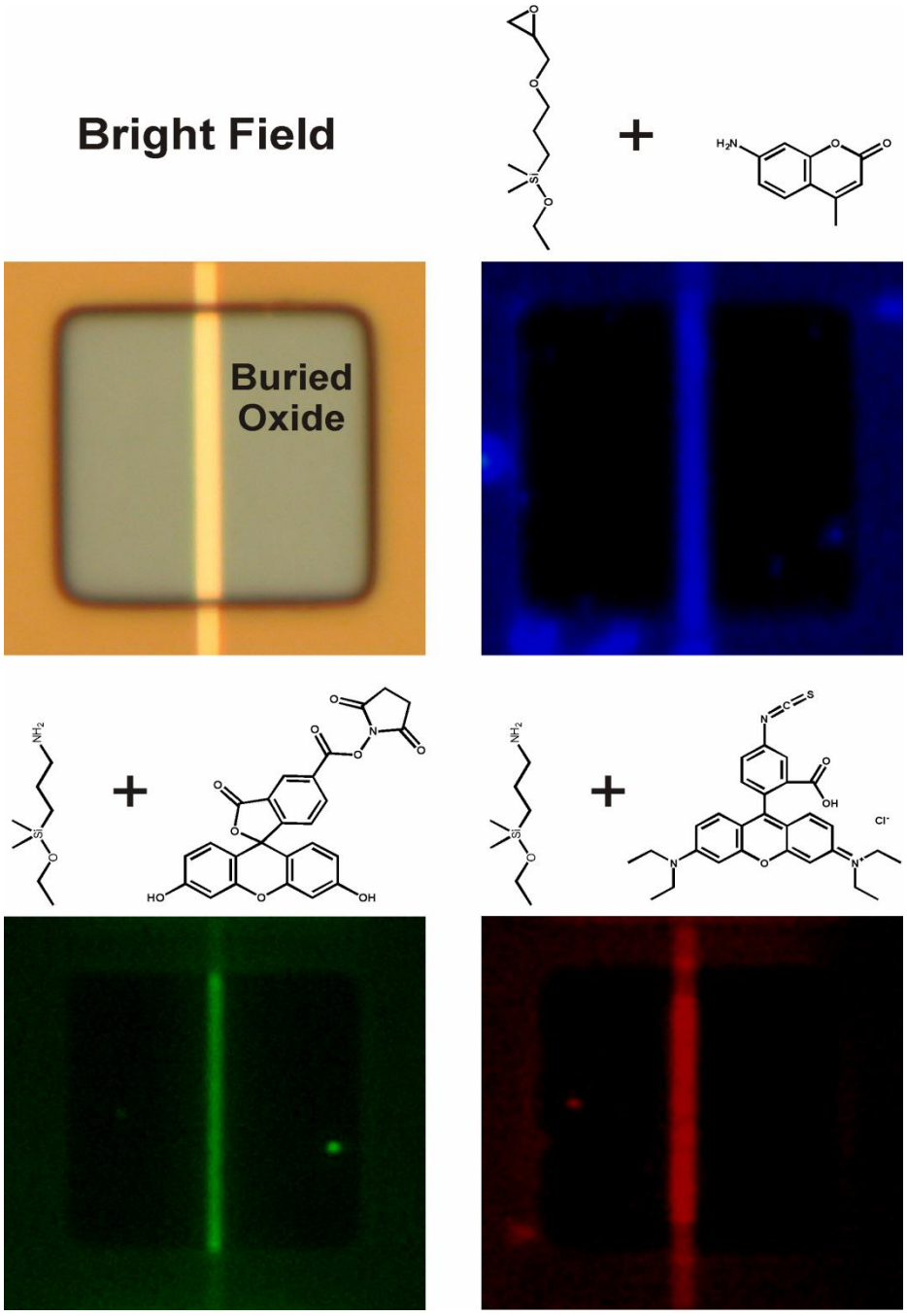


**Figure 3.9**. Silicon field effect devices were silanized and then reacted with fluorophores of varying chemistries. The bright field image shows a silanized device (metallic yellow) in the center of the release window, which shows the buried oxide (blue-violet). The devices were then allowed to react with various fluorophores, which are indicated atop each fluorescence image, along with the silane utilized for conjugation. The fluorophores reacted include an amino-coumarin (top, right), carboxyfluorescein-NHS ester (bottom, left), and rhodamine B-isothiocyanate (bottom, right).

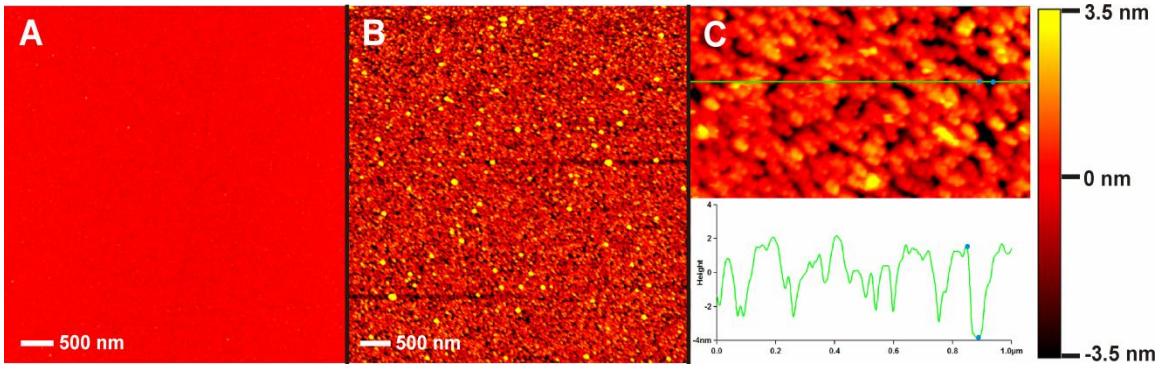


**Figure 3.10**. A 5µm tapping Mode AFM image of an APDMS coated substrate is shown in **A.** An APDMS substrate was then coated with citrate capped 5nm Au nanoparticles over a period of 1hr and a 5µm image taken in **B**, showing very high coverage. A 1µm image of the same area is shown in **C** with a line section taken (green). The section analysis shows a height difference of 5.7 nm, indicating a true monolayer of particles on the surface.

Another important technique widely used today for biomolecule detection is Surface Enhanced Raman Scattering (SERS). Interactions of analytes with enhanced optical fields are known to increase Raman scattering by $10^5$-$10^6$. In some cases, scattering enhancements of $10^{12}$-$10^{14}$ have been encountered, which may be sensitive enough for single molecule detections. Former SERS substrates were made out of electrochemically roughened metal surfaces, but in recent years noble metal nanoparticles have become a method of choice. Nanoparticle substrates offer the advantage of being renewable and having a high density of particles on the surface, which can lead to areas of intense field enhancement known as "hot spots"[66]. In Figure 3.10, we demonstrate the formation of high density Au nanoparticle surfaces via electrostatic adsorption with an APDMS monolayer. AFM images were taken before (Figure 3.10A) and after (Figure 3.10B) a 1 hour deposition of 5 nm Au particles in DI water. Figure 3.10A shows a smooth monolayer over a 25 $um^2$ area. After deposition (Figure 3.10B), the surface shows a high density of Au nanoparticles on the surface over the same area scale. A $1um^2$

image of the same area shows particles in tight clusters, with occasional gaps. A line scan across one of these small gap areas shows a height difference of 5.7 nm, indicating a homogeneous monolayer of nanoparticles.

## 3.5 CONCLUSIONS

We have developed a versatile, vapor-based method for the deposition of monofunctional silanes. By characterizing the system using ellipsometry, XPS, and AFM we were able to optimize the procedure to ensure a uniform, high density, true monolayer. The technique was shown to be successful not only on small substrates, such as ISFET's, but also on entire 6" Si wafers, leaving the possibility for incorporation into VLSI semiconductor processes.Subjecting the monolayers to conditions of elevated temperatures and extreme pH showed no decay of the monolayers through fluorescent attachment. We demonstrate the applicability of this subnanometer monolayer technology to various sensing platforms. The very high uniformity of the monolayers makes them ideal for applications in sensing, whether optical or electronically based. The low background noise and coefficient of variation make it attractive for microarrays and fluorescence applications. Moreover, the chemistry indicates recognition analytes would bind in high density to field effect sensors, enhancing the sensitivity of the devices. Finally, the high coverage of electrostatically adsorbed nanoparticles on the silane surface would make an ideal SERS substrate for detection of analytes and minimize background scattering. Overall, the deposition of monofunctional silanes is very versatile and robust, and is applicable to multiple biosensing platforms to help optimize their performance.

# 3.6 REFERENCES


[1]. Murphy, M. A.; Nordgren, C. E.; Fischetti, R. F.; Blasie, J. K.; Peticolas, L. J.; Bean, J. C., Structural Study of the Annealing of Alkylsiloxane Self-Assembled Monolayers on Silicon by High-Resolution X-Ray-Diffraction. *Journal Of Physical Chemistry* 1995, 99, 14039-14051.

[2]. Whitesides, G. M.; Laibinis, P. E., Wet Chemical Approaches to the Characterization of Organic-Surfaces - Self-Assembled Monolayers, Wetting, and the Physical Organic-Chemistry of the Solid Liquid Interface. *Langmuir* 1990, 6, 87-96.

[3]. Homola, J., Surface Plasmon Resonance Sensors for Detection of Chemical and Biological Species. *Chemical Reviews* 2008, 108, 462-493.

[4]. Fan, X. D.; White, I. M.; Shopoua, S. I.; Zhu, H. Y.; Suter, J. D.; Sun, Y. Z., Sensitive Optical Biosensors for Unlabeled Targets: A Review. *Analytica Chimica Acta* 2008, 620, 8-26.

[5]. Anker, J. N.; Hall, W. P.; Lyandres, O.; Shah, N. C.; Zhao, J.; Van Duyne, R. P., Biosensing with Plasmonic Nanosensors. *Nature Materials* 2008, 7, 442-453.

[6]. Bhunia, A. K.; Banada, P.; Banerjee, P.; Valadez, A.; Hirleman, E. D., Light Scattering, Fiber Optic- and Cell-Based Sensors for Sensitive Detection of Foodborne Pathogens. *Journal Of Rapid Methods And Automation In Microbiology* 2007, 15, 121-145.

[7]. Bosch, M. E.; Sanchez, A. J. R.; Rojas, F. S.; Ojeda, C. B., Optical Chemical Biosensors for High Throughput Screening of Drugs. *Combinatorial Chemistry & High Throughput Screening* 2007, 10, 413-432.

[8]. Grieshaber, D.; MacKenzie, R.; Voros, J.; Reimhult, E., Electrochemical Biosensors - Sensor Principles and Architectures. *Sensors* 2008, 8, 1400-1458.

[9]. Vestergaard, M.; Kerman, K.; Tamiya, E., An Overview of Label-Free Electrochemical Protein Sensors. *Sensors* 2007, 7, 3442-3458.

[10]. Rauf, S.; Gooding, J. J.; Akhtar, K.; Ghauri, M. A.; Rahman, M.; Anwar, M. A.; Khalid, A. M., Electrochemical Approach of Anticancer Drugs - DNA Interaction. *Journal Of Pharmaceutical And Biomedical Analysis* 2005, 37, 205-217.

[11]. Lange, K.; Rapp, B. E.; Rapp, M., Surface Acoustic Wave Biosensors: A Review. *Analytical And Bioanalytical Chemistry* 2008, 391, 1509-1519.

[12]. Sagiv, J., Organized Monolayers by Adsorption .1. Formation and Structure of Oleophobic Mixed Monolayers on Solid-Surfaces. *Journal Of The American Chemical Society* 1980, 102, 92-98.

[13]. Depalma, V.; Tillman, N., Friction and Wear of Self-Assembled Trichlorosilane Monolayer Films on Silicon. *Langmuir* 1989, 5, 868-872.

[14]. Wasserman, S. R.; Tao, Y. T.; Whitesides, G. M., Structure and Reactivity of Alkylsiloxane Monolayers Formed by Reaction of Alkyltrichlorosilanes on Silicon Substrates. *Langmuir* 1989, 5, 1074-1087.

[15]. Howarter, J. A.; Youngblood, J. P., Optimization of Silica Silanization by 3-Aminopropyltriethoxysilane. *Langmuir* 2006, 22, 11142-11147.

[16]. Jung, H.; Kulkarni, R.; Collier, C. P., Dip-Pen Nanolithography of Reactive Alkoxysilanes on Glass. *Journal of the American Chemical Society* 2003, 125, 12096-12097.

[17]. Naoto, S.; Jun, N.; Yoshitaka, E.; Atsushi, H.; Yoshitake, M.; Shigeru, I.; Yoshio, S., Liquid Manipulation Lithography to Fabricate a Multifunctional Microarray of Organosilanes on an Oxide Surface under Ambient Conditions. *Advanced Functional Materials* 2008, 18, 3049-3055.

[18]. Maboudian, R.; Ashurst, W. R.; Carraro, C., Tribological Challenges in Micromechanical Systems. *Tribology Letters* 2002, 12, 95-100.

[19]. Ashurst, W. R.; Carraro, C.; Maboudian, R., Vapor Phase Anti-Stiction Coatings for Mems. *Ieee Transactions On Device And Materials Reliability* 2003, 3, 173-178.

[20]. de Boer, M. P.; Mayer, T. M., Tribology of Mems. *Mrs Bulletin* 2001, 26, 302-304.

[21]. Mayer, T. M.; de Boer, M. P.; Shinn, N. D.; Clews, P. J.; Michalske, T. A., Chemical Vapor Deposition of Fluoroalkylsilane Monolayer Films for Adhesion Control in Microelectromechanical Systems. *Journal Of Vacuum Science & Technology B* 2000, 18, 2433-2440.

[22]. Ashurst, W. R.; Carraro, C.; Maboudian, R.; Frey, W., Wafer Level Anti-Stiction Coatings for Mems. *Sensors And Actuators A-Physical* 2003, 104, 213-221.

[23]. Saito, N.; Lee, S. H.; Takahiro, I.; Hieda, J.; Sugimura, H.; Takai, O., Surface-Potential Reversibility of an Amino-Terminated Self-Assembled Monolayer Based on Nanoprobe Chemistry. *Journal Of Physical Chemistry B* 2005, 109, 11602-11605.

[24]. Hozumi, A.; Yokogawa, Y.; Kameyama, T.; Sugimura, H.; Hayashi, K.; Shirayama, H.; Takai, O., Amino-Terminated Self-Assembled Monolayer on a Sio2 Surface Formed by Chemical Vapor Deposition. *Journal Of Vacuum Science & Technology A-Vacuum Surfaces And Films* 2001, 19, 1812-1816.

[25]. Hozumi, A.; Ushiyama, K.; Sugimura, H.; Takai, O., Fluoroalkylsilane Monolayers Formed by Chemical Vapor Surface Modification on Hydroxylated Oxide Surfaces. *Langmuir* 1999, 15, 7600-7604.

[26]. Hong, L.; Sugimura, H.; Furukawa, T.; Takai, O., Photoreactivity of Alkylsilane Self-Assembled Monolayers on Silicon Surfaces and Its Application to Preparing Micropatterned Ternary Monolayers. *Langmuir* 2003, 19, 1966-1969.

[27]. Miura, Y.; Sato, H.; Ikeda, T.; Sugimura, H.; Takai, O.; Kobayashi, K., Micropatterned Carbohydrate Displays by Self-Assembly of Glycoconjugate Polymers on Hydrophobic Templates on Silicon. *Biomacromolecules* 2004, 5, 1708-1713.

[28]. Hozumi, A.; Inagaki, M.; Shirahata, N., Vapor Phase Formation of a Well-Ordered Aldehyde-Terminated Self-Assembled Monolayer on a Sio2 Surface and Formation of Silver Film on the Surface Based on the Silver Mirror Reaction. *Surface Science* 2006, 600, 4044.

[29]. Kim, J.; Seidler, P.; Fill, C.; Wan, L. S., Investigations of the Effect of Curing Conditions on the Structure and Stability of Amino-Functionalized Organic Films on Silicon Substrates by Fourier Transform Infrared Spectroscopy, Ellipsometry, and Fluorescence Microscopy. *Surface Science* 2008, 602, 3323-3330.

[30]. Kim, J. Y.; Seidler, P.; Wan, L. S.; Fill, C., Formation, Structure, and Reactivity of Amino-Terminated Organic Films on Silicon Substrates. *Journal Of Colloid And Interface Science* 2009, 329, 114-119.

[31]. Gu, Q. L.; Cheng, X. H., Tribological Behaviors of Self-Assembled 3-Aminopropyltriethoxysilane Films on Silicon. *Current Applied Physics* 2008, 8, 583-588.

[32]. Vrancken, K. C.; Vandervoort, P.; Possemiers, K.; Vansant, E. F., Surface and Structural-Properties of Silica-Gel in the Modification with Gamma-Aminopropyltriethoxysilane. *Journal Of Colloid And Interface Science* 1995, 174, 86-91.

[33]. Kallury, K. M. R.; Macdonald, P. M.; Thompson, M., Effect of Surface-Water and Base Catalysis on the Silanization of Silica by (Aminopropyl)Alkoxysilanes Studied by X-Ray Photoelectron-Spectroscopy and C-13 Cross-Polarization Magic-Angle-Spinning Nuclear-Magnetic-Resonance. *Langmuir* 1994, 10, 492-499.

[34]. Jang, L. S.; Liu, H. J., Fabrication of Protein Chips Based on 3-Aminopropyltriethoxysilane as a Monolayer. *Biomedical Microdevices* 2009, 11, 331-338.

[35]. Hsiao, V. K. S.; Waldeisen, J. R.; Zheng, Y. B.; Lloyd, P. F.; Bunning, T. J.; Huang, T. J., Aminopropyltriethoxysilane (Aptes)-Functionalized Nanoporous Polymeric Gratings: Fabrication and Application in Biosensing. *Journal Of Materials Chemistry* 2007, 17, 4896-4901.

[36]. Baur, B.; Howgate, J.; von Ribbeck, H. G.; Gawlina, Y.; Bandalo, V.; Steinhoff, G.; Stutzmann, M.; Eickhoff, M., Catalytic Activity of Enzymes Immobilized on Algan/Gan Solution Gate Field-Effect Transistors. *Applied Physics Letters* 2006, 89.

[37]. Kharitonov, A. B.; Zayats, M.; Lichtenstein, A.; Katz, E.; Willner, I., Enzyme Monolayer-Functionalized Field-Effect Transistors for Biosensor Applications. *Sens. Actuator B-Chem.* 2000, 70, 222-231.

[38]. Voorthuyzen, J. A.; Keskin, K.; Bergveld, P., Investigations of the Surface Conductivity of Silicon Dioxide and Methods to Reduce It. *Surface Science* 1987, 187, 201-211.

[39]. White, L. D.; Tripp, C. P., Reaction of (3-Aminopropyl)Dimethylethoxysilane with Amine Catalysts on Silica Surfaces. *Journal Of Colloid And Interface Science* 2000, 232, 400-407.

[40]. Kanan, S. M.; Tze, W. T. Y.; Tripp, C. P., Method to Double the Surface Concentration and Control the Orientation of Adsorbed (3-Aminopropyl)Dimethylethoxysilane on Silica Powders and Glass Slides. *Langmuir* 2002, 18, 6623-6627.

[41]. Stalgren, J. J. R.; Eriksson, J.; Boschkova, K., A Comparative Study of Surfactant Adsorption on Model Surfaces Using the Quartz Crystal Microbalance and the Ellipsometer. *Journal Of Colloid And Interface Science* 2002, 253, 190-195.

[42]. Cuypers, P. A.; Corsel, J. W.; Janssen, M. P.; Kop, J. M. M.; Hermens, W. T.; Hemker, H. C., The Adsorption of Prothrombin to Phosphatidylserine Multilayers Quantitated by Ellipsometry. *Journal Of Biological Chemistry* 1983, 258, 2426-2431.

[43]. Vogel, A. I.; Cresswell, W. T.; Leicester, J., Bond Refractions for Tin, Silicon, Lead, Germanium and Mercury Compounds. *The Journal of Physical Chemistry* 1954, 58, 174-177.

[44]. Dannenberger, O.; Weiss, K.; Woll, C.; Buck, M., Reactivity of Self-Assembled Monolayers: Formation of Organized Amino Functionalities. *Physical Chemistry Chemical Physics* 2000, 2, 1509-1514.

[45]. Dannenberger, O.; Weiss, K.; Himmel, H. J.; Jager, B.; Buck, M.; Woll, C., An Orientation Analysis of Differently Endgroup-Functionalised Alkanethiols Adsorbed on Au Substrates. *Thin Solid Films* 1997, 307, 183-191.

[46]. Peterlinz, K. A.; Georgiadis, R., In Situ Kinetics of Self-Assembly by Surface Plasmon Resonance Spectroscopy. *Langmuir* 1996, 12, 4731-4740.

[47]. Rahn, J. R.; Hallock, R. B., Antibody-Binding to Antigen-Coated Substrates Studied with Surface-Plasmon Oscillations. *Langmuir* 1995, 11, 650-654.

[48]. Boksanyi, L.; Liardon, O.; Kovats, E. S., Chemically Modified Silicon Dioxide Surfaces Reaction of N-Alkyldimethylsilanols and N-Oxaalkyl-Dimethylsilanols with Hydrated Surface of Silicon Dioxide-Question of Limiting Surface Concentration. *Advances In Colloid And Interface Science* 1976, 6, 95-137.

[49]. Humbert, B., Estimation of Hydroxyl Density at the Surface of Pyrogenic Silicas by Complementary Nmr and Raman Experiments. *Journal Of Non-Crystalline Solids* 1995, 191, 29-37.

[50]. CalistriYeh, M.; Kramer, E. J.; Sharma, R.; Zhao, W.; Rafailovich, M. H.; Sokolov, J.; Brock, J. D., Thermal Stability of Self-Assembled Monolayers from Alkylchlorosilanes. *Langmuir* 1996, 12, 2747-2755.

[51]. Golub, A. A.; Zubenko, A. I.; Zhmud, B. V., Gamma-Aptes Modified Silica Gels: The Structure of the Surface Layer. *Journal Of Colloid And Interface Science* 1996, 179, 482-487.

[52]. Zhmud, B. V.; Pechenyi, A. B., Acid-Base Properties and Electrokinetic Behavior of Amine-Containing Organopolysiloxane Matrices. *Journal Of Colloid And Interface Science* 1995, 173, 71-78.

[53]. Laibinis, P. E.; Bain, C. D.; Whitesides, G. M., Attenuation of Photoelectrons in Monolayers of Normal-Alkanethiols Adsorbed on Copper, Silver, and Gold. *Journal Of Physical Chemistry* 1991, 95, 7017-7021.

[54]. Tripp, C. P.; Hair, M. L., Reaction of Methylsilanols with Hydrated Silica Surfaces - the Hydrolysis of Trichloromethylsilanes, Dichloromethylsilanes, and Monochloromethylsilanes and the Effects of Curing. *Langmuir* 1995, 11, 149-155.

[55]. Seurynck-Servoss, S. L.; White, A. M.; Baird, C. L.; Rodland, K. D.; Zangar, R. C., Evaluation of Surface Chemistries for Antibody Microarrays. *Analytical Biochemistry* 2007, 371, 105-115.

[56]. Stern, E.; Klemic, J. F.; Routenberg, D. A.; Wyrembak, P. N.; Turner-Evans, D. B.; Hamilton, A. D.; LaVan, D. A.; Fahmy, T. M.; Reed, M. A., Label-Free Immunodetection with Cmos-Compatible Semiconducting Nanowires. *Nature* 2007, 445, 519-522.

[57]. Cui, Y.; Wei, Q. Q.; Park, H. K.; Lieber, C. M., Nanowire Nanosensors for Highly Sensitive and Selective Detection of Biological and Chemical Species. *Science* 2001, 293, 1289-1292.

[58]. Cui, Y.; Zhong, Z. H.; Wang, D. L.; Wang, W. U.; Lieber, C. M., High Performance Silicon Nanowire Field Effect Transistors. *Nano Letters* 2003, 3, 149-152.

[59]. Zhang, G., *Electrochemistry of Silicon and Its Oxide*. Kluwer Academic: New York, 2001; p 510.

[60]. Abe, H.; Esashi, M.; Matsuo, T., Isfets Using Inorganic Gate Thin-Films. *Ieee Transactions On Electron Devices* 1979, 26, 1939-1944.

[61]. Matsuo, T.; Esashi, M.; Abe, H., Ph Isfets Using Al2o3, Si3n4, and Sio2 Gate Thin-Films. *Ieee Transactions On Electron Devices* 1979, 26, 1856-1857.

[62]. Matsuo, T.; Esashi, M., Methods of Isfet Fabrication. *Sensors and Actuators* 1981, 1, 77-96.

[63]. Elibol, O. H.; Reddy, B.; Bashir, R., Nanoscale Thickness Double-Gated Field Effect Silicon Sensors for Sensitive Ph Detection in Fluid. *Applied Physics Letters* 2008, 92.

[64]. Elibol, O. H.; Morisette, D.; Akin, D.; Denton, J. P.; Bashir, R., Integrated Nanoscale Silicon Sensors Using Top-Down Fabrication. *Applied Physics Letters* 2003, 83, 4613-4615.

[65]. Nair, P. R.; Alam, M. A., Design Considerations of Silicon Nanowire Biosensors. *Ieee Transactions On Electron Devices* 2007, 54, 3400-3408.

[66]. Li, W. Y.; Camargo, P. H. C.; Lu, X. M.; Xia, Y. N., Dimers of Silver Nanospheres: Facile Synthesis and Their Use as Hot Spots for Surface-Enhanced Raman Scattering. *Nano Letters* 2009, 9, 485-490.

[67]. Seah, M. P.; Spencer, S. J., Ultrathin Sio2 on Si. I. Quantifying and Removing Carbonaceous Contamination. *Journal Of Vacuum Science & Technology A* 2003, 21, 345-352.

# CHAPTER 4 : EFFECT OF BIOINTERFACING LINKER CHEMISTRIES ON THE SENSITIVITY OF SILICON NANOWIRES FOR ANALYTE DETECTION

## 4.1 ABSTRACT

As demands on the healthcare industry increase, a real need has developed for quicker and cost-effective diagnostic testing. Point-of-care diagnostics show promise in removing reliance on centralized lab testing facilities, and may help increase both the survival rate for infectious diseases as well as monitoring of chronic illnesses. CMOS compatible diagnostic platforms are currently being considered as they can be easily miniaturized and be cost-effective. Top-down fabricated silicon nanowires are a CMOS-compatible technology which demonstrate great sensitivities in detecting biological analytes, such as proteins, DNA, and RNA. However, the output response of nanowires to these analytes has varied widely across the field with several different protocols being tried, but with little characterization and understanding. Here we report protocols for fabrication and functionalization of silicon nanowires which yield highly stable nanowires in aqueous solutions, and limits of detection to ~1pg/mL of our model protein. A thorough characterization was done into optimizing the release of the silicon nanowires using combined dry and wet etch techniques, which yielded nanowires that could be directly compared to increase output statistics. Moreover, a range of different linker chemistries were tried for reacting the primary antibody, and its response to target and

non-specific antigens, with polyethylene glycol based linker BS(PEG) providing the best response. Consequently, this chemistry was used to characterize different oxide thicknesses and their responses to the mouse IgG antigen, which with the smallest oxide thickness yielded 0.1-1pg/mL limits of detection and a dynamic range over 3 orders of magnitude.

## 4.2 INTRODUCTION

The prevalence of chronic diseases such as diabetes, cancer, and obesity, are increasing globally at a daunting rate. According to the World health organization, 75% of death worldwide will be due to chronic illness by 2020.[1,2] Moreover, the growing population has put undue stress on healthcare organizations to simultaneously reduce costs while increasing clinical outcomes, allowing for point-of-care (POC) diagnostics to become a $16.5 billion market by 2016 (BCC reference). Point-of-care testing allows for decentralized diagnostic analysis, essentially bringing the laboratory to the patient. In order to realize this, point of care devices should be cost-effective, sensitive yet specific, easy to use, have rapid turnaround times, and contain minimal additional equipment. [3] The technology revolution which has occurred over the past decade, in large part due to the aggressive scaling of semiconductors dictated by Moore's Law[4], has allowed for Complementary Metal-Oxide Semiconductor (CMOS) technology to become a plausible platform to meet many of the above point-of-care requirements, especially when it comes to cost and miniaturization.[5]

Metal oxide semiconductor field-effect transistors (MOSFET's), the workhorse of CMOS technology, are typically composed of three terminals: the source, drain, and gate. A voltage is applied between the highly doped source and drain regions, which are

isolated from the gate metal by an insulating dielectric, to direct the flow of current in the transistor. When voltages are applied to the gate, an electric field develops across the gate dielectric, creating a charge density in the channel. When a large enough voltage is applied to the gate, a conducting channel forms between the source and drain, with this critical voltage being called the threshold voltage ($V_t$). Ion selective field effect transistors (ISFET's) have been in use as pH sensors for over 30 years, and are essentially MOSFETs with the top metal layer removed and the gate dielectric exposed to an electrolyte solution.[6] These properties of FET's, in conjunction with ISFET's, can be configured as a biosensor by modifying the gate dielectric with biological entities specific to the analyte of interest, creating bioFET's. The charge density (σ) in the conducting channel of the FET is related to the capacitance (C) of gate insulator and the potential at electrolyte-insulator interface ($\Psi_o$ ) by the equation $\sigma = C\Psi_0$. Thus, binding of a charged biomolecule results in a change of electric charges on the gate terminal, making FET's good candidates for electrical biosensors because the electric field generated from the binding of a charged biomolecule to the gate is analogous to applying a voltage to a gate. [7] Attachment of chemical and biological species to the gate surfaces has allowed for a wide variety of analytes to be detected such as metal ions[8-15], small molecules[16-25], proteins[26-32], and DNA[33-37].

However, the detection limits of biological analytes on planar bioFET's are usually not low enough to detect many cancer biomarkers in serum levels. Silicon nanowire FET's have proven to sense biomarkers in clinically relevant levels[38-45], and more recently demonstrated using CMOS compatible processing techniques[46-48]. The extraordinary sensitivities of nanowires have often been attributed to their high surface

area to volume ratio, as well as their widths being similar in dimension to biological species such as proteins and DNA.[49,50] Even though nanowires promise incredible sensitivity, the variety of device configurations (floating gates, with and without reference electrode, enhancement or depletion mode) in conjunction with the different functionalization and sensing protocols have led to large discrepancies in the magnitude of signal output. For example, FET devices for DNA detection have reported signals ranging from a few mV to close to 1.9V for successful DNA hybridization, the reasons for which are all still poorly understood and rarely coincide with theory.[51] Similar discrepancies have been observed with immunoFET's and other antibody-antigen interactions. One of reason for these discrepancies is the manner in which the devices are functionalized and passivated.

The optimization and characterization of surface functionalization protocols for protein detection using optical methods has been well established[52-57], with a multitude of protocols which yield detection limits in the pg-ng/mL range of analytes[58,59]. However, very little has been done in regards to understanding sensing protocols for electronic-based, label-free sensors. In contrast to optical based methods, such as fluorescence, the sensitivity depends more on the surface charge density and corresponding proximity to the dielectric interface, making protocols which contain polymers and multilayers not optimal. Moreover, solutions which contain high salts may be suitable for optical sensors based on refractive index, but are detrimental to the sensitivity of FET-based sensors.

In this work we characterize and provide possible solutions for two important problems in silicon nanowire sensing: the fabrication and device release of silicon on

insulator (SOI) based nanowire FET's, and the surface functionalization of nanowire FET's. Silicon nanowire FET's of different gate oxide thicknesses were fabricated and released using combined dry and wet etch techniques, yielding devices with threshold stabilities in the single mV range in aqueous solution. Previously we showed that monofunctional silanes could be used for high density, sub-nanometer interfacing to oxide surfaces, providing attractive qualities for interface dependent sensors.[60] Here we use these monofunctional silanes with different linkers to elucidate protocols for attaching primary antibodies to surfaces which yield high specificity and sensitivity, while adhering to mainstream functionalization techniques. Using mouse immunoglobulins as the model antigen, goat-antimouse IgG's were functionalized to the surfaces using an optimized protocol, which yielded sensitivities between 0.1-1 pg/mL for a 50Å gate oxide thickness. Moreover, sensitivities achieved against other similar IgG's from rabbits and different isotypes yielded minimal signal change. Current work involves using these protocols on foundry-grade CMOS chips to sense a wide variety of cancer biomarkers, in hope to improve the understanding of how to generate repeatable results on electronic-based biosensor platforms.

## 4.3 EXPERIMENTAL

### MATERIALS

The metals for e-beam evaporation and device fabrication (99.999% or greater purity) as well as the FABMATE e-beam crucibles were purchased from Kurt Lesker and used according to the manufacturer's instructions. Photoresists for optical lithography were acquired from Rohm and Haas (Shipley 1805), AZ Electronic Materials (AZ1518),

MicroChem (LOR1A and LOR3A), and stored at 4C before use. All buffered oxide etch (BOE), TMAH, and rinsing solvents were acquired from J.T Baker.

Dissucinimidyl Carbonate (DSC), glutaraldehyde (grade I, 50% in H2O), 1x PBS (molecular biology grade), Tween-20, and sodium cyanoborohyrdide were purchased from Sigma-Aldrich. The linker $BS(PEG)_5$ was acquired from Pierce Scientific and a septum applied to the vial for air-free extraction using a syringe. The molecule was stored at -20C until use.

## DEVICE FABRICATION

The fabrication of the $SiO_2$-based, accumulation mode silicon nanowire and nanoplate devices has been described previously. Briefly, the process flow starts with bonded silicon-on-insulator (SOI) wafers (SOITEC) with a buried oxide thickness of 1450Å and a top silicon thickness of 550Å. The top silicon is dry oxidized at 1050C, then wet etched in 10:1 BOE to thin the silicon layer to 300Å. Afterwards, the nanowire patterns are defined with e-beam lithography using a PMMA/LOR1A resist layer, and chrome evaporated on top with a subsequent lift-off to form the first hard mask. The nanoplates and other larger features are then defined using optical lithography, with a second evaporation of chrome and lift-off to form another hard mask. Finally, a TMAH etch of the exposed silicon layer is performed to define the active silicon devices, with a removal of the chrome hard mask using CR-14 etchant (CYANTEK Corp.). The source and drain regions were then boron-doped via ion implantation (simulations show $\sim 10^{19/}cm^2$) using a 1um thick photoresist mask. Dry oxidation to form the SiO2 gate dielectric, as well as simultaneous dopant activation, was performed at 1050C in a vertical furnace to a thickness of ~175 Å (confirmed by AFM step height analysis).

Following oxidation, a forming gas anneal at 400C in 5%$H_2/N_2$ was performed to passivate interface traps and dangling bonds. Via holes were etched into the contact regions, followed by patterning of 250ÅTi/750Å Pt to make the metal contacts to the source/drain regions of the devices. A 550C rapid thermal anneal was then performed to lower the contact resistance. Afterwards, a 4000Å thick PECVD silicon nitride passivation layer was deposited over the wafer. Optical lithography was used to define the release window areas for the devices and CF4 reactive ion etching (90W, 35mTorr, 60sccm) with subsequent 50:1 BOE to etch the underlying passivation layer and release the devices for testing. Finally, the devices undergo a second forming gas anneal to alleviate any RIE induced gate oxide damage.

## MONOLAYER FORMATION AND BIOCONJUGATION

The formation of APDMS monolayers on the nanowire surfaces has also been described in previous literature. Briefly, the devices were cleaned in a H2SO4:H2O2 solution (7:3) for 30mins, then in a 300W O2 plasma at 500mTorr for 1 minute. The devices were placed in a septum vial, modified with a well for the silane solution and flushed with $N_2$, then evacuated to a pressure of 10 Torr. A solution of APDMS/1% TEA (v/v) was then injected via hypodermic needle into the well and the vial place in a convection oven at 100C overnight. The devices were rinsed with acetone and methanol, then blown dry with $N_2$ gas and stored in a vacuum dessicator until use.

The linker chemistries were then reacted onto the chips before primary antibody attachment. The DSC, BS(PEG), and glutaraldehyde linker chemistries were reacted with the APDMS monolayer at 2% (w/v) in dry DMF for 2 hours, according to similarly published protocols. The glutaraldehyde layer was then reduced with a 1% sodium

cyanoborohydride solution to remove Schiff bases. All chips were finally rinsed in acetone and methanol, then blown dry with $N_2$. The primary antibody was then reacted on the chips in 150mM sodium bicarbonate buffer, pH 8.5 and rinsed with 1x PBS/0.05% Tween-20 for 1min, then 0.1x PBS for 1min. Devices were blocked with a 1x solution of BioFx Casein blocker for 30 mins, rinsed in 1xPBS/0.05% Tween-20 for 1min, then 0.1x PBS for 1min.

## MEASUREMENT DETAILS

Measurements were carried out using a Keithley SCS-4200 semiconductor characterization system and Agilent multiplexer. Devices were anchored to ceramic packages and wire bonded to leads on the outside of the package, and backfilled with epoxy for isolation. For fluidic measurements, the device was biased using an Ag/AgCl reference electrode in an aqueous electrolyte solution, and a PDMS fluidic well (volume ~10uL) was bonded on top of the chip (Figure 4.1). The platinum on-chip electrode was not utilized for measurements since its stability in solution was worse than the Ag/AgCl electrode and led to larger drifts.[61] A Harvard Apparatus syringe pump was used at a flow rate of 20uL/min to deliver analytes through microbore PTFE tubing (Upchurch Scientific) attached to micromanipulators, while a dry vacuum pump (Chemglass) was utilized to exchange solutions from the well. The ceramic package was put into a PC board linked to a switch matrix unit, which was hooked to the Source Measuring Units (SMU's) inputs of the Keithley SCS-4200 system. For a particular device, the source-drain current ($I_{DS}$) was measured while the gate voltage ($V_g$) was swept, and the $I_{DS}$-$V_g$ curves recorded. Each device was swept 5 times, with the average curve and standard deviation of each measurement being extracted.

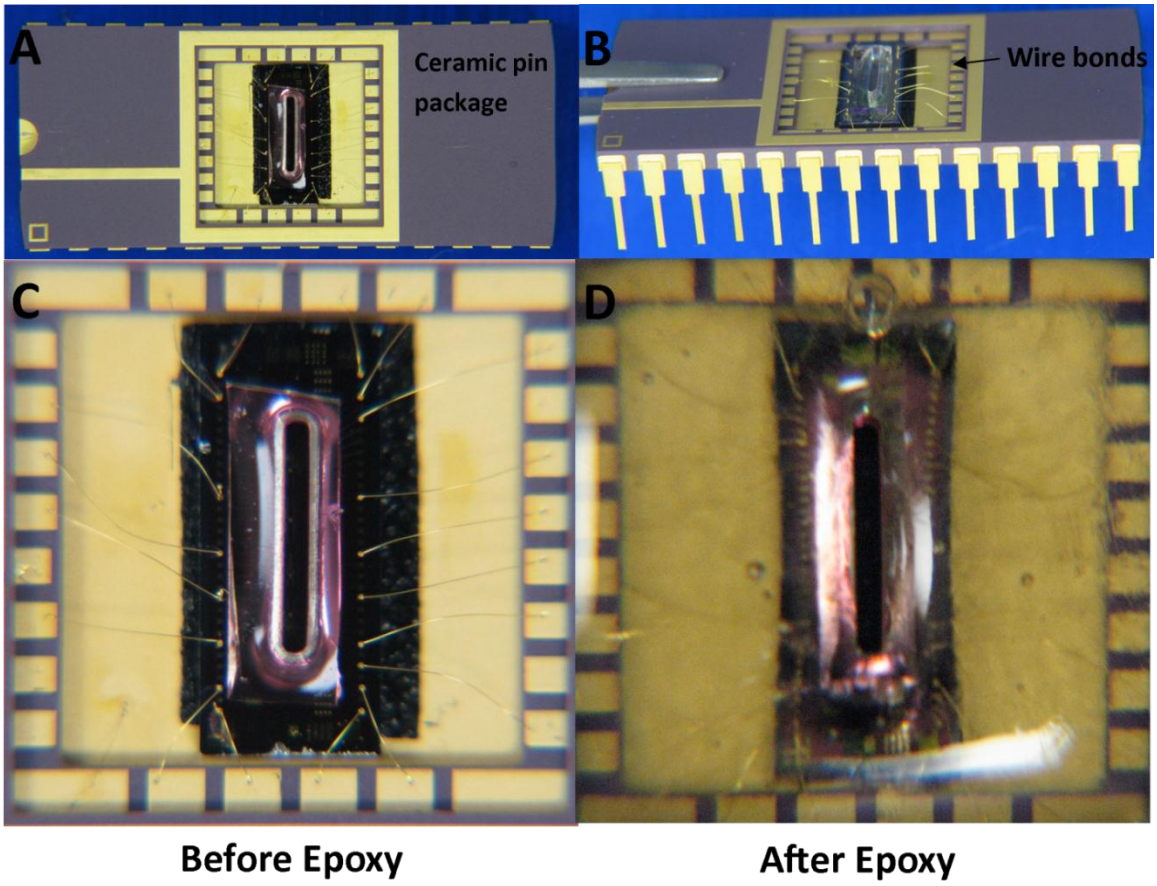


**Figure 4.1**. Pictures of silicon nanowire array device inside a ceramic pin package wired bonded (A), with a tilted picture illustrating the wire bonds in (B). A close up image of the center of the package is in (C). The image shows the conducting carbon tape which holds the chip to the package, the wire bonds attaching the device leads to the package outside, and the PDMS well bonded to the chip for holding the fluid. The device and top of the package is then epoxied in (D) to protect the wire bonds and prevent fluid leakage, while leaving the well area open to fluid transfer.

For electronic studies of primary antibody adsorption , the antibodies were flowed at a rate of 20uL/min for 5 min, then stopped and allowed to react with the given surface chemistries for 1 hour using the conjugation protocol above, and finally were measured in 0.01x PBS, pH 7.4. For target analyte detection using nanowires, the analytes were dissolved in 1x PBS/ 0.05% Tween-20 to their respective concentrations and flowed over the devices using a flow rate of 20uL/min for 5 minutes. The antibodies were allowed to

bind for 30 mins, then rinsed in 1x PBS/0.05% Tween-20 for 1min, 0.1x PBS for 1min, and finally measured in 0.01x PBS, pH 7.4.

### FLUORESCENCE IMAGING

Optical and fluorescent images for the binding specifities and primary antibody adsorption were taken with a Nikon Eclipse FN-1 microscope using a DS-R1 CCD camera and Mercury lamp. Texas Red labeled antibodies were conjugated to thermally oxidized silicon wafer pieces (1um thick via wet oxidation at 1000C) using the bioconjugation and rinsing procedures highlighted above, and imaged using a Y2E/C filter cube at an exposure of 400ms and gain of 1.5x. Similarly, Texas Red modified target immunoglobulins (4 moles dye/mole antibody) were imaged on nanowires and thermal oxide substrates using the same exposure as above for direct comparison.

## 4.4 RESULTS

Each chip was fabricated with different device widths and structures for sensing and application of biases to the solution. Figure 4.2A and 4.2B show optical micrographs of the device release window areas and the platinum (Pt) electrode before etching, with photoresist patterned to expose the device areas for etching. Scanning electron micrographs of the device geometries and zoomed in dimensions have been published previously by our group.[62,63] The color of the device release window area is due to the constructive and destructive interference of incident wavelengths of light through the dielectric layers, giving us a pink color before starting the device release. A schematic of the etching process with the device release window is shown in Figure 4.2C. Briefly, a $CF_4$ RIE etch is used to remove the passivation layer, and a 50:1 BOE wet etch applied to

thin the gate oxide. Using a wet etch for the final few nanometers helps remove any RIE damage the gate oxide may have been exposed to.

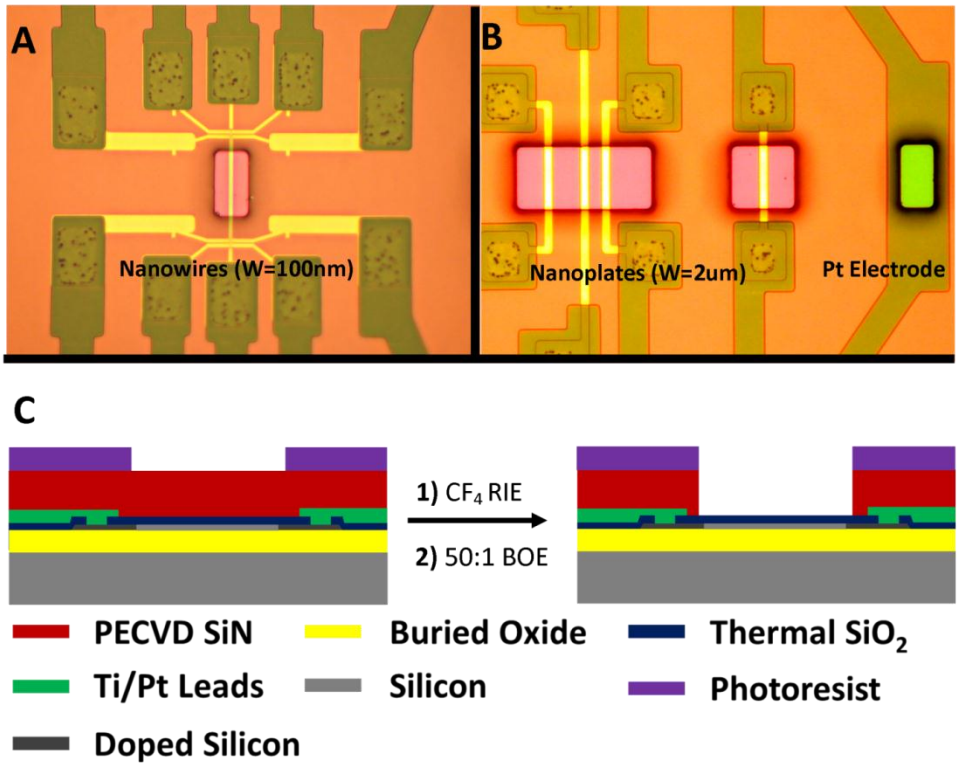


**Figure 4.2**. Optical micrographs of the device release windows and surrounding Ti/Pt leads for silicon nanowires (**A**), nanoplates, and the Pt electrode (**B**). The light hue surrounding the release window areas is due to the thickness of the patterned photoresist. A schematic of the device cross section is shown in (**C**) illustrating the etching process to release the devices. The legend for the different layers is below the cross sections.

In order to determine the time duration of the RIE etch for device release, the different etch rates of SiN, $SiO_2$, and Pt were determined. Sacrificial chips were etched for various times in $CF_4$, and the etch depth measured with a stylus profilometer. Moreover, optical images were taken of the release window to document the color at each etch depth. Figure 4.3A shows the etch depth vs. etch time for the device release window (blue circle) and the Pt electrode release window (black square). On top of the graph are optical micrographs of the nanoplate devices to indicate the color observed at each etch

step. It is well know the etch rates of SiN, thermal $SiO_2$, and Pt are quite different in $CF_4$ plasmas, leading to three different etching regimes, with their order of etching displayed in Figure 4.3C. For the device release window, PECVD nitride (regime 1) and thermal $SiO_2$ (regime 3) are encountered, while for the platinum electrode release window only PECVD nitride and platinum (regime 2) are encountered. We linearly fit each of the etching regimes in Figure 4.3A and extracted the etching rates, which are in Table 4.1.

| Etching Regime | Etch Rate (nm/min) | Std. Dev (nm/min) |
|---|---|---|
| Regime 1 ( SiN) | 78.2 | 2.3 |
| Regime 2 ( Pt) | 0.2 | 1.9 |
| Regime 3 ($SiO_2$) | 19.6 | 1.8 |

**Table 4.1**. Table of extracted etch rates and standard deviations of $CF_4$ based RIE etching for silicon nanowire device release.

PECVD silicon nitride is known to etch quite fast in $CF_4$, with a selectivity against thermal $SiO_2$ between 3:1 and 4:1, and platinum is known to act as an etch stop. These etch rates agree well with our findings. Moreover, the different release window areas etch at similar rates for PECVD nitride, indicating minimal issues due to loading effect. By linearly extrapolating the fits of the different etching regimes, we can estimate an RIE stop point time (dashed black line) before beginning the wet etch of the $SiO_2$ gate oxide, which is close to 300s.

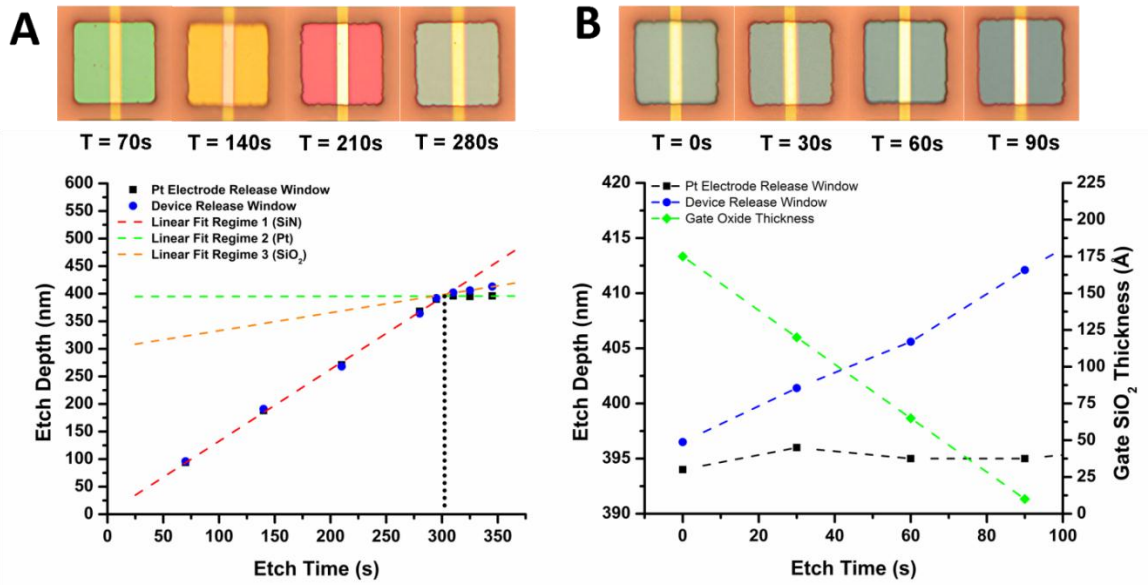


**Figure 4.3**. The etch depth of the device and platinum electrode release windows vs. RIE etch time is plotted in (**A**) with linear fits (dashed lines) to each of the etching regimes. The etch depth of the device and platinum electrode release windows for the 50:1 BOE etch is plotted in (**B**) with the extracted gate oxide thickness. Optical images illustrating the color of the underlying nitride/oxide for each release time step is on top of the graphs for (**A**) and (**B**).

After a 300s $CF_4$ RIE etch, 50:1 BOE was used to remove any local RIE damage and thin the gate oxide. The etch depth was monitored with a stylus profilometer as before, and the etching information displayed in Figure 4.3. The color of the device release window is also monitored, and displayed on top of Figure 4.3B. Similar to the $CF_4$ RIE etch, platinum (black square) does not etch in BOE and acts as a good reference etch stop, displayed in Figure 4.3B as no change in height above the platinum electrode is observed. The approximate gate oxide thickness (green diamond) is extrapolated from the depth change from the profilometer and the grown oxide thickness of 175Å, determined by AFM. These protocols were used successfully to determine the etch depth and approximate gate oxide thickness for further experiments.

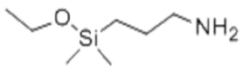

**3-aminopropyldimethlyethoxysilane (APDMS)**

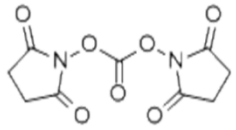

**Disuccinimidyl carbonate (DSC)**

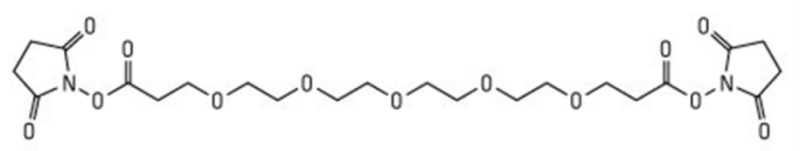

**Bis(succinimidyl) penta(ethylene glycol) (BS(PEG))**

**Glutaraldehyde**

**Figure 4.4**. Chemical structures of the monolayer and the different linking chemistries used in the functionalization protocols. The acronyms used in the manuscript are in brackets next to the chemical name.

For immunological sensing of various protein analytes, the surface must be functionalized with a primary antibody and blocked effectively in order to maximize the signal to noise. With regards to ISFET's this point is particularly important, since maximizing the charge density to interface while minimizing steric hindrance is paramount to the efficiency of the device. In order to determine an optimum linking protocol, a monofunctional aminosilane was vapor deposited and various linker groups (Figure 4.4) containing NHS esters or aldehydes were reacted to link amine or sulfahydryl containing groups on the primary antibody. The antibodies were then reacted and chips blocked according to the procedures outlined in the experimental section. In order to determine the best linker chemistries, fluorescence images were taken on functionalized blank $SiO_2$ surfaces and corresponding electrical response on the silicon nanowires, displayed in Figure 4.5.

Our model system was composed of Goat Anti-Mouse IgG with mouse IgG as the target and Rabbit IgG as the nonspecific binder. Each was either labeled with Texas Red (4 moles dye/per mole protein) or left unlabeled. The intensity of primary antibody attachment was first investigated using a concentration of 10ug/mL, a common coating concentration for ELISA assays. The binding specificity of the antibody to the target was determined using unlabeled primary antibody, then either the specific or nonspecific binder (Texas Red labeled) was added at a concentration of 1ug/mL. The fluorescence intensities for each of the linker chemistries are in Figure 4.5A.

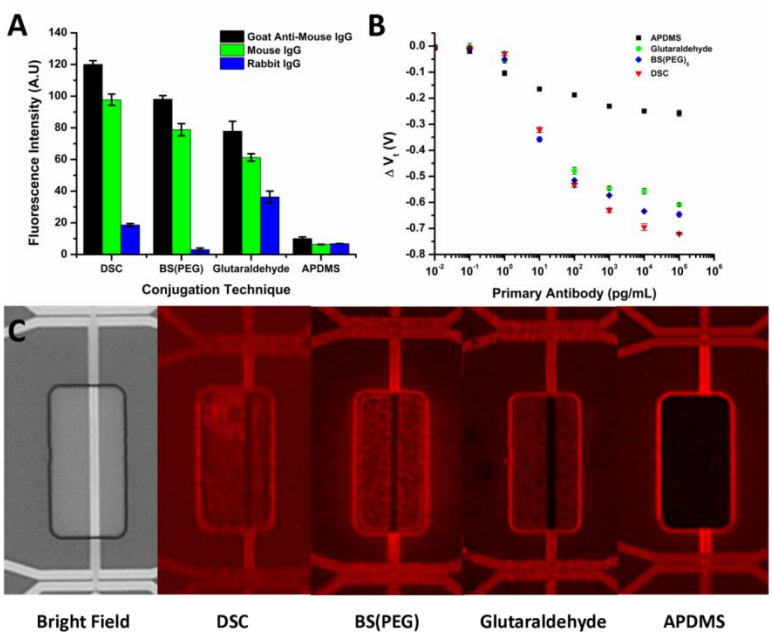


**Figure 4.5**. Fluorescence intensity bar graph (**A**) on thermally oxidized silicon surfaces showing the effect of conjugation linker on primary antibody fixation (Goat anti-mouse IgG) and subsequent analyte binding specificity (Mouse IgG vs. Rabbit IgG). Each antibody and immunoglobulin was Texas Red labeled in order for direct comparison. The threshold voltage shift ($V_t$) of the silicon nanowires with respect to the primary antibody concentration and the linker chemistry is shown in (**B**). Fluorescence micrographs of silicon nanowires after Texas Red labeled antibodies were deposited at 100ng/mL on the various linker chemistries are in (**C**).

From the intensities, we calculated the binding specificity and the percent coverage of the target analyte, which is displayed in Table 4.2. Even though the

fluorescent intensity for the DSC linker is the greatest, the specificity is the highest with the BS(PEG) linker. The glutaraldehyde linker displayed the worst specificity and antibody linkage, outside of the bare APDMS surface. We attribute the high specificity of the BS(PEG) to the inert nature of the poly(ethylene glycol) spacer units. We believe the poor linkage density of the glutaraldehyde layer is due to labile nature of the Schiff base formation for primary antibody coverage. As a result more aldehyde groups are accessible, even after blocking, for reacting with nonspecific analytes. The maximum percent coverage of the specific analyte is within error for each of the reaction chemistries, indicating the primary antibodies attach in similar conformations on the surface with the same binding affinities.

Since the coating conditions for large scale areas (100um-1mm) may vary at nanoscale dimensions, we characterized the response of the silicon nanowires to concentrations of reacted primary antibody with each linker. Each primary antibody concentration was reacted for 1 hour, which has been demonsrated to be enough time to reach saturation points for protein adsorption to monolayers. The devices were rinsed after incubation, and the threshold voltage extracted. The change in threshold voltage was then plotted for each of the linker chemistries in Figure 4.5B. From the curves we observe that saturation is nearly achieved at 100ng/mL antibody concentration for all layers, justifying 10ug/mL as being more than enough to reach a saturation linkage amount for the sensor in a 1 hour reaction time. When the threshold voltage shifts are normalized similar to the fluorescent intensities (Table 4.2), we notice how important the distance to the surface becomes, as the normalized electrical response of the varying linker chemistries is greater than the fluorescence. Moreover, the effect doesn't scale

proportionally to the fluorescence, although on average greater. We attribute this to the surface charge density having a more pronounced effect, leading towards saturation faster, than does fluorescence. This effect has been observed with DNA FET's, as probe adsorption densities can change an order of magnitude ($10^{11}$molecules/cm$^2$ to $10^{12}$ molecules/cm$^2$) with only 10-20mV changes due to ion concentration redistribution around the layer. [51] As a control, we took fluorescence micrographs after 100ng/mL adsorption for 1 hour of each of the different linker chemistries near the release windows. The fluorescence micrographs are displayed in Figure 4.5C. The fluorescence intensity trend correlates with the electrical response, with the highest fluorescence indeed being observed with DSC and tailing off towards the APDMS. The difference in the fluorescence intensity near the nanowires is not due to a change in the linkage density, but rather to fluorescence interference contrast by the underlying silicon layer.[64]

| Linker | Primary Antibody (A.U) | Primary Antibody (Normalized) | Mouse IgG (A.U) | Rabbit IgG (A.U) | Specificity | % coverage | ΔVt (V) | ΔVt (V) (Normalized) |
|---|---|---|---|---|---|---|---|---|
| DSC | 120.10 (2.34) | 1.0000 | 97.74 (3.55) | 18.61 (0.91) | 5.252 | 81.38% | -0.720 (0.012) | 1.000 |
| BS(PEG) | 98.10 (2.21) | 0.8169 | 78.83 (3.83) | 3.084 (0.95) | 25.563 | 80.36% | -0.646 (0.006) | 0.897 |
| glutaraldehyde | 77.93 (6.16) | 0.6489 | 61.27 (2.34) | 36.33 (3.66) | 1.687 | 78.63% | -0.608 (0.010) | 0.845 |
| APDMS | 10.02 (0.05) | 0.0834 | 6.34 (0.08) | 6.84 (0.09) | 0.927 | 63.28% | -0.258 (0.003) | 0.358 |

**Table 4.2**. Table of values for primary antibody and target fluorescence on blank $SiO_2$ surfaces and primary antibody electrical response on silicon nanowires.

Silicon nanowires are known to display higher pH sensitivities than planar ISFET's due to their increased surface area to volume ratio and are of high interest to enzyme modified reactions which generate hydrogen ions as the metabolic product. The sensing based upon pH changes on FET's is currently being used in genomics and semiconductor sequencing by such companies as DNA Electronics[65] and Ion Torrent[66]. For enzyme modified nanowires this requires access to pH sensitive groups

on the surface, the linkage monolayer, or the protein, which will alter the surface potential. We have looked at pH sensitivity of the silicon nanowires before monolayer deposition, after monolayer deposition, and after protein deposition and blocking. The threshold voltage was monitored vs. the pH of a 1mM Robinson buffer and the results displayed in Figure 4.6A. The range is quite linear for the bare SiO2 dielectric and the APDMS monolayer, but there is a distinct inflection point in the protein curve between pH 6 and 7. We attribute this to the protein being near the isolectric point, with different buffering capacities above and below the isoelectric point, leading to different pH sensitivities.[67,68] We linearly fit the curves starting at pH 7 (Figure 4.6B) and constructed a table of the pH sensitivities (Figure 4.6, inset). Overall, the highest pH sensitivity was conferred by the APDMS layer, as amines are known to have a higher buffering capacity than hydroxyl groups. However, the primary antibody had the lowest sensitivity, with only 32mV/pH unit. The advantage of this decrease in pH sensitivity is less drift of the device due to slight pH changes in the buffer solution, while the disadvantage being decreased signal for proton generating enzymes. In our case, the change is beneficial since our detection is strictly due to antibody-antigen binding.

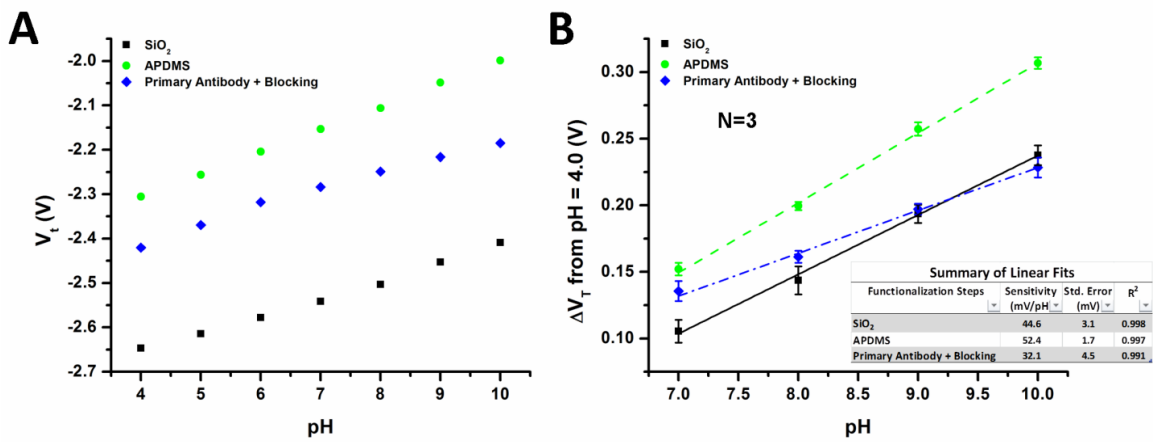


**Figure 4.6**. The threshold voltage ($V_t$ ) vs. the solution pH for different layers in the nanowire functionalization process is shown in (**A**). The change in threshold voltage ($\Delta V_t$) from pH 4.0 vs. the pH is in (**B**) with linear fits for each of these layers starting from pH 7.0. A table with the extracted parameters from the linear fit for pH sensitivity in (**B, inset**).

The high specificity of the silicon nanowires was demonstrated using competing antigens of similar structure to the analyte of interest, namely Mouse IgG. As negative controls, polyethylene oxide (PEO) MW 100,000 and the sensing buffer (0.01x PBS) were used. The competing antigens utilized in the experiments included Human and Rabbit IgG, as well as Mouse IgA. The Id-Vg curves for silicon nanowires were taken in 0.01x PBS after incubating the devices with 10ng/mL of the antigens for 1 hour, and are in Figure 4.7A. The corresponding shift in the threshold voltages with respect to the curve for 0.01x PBS is in Figure 4.7B, with the calculated device specificity towards Mouse IgG in Figure 4.7C. The Id-Vg curves show very little shift due to the nonspecific binding entities, with a high uniformity as these curves are averaged over 5 nanowires (N=5). The specificity towards the analyte of interest ranges between 15-26 times depending on the competing immunoglobulin. This result agrees well with the

fluorescence specificity in Figure 4.5, verifying that nanowires can provide specificities as good if not better than standard ELISA or fluorescent assays.

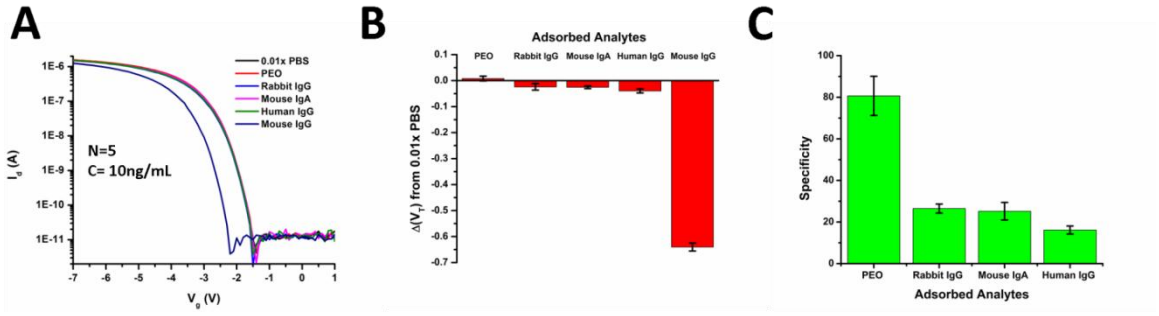


**Figure 4.7**. The Id-Vg response of nonspecific binding analytes vs. mouse IgG at a concentration of 10ng/mL is in (**A**). The change in the threshold voltage using 0.01x PBS as a reference for each of the biological analytes is plotted in (**B**) and the extracted specificity towards mouse IgG in (**C**).

The aforementioned protocols for functionalizing nanowires have shown they can be lead to highly stable measurements and provide high binding specificity. However, the limit of detection for nanowires using this BSPEG protocol or similar linking chemistries has been seldom studied. Moreover, the dependence on the gate oxide thickness has been poorly characterized. The gate oxide thickness, and thus gate capacitance, directly affects the amount the surface potential changes the current through the underlying conducting silicon channel. In Figure 4.8A we plot the normalized Id-Vg curves of nanowire devices with different gate oxide thicknesses. The extracted subthreshold slope (S.S.) for each gate oxide thickness is included as a table in Figure 4.8A. As the gate oxide thickness increases, the subthreshold slope becomes poorer and the devices threshold becomes more positive. This is in accordance with classical models for subthreshold swing in accumulation mode SOI MOSFET's. [69,70] The shift to the right of the threshold voltage with thicker gate oxides is due to extra fixed negative charge and interface traps

in the $SiO_2$ dielectric. We set the threshold voltage at $1x\ 10^{-3}$ on the normalized curve, denoted by a dashed line.

The sensitivity of the devices versus the thickness of the gate oxide is shown in Figure 4.8B. Concentrations of mouse IgG were titrated in for 30 min binding periods, then rinsed and measured in 0.01x PBS. The threshold voltage was extracted at the normalized value in Figure 4.8A for each gate oxide thickness, and plotted vs. the mouse IgG analyte concentration. The average of three devices was used for each gate oxide thickness. In agreement with theory, the largest gate oxide thickness showed the poorest sensitivity, with devices only starting to shift above the noise between 1-10ng/mL. However, the two thinner gate oxides begin to display sensitivity between the 0.1-1pg/mL range. The 90Å and 50Å gate oxide's also appear to have a $V_t$ response which scales linearly with respect to a logarithmic increase in mouse IgG concentration. This response appears to span 3 orders of magnitude from 0.1-100pg/mL for the 50Å gate oxide, while the 90Å oxide has a linear response from 1-1000pg/mL. These differences in the response of the devices vs. gate oxide thickness are encouraging, as the gate oxide thickness can be tailored to detect the range of the biomarker of interest.

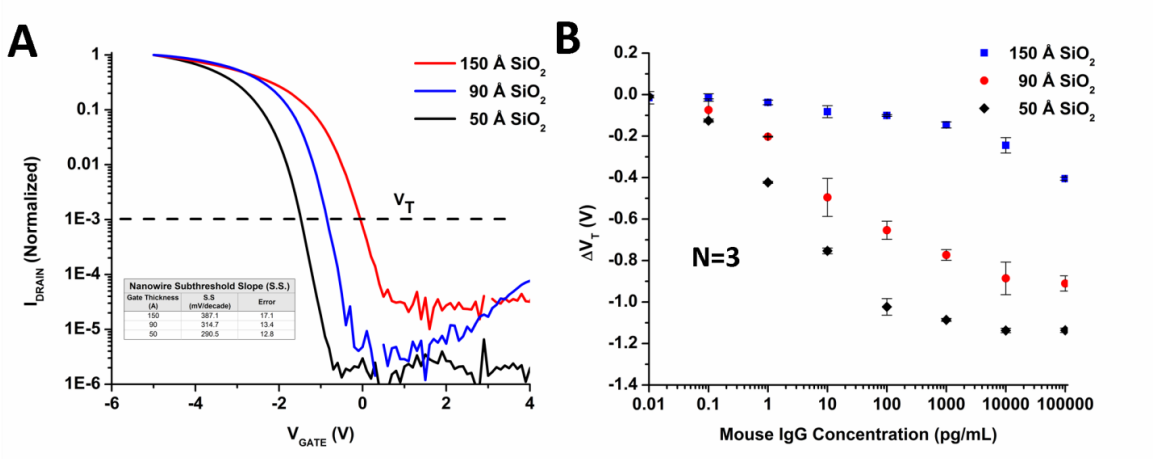


**Figure 4.8**. The representative Id-Vg curves of three different silicon oxide gate dielectric thicknesses (normalized) are shown in (A) . The subthreshold slopes (S.S) of each of the devices (inset table) show better S.S. with decreasing oxide thickness, and where the VT for the device is taken at 1x10-3, indicated by the dashed line. The change in the threshold voltage versus Mouse IgG concentration is shown in (B) for the three different oxide thickness devices shown in A.

## 4.5 CONCLUSIONS

In this work we successfully demonstrated a functionalization and device release protocol for silicon nanowires which is capable of sensing large immunoglobulins to sub pg/mL levels. By using a combined dry and wet etch technique, we were able to tailor the thickness of the gate oxide, thus changing the working dynamic range of the sensor. This method also yielded highly stable nanowires in solution capable of long-term measurements, with several wires yielding the same chracteristics. We evaluated several different linking chemistries which may be utilized for protein attachment by amine and thiol groups, both by fluorescence and the electrical response of silicon nanowires. The maximum amount of primary antibody and target antigen binding occurs with disuccinimidyl carbonate (DSC) linker, yet the best specificity is conferred with the BS(PEG) linker. The differences between the normalized fluorescence response and

electrical response were also characterized, demonstrating the electrical output is more sensitive than the fluorescent output using the same reaction conditions. In order to verify the results, fluorescence images were taken on the nanowires of the primary antibody reaction and showed a similarly scaling trend.

Using BS(PEG) as the model linking chemistry, the affinity of the nanowires for nonspecific binding was also explored. The silicon nanowires demonstrated excellent resistance to non-specific binders, yielding specifities (calculated from the threshold voltage shift) similar to those extracted from fluorescence. This result, given the output sensitivity being more on the nanowires, is quite encouraging and indicates the specificity being even better than that confirmed optically. Finally, the dose response of the nanowires to the target antigen (mouse IgG) versus the gate $SiO_2$ thickness was explored. The subthreshold slope of the devices demonstrated the proper scaling trend for increasing gate oxide thicknesses, and was used as a control to verify the oxide thickness. We demonstrate the sensitivities of the different oxide thicknesses to the antigen, showing the device sensitivity changes with the oxide thickness, as does the dynamic range of the sensor. The thinnest gate oxide demonstrated limits of detection to 1pg/mL using the BS(PEG) functionalization protocol, with a dynamic range spanning 3 orders of magnitude.

To our knowledge this is the first time an in-depth analysis of linker chemistries on silicon nanowires has been undertaken. Utilizing the best protocol, chosen from these findings, another study into different gate oxide thicknesses and their dose response to a model protein was undertaken, giving an even better in-depth perspective into the capabilities of nanowires as a point-of-care diagnostic platform. Gate dielectrics have

now turned towards high-k platforms, which can offer even better sensitivities without sacrificing device characteristics, such as increasing gate leakage. We hope by using new high-k platforms we can achieve even better sensitivity and more stable devices in the future, in hopes of bringing CMOS compatible platforms to the point-of-care market.

## 4.6 REFERENCES


[1]. Organization., W. H., Diet, Nutrition and the Prevention of Chronic Diseases. *Geneva, WHO* 2003.

[2]. STRONG, K.; MATHERS, C.; EPPING-JORDAN, J.; BEAGLEHOLE, R., Preventing Chronic Disease: A Priority for Global Health. *International Journal of Epidemiology* 2006, 35, 492-494.

[3]. Mabey, D.; Peeling, R. W.; Ustianowski, A.; Perkins, M. D., Diagnostics for the Developing World. *Nature Reviews Microbiology* 2004, 2, 231-240.

[4]. Moore, G. E., Cramming More Components onto Integrated Circuits. *Proceedings of the IEEE* 1998, 86, 82-85.

[5]. Barrettino, D. In *Design Considerations and Recent Advances in Cmos-Based Microsystems for Point-of-Care Clinical Diagnostics*, Kos, Kos, 2006; pp 4359-4362.

[6]. Bergveld, P., Thirty Years of Isfetology - What Happened in the Past 30 Years and What May Happen in the Next 30 Years. *Sensors and Actuators B-Chemical* 2003, 88, 1-20.

[7]. Schöning, M. J.; Poghossian, A., Recent Advances in Biologically Sensitive Field-Effect Transistors (Biofets). *Analyst* 2002, 127, 1137-1151.

[8]. Baccar, Z. M.; Jaffrezic-Renault, N.; Martelet, C.; Jaffrezic, H.; Marest, G.; Plantier, A., Sodium Microsensors Based on Isfet/Refet Prepared through an Ion-Implantation Process Fully Compatible with a Standard Silicon Technology. *Sensors and Actuators, B: Chemical* 1996, 32, 101-105.

[9]. Bratov, A.; Abramova, N.; Domínguez, C.; Baldi, A., Ion-Selective Field Effect Transistor (Isfet)-Based Calcium Ion Sensor with Photocured Polyurethane Membrane Suitable for Ionised Calcium Determination in Milk. *Analytica Chimica Acta* 2000, 408, 57-64.

[10]. Cazalé, A.; Sant, W.; Launay, J.; Ginot, F.; Temple-Boyer, P., Study of Field Effect Transistors for the Sodium Ion Detection Using Fluoropolysiloxane-Based Sensitive Layers. *Sensors and Actuators, B: Chemical* 2013, 177, 515-521.

[11]. Hajji, B.; Temple-Boyer, P.; Launay, J.; Do Conto, T.; Martinez, A., Ph, Pk and Pna Detection Properties of Sio2/Si3n4 Isfet Chemical Sensors. *Microelectronics Reliability* 1999, 40, 783-786.

[12]. Ho, K. I.; Lu, T. F.; Chang, C. P.; Lai, C. S.; Yang, C. M. In *Sodium and Potassium Ion Sensing Properties of Eis and Isfet Structures with Fluorinated Hafnium Oxide Sensing Film*, Christchurch, Christchurch, 2009; pp 1128-1131.

[13]. Lu, T. F.; Yang, C. M.; Wang, J. C.; Ho, K. I.; Chin, C. H.; Pijanowska, D. G.; Jaroszewicz, B.; Lai, C. S., Characterization of K and Na-Sensitive Membrane Fabricated by Cf 4 Plasma Treatment on Hafnium Oxide Thin Films on Isfet. *Journal of the Electrochemical Society* 2011, 158, J91-J95.

[14]. Rochefeuille, S.; Jimenez, C.; Tingry, S.; Seta, P.; Desfours, J. P., Mixed Langmuir-Blodgett Monolayers Containing Carboxylic Ionophores. Application to Na+ and Ca2+ Isfet-Based Sensors. *Materials Science and Engineering C* 2002, 21, 43-46.

[15]. Senillou, A.; Jaffrezic-Renault, N.; Martelet, C.; Griffe, F., A Miniaturized Ammonium Sensor Based on the Integration of Both Ammonium and Reference Fets in a Single Chip. *Materials Science and Engineering C* 1998, 6, 59-63.

[16]. Janata, J., Thirty Years of Chemfets - a Personal View. *Electroanalysis* 2004, 16, 1831-1835.

[17]. Covington, J. A.; Gardner, J. W.; Briand, D.; De Rooij, N. F., A Polymer Gate Fet Sensor Array for Detecting Organic Vapours. *Sensors and Actuators, B: Chemical* 2001, 77, 155-162.

[18]. Abramova, N.; Bratov, A., Photocurable Polymers for Ion Selective Field Effect Transistors. 20 Years of Applications. *Sensors* 2009, 9, 7097-7110.

[19]. Sant, W.; Temple-Boyer, P.; E.chanié; Launay, J.; Martinez, A., On-Line Monitoring of Urea Using Enzymatic Field Effect Transistors. *Sensors and Actuators, B: Chemical* 2011, 160, 59-64.

[20]. Antonisse, M. M. G.; Snellink-Ruël, B. H. M.; Engbersen, J. F. J.; Reinhoudt, D. N., H2po- 4-Selective Chemfets with Uranyl Salophene Receptors. *Sensors and Actuators, B: Chemical* 1998, 47, 9-12.

[21]. Reinhoudt, D. N., Durable Chemical Sensors Based on Field-Effect Transistors. *Sensors and Actuators: B. Chemical* 1995, 24, 197-200.

[22]. Diallo, A. K.; Djeghlaf, L.; Mazenq, L.; Launay, J.; Sant, W.; Temple-Boyer, P., Development of Ph-Based Elecfet Biosensors for Lactate Ion Detection. *Biosensors and Bioelectronics* 2013, 40, 291-296.

[23]. Sant, W.; Pourciel, M. L.; Launay, J.; Do Conto, T.; Martinez, A.; Temple-Boyer, P., Development of Chemical Field Effect Transistors for the Detection of Urea. *Sensors and Actuators, B: Chemical* 2003, 95, 309-314.

[24]. Burgmair, M.; Eisele, I. In *Contribution of the Gate Insulator Surface to Work Function Measurements with a Gas Sensitive Fet*, Orlando, FL, Orlando, FL, 2002; pp 439-442.

[25]. Wilson, D. M.; Hoyt, S.; Janata, J.; Booksh, K.; Obando, L., Chemical Sensors for Portable, Handheld Field Instruments. *IEEE Sensors Journal* 2001, 1, 256-274.

[26]. Koch, S.; Woias, P.; Meixner, L. K.; Drost, S.; Wolf, H., Protein Detection with a Novel Isfet-Based Zeta Potential Analyzer. *Biosensors and Bioelectronics* 1999, 14, 413-421.

[27]. Besselink, G. A. J.; Schasfoort, R. B. M.; Bergveld, P., Modification of Isfets with a Monolayer of Latex Beads for Specific Detection of Proteins. *Biosensors and Bioelectronics* 2003, 18, 1109-1114.

[28]. Eijkel, J. C. T.; Olthuis, W.; Bergveld, P., An Isfet-Based Dipstick Device for Protein Detection Using He Ion-Step Method. *Biosensors and Bioelectronics* 1997, 12, 991-1001.

[29]. Estrela, P.; Stewart, A. G.; Yan, F.; Migliorato, P., Field Effect Detection of Biomolecular Interactions. *Electrochimica Acta* 2005, 50, 4995-5000.

[30]. Marrakchi, M.; Dzyadevych, S. V.; Biloivan, O. A.; Martelet, C.; Temple, P.; Jaffrezic-Renault, N., Development of Trypsin Biosensor Based on Ion Sensitive Field-Effect Transistors for Proteins Determination. *Materials Science and Engineering C* 2006, 26, 369-373.

[31]. Olthuis, W.; Luo, J.; Bergveld, P., Characterization of Proteins by Means of Their-Buffer Capacity, Measured with an Isfet-Based Coulometric Sensor-Actuator System. *Biosensors and Bioelectronics* 1994, 9, 743-751.

[32]. Estrela, P.; Stewart, A. G.; Keighley, S. D.; Migliorato, P., Biologically Sensitive Field-Effect Devices Using Polysilicon Tfts. *Journal of the Korean Physical Society* 2006, 48, S22-S26.

[33]. Berney, H.; West, J.; Haefele, E.; Alderman, J.; Lane, W.; Collins, J. K., DNA Diagnostic Biosensor: Development, Characterisation and Performance. *Sensors and Actuators, B: Chemical* 2000, 68, 100-108.

[34]. Mascini, M.; Palchetti, I.; Marrazza, G., DNA Electrochemical Biosensors. *Analytical and Bioanalytical Chemistry* 2001, 369, 15-22.

[35]. Mikkelsen, S. R., Electrochemical Biosensors for DNA Sequence Detection. *Electroanalysis* 1996, 8, 15-19.

[36]. Souteyrand, E., DNA Chips: From Elaboration to Application. *Analusis* 1999, 27, 639-646.

[37]. Souteyrand, E.; Cloarec, J. P.; Martin, J. R.; Wilson, C.; Lawrence, I.; Mikkelsen, S.; Lawrence, M. F., Direct Detection of the Hybridization of Synthetic Homo-Oligomer DNA Sequences by Field Effect. *Journal of Physical Chemistry B* 1997, 101, 2980-2985.

[38]. Fang, Y.; Patolsky, F.; Lieber, C. M., Electrical Detection of Single DNA Molecules with Silicon Nanowire Devices. *Biophysical Journal* 2007, 551a.

[39]. Zheng, G. F.; Lu, W.; Lieber, C. M., Ultrahigh Sensitive Protein Detection by Frequency Analysis Using Nanowire Field Effect Sensors. *Abstracts of Papers of the American Chemical Society* 2006, 231, -.

[40]. Zheng, G. F.; Patolsky, F.; Lieber, C. M., Multiplexed Electrical Detection of Cancer Marker Proteins and Single Viruses by Nanowire Fet Arrays. *Abstracts of Papers of the American Chemical Society* 2005, 229, U782-U782.

[41]. Zheng, G. F.; Patolsky, F.; Cui, Y.; Wang, W. U.; Lieber, C. M., Multiplexed Electrical Detection of Cancer Markers with Nanowire Sensor Arrays. *Nature Biotechnology* 2005, 23, 1294-1301.

[42]. Wang, W. U.; Chen, C.; Lin, K. H.; Fang, Y.; Lieber, C. M., Label-Free Detection of Small-Molecule-Protein Interactions by Using Nanowire Nanosensors. *Proceedings of the National Academy of Sciences of the United States of America* 2005, 102, 3208-3212.

[43]. Cui, Y.; Wei, Q. Q.; Park, H. K.; Lieber, C. M., Nanowire Nanosensors for Highly Sensitive and Selective Detection of Biological and Chemical Species. *Science* 2001, 293, 1289-1292.

[44]. Fritz, J.; Cooper, E. B.; Gaudet, S.; Sorger, P. K.; Manalis, S. R., Electronic Detection of DNA by Its Intrinsic Molecular Charge. *Proceedings of the National Academy of Sciences of the United States of America* 2002, 99, 14142-14146.

[45]. Lu, W.; Lieber, C. M., Nanoelectronics from the Bottom Up. *Nature Materials* 2007, 6, 841-850.

[46]. Stern, E.; Vacic, A.; Rajan, N. K.; Criscione, J. M.; Park, J.; Ilic, B. R.; Mooney, D. J.; Reed, M. A.; Fahmy, T. M., Label-Free Biomarker Detection from Whole Blood. *Nature Nanotechnology* 2010, 5, 138-142.

[47]. Stern, E.; Vacic, A.; Li, C.; Ishikawa, F. N.; Zhou, C. W.; Reed, M. A.; Fahmy, T. M., A Nanoelectronic Enzyme-Linked Immunosorbent Assay for Detection of Proteins in Physiological Solutions. *Small* 2010, 6, 232-238.

[48]. Stern, E.; Klemic, J. F.; Routenberg, D. A.; Wyrembak, P. N.; Turner-Evans, D. B.; Hamilton, A. D.; LaVan, D. A.; Fahmy, T. M.; Reed, M. A., Label-Free

Immunodetection with Cmos-Compatible Semiconducting Nanowires. *Nature* 2007, 445, 519-522.

[49]. Nair, P. R.; Alam, M. A., Design Considerations of Silicon Nanowire Biosensors. *Ieee Transactions on Electron Devices* 2007, 54, 3400-3408.

[50]. Elfstrom, N.; Juhasz, R.; Sychugov, I.; Engfeldt, T.; Karlstrom, A. E.; Linnros, J., Surface Charge Sensitivity of Silicon Nanowires: Size Dependence. *Nano Letters* 2007, 7, 2608-2612.

[51]. Poghossian, A.; Cherstvy, A.; Ingebrandt, S.; Offenhäusser, A.; Schöning, M. J., Possibilities and Limitations of Label-Free Detection of DNA Hybridization with Field-Effect-Based Devices. *Sensors and Actuators, B: Chemical* 2005, 111-112, 470-480.

[52]. Scarano, S.; Mascini, M.; Turner, A. P. F.; Minunni, M., Surface Plasmon Resonance Imaging for Affinity-Based Biosensors. *Biosensors and Bioelectronics* 2010, 25, 957-966.

[53]. Marquette, C. A.; Corgier, B. P.; Heyries, K. A.; Blum, L. J., Biochips: Non-Conventional Strategies for Biosensing Elements Immobilization. *Frontiers in Bioscience* 2008, 13, 382-400.

[54]. Jonkheijm, P.; Weinrich, D.; Schröder, H.; Niemeyer, C. M.; Waldmann, H., Chemical Strategies for Generating Protein Biochips. *Angewandte Chemie - International Edition* 2008, 47, 9618-9647.

[55]. Voue, M.; Goormaghtigh, E.; Homble, F.; Marchand-Brynaert, J.; Conti, J.; Devouge, S.; De Coninck, J., Biochemical Interaction Analysis on Atr Devices: A Wet Chemistry Approach for Surface Functionalization. *Langmuir* 2007, 23, 949-955.

[56]. Muck, A.; Svatoš, A., Chemical Modification of Polymeric Microchip Devices. *Talanta* 2007, 74, 333-341.

[57]. Brétangol, F.; Valsesia, A.; Ceccone, G.; Colpo, P.; Gilliland, D.; Ceriotti, L.; Hasiwa, M.; Rossi, F., Surface Functionalization and Patterning Techniques to Design Interfaces for Biomedical and Biosensor Applications. *Plasma Processes and Polymers* 2006, 3, 443-455.

[58]. Korf, U.; Henjes, F.; Schmidt, C.; Tresch, A.; Mannsperger, H.; Löbke, C.; Beissbarth, T.; Poustka, A., Antibody Microarrays as an Experimental Platform for the Analysis of Signal Transduction Networks. Werther, M.; Seitz, H., Eds. 2008; Vol. 110, pp 153-175.

[59]. Bally, M.; Halter, M.; Vörös, J.; Grandin, H. M., Optical Microarray Biosensing Techniques. *Surface and Interface Analysis* 2006, 38, 1442-1458.

[60]. Dorvel, B.; Reddy, B.; Block, I.; Mathias, P.; Clare, S. E.; Cunningham, B.; Bergstrom, D. E.; Bashir, R., Vapor-Phase Deposition of Monofunctional Alkoxysilanes

for Sub-Nanometer-Level Biointerfacing on Silicon Oxide Surfaces. *Advanced Functional Materials* 2010, 20, 87-95.

[61]. Chen, S.; Nyholm, L.; Jokilaakso, N.; Karlstrm, A. E.; Linnros, J.; Smith, U.; Zhang, S. L., Current Instability for Silicon Nanowire Field-Effect Sensors Operating in Electrolyte with Platinum Gate Electrodes. *Electrochemical and Solid-State Letters* 2011, 14, J34-J37.

[62]. Dorvel, B. R.; Reddy, B., Jr.; Go, J.; Duarte Guevara, C.; Salm, E.; Alam, M. A.; Bashir, R., Silicon Nanowires with High-K Hafnium Oxide Dielectrics for Sensitive Detection of Small Nucleic Acid Oligomers. *ACS Nano* 2012, 6, 6150-64.

[63]. Reddy Jr, B.; Dorvel, B. R.; Go, J.; Nair, P. R.; Elibol, O. H.; Credo, G. M.; Daniels, J. S.; Chow, E. K. C.; Su, X.; Varma, M., et al., High-K Dielectric Al2o3 Nanowire and Nanoplate Field Effect Sensors for Improved Ph Sensing. *Biomedical Microdevices* 2011, 13, 335-344.

[64]. Lambacher, A.; Fromherz, P., Fluorescence Interference-Contrast Microscopy on Oxidized Silicon Using a Monomolecular Dye Layer. *Applied Physics a-Materials Science & Processing* 1996, 63, 207-216.

[65]. Kalofonou, M.; Toumazou, C., Semiconductor Technology for Early Detection of DNA Methylation for Cancer: From Concept to Practice. *Sensors and Actuators, B: Chemical* 2013, 178, 572-580.

[66]. Merriman, B.; Torrent, I.; Rothberg, J. M., Progress in Ion Torrent Semiconductor Chip Based Sequencing. *Electrophoresis* 2012, 33, 3397-3417.

[67]. Bergveld, P.; Vanhal, R. E. G.; Eijkel, J. C. T., The Remarkable Similarity between the Acid-Base Properties of Isfets and Proteins and the Consequences for the Design of Isfet Biosensors. *Biosensors & Bioelectronics* 1995, 10, 405-414.

[68]. Olthuis, W.; Luo, J.; Bergveld, P., Characterization of Proteins by Means of Their Buffer Capacity, Measured with an Isfet-Based Coulometric Sensor-Actuator System. *Biosensors & Bioelectronics* 1994, 9, 743-751.

[69]. Colinge, J. P.; Flandre, D.; Van De Wiele, F., Subthreshold Slope of Long-Channel, Accumulation-Mode P-Channel Soi Mosfets. *Solid-State Electronics* 1994, 37, 289-294.

[70]. Colinge, J. P.; Van de Wiele, F.; Flandre, D. In *Subthreshold Slope of Accumulation-Mode P-Channel Soi Mosfets*, Palm Springs, CA, USA, Publ by IEEE: Palm Springs, CA, USA, 1993; pp 146-147.

# CHAPTER 5: SILICON NANOWIRES WITH HIGH-K HAFNIUM OXIDE DIELECTRICS FOR SENSITIVE DETECTION OF SMALL NUCLEIC ACID OLIGOMERS

## 5.1 ABSTRACT

Nanobiosensors based on silicon nanowire field effect transistors offer advantages of low cost, label-free detection, and potential for massive parallelization. As a result, these sensors have often been suggested as an attractive option for applications in Point-of-care (POC) medical diagnostics. Unfortunately, a number of performance issues such as gate leakage and current instability due to fluid contact, have prevented widespread adoption of the technology for routine use. High-k dielectrics, such as hafnium oxide ($HfO_2$), have the known ability to address these challenges by passivating the exposed surfaces against destabilizing concerns of ion transport. With these fundamental stability issues addressed, a promising target for POC diagnostics and SiNWFET's has been small oligonucleotides, more specifically microRNA (miRNA). MicroRNA's are small RNA oligonucleotides which bind to messenger RNA's, causing translational repression of proteins, gene silencing, and expressions are typically altered in several forms of cancer. In this paper, we describe a process for fabricating stable $HfO_2$ dielectric based silicon nanowires for biosensing applications. Here we demonstrate sensing of single stranded DNA analogues to their microRNA cousins using miR-10b and miR-21 as templates, both known to be upregulated in breast cancer. We characterize the effect of surface

functionalization on device performance using the miR-10b DNA analogue as the target sequence and different molecular weight poly-l-lysine as the functionalization layer. By optimizing the surface functionalization and fabrication protocol, we were able to achieve <100fM detection levels of miR-10b DNA analogue, with a theoretical limit of detection of 1fM. Moreover, the non-complementary DNA target strand, based on miR-21, showed very little response, indicating a highly sensitive and highly selective biosensing platform.

## 5.2 INTRODUCTION

Point-of-care (POC) diagnostics has emerged as an exciting field where devices can provide rapid, cheap, and accurate results in a portable format. Such diagnostic devices have the potential to provide critical patient information more rapidly at cheaper costs than instruments in centralized lab facilities, reducing the turnaround time for results in critical care situations.[1,2] Moreover, POC diagnostics can present patients with more control of their own therapy[3], leading to greater patient satisfaction and improved clinical outcome[4]. In particular, treatment for various forms of cancer could benefit greatly from such POC devices. As our knowledge of cancer pathways rapidly grows, important indicators of cancer have been revealed, including changes in the genome, exome, transcriptome, and expression levels of several cancer biomarkers such as proteins and microRNA (miRNA). Devices that can rapidly detect cancer biomarkers in a rapid, accurate, multiplexed, and cost-efficient fashion would revolutionize cancer treatment, allowing for better evaluation of the efficacy of treatment, earlier detection of cancer, and de-convolution of the complex pathways that result in cancer.

Adaption of the ubiquitous field effect transistor (FET) technology has been proposed as a possible core technology for the sensing component of POC devices, due to the potential for low per unit cost, label-free detection, and amenability for scale-up and integration with signal processing electronics. Electrochemical detection methodologies based upon ion sensitive field effect transistor's (ISFETs) have been studied extensively[5], including its use as biosensors (bioFET)[6-10]. The performance of ISFET and bioFET relies on the charge of a binding biological analyte over the gate insulator of the FET, which induces changes in the source-drain current of the device. This allows for label-free, ultrasensitive, and rapid detection of relevant biological analytes.

Silicon nanowire FET devices (SiNWFETs), where the silicon channel has thicknesses and diameters in the tens of nanometers or less have further enhanced properties. Using SiNWFETs, researchers have demonstrated detection of biological analytes such as proteins[11-16], DNA[17-20], RNA [21], ions[22], and other small molecules[23] down to fM concentrations. The increased sensitivity of these devices is mainly attributed to the increased gate control of the silicon channel due to a higher surface area to volume ratio. Thus, silicon nanowires show promise in cancer diagnosis, since various cancer biomarkers may exist in small concentrations throughout the disease pathogenesis. Silicon nanowire FETs fabricated with "top-down" techniques[17,24-30] are particularly attractive, due to CMOS compatibility and high amenability for scale-up. However, though nanowire technology has existed for over a decade, several issues have prevented the technology from maturation into fully fledged POC products. Various issues have arisen regarding device stability in fluid such as measurement drift[31],

leakage paths through the sensing dielectric, high background l/f noise[32-34], and lack of repeatability. Silicon oxide, the traditional top gate dielectric, is one of the main culprits behind several of these issues, due to its relatively low dielectric constant, low pH buffering capacity, and susceptibility of gradual charge incorporation by ion diffusion when exposed to fluid. [35,36] To circumvent some of these issues, researchers have turned to high-k materials, including aluminum oxide (Al2O3)[37], hafnium oxide ($HfO_2$)[38], and tantalum oxide (Ta2O5)[39]. High-k materials enable high gate oxide capacitance values even with physically thicker gate oxides, allowing a reduction in leakage current. $HfO_2$ has arisen as a particularly promising dielectric for ISFET's and MOSFET's due to its stability on silicon and its acceptable bandgap and conduction band offset values. It can be deposited by chemical vapor deposition and yields improved pH sensitivity.[40,41]

To date, however, there have been very few reports that offer detailed characterization and application of hafnium oxide-based FETs for biosensing applications. Annealing of $HfO_2$ has been shown to improve pH sensitivity in a two terminal EIS (electrolyte-insulator-semiconductor) capacitor using capacitance-voltage curves.[42] However, such a structure does not take advantage of the main desirable property for a FET, its intrinsic high current gain (high transconductance). In addition, $HfO_2$ deposited at high CVD temperatures for ISFETs lead to leakage paths in the silicon in high aspect ratio areas and results in higher roughness[43], which is undesirable for a charge based biosensor. The demonstrated sensitivity for this structure was very low (biotin and streptavidin detected down to ~50ug/mL).[44] pH sensing has been

demonstrated with a FET structure with encouraging near-Nernstian results, but no molecular sensing has been reported to date.[38]

Here we describe a process for fabricating robust $HfO_2$ based silicon nanoFET sensors for biological applications. We use atomic layer deposition (ALD) to form the hafnium oxide dielectric and a wet etch based process for releasing the device structures. Unlike CVD methodologies, ALD is more conformal and can be performed at lower deposition temperatures with better process control. Additionally, the wet etch based process for device release eliminates the possibility of RIE induced damage to the delicate dielectric layer. We have characterized in detail the properties of this low temperature deposition process and optimized subsequent annealing conditions to create a high quality dielectric. Moreover, we discuss the electrical and chemical advantages of the process, which include $HfO_2$ becoming an excellent wet etch stop for acid, alkali, and oxidizing chemistries. By thoroughly characterizing the $HfO_2$-silicon interface, we were able to produce a high quality gate dielectric layer, resulting in a device with high repeatability and low hysteresis in fluid. The devices are highly stable and robust, and show minimal drift over hours in fluid. As a result, we were able to achieve ~56mV/pH unit response for nanowire devices. We then demonstrate the sensitive detection of a DNA analogue sequence of microRNA, which can be highly important cancer biomarkers. MicroRNA's (miRNA's) are small RNA oligonucleotides which bind to messenger RNA's, causing translational repression of proteins and gene silencing. In this work we focus on sensing DNA analogues of miRNA's, with templates based upon miR-10b and miR-21, miRNA's commonly upregulated in breast cancer.[45-49] Moreover, miR-21 is found in a 4 fold higher concentration than miR-10b in normal tissue[50],

making miR-10b a harder analyte to detect even when upregulated. The devices were functionalized with different molecular weight poly-lysine strands and DNA probes specific to the miR-10b DNA analogue sequence. Different sensitivities for the different molecular weight poly-lysines were achieved for miR-10b, with lower sensitivity being achieved on the higher molecular weight polymer. Analysis of the layers showed lower probe density and higher roughness for the higher molecular weight layer of poly-l-lysine. The devices were able to achieve 100fM detection limits for the miR-10b DNA in comparison against a miR-21 non-complementary target, with a theoretical limit of detection of 1fM. Various characteristic features of these systematic set of experiments are interpreted and supported by well calibrated theoretical models.

## 5.3 EXPERIMENTAL

### MATERIALS

All metals for e-beam evaporation were of 99.999% purity and purchased from Lesker Co. DNA and miDNA strands were purchased from Integrated DNA Technologies and purified using HPLC. Poly-l-lysine (PLL) of MW 9,000-14,000 and MW 70,000-150,000 were purchased from Sigma in powder form and used without further purification. Robinson buffer solutions composed of 1mM acetic acid, 1mM phosphoric acid, and 1mM boric acid were titrated with NaOH/HCl from pH's 4-12. All buffer components were purchased from Fisher Scientific. A leak-free Ag/AgCl reference electrode was used to apply bias to the fluid on top of the devices and was purchased from Warner Instruments.

# DEVICE FABRICATION

A detailed top down fabrication flow has been described previously for creating similar silicon nanoFET devices.[40] The fabrication flow began with bonded Silicon on Insulator (SOI) wafers, doped p-type at $10^{15}/cm^2$ with a buried oxide thickness of 1,450 Å and top silicon thickness of 550 Å. The top silicon was thinned to approximately 300 Angstroms by dry oxidation and stripping of the oxidized layer with 10:1 buffered oxide etch. The wires were then defined via electron beam lithography and wet etched with 25% TMAH to define the active silicon area. The source and drain regions were doped with boron (doping $\sim 10^{19}/cm^3$) by ion implantation, and annealed at 1000C for 5 minutes to active the dopants. The wafer was then dipped in 50:1 BOE for 20s to remove any native oxide, and an SC1/SC2 clean performed. The wafer then underwent a rapid thermal anneal at 1000C for 60s to help densify the native oxide layer. The $HfO_2$ gate dielectric was deposited by ALD at a temperature of 120 Celsius for 100 cycles. Following the gate dielectric formation, via holes were etched into the contact regions with 10:1 BOE, and a 100 Å Ni/50 Å TiN layer was deposited in the contact regions by RF sputtering. A rapid thermal anneal was performed at 500°C in Ar to form NiSi and reduce the contact resistance at the source and drain regions of the devices, while also densifying the $HfO_2$ and creating a wet etch stop. Next, 150nm of Al was sputtered and patterned over the contact areas. A 450C furnace anneal in Ar/H2 was performed for 30 min to anneal the contacts and remove interface traps in the oxide. Afterwards, a 5,000 Å thick passivation layer of PECVD SiOxNy was deposited over the entire wafer. Metal pad areas on the outside of the Al leads were defined by optical lithography and 10:1 BOE was used to etch the passivation layer. Metal pads composed of 50nm Ti/ 300nm

Ni/ 500nm Au were then deposited by e-beam evaporation. The final passivation layer etchback to release the $HfO_2$ devices was done using 10:1 BOE. Subsequently, the wafer is diced (American Precision Dicing) into chips of 1.5x1.5cm for testing.

## MATERIALS CHARACTERIZATION

For thickness characterization, $HfO_2$ of varying thicknesses was deposited by ALD onto polished Si wafers and annealed according to the device fabrication above. The wafer was then covered with photoresist and diced into 1x1cm dies. Ellipsometry measurements were taken using a Rudolph FEIII ellipsometer at a wavelength of 632.8nm and an angle of 70 degrees. Each measurement was taken over ten different areas of a chip and averaged together to get a thickness and standard deviation. For fluorescence measurements, a 1um thick thermal oxide was grown on a polished Si and then 100 cycles ALD $HfO_2$ deposited on top. The thick grown oxide was to limit signal degradation due to fluorescence interference contrast (FLIC).[64] The $HfO_2$ was subsequently annealed according to the device fabrication above. Fluorescent images were taken with a Nikon microscope at an exposure of 800ms and a gain of 1.3x. Atomic force microscopy images of the $HfO_2$ and PLL layers were taken with an Asylum Cypher AFM using a Force Modulation AFM probe tip (Budget Sensors) with a resonant frequency of 75kHz and a force constant of 1-3 N/m. Force applied to the substrates during contact mode was calibrated by taking the inverse optical lever sensitivity (invOLS) of the cantilever deflection on a bare $HfO_2$ surface and calculating the spring constant of the cantilever by fitting the thermal fluctuations. X-ray photoelectron spectroscopy of the $HfO_2$, DNA, and PLL layers were taken with a KRATOS Axis Ultra XPS at a take-off angle of 90 degrees. Survey spectra were acquired at a pass energy of

160eV with 2 sweeps collected. High resolution spectra of Hf4f, P2p, O1s, C1s, and N1s peaks were collected at a pass energy of 40eV with a total of 25 passes per peak.

## ELECTRICAL MEASUREMENTS

High frequency C-V measurements of $HfO_2$ MOS capacitors were performed at 1MHz using a Keithley semiconductor parameter analyzer (Keithley 4200) and corrected for series resistance. The capacitors had a top contact of 30nm TiN/100nm Al, and a back contact of 100nm Al, which were DC sputtered. Electrical current measurements and applied biases were controlled by the Keithley 4200 as well. Fluid gate biases were applied with a leak free Ag/AgCl reference electrode (Warner Instruments) that made contact to the solution. Back gate biases were applied using the conductive platform of the probing station which made contact to the backside of the FET dies. At any other times, the conductive platform served as the ground for the FET dies while biases were applied to the fluid gate electrode. The Robinson buffer pH solutions were made using 1 mM acetic, 1 mM phosphoric, and 1 mM boric acid with titrated HCl/NaOH to obtain the desired pH. All pH solutions were measured at the conclusion of the experiment to ensure that the pH had not changed significantly during the course of the experiment.

## PREPARATION OF DEVICES FOR DNA SENSING

Before depositing poly-l-lysine, chips were degreased with acetone and methanol, then rinsed in DI water for 1min. The chips then underwent an O2 plasma at 500mTorr and 200W for 5 minutes. Poly-l-lysine solutions were made to 0.2mg/mL concentration in 5mM Na2B4O7, pH 8.5. Chips are soaked in PLL solution for 2 hours, then taken out of the solution and rinsed in DI water for 1 min. Chips are then blown dry with N2 and

dessicated for 10min. The chips are baked at 85C in a vacuum oven for 4 hours afterwards.

DNA probe and targets were obtained from Integrated DNA Technologies and diluted to a stock concentration of 100uM in DI water. All stock solutions were stored at -20 Celsius until used. DNA probe solution (10uM in 3X SSC buffer) was spotted on the device in a 10uL volume and allowed to sit for 2 hours in a humidity chamber. The chip was then rinsed in 2X SSC, 0.2X SSC, and 5% EtOH for 1 min each, and blown dry with N2. To crosslink the DNA to the PLL, chips were baked at 85C for 2 hours in a convection oven. A PDMS well with an adhesive bottom tape was attached to the chip afterwards. Each well had a circular diameter of 5mm and a fluid volume of ~50uL. The target solutions for varying concentrations of miR-10b and miR-21 were made in 2X SSC buffer and put in the PDMS well for 30 mins to hybridize. The target was then rinsed off 3 times in 2X SSC buffer and 3 times in 0.2X SSC buffer before measuring in 0.02X SSC buffer.

# THEORETICAL MODEL FOR PH RESPONSE AND NOISE OF SINW SENSOR

The sensitivity of ISFET to pH fluctuations in the buffer is determined by the protonation/de-protonation kinetics of –OH functional groups at the gate oxide-electrolyte interface and the electrostatics of the system, as described by the equations in Table 5.1. For reaction kinetics of –OH functional groups, we use the site binding model with reasonably calibrated parameters ($N_s$, $K_a$, and $pK_b$ in Table 5.2) regarding $HfO_2$ surface due to unavailability of experimentally observed values in the literature. The model equations are discretized using finite difference scheme and self-consistently

solved using Newton iteration due to the strong non-linear nature of the equations. For the relevant device dimensions used in our experiments ($t_{Si}$ ~55nm, $t_{ox}$~4nm), the cylindrical gate oxide capacitance, $C_{cylind}=2\varepsilon_{ox}/(t_{Si}\times\ln(1+2t_{ox}/t_{Si}))$ is comparable to the corresponding planar gate oxide capacitance, $C_{cylind}=\varepsilon_{ox}/t_{ox}$. This allows us to reduce the computational complexity and solve the system of equations for the equivalent planar system. We assume Boltzmann distribution for the ions in the electrolyte and long channel with small drain bias to simply estimate the conductance of Si channel.

For the estimation of voltage noise in ISFET, we consider two major sources of noise: low frequency noise (1/f) and the electrolyte noise, as summarized in Table 5.2. We assume they are uncorrelated thus the total noise is given by $\sigma V = \sqrt{\sigma V_{1/f}^2 + \sigma V_e^2}$.

| Region | Model Equations | Description of variables |
|---|---|---|
| Si | Poisson Equation $-\nabla\cdot(\varepsilon_{si}\nabla\psi) = q(p-n-N_A)$<br>$p = n_i e^{-q(\psi-\psi_f)/k_B T}$, $n = n_i e^{q(\psi-\psi_f)/k_B T}$ | $\psi$-electrostatic potential, $\varepsilon_{si}$ = 11.9$\varepsilon_0$, $\varepsilon_0$ dielectric permittivity of vaccum, q-electronic charge, $N_A$-doping of Si ($10^{15}$ $cm^{-3}$), $n_i$ = $10^{10}$ $cm^{-3}$, $\psi_f$ -Fermi level in Si. |
| Gate dielectric | Poisson Equation $-\nabla\cdot(\varepsilon_{ox}\nabla\psi) = 0$<br>(Acceptor like interface traps ($D_{it}$) are assumed at Si/Gate oxide interface. For $SiO_2$/$HfO_2$ gate oxide stack, a fixed interface charge is assumed.) | $\varepsilon_{ox}$ = 3.9$\varepsilon_0$ ($SiO_2$) or 20.1$\varepsilon_0$ ($HfO_2$)<br>$D_{it}$: interface trap density at Si/Gate dielectric interface ($D_{it}$ ~ 4x$10^{11}$$cm^{-2}$/eV).<br>$Q_F$: fixed charge density at $SiO_2$/$HfO_2$ interface. |
| Gate dielectric-electrolyte interface | Protonation/de-protonation of OH groups $AOH \leftrightarrow AO^- + H_s^+$, $AOH_2^+ \leftrightarrow AOH + H_s^+$<br>OH surface density $N_s = [AOH]+[AO^-]+[AOH_2^+]$<br>Reaction constants $K_a = \frac{[AO^-][H_s^+]}{[AOH]}$ $K_b = \frac{[AOH][H_s^+]}{[AOH_2^+]}$<br>Boundary condition<br>$(\varepsilon_{ox}\nabla\psi\|_{0^-}) - (\varepsilon_w\nabla\psi\|_{0^+}) = q([AOH_2^+]-[AO^-])$ | $H_s^+$ - $H^+$ concentration at gate-oxide/electrolyte interface. $H_b^+$: $H^+$ concentration at the bulk electrolyte.<br>$H_s^+ = H_b^+ e^{-\frac{q\psi}{k_B T}}$ $pH = -\log_{10}(H_b^+)$<br>$N_s$ = 8e14 $cm^{-2}$ for $HfO_2$<br>$pK_a = -\log_{10}(K_a)$, $pK_b = -\log_{10}(K_b)$<br>($pK_a$, $pK_b$) = (6, 10) for $HfO_2$ |
| Electrolyte | Poisson-Boltzmann Equation<br>$-\nabla\cdot(\varepsilon_w\nabla\psi) = -2qn_0\sinh(q(\psi-V_{FG})/k_B T)$ | $\varepsilon_w$ =80$\varepsilon_0$,<br>$n_0$- buffer ion concentration (3mM, corresponding to 0.02X SSC buffer),<br>$V_{FG}$: fluid gate bias<br>$k_B$: Boltzmann constant, T-Temperature |

**Table 5.1**. Model equations of ISFET electrostatics

| Region | Model Equations | Description of Variables |
|---|---|---|
| Si-NW | Low-frequency voltage noise<br>$\sigma V_{1/f} = \sqrt{\int_{f_1}^{f_2} S_{V_{FB}} df} = \sqrt{\frac{q^2 k_B T N_t \lambda}{WLC_{eff}^2} \ln \frac{f_2}{f_1}}$<br>where $S_{V_{FB}} = \frac{q^2 k_B T N_t \lambda}{fWLC_{eff}^2}$<br>(Acceptor like interface traps ($D_{it}$) are assumed at Si/Gate oxide interface. For $SiO_2/HfO_2$ gate oxide stack, a fixed interface charge is assumed.) | $W = 0.1\mu$m, $L = 20\ \mu$m<br>$f_1$ = 1Hz, $f_2$ = 1kHz ($f_1$, $f_2$: low and high cutoff frequency)<br>$\alpha = 1.5\times10^5$ V s/C (Coulomb scattering coefficient)<br>$\lambda$ = 0.5 Å (tunneling parameter)<br>$N_t = 3\times10^{16}$ $eV^{-1}$ $cm^{-3}$, (trap density)<br>$C_{eff} = (1/C_{SiO2}+1/C_{HfO2})^{-1} = 8.17\times10^{-7}$ $F/cm^2$<br>$T$=300K |
| Electrolyte | Electrolyte bulk resistance<br>$\sigma V_e = \sqrt{\int_{f_1}^{f_2} S_{V_e} df} = \sqrt{4k_B T R_b (f_2 - f_1)}$<br>where $S_{V_e} = 4k_B T R_b$ s and $R_b \sqrt{\pi / WL} / \kappa$ | $\kappa = 0.124\times10^{-3}$ S/cm (electrolyte conductivity),<br>$k_B$: Boltzmann constant, T-Temperature |

**Table 5.2**. Model equations for noise estimation.

# 5.4 RESULTS

One of the most important components of any silicon based FET is the gate dielectric and its interface with silicon. We chose $HfO_2$ because it currently satisfies the requirements demanded for CMOS integration. Atomic layer deposition was chosen as the method for forming the gate dielectric because of its self-limiting growth process, meaning the thickness is controlled by the number of deposition cycles, allowing accurate thickness control and uniform step coverage. Moreover, due the reactive nature of the precursors, the temperature window for deposition is wide. However, the electrical and chemical properties of the film are temperature dependent as well. Before using $HfO_2$ as our gate dielectric we characterized the properties of the hafnium oxide layer as deposited and how the thermal treatments taken during our process affect the gate dielectric.

During the nanowire fabrication process, the hafnium oxide must be amenable to hydrofluoric acid wet etching in order to create the contact vias over the source-drain regions of the FET. The concentration of HF also must be gentle enough as to not deteriorate the photoresist leading us to use a 10:1 BOE as the reagent. During the course of characterization, we observed ALD deposition temperatures >200C resulted in a layer which would not etch in BOE solution. Layers deposited at <80C etched very quickly and had deposition rates much larger than the limiting rate of ~1Å/cycle. In our process we use a temperature of 120 Celsius, which gave us a good compromise between etching rate and deposition rate.

The characterization of the deposition thickness vs. number of cycles was done using ellipsometry and is shown in Figure 5.1A. Here we assumed a simple bilayer stack of $HfO_2$ and Si, with refractive indices taken from the Sopra Material Library. By depositing ALD films between 10 and 90 cycles and measuring the thickness we were able to verify the deposition rate per cycle and estimate the interfacial oxide thickness. The overall thickness (T) of the film on silicon is related to the $HfO_2$ deposition cycle number ($N_{HfO2}$) by:

$$T(nm) = R_{dep}N_{HfO2} + t_{sio2}$$

where $R_{dep}$ is the deposition rate and tsio2 the native oxide thickness. By fitting a line to the data in Figure 5.1A we get a deposition rate of 1.23 Angstroms per cycle and, if we extrapolate back to zero cycles, a native oxide thickness of 9 Angstroms. These results are within range of the reported growth rates of $HfO_2$[51,52] and thickness of a chemically grown native oxide[53].

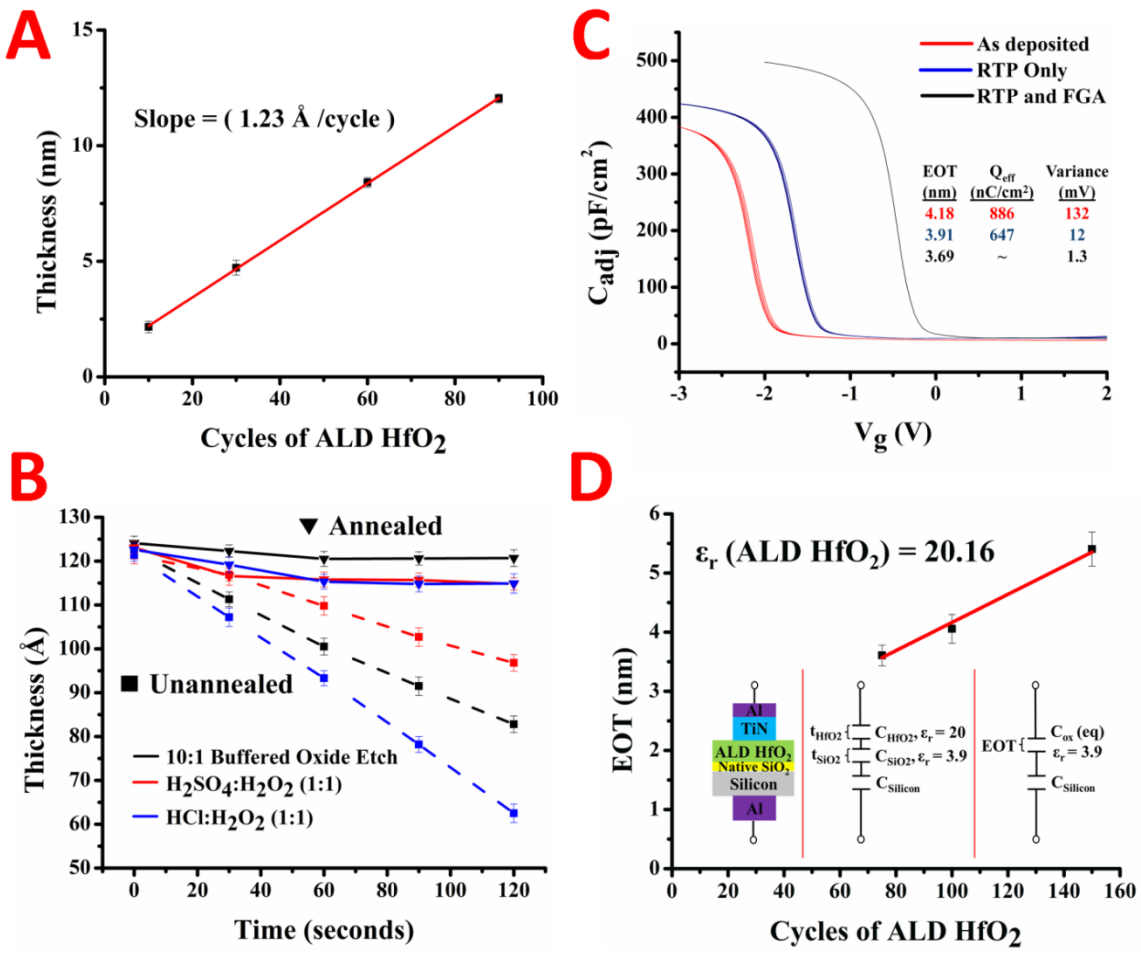


**Figure 5.1**. Characterization of the $HfO_2$ gate dielectric deposited by atomic layer deposition. The thickness of $HfO_2$ versus the amount of ALD cycles is shown in **A** with the slope inset. The effect of annealing the $HfO_2$ against chemical etchants is shown in **B** with the ellipsometric thickness versus etching time. High frequency capacitance-voltage curves for varying steps in the annealing procedure are in **C** with extracted values inset. The equivalent oxide thickness extracted from the C-V analysis versus the ALD cycle amount is plotted in **D** with the extracted dielectric constant inset.

After ALD of the hafnium oxide films, we investigated how annealing would affect the chemical and electrical properties of the gate dielectric. Annealing of the films is an important parameter in optimizing the electrical performance of the gate dielectric. $HfO_2$ begins to crystallize at temperatures >500C, and the crystallization temperature is thickness dependent, increasing with decreasing thickness.[54] Crystallization, although

helps increase the dielectric constant, is known to increase the leakage current through grain boundaries in MOS structures as well. Thus, leakage would be amplified even more in an aqueous setting where ions are even more mobile than with a top metal. During our process we decided to keep our anneal steps below 500C in order to avoid excess leakage affects. First, we perform a rapid thermal process in Ar at 500C for 60s to densify the gate dielectric. Then, after the deposition of the leads, we do a forming gas anneal (Ar/10%H2) at 450C for 30 minutes to passivate interface traps and anneal the leads. This constitutes our basic annealing procedure on the gate dielectric.

To examine how the anneal steps affected the gate dielectric chemically, we subjected the annealed and unannealed films to various strong acid etchants such as acid piranha and SC2, as well as in 10:1 BOE. The etch rates for hafnium oxide annealed vs. unannealed are presented in Figure 5.1B. The films deposited at 120C show etch susceptibility for all the etching solutions. Etch rates between 15-40 Angstroms per minute are achieved with the various etching parameters. After the rapid thermal anneal and forming gas treatments, the hafnium oxide becomes chemically inert. The ellipsometric thickness of the films only changes by ~5 Angstroms for each of the etchants. We attribute the thickness change to a thin carbonaceous layer on top of the film which is subsequently removed during exposure to the etching solutions.

In order to determine how the annealing affects the system electrically, MOS capacitors were formed by sputtering 30nm TiN then 100nm Al on the $HfO_2$ and 100nm Al on the back of p-type silicon contact to create a capacitor with a structure shown in Figure 5.1D. High frequency capacitance-voltage curves were taken for as-deposited, RTP only, and RTP+forming gas $HfO_2$ substrates. The results for a 100 cycle ALD $HfO_2$

film are shown in Figure 5.1C. Each device was swept ten times to give insight into its stability. Using the high frequency capacitance we can extract parameters such as the oxide thickness, dielectric constant, effective charge, and flatband voltage. For a p-type MOS-C, the accumulation region of the C-V curve is observed when negative voltages are applied to the gate. The oxide capacitance (COX) is the high frequency capacitance when the device is biased for strong accumulation. If we assume the oxide is one entity, MOS-C acts like a single parallel-plate capacitor and COX is related to the total oxide thickness (Tox) by:

$$C_{ox} = \frac{\varepsilon_0 K_{eff} A}{t_{ox}},$$

where $\epsilon_0$ is the permittivity of free space, A the capacitor area, and $K_{eff}$ the relative dielectric constant. From Figure 5.1C, we can see that $C_{ox}$ increases as we perform the annealing procedures, indicating that Keff is increasing and thus producing a higher quality $HfO_2$ layer. As we anneal the samples, we also notice the flatband voltage of the MOSCap's shifts to more positive potentials and the drift (or variance) becomes minimized for the RTP and forming gas system. The flatband voltage (Vfb) for MOSCap's can be expressed as:

$$V_{fb} = \emptyset_{MS} - \frac{Q_{EFF}}{C_{ox}}$$

where $\phi_{MS}$ is the work function difference between the metal and the semiconductor and $Q_{EFF}$ is the effective oxide charge density, given by the sum of the oxide fixed charge ($Q_F$), oxide mobile charge ($Q_M$), and oxide trapped charge ($Q_{OT}$) with $Q_{EFF} = Q_F + Q_M + Q_{OT}$. We extract the flatband voltage from the flatband capacitance by interpolating between the closest voltages around the flatband capacitance value. We

then extract the variance and Qeff for each MOSCap under study from the flatband voltages for each curve. The Qeff and variances for each of anneals is found in the inset in Figure 5.1C. By annealing the substrates we eliminate most of the effective charge and variance in the system. This is probably due to the removal of dangling bonds in the oxides and passivation of interface traps at the $HfO_2$-$SiO_2$ and $SiO_2$-Si interfaces.[55]

To determine the dielectric constant of the annealed $HfO_2$, different cycles amounts of $HfO_2$ were deposited and Cox determined. If we assume the dielectric is composed entirely of $SiO_2$ (since the dielectric constant is known) we can replace the Keff in equation 1 with the dielectric constant of $SiO_2$ (3.9) and extract an equivalent oxide thickness (EOT) for the layer. An example of this is found in the inset of Figure 5.1D, along with the stack for the MOS capacitors. The EOT of the $HfO_2$ MOSCap's was plotted versus the ALD cycle number (N) and is shown in Figure 5.1D. The EOT is a combination of the $HfO_2$ thickness and dielectric constant with the interfacial oxide thickness and dielectric constant. It can be expressed in a linear form by:

$$EOT(N) = \left(\frac{3.9}{K}\right) R_{dep} N + t_{sio2}$$

The dielectric constant can be extracted from the slope of the line $\left(\frac{3.9}{K}\right) R_{dep}$ assuming the deposition rate is known, which we extracted from ellipsometry. The interfacial oxide thickness is equivalent to the y-intercept of the line, or by extrapolating the fit back to zero cycles. By fitting the points in Figure 5.1D we determine a dielectric constant of 20.1 for the deposited ALD film, which meets expectations for a high-quality ALD $HfO_2$ film.[56] The extrapolated interfacial oxide thickness is ~17 Angstroms, which agrees well with literature.[57] This value is substantially higher than the extracted value from ellipsometry of ~9 Angstroms. We attribute this to the high diffusivity of

oxygen in $HfO_2$, which commonly increases the interfacial oxide thickness during anneals.[58,59]

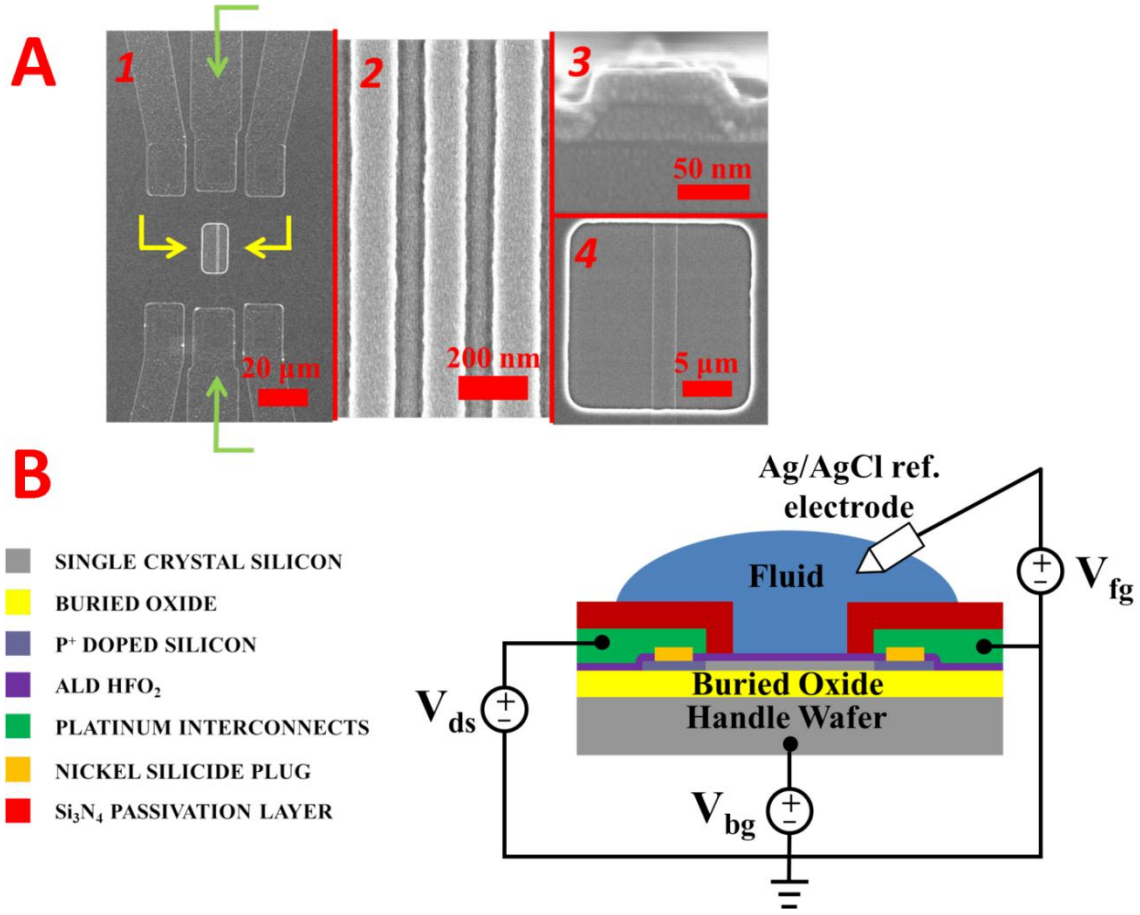


**Figure 5.2**. Scanning electron micrographs of the silicon nanowires are in **A**. Image 1 shows an overview of the nanowire sensing area, with the source-drain metal leads (green arrows) and release window (yellow arrows) highlighted. A high magnification top-down image of the nanowires is shown in 2. A cross-sectional image of a nanowire is in 3 while a top down image a nanoplate is in 4. A horizontal cross sectional schematic of sensing setup is represented in **B**. The relevant structures are color coded to the left, with an example electrical measurement setup for the source drain (Vds), fluid gate (Vfg), and back gate (Vbg).

Top down and cross section images of the nanowires and nanoplates are shown in Figure 5.2A. Part 1 of Figure 5.2A shows an overall top down image of the nanowires. The release window is in the center (highlighted by the yellow arrows) while the metal

leads connecting to the nanowires is highlighted by a green arrow. A high magnification image of the nanowires in (1) is shown in Figure 5.2A (2). The brighter areas represent the nanowires as silicon lies below the beam, increasing the secondary electron emission. The nanowires appear to be ~150nm in width from the top down image in (2), but the cross section in (3) shows them to be ~100nm wide. The cross section in (3) shows the trapezoidal nature of the nanowires from the TMAH anisotropic etch, as well as the surrounding $HfO_2$ gate dielectric. The thickness of the $HfO_2$ is approximately 13nm from the image, although it is hard to measure it precisely due to the grain size of the metal sputtering. This thickness agrees well with the thickness information obtained from Figure 5.1. A top down image for a nanoplate inside the release window is in (4), and shows a nanoplate of ~2um width.

A schematic showing the full cross section of a nanowire and the setup for device testing is in Figure 5.2B. For fluid testing, a leak free Ag/AgCl reference electrode is biased and swept, with a constant source-drain bias applied. The back of the handle wafer is grounded, and the Id-Vg transfer curve measured.

The stability of the device under operation in 0.02X SSC buffer is shown in Figure 5.3. Id-Vg curves were swept from positive to negative bias with the Ag/AgCl electrode and cycled 5 times, shown in Figure 5.3A. The subthreshold slope extracted for the device is 112mV/decade, comparatively on the low end for nanowire devices in fluid testing. Detailed numerical simulations were performed to validate experiment data (transfer characteristics in Fig. 3a) and to further explore the sensitivity of our devices for pH sensing. In this numerical model, we solve the non-linear Poisson-Boltzmann electrostatics for the sensor system (see Methods section for details). The simulation in

Figure 5.3B show that our detailed numerical simulation interprets the experimental results (red circles) consistently from subthreshold to super-threshold regime. The simulations accurately reproduce experimental transfer curves with the following parameters: Interface trap densities ($D_{it}$) of $4\times10^{11}$ $cm^{-2}eV^{-1}$, and fixed (negative) charge located at $SiO_2/HfO_2$ interface with density of ~ $5\times10^{11}$ $cm^{-2}$. These values of interface trap density are consistent with widely accepted density of dangling Si bonds at unpassivated $Si/SiO_2$ interface and the estimate of fixed trap density is also consistent with those reported the literature.

The standard deviation for threshold voltage on the devices is 2.7mV. The combination of a low standard deviation and a low subthreshold slope indicate the combination of a high stability device and low drift reference electrode in electrolytic solutions. Moreover, the fluid is exposed to a ~ 0.2 $cm^2$ area on the chip, which if not passivated properly would cause leakage current much higher than the measured device current. The leakage throughout this area ranged from 300pA to 1nA, or 1.5 $nA/cm^2$ to $5nA/cm^2$. An example of long term device stability in 0.02X SSC buffer is shown in Figure 5.3C. The threshold voltage after each sweep and the time was recorded and repeated over an hour. The change in threshold voltage over time decreases rapidly for the first 10 minutes, then stabilizes. The overall change is 65mV/hour, with only 10mV change happening after the first 10 minutes. In planar ISFETs, the gate voltage instability can be described by a stretched exponential that is characteristic of dispersive transport in disordered materials expressed by:

$$\Delta V_T(t) = \Delta V_{T_\infty}\left(1 - \exp\left(\frac{-t}{\tau}\right)^{\beta}\right)$$

where $\Delta V_{T_\infty}$ is the maximum $V_T$ change, $\tau$ is the time constant, and $\beta$ is the dispersion parameter that takes a value between $0 < \beta < 1$. As shown in Figure 5.3C, the theoretical fits according to this model (Eq. 1) agree well with the experimental data. By rearranging Eq.1 and plotting the natural logarithm versus the natural log of time (Figure 5.3D) we are able to extract the time constant ($\tau$) and the dispersion parameter ($\beta$), which are also inset in Figure 5.3D. The values for $\Delta V_{T_\infty}$ , $\beta$, and $\tau$ are 55 mV, 0.7935, and 76.75 seconds, respectively. The standard deviation of the device over 5 sweeps surrounding each time point was also plotted. Briefly, the standard deviation for sweep 15 would include points from sweep 13-17. The standard deviation shows a ~1mV standard deviation per 5 sweeps over the period of the hour. As the device equilibrates, the standard deviation between sweeps goes down. The solid red line indicates the theoretically estimated voltage noise of SiNW pH sensor composed of low-frequency noise and electrolyte noise (See Method section for the details), showing that the sensitivity is limited by the noise from measurement instrument (red triangles), not by the device's intrinsic noise. The leakage to the fluid gate, plotted over the course of an hour, stays relatively stable near 800pA (Figure 5.4). This indicates little degradation to the $HfO_2$ dielectric or passivation layer over that time period.

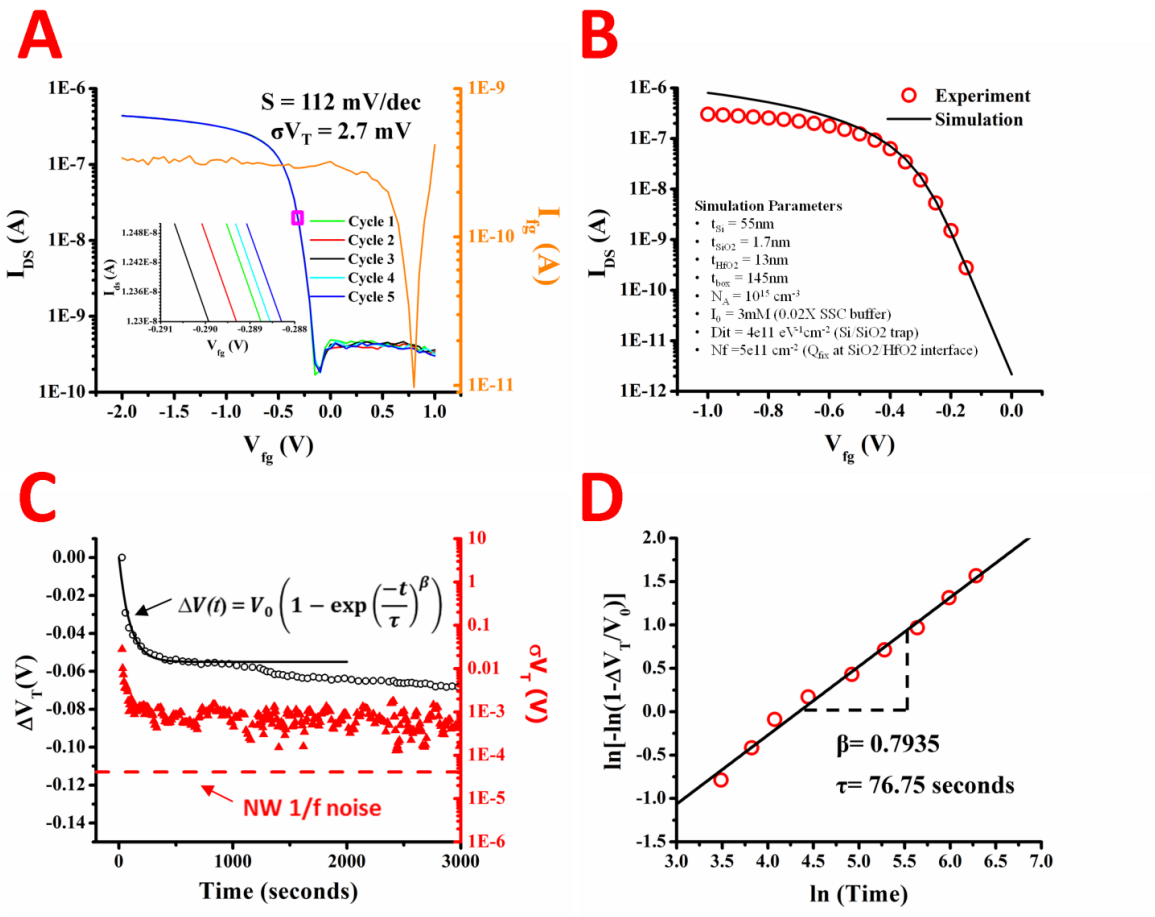


**Figure 5.3**. Representative source-drain current verse fluid gate voltage for a nanowire is shown in **A**. The nanowires were swept for 5 cycles with the fluid gate leakage also measure (right side of graph) and an enlarged view of the curve repeatability is inset in **A**. The numerical simulation (black line) of the average of the experimental transfer curves in **A** (red circles) is shown in **B** with the simulation parameters (inset).The change in the threshold voltage (left side) and standard deviation in threshold (right side) versus time for a nanowire is in **C**. The equation for modeling the gate voltage instability is inset in **C**, with the fit to the experimental data represented as the black line. The theoretically estimated low frequency voltage noise is represented as a dashed red line. The experimental $\Delta V_t$ data in **C** was rearranged according to the equation in **C** to extract the time constant and dispersion parameter. The natural log of the rearrangement is plotted in **D** versus the natural log of the time (red circles), with the linear fit to the data (black line) and the extracted parameters (inset).

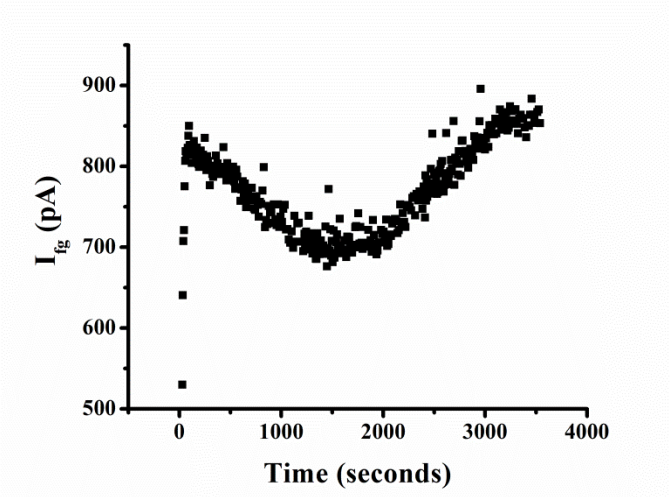


**Figure 5.4**. The measured leakage current from the device to the fluid gate ($I_{fg}$) over time for a nanowire.

The response and stability of the devices to changes in pH was demonstrated using Robinson buffers for the nanowires and nanoplates. The changes in pH will cause a change in the surface potential on the device due to the proton reactive groups on top of the $HfO_2$ surface. Robinson buffer solutions ranging from pH's of 4.3-10.5 were used and the threshold voltages of nanowires and nanoplates extracted from the Id-Vg curves. The change in the surface potential with respect to the pH 7.4 solution, set at zero, was plotted vs. pH for 3 nanowires and 3 nanoplates, and is shown in Figure 5.5. We achieve a 55.8 mV/pH sensitivity for the nanowires and 51.0 mV sensitivity for the nanoplates, with the Nernstian limit being 59mV/pH. The sensitivity of nanowires being higher than nanoplates or microwires agrees well with literature[16], as does the range of pH sensitivities found for the $HfO_2$ sensing dielectric. Our numerical simulations that applied a self-consistent solution of Poisson-Boltzmann electrostatics coupled with OH functional group site-binding model (Eqs. 5-6, see Methods section for details) reproduces key experimental trends (see insets on the right side of Fig. 5). Specifically,

the model predicts a pH sensitivity of 51mV/pH, which is very close to the experimental results.

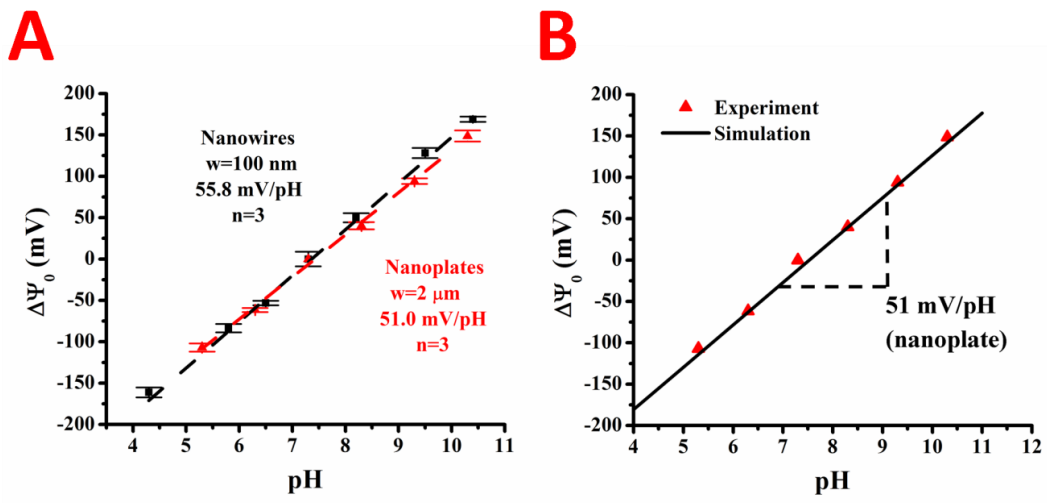


**Figure 5.5**. The change in surface potential of the $HfO_2$ sensing dielectric versus solution pH for nanowires (black) and nanoplates (red) is shown in **A**. The pH sensitivity for nanowires and nanoplates was extracted through linear regression and is displayed inset. Numerical simulations (black line) of the nanoplate data (red triangles) using self-consistent Poisson-Boltzmann electrostatics and an OH group site binding model is shown in **B,** with the extracted pH sensitivity inset.

The sensing of DNA target was done with different molecular weight PLL functionalizations using the same probe molecule. The procedure for modifying the surface is explained in detail in the Experimental section, but outlined in Figure 5.6A. Briefly, the poly-l-lysine is electrostatically adsorbed onto the $HfO_2$ surface and baked on a hotplate at 85C to ensure a good linkage. Then, the ssDNA probe is electrostatically bound to the $HfO_2$ surface and excess rinsed off. The ssDNA probe is then baked, which covalently links part of the sugar and phosphate backbone to the poly-l-lysine through free radical generation. The target is then hybridized with the probe and sensed on the device. Poly-l-lysine was chosen since it can be deposited from aqueous solution and

electrostatically bound to both the $HfO_2$ and phosphate backbone of probe DNA. This allows for the probe DNA, and binding target, to be in a horizontal conformation.[60] As opposed to a vertical conformation, a horizontal conformation allows for charge density to be closer to the surface, thus creating a larger shift in the surface potential. A horizontal conformation allows for more charge to be felt in the channel at a certain Debye length of electrolyte solution.

The sensitivities for the devices with different molecular weight poly-l-lysines are quite different, which we discuss in Figure 5.7. A lower sensitivity would occur if the overall effective charge density during binding is less, or the charges were farther removed from the surface. A few possibilities which would lead to this are the morphology of the poly-lysine layers as well as the probe density. Thus, we characterized the poly-lysine layers and probe attachment to understand the underlying reasons for this discrepancy.

We used a combination of ellipsometry, AFM, and XPS to look into the morphology, thickness, and probe densities (Table 5.3). When the PLL layers were deposited, the ellipsometric thicknesses came out to be within error of each other at ~11Å each. This indicates the formation of a polylysine monolayer on the surface. The ssDNA probe attachment came out to be within error as well, at ~20.5Å each, which leads us to believe the DNA rests in a horizontal configuration. The similar thicknesses for both indicate we should get similar sensitivity levels for target detection.

| | Ellipsometric Thickness (Å) | AFM Thickness (Å) | Roughness (Å) | XPS P 2p Peak Area |
|---|---|---|---|---|
| **$HfO_2$ layer** | 120.1 ± 3.2 | — | 1.1 | — |
| **PLL 9-14K** | 11.3 ± 1.5 | 11.2 | 1.6 | — |
| **PLL 70-150K** | 12.1 ± 2.1 | 9.8 | 3.4 | — |
| **ssDNA (PLL 9-14K)** | 21.6 ± 2.3 | — | 1.9 | 145.7 |
| **ssDNA (PLL 70-150K)** | 19.8 ± 2.7 | — | 2.9 | 74.2 |

**Table 5.3**. Characterization of the thickness, roughness, and probe density of the HfO2 surface functionalization process.

Thus, we utilized atomic force microscopy (AFM) to characterize the morphology of the 100 cycle ALD $HfO_2$ layer and the PLL layers. The tapping mode images in Figure 5B are numbered 1-3 in the image set for the untreated $HfO_2$, PLL (9-14k), and PLL (70-150k), respectively. The images for the untreated $HfO_2$ and PLL (9-14k) indicate very smooth and uniform layers. The roughness values extracted for the $HfO_2$ and PLL (9-14k) are 1.1 and 1.6Å RMS, respectively. The morphology of the PLL (70-150k) is much rougher and has a porous, spongelike appearance. These pores, represented by the darker spotted areas in the image, appear to be the thickness of the monolayer or close to it. Moreover, we were able to determine the thickness of the films by applying a 50nN force to the tip in contact mode and scratching away the PLL layers, then reimaging a larger area in tapping mode. A 50nN force is known to be more than enough to remove organic monolayers and silane layers, without damaging the underlying surface.[61] The images after a 50nN force are 4-6 in the image set. The untreated $HfO_2$ shows no changes in height, indicating a hard surface. The PLL layers show distinct changes in thickness, indicated by the square scratched area visualized in images 5 and 6. Taking a section analysis across the scratched areas gives us the thickness of the PLL films, and is shown in Figure 5.6C. The images 4-6 in 5B are color coded to match up with section analyses in Figure 5.6C. The section analyses showed a similar thickness for the PLL layers

compared to ellipsometry and are in Table 5.3. However, the buildup of material on the side of the scratched away area was much greater for the lower molecular weight layer (data not shown). This indicates the amount of material for the higher molecular weight PLL on the substrate was less, leaning towards the evidence of a more porous and incomplete layer.

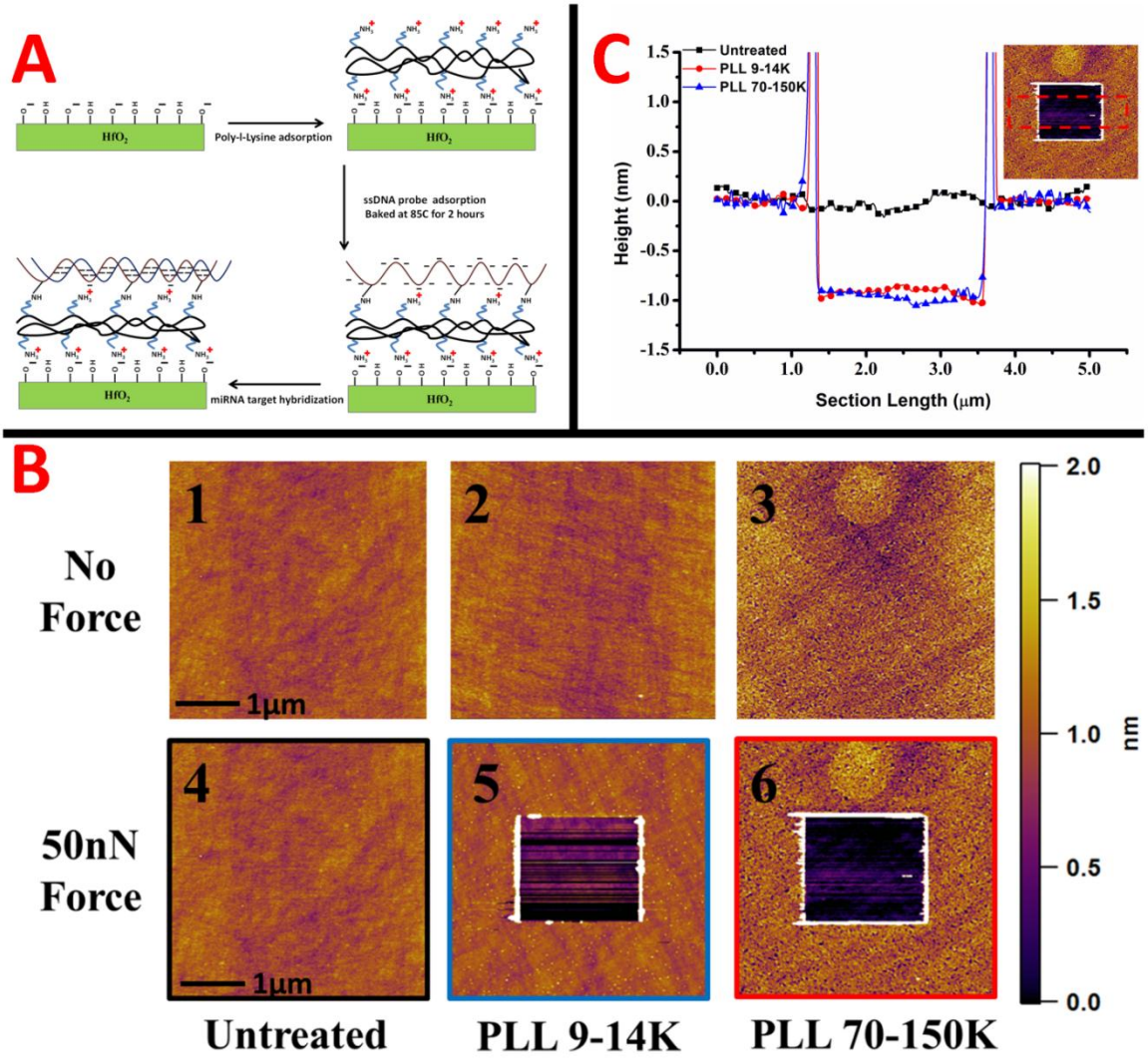


**Figure 5.6**. A schematic of the surface functionalization of the $HfO_2$ surface for microRNA (DNA analogue) sensing is shown in **A**. AFM images of the HfO2 and poly-l-lysine layers of different molecular weights are shown in **B**. Tapping mode images with no force applied (upper) for the different layers, and after a 50nN scratching force (bottom) are displayed. The scale bar for all AFM images is on the right. A cross section for the images with 50nN force applied is in part **C**. The cross sections are color coded to images in **B** with an inset representing the cross sectional area.

Attachment of the probe DNA to the PLL layers was measured using two techniques: (1) XPS for the P2p peak intensity from the DNA backbone and (2) fluorescence with a Texas Red labeled miR-10b probe. The XPS P2p signal intensity for

the $HfO_2$ and probe DNA on the two PLL layers is in Figure 5.7A. The peak for the ssDNA on PLL(9-14k) is much larger than the one on PLL (70-150k), indicating a higher probe density. The peak intensities are in Table 5.3, with a ratio of approximately 1.8:1 for the PLL(9-14k):PLL(70-150k). The fluorescently labeled micrographs of bare $HfO_2$ and PLL layers, both with and without probe are in Figure 5.7B. The quantification of the fluorescent intensity is in the bar graph in Figure 5.7C. Images 1 and 2 show the bare $HfO_2$ layer with and without the probe attachment procedure. The amount of background fluorescence for the $HfO_2$ with and without probe is about the same. Thus, DNA has very little non-specific adsorption to $HfO_2$, which should make for better selectivity and less issues with blocking. Images 3 and 4 show the background fluorescence for the PLL layers. The PLL (9-14k) layer shows slightly higher background, as to be expected since there are more optically active surface groups according to AFM. The images for the attachment of the miR-10b probe DNA show slightly greater than a two-fold intensity difference between the PLL layers, with PLL (9-14k) containing the higher probe density. This reaffirms the XPS results in Figure 5.7A, indicating the probe density is much higher on the lower molecular weight PLL layer.

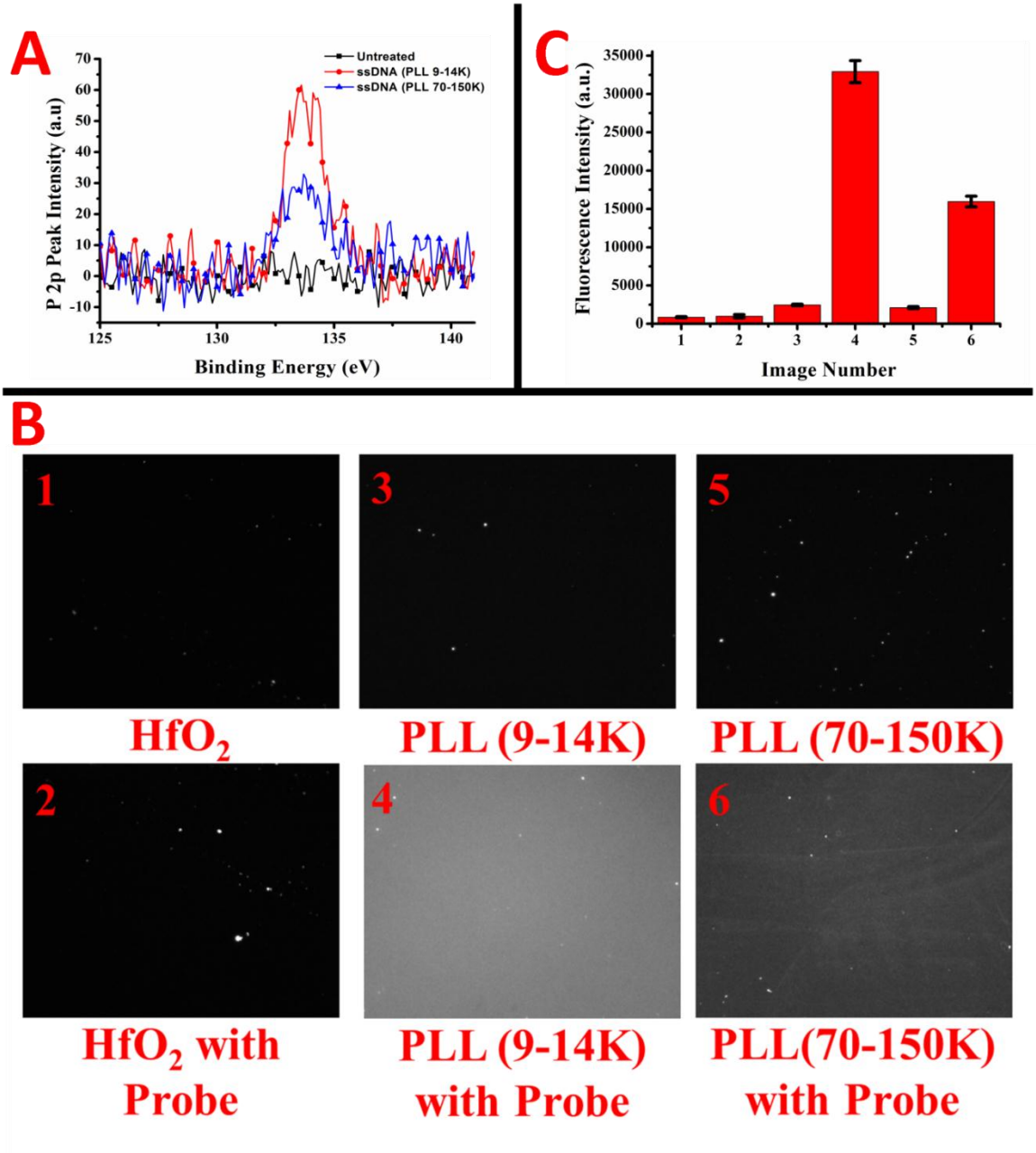


**Figure 5.7**. P2p peak intensities from XPS are shown in **A** for ssDNA adsorption onto the poly-l-lysine layers of different molecular weights, and onto the bare HfO2 surface. Fluorescent micrographs of ssDNA probe immobilization are shown in **B** for HfO2 and the different molecular weight poly-l-lysines, both with and without exposure to ssDNA probe. Fluorescent intensities for images 1-6 in **B** are plotted in column format in **C**.

The demonstration of sensing of miR-10b DNA analogue target on the $HfO_2$ silicon nanowires is in Figure 5.9, with the DNA probe and target sequences in Table 5.4. To make sure the devices were being functionalized properly, Id-Vg curves at key steps during the probe attachment process were taken to examine the changes in threshold voltage (Figure 5.8). First, a reference of the bare $HfO_2$ was taken in the 0.02X SSC sensing buffer. The deposition of PLL then shifts the threshold voltage to the left by ~160mV. The direction of change is proper since the PLL is positively charged and the device operates in accumulation mode, thus creating a more negative threshold to compensate for the positive increase in surface potential. In contrast, when we adsorb the probe DNA we cause a shift in the opposite direction of ~90mV relative to the PLL, which is also expected due to the negative charge density of the phosphate backbone.

| | **Sequence** |
|---|---|
| **DNA probe** | 5'-CACAAATTCGGTTCTACAGGGTA -3' |
| **miR-10b DNA complementary target** | 5'-TACCCTGTAGAACCGAATTTGTG-3' |
| **miR-21 DNA non-complementary target** | 5'-TAGCTTATCAGACTGATGTTGA-3' |

**Table 5.4**. Nucleic acid sequences for the immobilized probe and DNA targets.

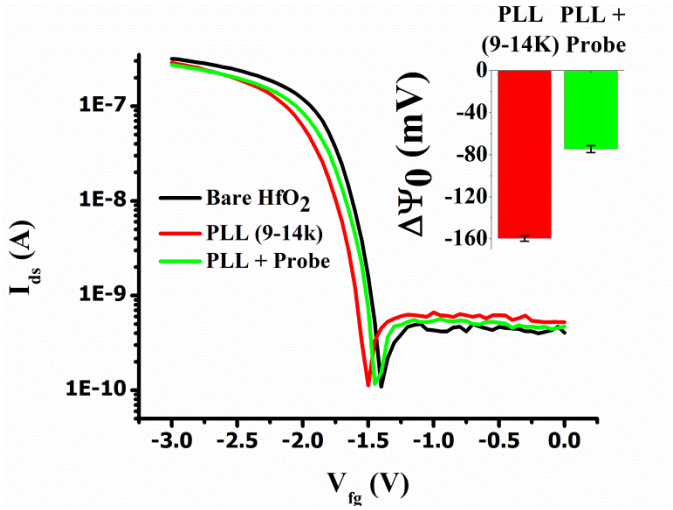


**Figure 5.8**. Id-Vg transfer curves of the surface functionalization process with PLL (9-14K) and probe DNA**.** The changes in surface potential from the reference $HfO_2$ ( inset) show a negative shift for the PLL deposition and a corresponding positive shift for the probe immobilization. The deposition of PLL shifts the threshold voltage to the left by ~160mV, relative to the $HfO_2$ reference. The probe DNA immobilization shifts the threshold voltage back to the right by ~90mV, relative to the PLL functionalization.

After conjugating the ssDNA probe to the PLL surface, various concentrations of miR-10b target were allowed to interact with the sensor for 30 mins (to offer sufficient time for diffusion limited transport down to 100 fM concentration[62]), then rinsed off and Id-Vg curves recorded in the .02X SSC sensing buffer. The threshold voltage change with varying RNA target concentrations was then measured relative to the ssDNA probe reference (shown in Figure 5.9A). The signal-to-noise ratio (SNR) for the measurements was computed and a blue line drawn for 3xSNR, assumed to be the limit of detection for the device. For the lower molecular weight poly-lysine, at least 100fM of miR-10b target was able to be sensed, with an extrapolated limit of detection of 1fM. However, for the higher molecular weight poly-lysine, the limit of detection at 3xSNR is close to 1nM, close to 6 orders of magnitude higher. When the mismatch miR-21 target was allowed to hybridize with the miR-10b probe, the signal was very small and steady from 100fM all

the way to 1uM concentrations. Most of the miR-21 signals were close to or between 0-5mV change in signal. Error bars for the standard deviation of sweeps over the measurement are also presented on the graph for each case.

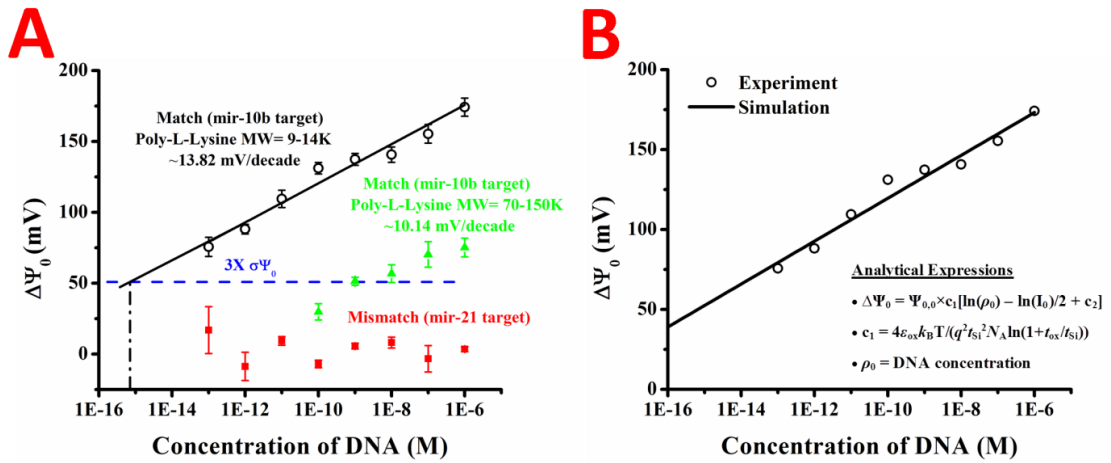


**Figure 5.9**. The change in surface potential versus the concentration of target in solution is plotted in **A** for the two different poly-l-lysines. The change in surface potential for the mismatched target is shown to be negligible (red squares) and a theoretical limit of detection line is drawn in blue. The change in surface potential versus the DNA concentration for the PLL (9-14K) data was also theoretically calculated, and is shown in **B**. The change in the surface potential (black circles) matches the theoretical prediction (black line) well. The analytical expressions used for the calculation are inset in **B**. The parameters used in the theoretical calculation of $\Delta\Psi_0$ are: $t_{Si}$ = 55nm, $t_{ox}$ (EOT) = 4.22nm, NA = $10^{15}$cm$^{-3}$, and $I_0$ = 3mM. The device specific parameters are $\Psi_{0,0}$ = 58.3mV and c2=40.63.

An important feature of the DNA detection sensitivity of NW sensor is that it follows the *logarithmic* dependency on the molecular concentration due to screening by the salt (i.e., $\Delta\Psi_0 \sim \ln(\rho_0)$, where $\rho_0$ is the DNA concentration).[63] The black solid line represents (Figure 5.9B) the corresponding theoretical estimation of $\Delta\Psi_0 = \Psi_{0,0} \times c_1[\ln(\rho_0) - \ln(I_0)/2 + c_2]$ where $c_1 = 4\varepsilon_{ox}k_BT/(q^2 t_{Si}^2 N_A \ln(1+t_{ox}/t_{Si}))$ $\Psi_{0,0}$ and $c_2$ are parameters that depend on device properties, pH and duration of sensing (e.g. 30 min).

The fact that the lower molecular weight PLL shows such higher sensitivity may be attributed to differences in the monolayers. Most important, the overall probe

attachment density is much less on the higher molecular weight layer. This will decrease the total amount of binding target, thus causing smaller shifts in surface potential. Moreover, the roughness of the high molecular weight PLL is larger and looks porous compared to the other layer. If the pore sizes are of the width of the nanowires or smaller, this would lead to large void spaces over the nanowire area without probe, making the microscopic amount of probe DNA even less than in the case for a macroscopic image.

## 5.5 CONCLUSIONS

In this paper, we have presented a process for the fabrication of $HfO_2$ based top down silicon nanowires and nanoplates with high stability and robustness in fluid. The ALD process for creating the $HfO_2$ gate dielectric was thoroughly characterized by ellipsometry, AFM, and CV measurements to assure us of a high quality layer. The devices respond to pH in accordance to sensitivities of other $HfO_2$ ISFET's, with nanowires slightly more sensitive than plates. Moreover, we characterized the difference between different molecular weight layers of PLL in terms of their surface morphology, thickness, and probe attachment densities. The average thicknesses of the layers were found to be about the same by AFM and ellipsometry, however the probe density of the lower molecular weight PLL was about twice as much as the higher molecular weight one. This was confirmed by both fluorescence and XPS. Moreover, the AFM indicated the higher molecular weight PLL was much rougher and porous, perhaps contributing to the lower response to DNA target using this polymer. Using these different layers for sensing of single stranded DNA oligomers on a nanowire yielded limit of detection differences over 5 orders of magnitude, with the lower molecular weight PLL having higher sensitivity. By using the lower molecular weight poly-l-lysine, we were able to

detect down to 100fM of miR-10b DNA analogue with a theoretical limit of detection of 1fM.

## 5.6 REFERENCES


[1]. Harvey, M. A., Point-of-Care Laboratory Testing in Critical Care. *American Journal of Critical Care* 1999, 8, 72-83.

[2]. Kilgore, M. L.; Steindel, S. J.; Smith, J. A., Evaluating Stat Testing Options in an Academic Health Center: Therapeutic Turnaround Time and Staff Satisfaction. *Clinical Chemistry* 1998, 44, 1597-1603.

[3]. Douketis, J. D., Patient Self-Monitoring of Oral Anticoagulant Therapy: Potential Benefits and Implications for Clinical Practice. *American journal of cardiovascular drugs : drugs, devices, and other interventions* 2001, 1, 245-251.

[4]. Price, C. P., Regular Review: Point of Care Testing. *British Medical Journal* 2001, 322, 1285-1288.

[5]. Bergveld, P., Thirty Years of Isfetology: What Happened in the Past 30 Years and What May Happen in the Next 30 Years. *Sensors and Actuators, B: Chemical* 2003, 88, 1-20.

[6]. Kimura, J.; Kuriyama, T., Fet Biosensors. *Journal of Biotechnology* 1990, 15, 239-254.

[7]. Lee, C. S.; Kyu Kim, S.; Kim, M., Ion-Sensitive Field-Effect Transistor for Biological Sensing. *Sensors* 2009, 9, 7111-7131.

[8]. Sandifer, J. R.; Voycheck, J. J., A Review of Biosensor and Industrial Applications of Ph-Isfets and an Evaluation of Honeywell's "Durafet". *Mikrochimica Acta* 1999, 131, 91-98.

[9]. Schöning, M. J.; Poghossian, A., Bio Feds (Field-Effect Devices): State-of-the-Art and New Directions. *Electroanalysis* 2006, 18, 1893-1900.

[10]. Yuqing, M.; Jianguo, G.; Jianrong, C., Ion Sensitive Field Effect Transducer-Based Biosensors. *Biotechnology Advances* 2003, 21, 527-534.

[11]. Patolsky, F.; Zheng, G. F.; Lieber, C. M., Fabrication of Silicon Nanowire Devices for Ultrasensitive, Label-Free, Real-Time Detection of Biological and Chemical Species. *Nature Protocols* 2006, 1, 1711-1724.

[12]. Zheng, G. F.; Patolsky, F.; Cui, Y.; Wang, W. U.; Lieber, C. M., Multiplexed Electrical Detection of Cancer Markers with Nanowire Sensor Arrays. *Nature Biotechnology* 2005, 23, 1294-1301.

[13]. Cui, Y.; Wei, Q. Q.; Park, H. K.; Lieber, C. M., Nanowire Nanosensors for Highly Sensitive and Selective Detection of Biological and Chemical Species. *Science* 2001, 293, 1289-1292.

[14]. Stern, E.; Vacic, A.; Rajan, N. K.; Criscione, J. M.; Park, J.; Ilic, B. R.; Mooney, D. J.; Reed, M. A.; Fahmy, T. M., Label-Free Biomarker Detection from Whole Blood. *Nature Nanotechnology* 2010, 5, 138-142.

[15]. Stern, E.; Vacic, A.; Li, C.; Ishikawa, F. N.; Zhou, C. W.; Reed, M. A.; Fahmy, T. M., A Nanoelectronic Enzyme-Linked Immunosorbent Assay for Detection of Proteins in Physiological Solutions. *Small* 2010, 6, 232-238.

[16]. Stern, E.; Klemic, J. F.; Routenberg, D. A.; Wyrembak, P. N.; Turner-Evans, D. B.; Hamilton, A. D.; LaVan, D. A.; Fahmy, T. M.; Reed, M. A., Label-Free Immunodetection with Cmos-Compatible Semiconducting Nanowires. *Nature* 2007, 445, 519-522.

[17]. Li, Z.; Chen, Y.; Li, X.; Kamins, T. I.; Nauka, K.; Williams, R. S., Sequence-Specific Label-Free DNA Sensors Based on Silicon Nanowires. *Nano Letters* 2004, 4, 245-247.

[18]. Hahm, J.; Lieber, C. M., Direct Ultrasensitive Electrical Detection of DNA and DNA Sequence Variations Using Nanowire Nanosensors. *Nano Letters* 2004, 4, 51-54.

[19]. Fritz, J.; Cooper, E. B.; Gaudet, S.; Sorger, P. K.; Manalis, S. R., Electronic Detection of DNA by Its Intrinsic Molecular Charge. *Proceedings of the National Academy of Sciences of the United States of America* 2002, 99, 14142-14146.

[20]. Gao, A.; Lu, N.; Dai, P.; Li, T.; Pei, H.; Gao, X.; Gong, Y.; Wang, Y.; Fan, C., Silicon-Nanowire-Based Cmos-Compatible Field-Effect Transistor Nanosensors for Ultrasensitive Electrical Detection of Nucleic Acids. *Nano Letters* 2011, 11, 3974-3978.

[21]. Zhang, G. J.; Chua, J. H.; Chee, R. E.; Agarwal, A.; Wong, S. M., Label-Free Direct Detection of Mirnas with Silicon Nanowire Biosensors. *Biosensors & Bioelectronics* 2009, 24, 2504-2508.

[22]. Luo, L.; Jie, J.; Zhang, W.; He, Z.; Wang, J.; Yuan, G.; Wu, L. C. M.; Lee, S. T., Silicon Nanowire Sensors for Hg2+ and Cd2+ Ions. *Applied Physics Letters* 2009, 94.

[23]. Wang, W. U.; Chen, C.; Lin, K. H.; Fang, Y.; Lieber, C. M., Label-Free Detection of Small-Molecule-Protein Interactions by Using Nanowire Nanosensors. *Proceedings of the National Academy of Sciences of the United States of America* 2005, 102, 3208-3212.

[24]. Elibol, O. H.; Morisette, D.; Akin, D.; Denton, J. P.; Bashir, R., Integrated Nanoscale Silicon Sensors Using Top-Down Fabrication. *Applied Physics Letters* 2003, 83, 4613-4615.

[25]. Kim, A.; Ah, C. S.; Yu, H. Y.; Yang, J. H.; Baek, I. B.; Ahn, C. G.; Park, C. W.; Jun, M. S.; Lee, S., Ultrasensitive, Label-Free, and Real-Time Immunodetection Using Silicon Field-Effect Transistors. *Applied Physics Letters* 2007, 91.

[26]. Choi, S.; Park, I.; Hao, Z.; Holman, H. Y. N.; Pisano, A. P., Quantitative Studies of Long-Term Stable, Top-Down Fabricated Silicon Nanowire Ph Sensors. *Applied Physics A: Materials Science and Processing* 2012, 1-8.

[27]. Ginet, P.; Akiyama, S.; Takama, N.; Fujita, H.; Kim, B., Cmos-Compatible Fabrication of Top-Gated Field-Effect Transistor Silicon Nanowire-Based Biosensors. *Journal of Micromechanics and Microengineering* 2011, 21.

[28]. Park, I.; Li, Z.; Pisano, A. P.; Williams, R. S., Top-Down Fabricated Silicon Nanowire Sensors for Real-Time Chemical Detection. *Nanotechnology* 2010, 21.

[29]. Tong, H. D.; Chen, S.; Van Der Wiel, W. G.; Carlen, E. T.; Van Berg, A. D., Novel Top-Down Wafer-Scale Fabrication of Single Crystal Silicon Nanowires. *Nano Letters* 2009, 9, 1015-1022.

[30]. Chen, S.; Bomer, J. G.; Van der Wiel, W. G.; Carlen, E. T.; Van Den Berg, A., Top-Down Fabrication of Sub-30 Nm Monocrystalline Silicon Nanowires Using Conventional Microfabrication. *ACS Nano* 2009, 3, 3485-3492.

[31]. Chen, S.; Nyholm, L.; Jokilaakso, N.; Karlstrm, A. E.; Linnros, J.; Smith, U.; Zhang, S. L., Current Instability for Silicon Nanowire Field-Effect Sensors Operating in Electrolyte with Platinum Gate Electrodes. *Electrochemical and Solid-State Letters* 2011, 14, J34-J37.

[32]. Kim, S.; Kim, K.; Rim, T.; Park, C.; Cho, D.; Baek, C. K.; Jeong, Y. H.; Meyyappan, M.; Lee, J. S. In *Ph Sensing and Noise Characteristics of Si Nanowire Ion-Sensitive Field Effect Transistors*, Kaohsiung, Kaohsiung, 2011; pp 1233-1236.

[33]. Lu, M. P.; Hsiao, C. Y.; Lai, W. T.; Yang, Y. S., Probing the Sensitivity of Nanowire-Based Biosensors Using Liquid-Gating. *Nanotechnology* 2010, 21.

[34]. Rajan, N. K.; Routenberg, D. A.; Chen, J.; Reed, M. A., Temperature Dependence of 1/F Noise Mechanisms in Silicon Nanowire Biochemical Field Effect Transistors. *Applied Physics Letters* 2010, 97, -.

[35]. Zemel, J. N., Microfabricated Nonoptical Chemical Sensors. *Review of Scientific Instruments* 1990, 61, 1579-1606.

[36]. Bousse, L.; Bergveld, P., The Role of Buried Oh Sites in the Response Mechanism of Inorganic-Gate Ph-Sensitive Isfets. *Sensors and Actuators* 1984, 6, 65-78.

[37]. Chen, S.; Bomer, J. G.; Carlen, E. T.; Van Den Berg, A., Al2o3/Silicon Nanoisfet with near Ideal Nernstian Response. *Nano Letters* 2011, 11, 2334-2341.

[38]. Zafar, S.; D'Emic, C.; Afzali, A.; Fletcher, B.; Zhu, Y.; Ning, T., Optimization of Ph Sensing Using Silicon Nanowire Field Effect Transistors with Hfo2 as the Sensing Surface. *Nanotechnology* 2011, 22.

[39]. Rothberg, J. M.; Hinz, W.; Rearick, T. M.; Schultz, J.; Mileski, W.; Davey, M.; Leamon, J. H.; Johnson, K.; Milgrew, M. J.; Edwards, M., et al., An Integrated Semiconductor Device Enabling Non-Optical Genome Sequencing. *Nature* 2011, 475, 348-352.

[40]. Reddy Jr, B.; Dorvel, B. R.; Go, J.; Nair, P. R.; Elibol, O. H.; Credo, G. M.; Daniels, J. S.; Chow, E. K. C.; Su, X.; Varma, M., et al., High-K Dielectric Al2o3 Nanowire and Nanoplate Field Effect Sensors for Improved Ph Sensing. *Biomedical Microdevices* 2011, 13, 335-344.

[41]. Robertson, J., High Dielectric Constant Oxides. *European Physical Journal-Applied Physics* 2004, 28, 265-291.

[42]. Lai, C. S.; Yang, C. M.; Lu, T. F., Ph Sensitivity Improvement on 8 Nm Thick Hafnium Oxide by Post Deposition Annealing. *Electrochemical and Solid-State Letters* 2006, 9, G90-G92.

[43]. Van Der Wal, P. D.; Briand, D.; Mondin, G.; Jenny, S.; Jeanneret, S.; Millon, C.; Roussel, H.; Dubourdieu, C.; De Rooij, N. F. In *High-K Dielectrics for Use as Isfet Gate Oxides*, 2004; pp 677-680.

[44]. Chen, Y. W.; Liu, M.; Kaneko, T.; McIntyre, P. C., Atomic Layer Deposited Hafnium Oxide Gate Dielectrics for Charge-Based Biosensors. *Electrochemical and Solid-State Letters* 2010, 13, G29-G32.

[45]. Gabriely, G.; Teplyuk, N. M.; Krichevsky, A. M., Context Effect: Microrna-10b in Cancer Cell Proliferation, Spread and Death. *Autophagy* 2011, 7, 1384-1386.

[46]. Iyevleva, A. G.; Kuligina, E. S.; Mitiushkina, N. V.; Togo, A. V.; Miki, Y.; Imyanitov, E. N., High Level of Mir-21, Mir-10b, and Mir-31 Expression in Bilateral Vs. Unilateral Breast Carcinomas. *Breast Cancer Research and Treatment* 2012, 131, 1049-1059.

[47]. Ma, L.; Reinhardt, F.; Pan, E.; Soutschek, J.; Bhat, B.; Marcusson, E. G.; Teruya-Feldstein, J.; Bell, G. W.; Weinberg, R. A., Therapeutic Silencing of Mir-10b Inhibits Metastasis in a Mouse Mammary Tumor Model. *Nature Biotechnology* 2010, 28, 341-347.

[48]. Ma, L.; Teruya-Feldstein, J.; Weinberg, R. A., Tumour Invasion and Metastasis Initiated by Microrna-10b in Breast Cancer. *Nature* 2007, 449, 682-688.

[49]. Cissell, K. A.; Rahimi, Y.; Shrestha, S.; Hunt, E. A.; Deo, S. K., Bioluminescence-Based Detection of Microrna, Mir21 in Breast Cancer Cells. *Analytical Chemistry* 2008, 80, 2319-2325.

[50]. Liang, Y.; Ridzon, D.; Wong, L.; Chen, C., Characterization of Microrna Expression Profiles in Normal Human Tissues. *BMC Genomics* 2007, 8.

[51]. Hausmann, D. M.; Kim, E.; Becker, J.; Gordon, R. G., Atomic Layer Deposition of Hafnium and Zirconium Oxides Using Metal Amide Precursors. *Chemistry of Materials* 2002, 14, 4350-4358.

[52]. Kukli, K.; Ritala, M.; Sajavaara, T.; Keinonen, J.; Leskelä, M., Atomic Layer Deposition of Hafnium Dioxide Films from Hafnium Tetrakis(Ethylmethylamide) and Water. *Chemical Vapor Deposition* 2002, 8, 199-204.

[53]. Bohra, F.; Jiang, B.; Zuo, J. M., Textured Crystallization of Ultrathin Hafnium Oxide Films on Silicon Substrate. *Applied Physics Letters* 2007, 90.

[54]. Wilk, G. D.; Wallace, R. M.; Anthony, J. M., Hafnium and Zirconium Silicates for Advanced Gate Dielectrics. *Journal of Applied Physics* 2000, 87, 484-492.

[55]. E.H Nicollian, J. R. B., *Mos Physics and Technology*. Wiley: New York, NY, 1982.

[56]. Callegari, A.; Cartier, E.; Gribelyuk, M.; Okorn-Schmidt, H. F.; Zabel, T., Physical and Electrical Characterization of Hafnium Oxide and Hafnium Silicate Sputtered Films. *Journal of Applied Physics* 2001, 90, 6466-6475.

[57]. Zhong, L.; Daniel, W. L.; Zhang, Z.; Campbell, S. A.; Gladfelter, W. L., Atomic Layer Deposition, Characterization, and Dielectric Properties of Hfo2/Sio2 Nanolaminates and Comparisons with Their Homogeneous Mixtures. *Chemical Vapor Deposition* 2006, 12, 143-150.

[58]. Goncharova, L. V.; Dalponte, M.; Feng, T.; Gustafsson, T.; Garfunkel, E.; Lysaght, P. S.; Bersuker, G., Diffusion and Interface Growth in Hafnium Oxide and Silicate Ultrathin Films on Si(001). *Physical Review B - Condensed Matter and Materials Physics* 2011, 83.

[59]. Rudenja, S.; Minko, A.; Buchanan, D. A., Low-Temperature Deposition of Stoichiometric Hfo2 on Silicon: Analysis and Quantification of the Hfo2/Si Interface from Electrical and Xps Measurements. *Applied Surface Science* 2010, 257, 17-21.

[60]. Saprigin, A. V.; Thomas, C. W.; Dulcey, C. S.; Patterson Jr, C. H.; Spector, M. S., Spectroscopic Quantification of Covalently Immobilized Oligonucleotides. *Surface and Interface Analysis* 2005, 37, 24-32.

[61]. Crampton, N.; Bonass, W. A.; Kirkham, J.; Thomson, N. H., Formation of Aminosilane-Functionalized Mica for Atomic Force Microscopy Imaging of DNA. *Langmuir* 2005, 21, 7884-7891.

[62]. Nair, P. R.; Alam, M. A., Performance Limits of Nanobiosensors. *Applied Physics Letters* 2006, 88, -.

[63]. Nair, P. R.; Alam, M. A., Screening-Limited Response of Nanobiosensors. *Nano Letters* 2008, 8, 1281-1285.

[64]. Lambacher, A.; Fromherz, P., Fluorescence Interference-Contrast Microscopy on Oxidized Silicon Using a Monomolecular Dye Layer. *Applied Physics a-Materials Science & Processing* 1996, 63, 207-21.

# CHAPTER 6: CONCLUSIONS AND FUTURE WORK

To conclude this thesis I would like to summary our work and the contributions we have made to the field. In the beginning we addressed the fundamental problems of functionalizing the interfaces of oxide based FET's, and how a pristine interface is key into achieving optimum sensitivity. We describe a method of vapor based deposition of monofunctional silanes for biointerfacing molecules to oxide substrates. These monofunctional silanes erased the issue of added roughness and polymerization, a common problem with other linking chemistries, and provided a highly uniform and dense interface for bioconjugation. Moreover, we thoroughly characterized the system and demonstrated its application not only to silicon nanowires, but to microarrays, and nanoparticle depositions.

Second, we tackled the issues of fabricating repeatable devices and developing protocols for their functionalization buy using the devices as the standard. We demonstrate effective protocols for releasing devices and annealing them to provide highly stable systems, and describe them in detail so others may follow. Additionally, we characterize the functionalization process on the FET's electrically, using the above silane monolayer process with different linkers, and develop a protocol for bioconjugation which give optimum sensitivity and specificity. We demonstrate this protocol using immunoglobulins on multiple devices which can be compared due to similar characteristics, and with different oxide thicknesses. The devices demonstrate detection limits down fM levels, with dynamic ranges that can cover 4 orders of magnitude, and depends on the oxide thickness.

Finally, we take the fabrication of devices a step further by using hafnium oxide as a gate dielectric for sensing. This was able to provide us with capacitances higher than the previous device structures, without sacrificing device integrity. We characterized the fabrication of these devices in detail using classic semiconductor methods, and the functionalization protocols. We fabricate devices of different widths and show the differences in there sensitivities towards clinically relevant microRNA targets on multiple devices. Using an optimized high-k silicon nanowire process, we demonstrate the detection of a clinically relevant microRNA strand (mir-10b) with detection limits down to 10fM, against a similar competing microRNA strand (mir21), which shows minimal binding over 6 orders of magnitude.

In the future, we are hoping to bring this technology to the foundry level, so it may be scaled up and provide even higher quality devices. We are currently collaborating with foundries to make this process a reality. Moreover, we are attempting to integrate this fabrication process where monitoring multiple devices at once is easier. We are in the process of attempting to create packages for chips where leads can be wire bonded to a PCB, and the package inserted into a multiplexor, so that device reading may be taken, and then cycled to the next device instead of manual probing. We hope these steps we have taken bring the concept of silicon nanowires FET as a biosensor to becoming a reality.